Max-Planck-Institut für Quantenoptik
Physik-Department der Technischen Universität München

Reactive Cluster Impact Dynamics and Ion Processes Investigated by Cluster Impact Mass Spectrometry

Christoph R. Gebhardt

Vollständiger Abdruck der von der Fakultät für Physik der Technischen Universität München zur Erlangung des akademischen Grades eines
Doktors der Naturwissenschaften
genehmigten Dissertation.

Vorsitzender: Univ.-Prof. Dr. S. Fischer

Prüfer der Dissertation:

1. apl. Prof. Dr. K.-L. Kompa,
   Ludwig-Maximilians-Universität München
2. Univ.-Prof. Dr. Dr. h.c. D. Menzel
3. Priv.-Doz. Dr. G. Dollinger (schriftliche Beurteilung)

Die Dissertation wurde am 19.05.2000 bei der Technischen Universität München eingereicht und durch die Fakultät für Physik am 19.09.2000 angenommen.

Summary

The motivation behind this work is the desire to obtain direct insight into the physical and chemical processes of bulk liquids, in particular charge transfer or charge separation processes in a polar solvent. This class of processes are fundamental to our every day experience, nevertheless they still lack complete understanding, not least with respect to their inherent dynamics. Typical examples are electron transfer reactions like the spontaneous ionization of alkali atoms in liquid ammonia, proton transfer reactions as exemplified in the autoprotolysis reaction of bulk water, and solvation phenomena like the dissolution of sodium chloride in a solvent. Direct observation of these processes has up to now been impeded by the contrast between the high particle density which defines these bulk processes and the need to do analysis on a single particle level.

The central idea presented in this work is to employ molecular clusters as 'test tubes' in which the above processes can be initiated at bulk density, and to inspect the result by disintegrating the cluster via a low-energy cluster-surface collision. The fragmentation of the cluster causes the contents of the 'test tube' to spill out and it transfers the reaction products into the gas phase in the form of single molecules or small-sized aggregates that allow for straightforward and unambiguous analysis in a mass spectrometer. Of central importance is the unique division between strong intramolecular and weaker intermolecular binding energy regimes which occurs in molecular clusters. By coupling energy into the cluster via a low-energy surface collision, the weak intermolecular bonds can be ruptured without activating the strong intramolecular ones, so that the chemical nature of the cluster constituents is not changed. Whilst in general, mass spectrometric analysis requires suitable post-ionization of the released cluster content, the aforementioned processes all result in charged products which can be directly analyzed.

For the experimental analysis of bulk processes via collision-induced fragmentation of molecular clusters – termed Cluster Impact Mass Spectrometry (CIMS) – a molecular beam apparatus which is capable of producing and characterizing molecular clusters including mixed species containing different reactants, was constructed. The analysis stage consists of a collision target, on which alkali metal adsorbates can be deposited, and a home-built large-extraction-volume time-of-flight spectrometer. The latter allows for bi-polar as well as quantitative ion detection. During the course of the work, a new design for the TOF spectrometer electrodes was developed, the composition of mixed clusters has been investigated and modeled, and electron-recapture processes during the ionization of molecular clusters were discovered.

A proof-of-principle demonstration of the CIMS method is given in terms of the first

direct observation of autoprotolysis in a water cluster. The main result of the present work consists of the elucidation of the microscopic mechanism behind the hitherto unexplained charge generation which occurs during the low-energy cluster-surface collision of water as well as sulphur dioxide clusters. CIMS measurements revealed an electron-transfer reaction between a reactant picked up during the cluster-surface collision and the cluster constituents. Backed by evidence from experiments with different clusters of e.g. sulphur dioxide, water, ammonia and sulphur tetrafluoride, in combination with alkali and indium surface adsorbates, this mechanism (termed the 'Clusterelectric Effect' (CEE)) is recognized as a new electrification mechanism that in general pertains to systems consisting of polar molecule clusters and easy-to-ionize surface adsorbates. The mechanism itself is modeled via three fundamental steps that take place in a concerted way during the picosecond time scale of the cluster-surface collision. During impact, the surface adsorbate is picked up by the cluster (1), due to the interaction with the polar cluster constituents it looses its valence electron (2) and the thereby formed geminate ion pair is separated by the collision-induced cluster fragmentation (3). The proposed mechanism of Cluster-Induced Desorption of the adsorbate is based on the impulsive interaction of the cluster constituents with the collision surface as well as with the adsorbate directly. The coincidence of desorption with the presence of the cluster at the surface leads to an efficient incorporation of the alkali atom into the cluster. Delocalization of e.g. alkali valence electrons in polar solvents, is generally known from previous equilibrium investigations of the bulk as well as of clusters. However, the rapid time scale of the cluster-surface collision, as well as the perturbation induced by the impact, precludes the formation of an equilibrium solvation structure around the picked up species. To explain the observed ion pair formation within the cluster, a fast electron transfer mechanism is proposed that is based on field ionization by the partial point charges connected to the polar cluster constituents. The separation of the geminate charge pair takes place if they are embedded on different cluster fragments. The energy to overcome the mutual Coulomb interaction and to form the free charge carriers is provided – in the form of Inertial Charge Separation – via the kinetic energy of the respective cluster fragment. Experimental evidence is given that the incorporated charge carriers can induce a variety of ion-molecule reactions in the surrounding solvent, for example, the electron-induced fluoride transfer between clustered SF_4 molecules. This indicates the possibility to investigate ion-molecule reactions or electron-induced reactions using a combination of alkali atom pickup and CIMS.

Both, the CIMS technique as well as the CEE promise a broad applicability. While the first can be employed to study solvation and dissolution processes as well as ion-molecule reactions, the latter has relevance as an ion-source, for surface analysis, cleaning and structuring, for the transfer of large molecule into gas-phase ions and even implications for natural electrification processes. Future work should address the quantitative influence of the molecular dipole moment, of cluster velocity, and cluster size. The Cluster-Induced Desorption model should be tested using cluster constituents and surface adsorbates of varying mass ratios, and the influence of a surface dipole of the adsorbate should be investigated via measurements taken at defined but variable adsorbate coverage.

Contents

Chapter 1

Molecular Clusters as 'Test Tubes' - An Introduction

The term *cluster*, denoting "a number of things of the same kind, growing together or gathered together" [1], is currently used in a wide variety of different contexts. In the present work, cluster denotes a *collection of molecules* ranging from two moieties, via aggregates of some hundreds, to sizes larger than several thousand constituents, all bound together by weak *Van der Waals* or *dipole forces*. Due to the broad size range which is covered by clusters, they are often considered to link the properties of individual atoms or molecules with condensed matter physics as well as macroscopic chemistry [1]. However, as will be shown here using the newly developed technique of *cluster impact mass spectrometry* (CIMS), the use of molecular clusters as a means to investigate physical and chemical processes under bulk-like conditions offers exciting new aspects for cluster research apart from the investigation of cluster size dependencies.

Molecular Clusters

One of the striking properties of clusters in general is their large surface to volume ratio. Especially in the case of smaller clusters comprising some ten molecules, almost all constituents contribute to the surface. For a larger cluster with one thousand molecules, still roughly 40 percent of the constituents are at the surface. On the other hand, the small volume contained inside molecular clusters rapidly approaches bulk behavior, for example, with respect to the solvation of ions and electrolytes: Often cluster sizes of some ten molecules already reproduce a macroscopic environment [1]. In addition, molecular clusters are characterized by a large number of closely spaced energy states, a large number of isomeric structures, as well as a large number of internal degrees of freedom, the abundance of which all increases rapidly with the number of cluster constituents. As a result, a molecular cluster can store considerably larger amounts of energy than its single constituent binding energy for short periods of time: The energy is distributed within the cluster and fluctuates between the various degrees of freedom. On longer time scales, such 'metastable clusters' are efficiently stabilized by monomer evaporation. Thus, molecular clusters can be considered as a dissipative, cold heat bath. Another unique property of molecular clusters is the division of their binding energies into two regimes. Whereas the molecular con-

[1] see *Webster's New Twentieth Century Dictionary*

stituents themselves feature strong chemical bonds with binding energies of several electronvolts, the strength of the intermolecular interaction within the cluster is typically one order of magnitude weaker. This separation, which is absent e.g. in metal clusters, allows for the investigation of physical and chemical processes between individual particles, which are assembled in high density within the cluster by the weak binding forces. Moreover, as will be shown here, a low-energy cluster-surface collision can be used to deliberately destroy the weak intermolecular bindings within molecular clusters without affecting the chemical nature of the cluster constituents. Analysis of the emerging individual cluster constituents and cluster fragments provides an unprecedented clear view on the processes inside the cluster.

Size Dependencies

So far, a major focus of cluster research has been the study of the physical and chemical cluster properties as a function of cluster size [1]. Considerable effort has been devoted to observing and understanding the transition from the molecule to the condensed phase: How large has a cluster to be before it will display some bulk behavior, and does the size dependence for one property also reflect the situation for other ones? Examples are experiments monitoring the evolution of interatomic distances from the dimer to the bulk value: Embedded copper clusters with diameters up to 150 Å have been investigated with X-ray spectroscopy [2]. The presence of an fcc-structure was already found for thirteen constituents as well as a general increase in the nearest-neighbor distance with growing cluster size. The latter was explained in terms of an increasing coordination number for the clustered copper atoms. Furthermore, the size dependence of the ionization potential as well as the electron affinity of metal clusters have been investigated [3]. Both properties have been found to converge on the bulk work function with increasing cluster size. For alkali systems and some non-alkali systems the average size dependence is reproduced by a modified jellium model [3]. This demonstrates that cluster properties are to a certain extent 'shape determined' [4]: Classical models neglecting the microscopic structure and dynamics of the constituents [5, 6] often describe the behavior of the cluster surprisingly well. In addition, investigations of the size dependent catalytic properties of transition metal clusters have been carried out [7]: Iron clusters in the size range of 13-23 constituents displayed an abrupt change in their chemical properties. The variation in reactivity with hydrogen over three orders of magnitude as cluster size increased was explained in terms of fundamental changes in the structure of the iron clusters.

Clusters as Test Tube

In the present work, molecular clusters are subject to a somewhat different philosophy. Rather than focusing on the size dependent physical and chemical properties of the cluster itself, this investigation uses clusters as a means to facilitate analysis of bulk phenomena. In this context, the cluster has a function similar to that of the *test tube* in standard chemistry (see Fig. 1.1). The cluster exhibits strong similarities to its macroscopic counterpart: Inside, it has a particle density comparable to the condensed phase. On the other hand, the cluster has the character of an easy-to-manipulate gas phase particle with a very limited spatial extension. Often, a single reactive system can be prepared within the host cluster. Moreover, the weakly-bound molecular cluster represents a very efficient heat bath with low characteristic temperature: The high cluster density guarantees a fast thermal equilibration within the cluster, while evaporation of monomers from the surface represents an efficient cooling mechanism that sets an upper limit to cluster temperature. Consequently, reactive

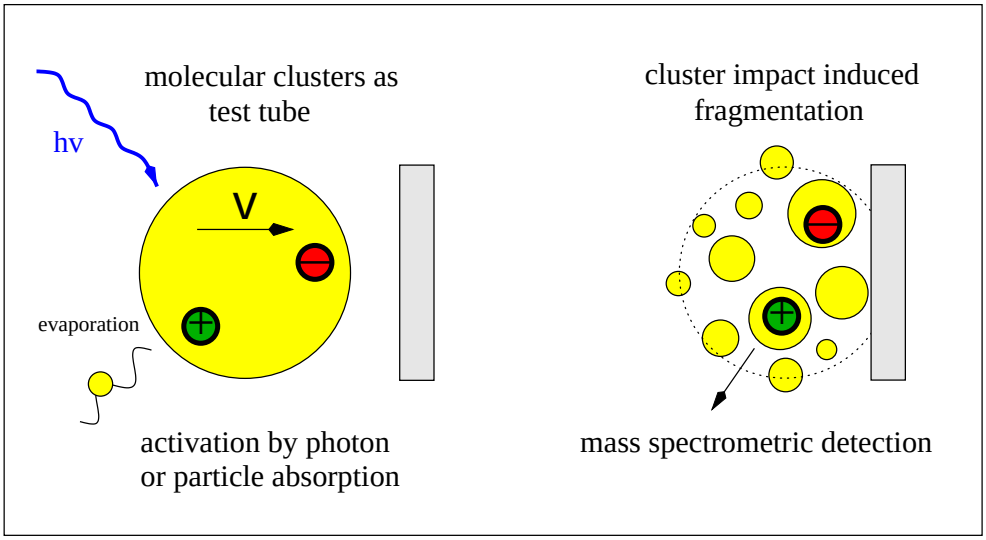

Figure 1.1: The cluster as a 'molecular test tube'. Compared to their macroscopic counterpart, molecular clusters provide the same high particle density but combined with a tiny overall volume, a gas phase character and a large surface-to-volume ratio which guarantees fast energy dissipation. Reactive systems incorporated into the cluster can be activated by providing energy from outside, e.g., by means of a photon or a high-energy cluster-surface collision. The energy supply naturally defines a time zero, so that dynamic processes can also be studied. The panel schematically depicts a charge transfer process within the cluster, initiated by photo-excitation. Although a geminate charge pair is created within the cluster, the charges can not be directly observed by mass spectrometry due to their mutual shielding. This is also true for strong exothermic reactions, since the cluster will always stabilize itself by evaporation of more weakly-bound neutral monomers. A subsequent cluster-surface collision changes the situation (right): In the low-energy impact regime relevant to the present work, energy is coupled predominantly into the intermolecular vibrations of the cluster, where it induces extensive cluster fragmentation. This spreading out of the contents of the molecular test tube separates the geminate charge pair and allows for direct mass spectroscopic analysis. Moreover, the smaller size of the fragments drastically simplifies an unambiguous analysis. The combination of surface-collision induced cluster fragmentation with a mass spectrometric technique to analyze the nature of reactions induced in the molecular cluster, especially charge transfer or charge separation processes, is referred to in the following as 'Cluster Impact Mass Spectrometry' (CIMS). In particular, the surface collision can be used to introduce reactive systems into the cluster via the pickup of surface adsorbates.

systems are stable within the molecular cluster, even if a reaction is prevented only by a small activation energy, since the large number of weakly-bound surface molecules (typical binding energies between 0.01 eV and 0.5 eV) makes an evaporative process more likely compared to the spontaneous accumulation of energy in the reactive coordinate. This thermodynamic property of a molecular cluster can be described in terms of an 'evaporative ensemble' [8].

Solvation

Spectroscopic studies of guest molecules in molecular clusters, which have been performed to elucidate macroscopic solvation processes, represent a first step in the direction towards the proposed molecular test tube approach. For example, it is well

known that if NaCl is placed into bulk water, dissolution takes place. The crystal lattice of NaCl is broken down by the interaction with the water molecules followed by the formation of distinct solvated structures. These structures are then surrounded by more or less undisturbed water. With the help of molecular clusters made from solvent molecules and containing the respective ions, these substructures can be 'cut out' of the bulk material and can be investigated separately in the gas phase. The cluster provides a kind of natural but confined environment. Besides investigating size, structure and energetics of the solvation shells around various cations [9, 10], questions about the solvation of electrolytes and concomitant ion pair formation are worked on; e.g., how many solvent molecules have to cooperate to split an electrolyte into solvated ions [11, 12] ?

Charge Transfer Reactions

In the present work, charge transfer and charge separation processes pertaining to bulk liquids are investigated using molecular clusters as microscopic test tubes. Although in this case a geminate charge pair is generated within the molecular cluster, it eludes direct mass spectroscopic analysis, due to the mutual shielding of the oppositely charged ions: In spite of the incorporated charge carriers, the cluster as a whole remains neutral. Even if energy is injected into the cluster in the course of the charge transfer, it will not evaporate on of the more tightly bound charge carriers, but will stabilize via sequential evaporation of neutral monomers. This difficulty can be overcome by fragmenting the cluster after the intracluster charge transfer has been induced, but before mass analysis is performed. If the incorporated ions reside on different cluster fragments, they become separated by the inertial movement of the cluster fragments and their mutual shielding ceases. In this case, charge cluster fragments emerge, which can be mass analyzed directly, even without post-ionization.

Cluster-Surface Collisions

A promising way to achieve cluster fragmentation is the *cluster-surface collision* [13, 14, 15, 16]. The concept behind it is simple: a molecular cluster impacts on a hard surface with a velocity ranging between several 100 m/s up to 100 km/s. In the idealized picture, the front of the cluster is reflected upon impact and starts moving against the back part of the cluster which is still approaching the surface. Thus, a zone is formed within the cluster that is characterized by an increased particle density and a broad distribution of particle velocities and in which the initial kinetic energy of the molecular cluster is transferred into the internal degrees of freedom of the cluster. This 'reflection' at the surface is equivalent to a picture of two identical clusters colliding centrally with opposite velocities. The advantage of surface collisions compared to crossed beam experiments is the unit collision probability: all clusters hit the surface centrally. The energy transfer into the surface is typically accounted for by rescaling the impact energy. A source of the initial kinetic energy of the cluster can be the cluster formation process, e.g., adiabatic expansion. For collision velocities larger than 2-3 km/s, the cluster has to be post-accelerated in an electric field, after it has been suitably ionized.

Energy Transfer

The cluster-surface collision couples the directed kinetic energy stored in the center-of-mass movement of the impinging molecular cluster into the various degrees of freedom within the cluster [17]. As previously pointed out, it is peculiar to molecular clusters that their internal degrees of freedom consist of two distinct energy ranges, namely the low-energy intermolecular vibrations and rotations on the one side and the high-energy intramolecular vibrations on the other. The relative population of these

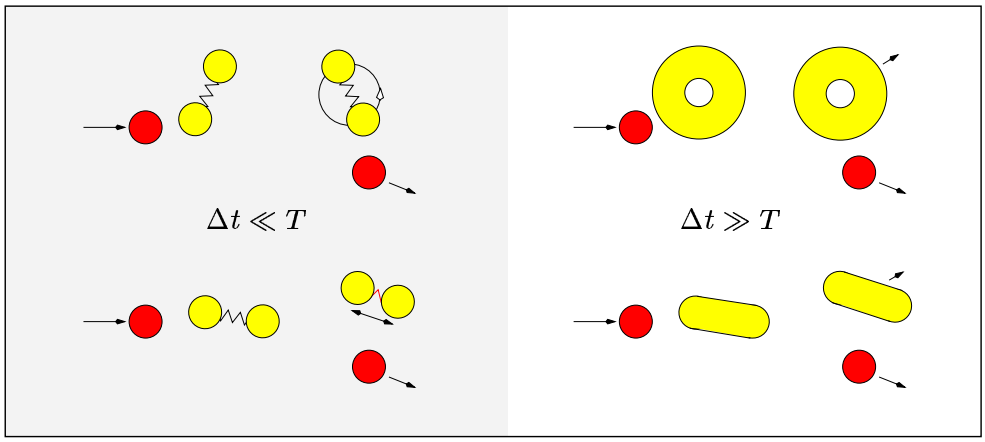

Figure 1.2: Collision-induced rotational and vibrational excitation. Inside the cluster two constituents collide, consisting of a rare gas atom (dark sphere) and a diatomic molecule. While the upper half discusses rotational excitation, the lower half is concerned with vibrational excitation. For each degree of freedom two situations are depicted: on the left side, the duration of the collision is much faster than the internal motion of the diatomic molecule, while on the right side it is much slower. As schematically illustrated, the duration of the collision Δt has to be short compared to the period T of the respective degree of freedom to efficiently induce rotations or intramolecular vibrations. Only then, will collisions with individual atoms take place (left). Otherwise, the rare gas atom interacts with a time-averaged conformation of the molecule, wiping out all internal degrees of freedom (right).

two classes strongly depends on the time-scale of the cluster-surface collision. Every degree of freedom within the cluster can be addressed by a *characteristic frequency*. In a simplified model, population takes place only if the induced disturbance by the cluster-surface collision contains a non-negligible Fourier component of the respective frequency [18]. This is achieved if the external perturbation is at least on the same time scale or faster than the movement associated with the respective degree of freedom (see Fig. 1.2). For small clusters, consisting of some hundred constituents, a simple estimate of the impact duration is given by the *advection time* of the cluster, which is the ratio of cluster diameter and cluster velocity. For large clusters, the situation can be pictured as multiple shock fronts propagating through the cluster [19]. In this case the characteristic time of excitation is given by the ratio of the width of the shock front, being typically some particle layers, and the shock front velocity. At least in microscopic systems, the latter can be approximated by the impact velocity. Therefore, simply by increasing the impact velocity, it is possible to move from pure intermolecular excitation within the cluster to its full excitation including the *intra*molecular degrees of freedom. The correlation of the cluster velocity with the duration of the cluster-surface collision allows for the specific addressing of the two energetically different classes of degrees of freedom inside a molecular cluster.

Fragmentation Regime

The work presented here deals with comparatively slow cluster-surface collisions with impact velocities in the range of 1 km/s to 2 km/s. The duration of the perturbation induced by the impact, estimated from the advection time of a typical cluster

of diameter 20 Å, is in the order of one picosecond. Consequently, mainly the intermolecular degrees of freedom get populated which give rise to a fast fragmentation of the cluster upon impact. Since the higher-energetic intramolecular degrees of freedom remain largely unaffected, the cluster constituents themselves are not activated and their chemical nature is not altered by the cluster fragmentation process. However, by breaking the weak dispersive bonds between the cluster constituents, changes in their covalent bonds or changes in their charge state due to previous bulk reactions become easily observable. Therefore, the spilling out of the content of the reaction chamber by means of a low-velocity cluster-surface collision has considerable advantages. Isobaric processes[2] with respect to the whole cluster, e.g. hydrogen transfer, become easily observable by analysis of the chemical nature of the individual cluster constituents. In particular, charge transfer processes can be directly analyzed by mass spectrometry, due to the fragmentation-induced spatial separation of the geminate charge pair inside the cluster (see Fig. 1.1). Additionally, the smaller masses of the constituents drastically simplify unambiguous compound identification. If clusters can be employed advantageously as 'test tubes', cluster fragmentation is the method to inspect the results.

Cluster Impact Induced Chemistry

Some remarks on future prospects as well as on related directions of investigation shall further illustrate the widespread applicability of the *molecular test tube* approach. Simply by increasing the initial velocity of the impinging cluster, a transition is made from the cluster fragmentation regime, ideal for inspection of bulk charge transfer processes, to the regime of efficient population of *intra*molecular degrees of freedom within the cluster. As pointed out theoretically by Raz and Levine, the short-time (100 fs) localized heating achieved during high-velocity cluster-surface collision (5-20 km/s) can efficiently drive chemical reactions [20]. Predictions based on molecular dynamics simulation and maximum entropy formalisms include simple bond dissociation of diatomic molecules [21, 13] and various kinds of four-center reactions [22, 20, 23] like the uni-molecular norbornadiene/quadricyclane isomerization as well as the bimolecular $H_2 + I_2$ or $N_2 + O_2$ reactions. The latter are expected to have a high activation barrier [24]. Molecular dynamics simulations of the 'burning of air' reaction between nitrogen and oxygen showed that in the compressed reactive zone multi-center mechanisms with more than four atoms participating make a reactive contribution [25]. They are possible only in the high density cluster environment. Moreover, high barrier reactions are especially suited to the cluster-impact method with its fast energy supply (surface collision) and drain (cluster fragmentation). The coupling of the 'extreme', energy-rich state in the compressed cluster to the very short collision time scale of cluster-surface collisions is of central importance, since otherwise the reactive system escapes through reaction channels lower in energy (slow conventional heating) or is completely destroyed (long prevalence of the energy-rich state). First experiments to explore this new regime of chemistry

[2] With mass and charge conservation in the closed system of a molecular cluster, this would include all chemical processes. However, often sufficient energy is deposited in the cluster during the process to evaporate a reaction partner so that the processes can be observed by mass spectrometry. However, due to their high binding energy, geminate charge pairs in a molecular cluster never get separated by evaporative stabilization. Consequently, due to their mutual shielding, they elude a direct mass spectrometric analysis.

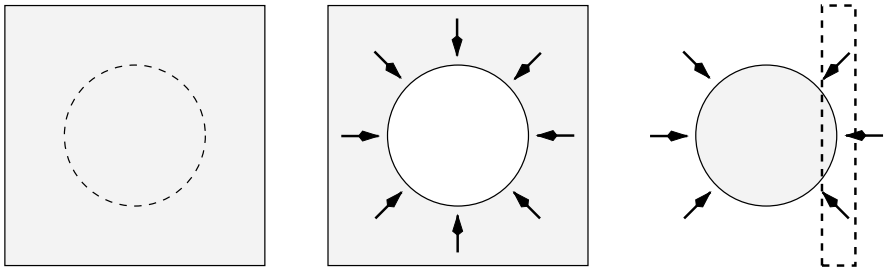

Figure 1.3: Bubble cavitation and cluster-surface collision; two of a kind. The creation of extreme conditions in macroscopic samples, faces the problem of the prohibitively high amounts of energy needed and the large time constants for energy supply and drain. The localized excitation, due to the cavitation of a bubble, presents an alternative. The energy stored in the oscillation of an ultrasonically driven bubble is focused into a tiny volume during the process of cavitation. From light emission (sonoluminescence) it can be inferred that extreme conditions prevail on the 100 picosecond timescale [27]. The coupling with the surrounding liquid provides an efficient cooling mechanism. Sonochemistry and cluster-surface collisions (right panel) are related by a kind of *Babinet* principle; instead of cutting a bubble into the macroscopic medium, the cluster is cut out of it. By means of a surface collision, the energy stored in its center-of-mass movement is injected into a compressed region within the colliding cluster, thus creating an energy-rich state. The ease by which kinetic energy can be provided is set back by the asymmetrical compression of the cluster which is not as efficient in heating up the reactive zone as the spherical collapse of the bubble. On the other hand, cluster fragmentation provides a rapid cooling mechanism to stabilize hot reaction products which is superior to the heat conduction in the bulk.

have recently been performed [26]. There exists a close similarity between the processes involved in high-energy cluster-surface collisions and bubble cavitation, e.g., in sonoluminescence. As pointed out in Fig. 1.3, in both cases energy is focused in a compression wave into a small volume. A cluster and a bubble are complementary to each other, but in the 'compressed singularity' they are equal and similar conditions prevail. However, in the case of bubble cavitation, the duration of the 'extreme conditions' is with over 100 ps [27, 28] much longer than the 100 fs achieved in high-velocity cluster-surface collisions. This emphasizes the fast cooling mechanism by fragmentation as compared to heat conduction in the bulk.

Interaction with Intense Laser Fields

Another application of molecular test tubes is the exposure of atomic and molecular clusters to unprecedented high energy densities as realized in the focus of ultra-short, intense laser radiation. Clusters can be employed to provide a bulk density target directly in the focus of the laser. Their gas phase character facilitates the investigation of reaction products via mass spectrometry. Studies of rare-gas clusters heated with intensities of greater than 10^{16} W/cm^2 revealed that a highly ionized micro-plasma is produced, ejecting ions with substantial kinetic energy of up to 1 MeV [29]. This energy is four orders of magnitude higher than Coulomb explosion energies of small molecules, indicating a fundamental difference in the nature of intense laser-matter interactions between single molecules and high density material. Nuclear fusion has recently been reported [30] upon intense irradiation of deuterium clusters. Also,

very efficient production of X-rays upon intense irradiation of rare gas clusters has been observed [31]. A proposed mechanism is the ionization of inner shells due to inelastic collision events with the coherently moving field ionization electrons inside the cluster. This explanation combines the high density within the cluster with its gas phase character, which is one of the unique features of the 'molecular test tube approach.'

In the present work, we will not venture into the field of 'extreme conditions' as realized in a laser focus or by high-velocity cluster-surface collisions, but will focus on the intermediate velocity range. Here, the cluster-surface collision induces mainly fragmentation of the molecular test tube, without changing the chemical nature of its contents. Therefore, this regime is ideal to investigate physical or chemical processes in the bulk as simulated by the high-density molecular cluster. As a prototype for this kind of study, the present work discusses the electron transfer reaction induced by the pickup of an alkali surface adsorbate inside a polar molecule cluster. This intracluster charge transfer is made visible by means of cluster fragmentation which separates the formed geminate charge pair spatially and thus destroys its mutual shielding.

Road Map

The further structure of this work is organized according to the sequential steps of the described experiments. At the beginning, an adequate 'test tube' in the form of a molecular cluster has to be assembled from educts within the desired size range and with a given composition as well as kinetic energy. *Chapter 2* recalls the theoretical as well as experimental background for the creation of clusters by adiabatic expansion. Mixed gas expansions are introduced as a means to vary the cluster velocity via the seeded beam technique or to influence the cluster composition. In the next step, the cluster beam has to be characterized. Neutral particles, however, are relatively difficult to manipulate or to detect since their interaction with the environment is weak. After ionizing the cluster, the strong Coulomb interaction establishes a kind of 'handle' to the cluster. *Chapter 3* deals with the creation and the properties of molecular cluster ions. It discusses the electron impact ionization process and reveals for the first time the importance of electron recapture in molecular clusters with electron affinity. Moreover, it outlines basic procedures to characterize the cluster beam, namely its inherent size distribution and the beam velocity. *Chapter 4* introduces an important method to investigate individual cluster ions or charged cluster fragments, namely time-of-flight (TOF) mass spectrometry. Some emphasis is given to the special design of the TOF spectrometer used and to the problem of large cluster detection. A novel way to establish homogenous potential gradients is presented. Experimental investigations of cluster-surface collisions are the heart of the present work. Starting from the surprising observation that abundant positive and negative charges emerge during low-energy impact of water and sulphur dioxide clusters on arbitrary surfaces, experiments have been performed to elucidate the mechanism behind this phenomenon. As described in *Chapter 5,* it was discovered that the key to cluster impact induced charge separation is the pickup of alkali atoms during surface contact. The polar environment of the cluster strips the alkali atom of its valence electron and a geminate charge pair is formed within the cluster. The subsequent collision-induced cluster fragmentation leads to a macroscopic charge separation, so that charged cluster fragments are formed. It thus bears witness to the charge transfer process within the cluster. This highly efficient charging mechanism is demonstrated

to be applicable to the class of polar molecule clusters in combination with easy-to-ionize surface adsorbates. *Chapter 6* discusses the observed charge delocalization mechanism. The interaction of alkalis with bulk polar solvents as well as with the respective solvent clusters is dealt with. The unique insight into dynamical processes provided by the cluster impact method allows for the extension of previous equilibrium investigations. Based on the experimental findings, a fast electron transfer mechanism is proposed that proceeds by electron delocalization in the Coulomb field of the partial point charges of the polar cluster constituents, in analogy to field ionization. *Chapter 7* illustrates the richness and wide applicability of the proposed microscopic mechanism by presenting results for different polar molecule clusters. Each of the given examples focuses on a new aspect of the basic mechanism. *Chapter 8* illustrates the wide applicability of the effect, which led to the application for a patent [32], as well as some implications of Cluster Impact Mass Spectrometry. Finally, *Chapter 9* summarizes the findings of the previous chapters and points out directions for further scientific work, be it with the charge separation in its focus, or by using the effect itself as means of investigation. The appendix provides a reprint of a letter to *Nature* [33], in which results from this work have been published.

Chapter 2

Creation of Molecular Clusters

To perform experiments as outlined in the introduction, adequate molecular clusters within the desired size range, with a defined composition as well as kinetic energy have to be assembled. Various sources for cluster beams have been developed [34]. They are mostly based on aggregation processes starting from the monomer vapor. The statistical growth process, which all methods have in common, always creates a broad distribution of clusters with respect to size and composition. Depending on the strength of the interaction between the moieties, one can discriminate between 'gas aggregation sources' and 'free jet expansions' for example. Strongly interacting monomers, like metal atoms, are clustered simply by injecting the vapor into a cold quench gas. By means of collisions with the buffer, the cluster constituents are cooled down and cluster growth is initiated. The strong interaction makes aggregation easy but renders the creation of the respective initial vapor difficult. Besides high-temperature ovens, surface erosion processes, like sputtering or laser-ablation, are often used together with gas aggregation sources. The present work deals with clusters of gaseous molecules that only weakly interact by Van der Waals or hydrogen bonds. Therefore, production methods are required that subject the monomeric vapor to intensive cooling so that the necessary supersaturation for cluster growth can be reached. This is typically achieved by adiabatic expansion of the relevant gas mixture through a nozzle into a vacuum chamber. As will be outlined in the following, cluster size distribution, cluster velocity, and cluster composition can be controlled by means of gas mixture and the expansion parameters like stagnation pressure, nozzle temperature, and orifice diameter.

2.1 Cluster Creation by Adiabatic Expansion

2.1.1 Adiabatic Expansions

Effusive Source

A typical beam setup includes a reservoir held at temperature T_0 that contains the respective gas or gas mixture at the stagnation pressure p_0. It is connected to a vacuum chamber held at negligible background pressure p_b via a sharp-edged circular orifice or converging nozzle. At low reservoir pressures the mean free path length of the contained gas particles can be bigger than the orifice diameter. In this case the gas particles can leave the reservoir without mutual interaction, which results in

a so-called *effusive expansion.* The rate $\dot{N}$ at which particles leave the reservoir is given by the particle-wall collision rate on the orifice area A:

$$\dot{N}_{\text{eff}} = A \cdot \frac{1}{4} \cdot n_0 \cdot \bar{c} = A \cdot \frac{1}{4} \cdot n_0 \cdot \sqrt{\frac{8\, k_B\, T}{\pi\, m}}, \tag{2.1}$$

where n_0 denotes the particle density in the reservoir and $\bar{c}$ the mean thermal velocity of a particle with mass m inside the reservoir of temperature T. Under these circumstances, the orifice randomly 'samples' particles that move towards it from the reservoir, without changing the velocity components. The escaping particles therefore exhibit a directed Maxwell velocity distribution and emerge from the nozzle with a cosine flux dependence.

Supersonic Source

By increasing the stagnation pressure to the point where the mean free path of the particles within the reservoir becomes smaller than the orifice diameter, the physical situation changes. The gas particles undergo many collisions during the transition into the vacuum chamber, thus establishing local equilibrium at any point. The gas behaves like a macroscopic fluid, that is streaming towards the orifice. The fluid accelerates as the available 'cross section' normal to the streamlines[1] gets smaller and even reaches sonic velocities at the throat of the nozzle (minimum orifice diameter), if the ratio between reservoir pressure and background pressure in the vacuum system exceeds an easily achievable critical value [35],

$$p_0/p_b \geq [(\kappa+1)/2]^{\kappa/(\kappa-1)} \approx 2, \tag{2.2}$$

where $\kappa = c_p/c_v$ is the ratio of specific heats at constant pressure and constant volume, which generally is a function of temperature. If a sonic velocity is reached at the orifice, then, instead of being decelerated by interaction with the background pressure in the vacuum chamber, the beam accelerates further to supersonic velocities, as the sonic velocity at the orifice prevents any 'sensing' of boundary conditions to which the beam could accommodate, in the vacuum chamber ahead. During the whole acceleration process collisions transfer the thermal energy of the gas connected to its statistical velocity distribution into a directed molecular flow characterized by a narrow velocity distribution around a flow velocity u. The particles perform work by accelerating preceding layers of gas like a piston through the nozzle. This process can often be described as adiabatic; i. e., without energy exchange with the nozzle walls, as well as isentropic, in the sense of a reversible process. In the case of negligible viscosity effects, the specific enthalpy h is conserved along any streamline of the expansion [36]. The expansion converts the stagnation enthalpy h_0 into kinetic energy of the directed mass flow and a rest enthalpy h. The latter is stored in the statistical velocity distributions parallel and normal to the flux velocity as well as residual rotational and vibrational excitation:

$$h_0 = c_p\, T_0 \; = h + \frac{1}{2} m u^2 = c_p\, T \; + \frac{1}{2} m u^2, \tag{2.3}$$

where for each streamline a local temperature T has been defined.

[1] The concept of streamlines is very common in fluid dynamics. The tangent to the streamline gives the direction of flow velocity at that point. In steady flow they coincide with the path of the fluid particles. See, e.g., Landau, Lifshitz *Fluid Dynamics* Pergamon Press 1993 p. 8.

The flow velocity u is maximized, if the inner energy of the expanded gas approaches zero. The highest possible kinetic energy and the corresponding highest beam velocity is given by

$$E_{\rm kin}^{\rm max} = \frac{1}{2}\, m\, u_{\rm max}^2 = c_{\rm p}\, T_0 \qquad \text{with} \quad u_{\rm max} = \sqrt{\frac{2\, c_{\rm p}\, T_0}{m}}. \tag{2.4}$$

The subsonic flow within the nozzle can be approximated by a quasi one-dimensional compressible flow that reaches sonic velocity at the source orifice [36]. This allows for the calculation of the flow rate through the nozzle:

$$\dot{N} = A^*\, n_0 \sqrt{\frac{2\, k_B\, T_0}{m}} \left(\frac{\kappa}{\kappa+1}\right)^{1/2} \left(\frac{2}{\kappa+1}\right)^{1/(\kappa-1)} = 2\, F(\kappa)\, \dot{N}_{\rm eff}\,, \tag{2.5}$$

where A^* represents an effective orifice area, corrected, e.g., for the influence of boundary layers. For κ ranging between 1 and 5/3, the values of $F(\kappa)$ lie between 0.43 and 0.51 so that the total flow rate of the free jet is of the same order of magnitude as an equivalent effusive flow. Yet the angular velocity distribution of supersonic beams is not cosine-like but peaked in the direction of the centerline [36]. Although beam velocities reached in adiabatic expansion are not much higher than in normal effusive beams (see Fig. 2.2), they are large compared to local sound velocity. Therefore this type of expansion is called 'supersonic'.

Mach Number

By introducing the local Mach number $\mathcal{M}(z)$ as the ratio between the stream velocity $u(z)$ and the local speed of sound $c(z) = \sqrt{\kappa\, k_B\, T(z)/m}$, all local thermodynamic variables like temeprature T, pressure p, density ϱ and flow velocity u can be expressed in terms of the distance z downstream of the nozzle, the corresponding stagnation values and the evolution of the Mach number during the expansion:

$$T(z) = T_0 \left[1 + \frac{\kappa-1}{\kappa}\mathcal{M}(z)^2\right]^{-1}, \tag{2.6}$$

$$p(z) = p_0 \left[1 + \frac{\kappa-1}{2}\mathcal{M}(z)^2\right]^{-\kappa/(\kappa-1)}, \tag{2.7}$$

$$\varrho(z) = \varrho_0 \left[1 + \frac{\kappa-1}{2}\mathcal{M}(z)^2\right]^{-1/(\kappa-1)}, \tag{2.8}$$

$$u(z) = \mathcal{M}(z) \left[\frac{2}{\kappa-1} + \mathcal{M}(z)^2\right]^{-\frac{1}{2}} \cdot u_{\rm max}. \tag{2.9}$$

The square of the Mach number $\mathcal{M}$ is a measure of the ratio of the energy in the directed mass flow and the thermal energy remaining in the beam. To obtain the local values of $\mathcal{M}$ after the particles have left the nozzle, the partial differential equations for conservation of mass, conservation of momentum, and conservation of energy for the isentropic, compressible flow have to be solved. The momentum equation is a vector equation which provides for axisymmetric flow and under supersonic conditions ($\mathcal{M} > 1$) two hyperbolic partial differential equations, that can be solved numerically [36]. The initial condition is given by the 'sonic line' at the source exit

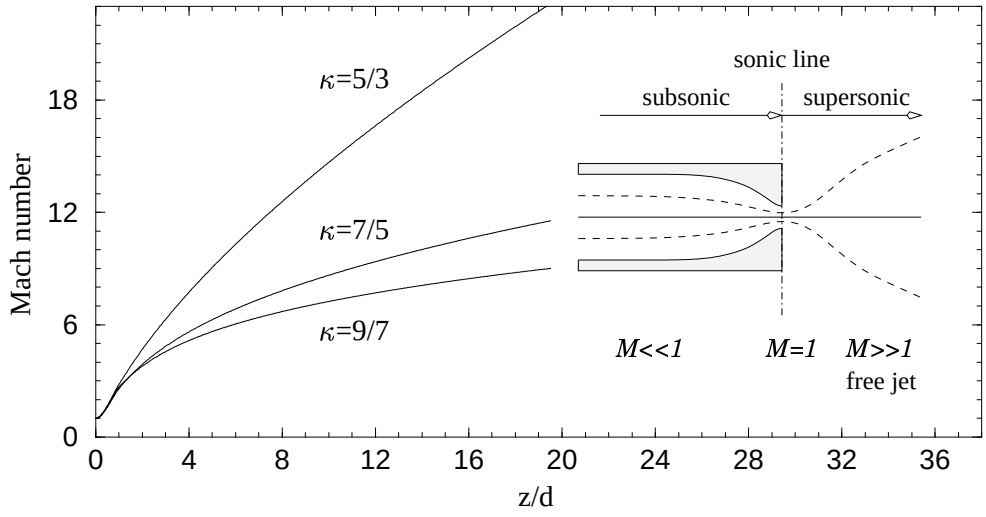

Figure 2.1: Centerline Mach number for axisymmetric expansions with different κ [36] versus distance z in terms of nozzle diameters d (free jets are often characterized with the nozzle diameter as length scale [35], since identical beam conditions are observed for free jets having different apertures but otherwise identical expansion parameters at the same number of nozzle diameters downstream from the nozzle). As depicted in the inset, the flow starts from rest with $\mathcal{M}$=0 and accelerates towards the orifice, where it reaches sonic velocity ($\mathcal{M}$=1) provided the pressure gradient is sufficiently high. In this case, the acceleration proceeds further, reaching supersonic velocities. The adaption to boundary conditions, like background pressure, happens via a shock front. However, at low background pressure the shock front lies in a region of low density and long mean free path [36] so that it is smoothed out. Decreasing density is also responsible for deviations from the continuum model predictions. At a certain nozzle distance, the Mach number 'freezes' due to lack of collisions.

with $\mathcal{M} = 1$. Especially short, converging sources, as used in the following experiments, provide a nearly uniform ideal planar sonic surface at the exit [37].

Figure 2.1 shows $\mathcal{M}(z)$ along the centerline of an axisymmetric free jet. The graphs represent analytical functions that have been fitted to the numerically computed solutions [36]. Since it is common to cut out the center of the free jet by means of a skimmer, the centerline properties of the beam are sufficient for all practical purposes. Fortunately, the Mach number varies only slowly around the centerline [36]. From the evolution of the Mach number during the expansion, the local properties of the beam can be calculated according to Eqs. (2.6)-(2.9). This has been done in Fig. 2.2 for the centerline of an axisymmetric free jet of a monoatomic ideal gas ($\kappa = 5/3$). Remarkably, the beam velocity rapidly increases immediately after leaving the orifice, whereas the beam temperature drops more slowly.

Energy Transfer by Collisions

The continuum model, on which Fig. 2.1 is based, is only valid up to some distance from the nozzle. Due to the decreasing particle density and beam temperature, two-body collisions become less frequent and at some point cease. However, collisions are the motor behind energy transfer from the various degrees of freedom into the directed flow velocity. They establish the local equilibrium on which the contin-

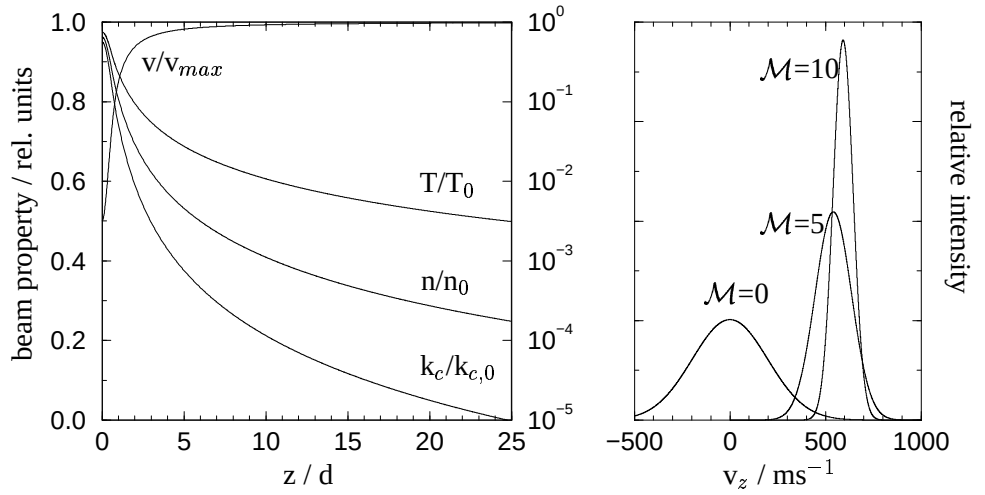

Figure 2.2: Left panel: Centerline properties of a free jet expansion (κ=5/3) versus distance in source diameters. Whereas the beam velocity rapidly approaches its terminal value, temperature decreases over a large distance from the nozzle. The decrease of the two body collision rate $k_c/k_{c,0}$, connected to the temperature T/T_0 and density n/n_0 decrease, leads to a break down of the continuum model as local equilibrium can no longer be maintained. Whereas this has only minor effects on the terminal beam velocity, the temperature decrease 'freezes' at this point. Right panel: Velocity distribution along the centerline of a pure SO_2 (κ=1.26, T=300 K) expansion. Within the reservoir ($\mathcal{M}$=0) the distribution is thermal. The free jet expansion narrows the distribution and shifts it to higher mean velocities. Depending on when the transition from continuum to molecular flow occurs, the Mach number freezes at different values. If the transition occurs at z/d=3.73 the terminal Mach number is 5, at z/d=27.3 a Mach number of 10 is achieved (Fig. 2.1). Comparing the latter two distributions shows that there are only minor differences in beam velocity (see Eq. (2.9)), however, the difference in the thermal spread is obvious. With non-condensing monoatomic gases, e.g., He, Mach numbers up to 100 can be reached. This results in very sharp velocity distributions.

uum model is based; before expansion all molecules in the reservoir are in thermal equilibrium. The velocity distribution, as well as the population of the vibrational and rotational levels, follows a Boltzmann distribution with a uniform temperature T equal to the reservoir temperature. The efficiency with which collisions can drain the various resources during expansion can be characterized by means of cross sections. Their relative magnitude is given by $\sigma_{\text{trans}\rightarrow\text{trans}} > \sigma_{\text{rot}\rightarrow\text{trans}} > \sigma_{\text{vib}\rightarrow\text{trans}}$. The total number of binary collisions experienced by a molecule during free jet expansion is typically on the order of 10^2 to 10^3. Any kinetic process that requires more than this number of binary collisions to approach equilibrium, will be subjected to kinetic lags or relaxation effects during expansion. The corresponding degree of freedom 'freezes' without its energy being converted into directed flow. Vibrational modes of diatomic molecules typically require in excess of 10^4 collisions and consequently do not participate in the expansion. The weak energy transfer is connected to the long collision duration as compared to the fast vibrational motion (see Fig. 1.2). This is different with large polyatomic molecules. Generally, the distribution of vibrational

levels after expansion does not follow a Boltzmann distribution. Nevertheless, for practical reasons, it is often described by an effective vibrational temperature T_{vib} approximating the real situation. Rotational-translational energy transfer requires a much smaller number of collisions. Therefore rotational degrees of freedom are considerably cooled during expansion. Since normally $\sigma_{\mathrm{rot}\to\mathrm{rot}} > \sigma_{\mathrm{rot}\to\mathrm{trans}}$, the population of rotational levels can be described in terms of an equilibrium distribution, which is characterized by a temperature T_{rot}. At the point when there are too few collisions to couple the rotational degrees of freedom to the expansion, the very efficient translational-translational energy transfer is still at work. Therefore, after expansion, the relationship between the different temperatures is given by $T_{||} < T_{\mathrm{rot}} < T_{\mathrm{vib}}$ where $T_{||}$ stands for the narrowed velocity distribution around the flow velocity. This relation reflects the different points during expansion at which the different degrees of freedom freeze due to insufficient collisions.
Finally, translational equilibration also ceases. At that point, the Mach number 'freezes' and remains constant. The point of transition from continuum flow to free molecular flow scales with $n_0 d\sigma^2$ [36] where σ is a measure for the total collision cross section of the gas. The expression itself is proportional to the inverse Knudsen number $1/Kn_0$ of the source, which stands for the ratio of the free mean path length in the reservoir and the orifice diameter. The terminal Mach number can be estimated from [36]

$$\mathcal{M}_{||,\infty} = l \cdot \sqrt{\frac{2}{\kappa}} \cdot \left[\frac{1}{Kn_0}\right]^m, \qquad \begin{aligned} \kappa = 5/3: &\quad l = 0.527, \quad m = 0.545 \\ \kappa = 7/5: &\quad l = 0.783, \quad m = 0.353. \end{aligned}$$

Therefore, final 'beam temperatures' depend on stagnation conditions as well as source diameter. On the other hand, mean beam velocity and beam energy, due to their rapid increase close to the nozzle, are described very accurately in the continuum model. The final velocity distribution parallel to the beam velocity can be approximated by a drifting Maxwellian model:

$$f(v_z) = \sqrt{\frac{m}{2\,\pi\,k_B\,T_{||}}}\ \exp\left(\frac{-m(v_{||}-u)^2}{2\,k_B\,T_{||}}\right). \tag{2.10}$$

The temperature has been separated into two components as a measure of the velocity spread in the two directions. The influence of the terminal Mach number on the thermal spread of a pure SO_2 beam is depicted on the right panel of Fig. 2.2. The velocity distribution perpendicular to the beam axis has a more complicated shape [36].

2.1.2 Adjusting the Kinetic Energy: Seeded Beam Technique

The simple model of adiabatic expansion presented above predicts that the kinetic energy of the particles after the expansion is roughly equal to their original enthalpy in the reservoir. A straightforward way to higher kinetic energies per particle and thus to higher beam velocities is to increase the original enthalpy by raising the temperature

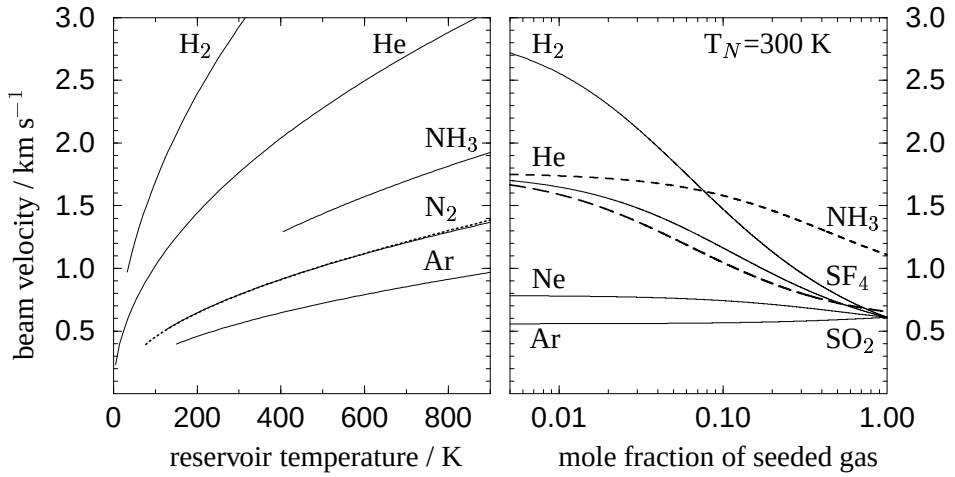

Figure 2.3: Temperature dependence and composition dependence of ideal adiabatic expansions. In the left panel the dependence of the final beam velocity on the temperature of the nozzle (respectivly the reservoir) for several gases is given. The values are derived from the ideal model contained in Eq. (2.12). For nitrogen, the dotted line gives the velocity if the temperature dependence of the heat capacity is taken into account. The right panel depicts the dependency of the final beam velocity on the gas composition (T=300 K) as calculated from Eq. (2.11) for SO_2 in Ar, Ne and H_2 (solid line), as well as for SF_4 in He (long dashed line) and NH_3 in He (dashed line). It shows that by seeding gases in light rare gases, considerably higher beam velocities can be achieved with respect to the pure gas. However, seeding can also result in deceleration as it is shown in the case of SO_2 / Ar mixtures.

of the reservoir. Due to material constraints, an increase by a factor of 2-3 with respect to room temperature kinetic energy can be achieved for pulsed nozzles and a factor of 8-10 for continuous beams. Fig. 2.3 gives examples of the corresponding velocities for the temperature range of pulsed nozzles.
However, as will be pointed out in the next section, raising the reservoir temperature has a detrimental influence on cluster growth. Therefore, this method of increasing the beam velocity is not compatible with strongly condensed beams. However, the generalization of the continuum model for adiabatic expansion to gas mixtures shows another way. For mixtures of ideal gases, the total enthalpy is simply the sum of the individual enthalpies h_i. Superposition of Eq. (2.4) for the beam energy of the individual constituents gives:

$$\begin{aligned} X_1\, h_1 \approx X_1\, c_{p1}\, T &= \frac{1}{2} X_1\, m_1\, u_1^2 \\ X_2\, h_2 \approx X_2\, c_{p2}\, T &= \frac{1}{2} X_2\, m_2\, u_2^2 \\ \cdots &= \cdots \\ \sum_i X_i\, h_i \approx T \sum_i X_i\, c_{pi} &= \frac{1}{2} \sum_i X_i\, m_i\, u_i^2 \stackrel{!}{=} \frac{1}{2}\, u^2 \sum_i X_i\, m_i, \end{aligned} \quad (2.11)$$

where X_i represents the molar fraction of the corresponding constituent in the gas

mixture. Whereas the situation in the reservoir can be described in terms of non-interacting gases with given partial pressures and different mean velocities, the adiabatic expansion brings down the different theoretical beam velocities u_i to a uniform beam velocity u by means of two body collisions (Eq. (2.11)). Therefore, the beam velocity of an ideal supersonic beam originating from the expansion of a gas mixture has a velocity:

$$u = \sqrt{2\,\frac{\overline{c_p}}{\overline{m}}\,T} \quad \text{with} \quad \overline{c_p} = \sum_i X_i\, c_{pi} \qquad (2.12)$$
$$\overline{m} = \sum_i = X_i\, m_i.$$

Especially by using high concentrations of light weight gas components, which have a high natural expansion velocity, the velocity of heavier gas constituents can be considerably increased (see Fig. 2.3).
Given the limited number of collisions during the expansion, the equalization of velocities is not complete, but a so called 'velocity slip' occurs. This denotes a difference in terminal speeds for the different species; heavier species tend lag somewhat behind. For the case of binary mixtures, this effect can be quantitatively described [36] by introducing a 'velocity slip parameter'. For the present studies, in which very diluted mixtures as well as large stagnation pressures and comparatively large orifices are employed, the influence of velocity slip can be neglected.

2.1.3 Condensation in Molecular Beams

Supersaturation

The low local temperature which is achieved in supersonic beams allows the formation of weakly bound systems like Van der Waals or hydrogen-bonded clusters. Generally, the vapor pressure of a system decreases much more rapidly during an expansion than the local pressure, resulting in a higher pressure than the corresponding vapor pressure in some regions of the expansion zone. In a T-p-diagram the system follows an adiabate until it intersects the vapor pressure line. Starting from here, clusters represent a stable state and can be formed. However, the rapid cooling and pressure decrease continue further and the system gradually approaches the vapor pressure line corresponding to local conditions, that have been additionally influenced by the heat released during the condensation process. Under conditions of supersaturation, cluster formation proceeds —at least at the beginning— by monomer aggregation, provided that a sufficient number of collisions take place before the beam reaches the region of free molecular flow. The formation of the initial dimer is the crucial step. Due to energy and momentum conservation, dimers can form only by three body collisions; two particles collide and form an activated complex. To prevent the dissociation of the overheated two-body system, a third collision has to occur within a time window on the order of the intermolecular vibration. On the other hand, larger clusters can distribute the heat of formation released by each condensation step over all their internal degrees of freedom. From there it can be removed by subsequent collisions on a much longer time scale. Consequently, with increasing size, clustering is expected to evolve from three body kinetics to two body kinetics.

Preexisting Dimers

Dimers form not only during the expansion of the gas but they are also present in the equilibrium composition of the gas in concentrations which vary with pressure and temperature. Although their concentration away from the boiling point of the gas is generally low, their effect on the clustering process can be considerable with regard to the difficult dimer formation during the short expansion time. The strong influence of such 'preexisting dimers' on the amount and the size distribution of produced clusters has been investigated [38, 39]. For the basic dimerization reaction $2\,A \rightleftharpoons A_2$ an equilibrium constant K can be written and related to the standard enthalpy and entropy change of dimerization ΔH and ΔS [38]. Assuming that the fugacity of a species is approximated by its partial pressure,

$$K = \frac{p_{A_2}\, p^0}{p_A^2} = \exp[-(\Delta H^0 - T\Delta S^0)/RT], \tag{2.13}$$

where p^0 is the standard pressure taken to be 1 atm. When changing the stagnation conditions from (p_1, T_1) to (p_2, T_2) the concentration of the preexisting dimers can be kept constant by using the relation

$$\ln(p_1/p_2) = \frac{1}{2}(\Delta H^0/R)(1/T_1 - 1/T_2). \tag{2.14}$$

For homogeneous expansion of H_2O and NH_3 it has been shown [38] that the cluster size distribution, monitored by the distribution of the ionized cluster distribution, remains unchanged when the concentration of preexisting dimers is kept constant by varying the expansion conditions according to Eq. (2.14). On the other hand, a pronounced change in the distribution was observed upon deviating from the above expression.

Cluster Growth

Starting from the dimer, the further growth of the clusters proceeds by single association steps via monomer addition and in strongly clustered beams also by means of cluster-cluster aggregation [40]. Cluster size is generally connected to the total number of collisions during expansion, which itself depends on stagnation parameters. The ratio of clustered to uncondensed molecules, as well as average cluster size, increases with increasing stagnation pressure, increasing orifice cross section, and decreasing reservoir temperature; higher stagnation pressure moves the onset of supersaturation upstream and increases the degree of supersaturation. Therefore, more collisions take place under supersaturation and, consequently, more and larger clusters are formed [35]. Decreasing the reservoir temperature has the same effect, but stronger, due to the exponential dependence of vapor pressure on temperature. Expansions from smaller orifices run out of collisions sooner which leads to smaller clusters.

The theoretical treatment of the growth process is difficult. For example, the expanding gas flow can not be separated from condensation, which increases local temperature and reduces the Mach number. Moreover, growth generally depends non-linearly on local beam properties, and thus is sensitive to small variations in the substantial changes these properties undergo during adiabatic expansion. Different approaches have been attempted to describe the condensation process theoretically [40]: Classical nucleation theory [41] developed for isothermal, supersaturated gases provides a good qualitative picture of the thermodynamics of cluster growth. Problems of this

equilibrium approach result from the usage of macroscopic properties like surface tension, the neglect of internal degrees of freedom for the critical size condensation nucleus and the equilibrium approximation with respect to condensation in the rapidly changing expansion. The latter can be improved by employing time dependent approaches [42]. On the other hand, molecular dynamics [43] simulations have explored, for example, the importance of cluster-cluster nucleation with regard to single addition steps. However, the calculations are difficult to extend to the μs time scales on which the expansion takes place.

Cooling Mechanisms

Continuous cluster growth requires cooling mechanisms, as growth is counteracted by unimolecular decay processes if the clusters become vibrationally hot. A schematic representation of this process is given in the right panel of Fig. 2.4. Each successive growth step releases the binding energy into the cluster as well as reorganization energy connected to additional bonds being formed within the cluster. This energy can be stored to some extent in the internal degrees of freedom, heating up the cluster, so that during its growth the cluster resembles a kind of boiling hot droplet. However, at a certain location, the fluctuating energy can reach the dissociation energy which leads to ejection of an already attached molecule. The influence of surface energy makes sequential evaporation of monomers a more likely cooling process for excited clusters than ejection of larger fragments. The monomer takes away the binding energy plus the energy stored in the translational, rotational or vibrational degrees of freedom ('evaporative cooling'). In the collision-free region no further heating takes place, and the 'metastable' cluster cools down by successive evaporation steps. By seeding the clustering gas in a non-attaching rare gas, an additional cooling mechanism is provided. Collisions with the seed gas atoms carry away internal energy of the cluster. To prevent evaporation, non-attaching collisions have to take place on a time scale shorter than the 'thermal' evaporation rate of the cluster.

Seed Gas

By strongly diluting the clustering species in a non-attaching seed gas, much of the theory of non-condensing molecular beams remains at least qualitatively correct. In this case, condensation proceeds within a kind of heat bath, which also governs the internal energy of the cluster. As adiabatic expansion without condensation can reach very low beam temperatures, the seeded beam method allows for the creation of considerably colder clusters than in pure expansions. Moreover, the addition of an inert carrier gas has in many cases led to enhanced cluster formation. This can be explained in terms of the efficient removal of condensation energy, so that the attachment probability of a further monomer increases for colder clusters. The nature of the seed gas also influences the aggregation process. Heavier seed gases with low heat capacity lead to slower beams and larger clusters, since there are more collisions before the expansion terminates. The mass ratio between clustering and non-clustering species influences the efficiency of the energy transfer from the cluster.

Scaling Laws

Cluster formation is strongly influenced by the expansion parameters. Nozzle temperature T_0, nozzle diameter d , and stagnation pressure p_0 can be taken as coordinates in a three-dimensional coordinate system. To explore this multidimensional parameter space, Hagena [44, 45, 46] has derived scaling laws to correlate expansion conditions that lead to the same mean cluster size $\overline{N}$. They are based on the idea to keep the kinetic conditions (unimolecular as well as bimolecular) in the flow constant. As the temperature dependence of the involved cross sections, lifetimes and

reaction probabilities is generally not known, only finite intervals $[T;\, T \pm dT]$ with the same temperature are considered. The scaling surface can be described as

$$\frac{n_0}{n_{0,\mathrm{ref}}} = \left(\frac{T_0}{T_{0,\mathrm{ref}}}\right)^{f/2-s\cdot q} \left(\frac{d}{d_{\mathrm{ref}}}\right)^{-q}, \tag{2.15}$$

where the parameters f=2/(κ-1) and s=(f-2)/4 have been introduced. It correlates a new set of expansion parameters to a reference state (index *ref*) in such a way that the obtained cluster size distribution remains approximately the same. The value of q has to be determined experimentally and lies within the range $0.5 < q < 1$. For scaling laws concerning the influence of a diverging hypersonic section attached to the simple converging nozzle used in the present experiments see Ref. [46]. Generally, such nozzles produce similar centerline flow fields at a reduced mass flow. These advantages are restricted by boundary layer effects which disturb the core of the nozzle flow. The experimental evidence for the scaling laws, especially in connection with small clusters, is strongly influenced by the detection process (ionization-induced fragmentation). Nevertheless, they give a qualitative picture of the influence of expansion conditions.

Cluster Temperature

Although being a finite system, the energy stored in the internal degrees of freedom of the cluster is often characterized by a temperature. A direct approach to cluster temperature is provided by high energy electron diffraction measurements which assign temperature based on the mean vibrational amplitude of the cluster constituents around an assumed lattice position. For large dielectric clusters, a useful empirical rule for the observed final temperature was obtained [47]:

$$T_{\mathrm{final}} \approx 0.5\, T_m \approx 0.33\, \epsilon/k_B, \tag{2.16}$$

where T_m is the bulk melting temperature and ϵ the well depth of the binary interatomic or intermolecular potential. For the rare gases He, Ne, Ar, and Xe this relation predicts cluster temperatures of 3.4 K, 11.8 K, 41 K and 76 K. On the other hand, temperature can be introduced via the evaporative behavior of the cluster. After the expansion, cluster cooling is achieved by evaporation of cluster constituents. The statistical RRK-theory predicts an evaporation rate for a cluster built from N atoms

$$k(E^*) = \nu\, g\, (1 - \frac{D_N}{E^*})^{s-1} \stackrel{s\to\infty}{=} \nu\, g\, \exp(-D/k_B\, T), \tag{2.17}$$

with $s = 3N-6$ being the number of vibrational degrees of freedom, ν the characteristic vibration frequency in the range of 10^{12}-10^{13} Hz, E^* the thermal energy of the cluster, D_N the energy to remove one particle from the cluster of size N, and g the degeneracy of the system, which is normally taken to be proportional to the number of surface particles. In this model the cluster is treated like s strongly coupled oscillators (Einstein model) and the classical probability to find more than the dissociation energy D_N in one vibrational coordinate is calculated. The evaporation reduces the thermal energy E^* of the cluster and thus decreases the rate of evaporation. Assuming that on average each vibrational degree of freedom is endowed with energy k_BT, a quasi-temperature can be assigned via $E^* = s \cdot k_BT$. The right-hand side of Eq. (2.17) gives the limit for large clusters, which is valid starting from $N \approx 30$.

A better approximation is given in [48]. The evaporative cooling mechanism is important at cluster temperatures $0.3\,\epsilon/k_B < T < 0.6\,\epsilon/k_B$ [49]. The evaporation rate is governed by temperature scaled by the dissociation energy. This equation can be used to calculate whether the clusters in some experiment are stable within the time window of observation, or, provided the clusters have been found to be stable during the time of observation, to estimate an upper limit for the cluster temperature. In ionic clusters, evaporation is hindered by the additional polarization energy binding the cluster constituents. This is significant for small clusters (e.g. water with N=10) but negligible for larger ones (N>100) [50]. For a given ensemble of clusters having the same size, the distribution of internal energies has a width approximately equal to the energy loss per evaporation step. As the decay rate is strongly dependent on the internal energy, such an ensemble can not be assigned a unique life time, as its decay would be non-exponential.
So far, no closed theoretical description of the full condensation process in free jets is available. On the other hand, mean cluster size is easily experimentally adjusted by means of stagnation conditions. Therefore, the desired cluster size range for the experiments will be achieved iteratively. The methods for the measurement of cluster size distribution are introduced in Chapter 3.

2.1.4 Gas Mixtures

As has been demonstrated in the previous section, gas mixtures are frequently employed in free jet expansions to increase mean beam velocity or to create colder clusters. For these applications, weakly interacting species, such as small rare gas atoms, that do not participate in the condensation process, are generally added. For experiments with molecular test tubes, it is often desirable to produce mixed clusters composed from the various educts. Again, adiabatic expansion provides the means to form such mixed clusters. However, there is no one-to-one correspondence between cluster composition and the composition of the expanded gas. The temperature and density of a volume element that participates in the adiabatic expansion of a gas mixture out of the condensable species A and B with molar fractions X_A and X_B, will decrease as the volume element is accelerated. Assuming a constant molar fraction, the number of collisions of the monomers with an existing cluster within the volume element is proportional to their mean thermal velocity at the local temperature and is therefore smaller for heavier species than for lighter ones. Thus, the lighter species gets more chances to incorporate into the cluster. Moreover, each attachment introduces its respective binding energy $D_A(N_A, N_B)$ or $D_B(N_A, N_B)$ into the cluster. This binding energy may depend on cluster size and composition. The cluster becomes hotter with each attachment and associated with this is the increased probability of monomer evaporation. As is evident from Eq. (2.17), the evaporation process strongly favors the ejection of weakly bound constituents. The more endothermic channels are exponentially suppressed, so that the stronger bound species will substantially accumulate within the cluster. Thus, the composition of the original gas mixture, characterized by X_A and X_B, gets distorted during the composition of the cluster by a transfer function which depends parameters such as the mass of the species, and in a strongly nonlinear way its binding energy. The determination

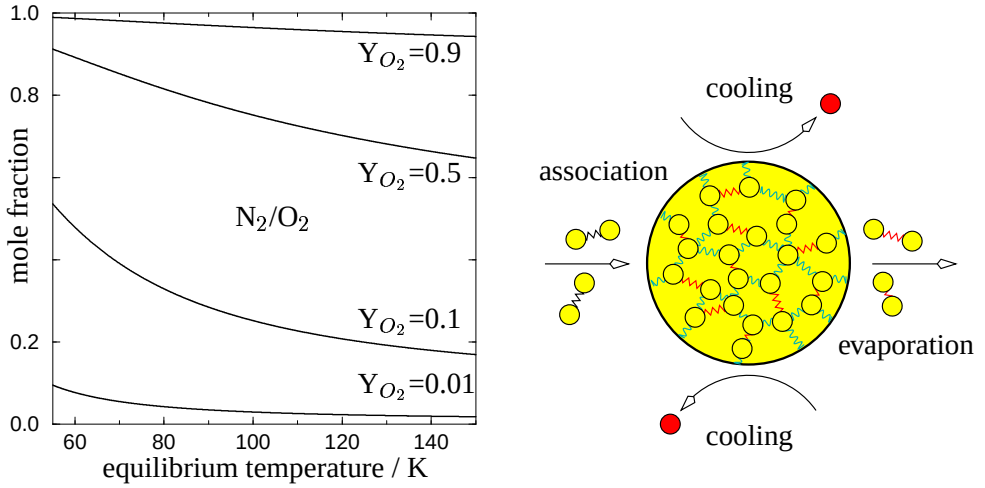

Figure 2.4: Left panel: Simple macroscopic model correlating the composition of a cluster with the composition of the surrounding gas phase for a binary mixture calculated according to Eq. (2.19). The parameters correspond to a system of N_2/O_2. The solid lines give the mole fraction of oxygen inside the cluster for a composition of the surrounding gas as indicated by the labels. The species with the higher binding energy accumulates considerably within the cluster. With higher temperatures this effect decreases, nevertheless it is still prominent. The right panel gives a schematic representation of the cooling processes for clusters in supersonic beams. They dissipate the energy which is deposited into the cluster via each nucleation step. On the one hand, there is *collisional cooling*; i.e., the relaxation of internal degrees of freedom via non attaching collisions with other monomers or the carrier gas. They are only active until the beam reaches the collision free regime. The second mechanism is *evaporative cooling*; i.e., unimolecular dissociation of large metastable clusters, which generally proceeds up to the detection point. Whereas the first process only influences cluster temperature, the latter, together with the nucleation steps, influences the composition of mixed clusters. The accumulation process of one species within the cluster, due to the frequent association and evaporation steps, demonstrates similarities to macroscopic distillation processes.

of cluster composition (e.g. by integrating a system of rate equations for association and evaporation steps) is not straight forward, since little is known about the binding energy $D(N_A, N_B)$, which together with the cluster temperature governs the final composition in a delicate manner.

Cluster Composition

There have been several attempts to predict cluster compositions that result from binary nucleation [51, and references therein], however, no complete theory is available for the case of small, fast growing clusters. For a qualitative understanding, a simple macroscopic model, based on the behavior of bulk binary mixtures, is presented here. The composition of the gas-phase above a plane interface with an ideal, binary liquid is given by the *Raoult* law. The partial gas pressure of the respective constituent corresponds to the product of its molar fraction in the mixture and its vapor pressure according to the chosen temperature. Thus, the mole fractions of the liquid X_A, X_B are connected to the mole fractions Y_A, Y_B in the gas phase and vice versa

$$Y_A = \frac{X_A \cdot p_{v,A}(T)}{X_A \left[p_{v,A}(T) - p_{v,B}(T)\right] + p_{v,B}(T)} \qquad Y_B = 1 - Y_A \tag{2.18}$$

$$X_A = \frac{Y_A \cdot p_{v,B}(T)}{Y_A\,[p_{v,B}(T) - p_{v,A}(T)] + p_{v,A}(T)} \qquad X_B = 1 - X_A, \tag{2.19}$$

where p_v(T) stands for the vapor pressure of the respective species. If the interface to the gas-phase is not planar but features a curvature, the vapor pressure is increased. This effect can be accounted for by the *Kelvin* formula

$$p_v(r) = p_v(\infty) \cdot \exp(2\,\gamma\,V_m\,/\,r\,RT), \tag{2.20}$$

where V_m represents the mole volume of the liquid and γ the surface tension. In a simplified model, this vapor pressure enhancement for a preformed mixed cluster can be characterized by some mean value for mole volume and surface tension of the cluster constituents. In this case, the Kelvin effect does not influence the equilibrium composition, although in accordance with classical nucleation theory [51] it determines the minimum stable cluster size under a given supersaturation. Thus, the equilibrium composition of the cluster for a given composition of the gas phase is given by Eq. (2.19). As an example, the left panel of Fig. 2.4 shows cluster compositions for a N_2/O_2 gas mixture. The higher boiling point of oxygen with respect to nitrogen at standard conditions indicates a stronger interaction of the oxygen molecules and consequently a higher binding energy. Consequently, there is considerable oxygen accumulation within the cluster with respect to the mole fraction of O_2 in the gas phase, although O_2 is the heavier molecule. The over-representation decreases with increasing temperature, nevertheless it is still prominent. The limitation of this simple approach is the macroscopic treatment of the cluster by using properties such as surface tension or vapor pressure, and the equilibrium assumption. During expansion the temperature within the considered volume element is not constant but rapidly decreases. Moreover, the temperature assigned to the internal excitations of the cluster and the temperature of the surrounding gas mixture are generally not equal. Nevertheless, the simple model allows for the determination of the key factors for cluster composition, namely internal cluster temperature and binding energy of the constituents. With regard to the difficulties in predicting cluster composition, an iterative approach to the creation of clusters of a given composition once again seems appropriate. Feedback information for this iteration process can be obtained by ionizing the cluster distribution followed by analysis of the composition of the cluster ions; e.g., by time-of-flight mass spectrometry (Chapter 4). The mixture of the expanded gas can then be changed until the desired composition becomes dominant within the cluster spectrum. In this context, the question arises, to which degree the composition of cluster ions corresponds to that of the neutral clusters. At least for larger clusters in quasi-equilibrium, the ionization-induced evaporation of constituents should not greatly alter the mean composition, as the preceding neutral cluster stabilized itself by evaporations, with ionization introducing further amounts. However, caution is appropriate.

Fig. 2.5 shows mass spectra for pure O_2 clusters and mixed N_2/O_2 clusters, obtained in the present work, following electron impact ionization of the respective neutral beams. The spectrum of the pure expansion consists of an equidistantly spaced series of peaks separated by the mass of a single constituent. An additional series which is due to dissociative ionization of oxygen exemplifies the influence of the ionization

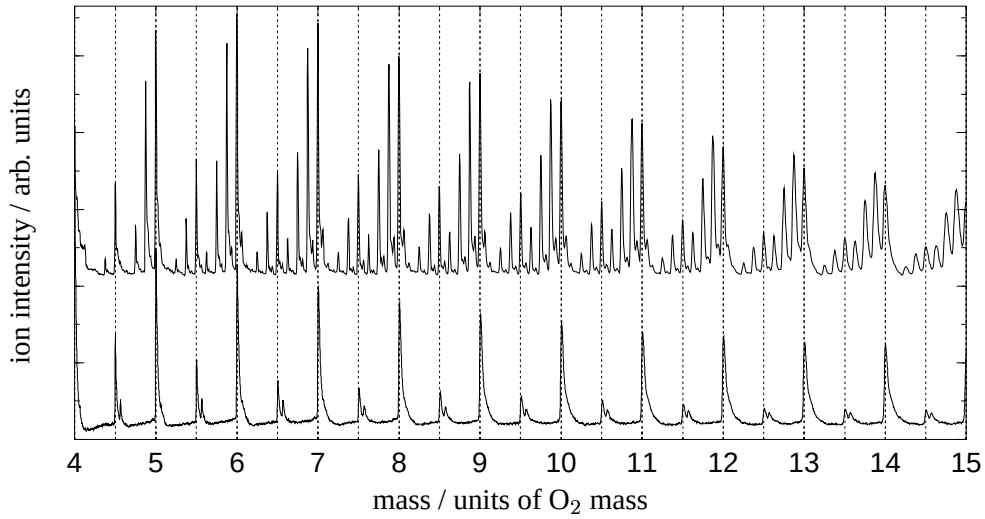

Figure 2.5: Mixed clusters of N_2 and O_2. The lower trace shows a mass spectrum of pure O_2 clusters (stagnation pressure p_S=20 bar, reservoir temperature T=300 K, nozzel diameter d=0.5 mm). The main peak progression can be described in terms of $(O_2)_n^+$ cluster ions. During electron impact ionization, fragmentation of the oxygen molecule also occurs, resulting in the smaller progression $O(O_2)_n^+$. The expansion of a mixture of 1:1 O_2 and N_2 (p_S=30 bar, T=190 K, d=0.5mm) is shown in the upper trace. Instead of a single mass peak for cluster size N, there is a manifold of clusters with different compositions, with the sum of the number of oxygen and nitrogen molecules being equal to N. The splitting of the manifold is given by the mass difference of 4 u. In spite of the equimolar gas mixture, the clusters are dominated by oxygen, as can be seen from the asymmetry of the envelope for one cluster size N. For $N > 10$ the pure oxygen cluster becomes smaller than the cluster in which one oxygen has been replaced by one nitrogen molecule due to the higher combinatorial weight. If only combinatorial factors are taken into account, the cluster size for which both are equal, can be used to compute an effective gas mixture which reproduces the observed cluster composition.

process. For the mixed 1:1 expansion of N_2 and O_2, the peak for each cluster size N splits up into a manifold of $N+1$ peaks separated by the mass difference between the constituents (4 atomic mass units). Each such peak represents a cluster of composition of n oxygen molecules and $N-n$ nitrogen molecules, with their relative intensity being determined by the composition of the mixture. Since the width of the corresponding group of peaks increases with increasing total cluster size, there is overlap starting from $N_{\mathrm{overlap}} \approx M/\Delta m$, where M stands for the mass of the lighter constituent and Δm for the mass difference between the two (e.g., a peak at mass 224 u could contain clusters composed of 7 O_2 molecules or 8 N_2 molecules). This problem constrains experiments with exactly defined cluster composition to small clusters.
Starting from the mass spectra, it is tempting to describe the observed abundance distributions for a given cluster size N in terms of a binominal distribution. This assumes that all the dynamic processes of association and evaporation, with their delicate temperature dependence, can be described by an effective composition of a gas mixture from which clusters grow based on combinatorial principles. The combinatorial abundance distribution for a cluster of size N, grown from a binary mixture

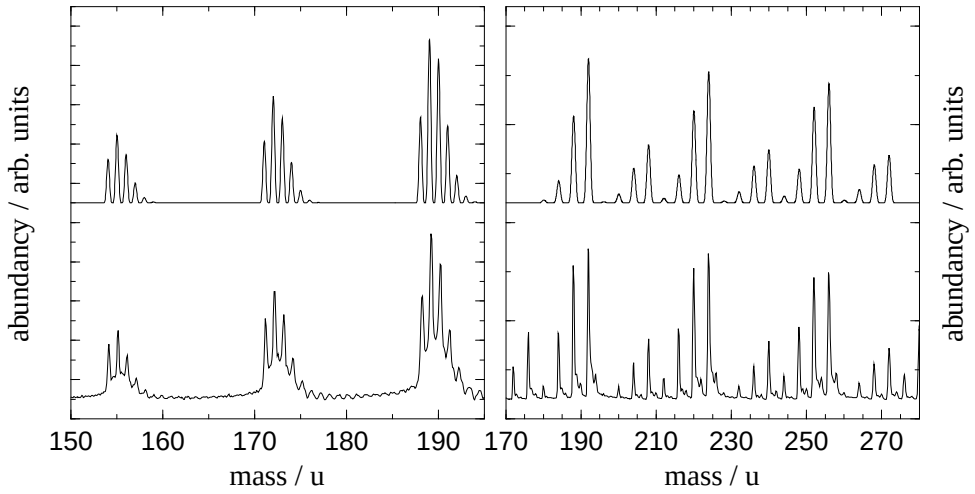

Figure 2.6: A simple combinatorial model for the description of cluster compositions. While the lower curve has been measured experimentally, the upper curve corresponds to the theoretical model description. Left panel: Mixture of H_2O and NH_3 in terms of a hypothetical 17:20 mixture which simulates the observed $NH_4^+(NH_3)_n(H_2O)_m$ progression. The overall abundance of each cluster size has been adjusted separately. Right panel: Mixture of N_2:O_2 in terms of a hypothetical 1:11 mixture. The experimentally observed second progression, anchored on O^+ instead of O_2^+, is described by shifting the main progression by 16 mass units and scaling its overall height. The much larger tendency of oxygen to form clusters is reflected by the discrepancy between the gas composition obtained from the simulation and that which is used experimentally; N_2:O_2=1:1.

A and B with molar fractions X_A and X_B, can formally be written as:

$$(X_A + X_B)^N = \sum_{k=0}^{N} \binom{N}{k} X_A^{(N-k)} X_B^k \tag{2.21}$$

$$\text{e.g. N=3: } (X_A + X_B)^3 = 1 \cdot X_A^3 + 3 \cdot X_A^2 X_B + 3 \cdot X_A X_B^2 + 1 \cdot X_B^3.$$

Each term within the sum defines a mass peak; the prefactor gives the number of permutations for a given composition under the assumption of discernable constituents. The individual probability of a composition is given by the following product of the molar fractions to the respective powers. The powers of the molar fraction stand for the number of respective molecules contained in the peak and the corresponding mass can be obtained by summing the product of the powers with the respective single constituent mass. Naturally, such a model can not account for the overal enevlope of a measured cluster size distribution, nor for especial structural stabilities for certain cluster sizes and cluster compositions (see the *magic numbers* in Chap. 3). Fig. 2.6 demonstrates the application of Eq. (2.21) to experimental data, namely to a H_2O/NH_3 mixture (left panel) and to a N_2/O_2 mixture (right panel). Whereas the latter mixture contained nitrogen and oxygen in the ratio 1:1, the combinatorial distribution can best be explained in terms of a hypothetical mixture of 1:11. This emphasizes the distortion of the cluster composition with respect the expansion gas. The

oxygen-containing peaks are dominant, with the pure oxygen cluster being the most prominent up to N=8. However, due to the fast growing number of permutations for mixed compositions with increasing cluster size, the cluster containing one nitrogen molecule becomes larger than the pure oxygen cluster for $N > 12$ (not shown). The cluster size for which adjacent peaks are of the same size, can be used to calculate the combinatorial mixture for the observed spectrum. However, the description in terms of a single combinatorial mixture represents an approximation, the quality of which depends of the chosen system. Whereas the left panel of Fig. 2.6 presents a good example for the case of ammonia/water clusters, the right panel depicting results for the N_2/O_2 system with its additional effects such as dissociative ionization, shows poorer agreement. This deviation from the model indicates that the observed clusters have not been created in a purely statistical process. The problem of correlating the combinatorial mixture to the real composition of the expansion gas is absent, if a single gas species having several isotopes is used. With the chemical properties being equal, the cluster composition should in very good approximation reflect the gas composition. In this case, the outlined method should allow the determination of the isotopic content of a given probe.

2.1.5 Pulsed Adiabatic Expansion

Condensation of molecular clusters in adiabatic expansions is enhanced by increasing the stagnation pressure, by decreasing the nozzle temperature, by adding carrier gases to the expansion as well as by increasing the nozzle diameter. However, all of these options increase the total gas load the vacuum system has to cope with. Experiments therefore are often performed using differentially pumped setups in which the main gas load is pumped away in an expansion chamber at a working pressure of 10^{-3} mbar. At this high pressure, standard vacuum pumps with pump speeds around 1000 l/s transport gas loads of 1 mbar l/s. However, the corresponding short mean free path length of a few centimeters is prohibitive for a variety of experiments. Therefore, the central part of the cluster beam is transferred by means of a skimmer into an experimental chamber at much better vacuum. By admitting only a fraction of the gas load, similar pumps such as used in the expansion chamber, can maintain a much better vacuum. A typical value for gas load reduction and the decrease in the average background pressure is a factor of 1000.

To further increase stagnation pressure with a given vacuum system, pulsed expansions can be employed [52, 53]. The resulting beams have instantaneous intensities that are orders of magnitude higher and consequently contain more clusters. The lower duty circle is often no disadvantage, especially in connection with other pulsed devices (e.g., high power lasers). A more serious problem is the fact that beam velocity, temperature and cluster distribution are not uniform throughout the pulse (see Fig. 2.7).

Pulsed Beam

Ideally speaking, a pulsed beam is generated by 'gating' a steady-state beam. A gas pulse created by a typical gate opening of 100 μs and having an average beam velocity of 1000 m/s can be pictured as a 10 cm long 'cone' moving through the apparatus. Having these small dimensions, the pulse is able to completely traverse the vacuum chamber before the background pressure rises due to scattering from the

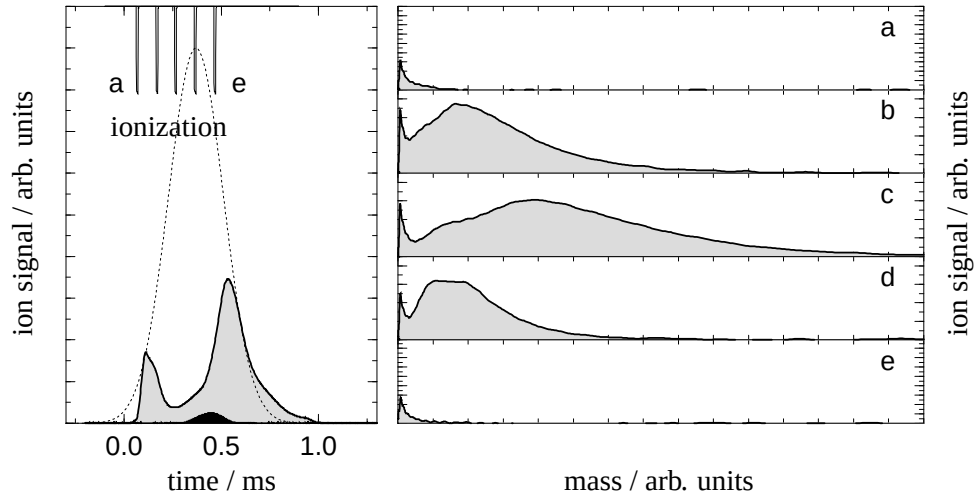

Figure 2.7: Pulse shape and position dependent cluster size distribution. The left panel gives the shape of a heavily clustered, unseeded N_2/O_2 adiabatic expansion, as measured via electron impact ionization. Considerable deviation from a simple smooth curve, that would be observed with unclustered beams (dotted line), is observed. The dip in the signal corresponds to the regions of strong clustering. This can be understood from a reduced ionization cross section of large clusters (see Chap. 3), and an increased scattering of monomers, due to the local condensation process, out of the beam. The black shaded curve corresponds to the ion signal from clusters larger than 160 constituents. The shift to later times with respect to the dip in the total signal is partly connected to a time-of flight separation. Following ionization, the ions are accelerated. For heavier species this acceleration results in a smaller velocity, so that these ions reach the detector later than the lighter ions. As shown in the right panel, this can be used to investigate the local cluster distribution within the gas pulse. At the positions a) to e) the pulse is ionized by a short electron pulse (τ=10 μs). The resulting ion current is measured at some distance. Whereas at positions a) and e) almost no clusters are present, positions b) to d) show pronounced clustering, however, to quite different extents. The distributions of small ions, present in all spectra, are partly connected to fragmentation during the ionization process. Unseeded, high pressure expansions present an extreme situation with respect to variation of the cluster size distribution with pulse position. Seeded beam expansions, as have been employed in most of this work, generally show a much greater homogeneity (see Chap. 3), nevertheless the effect is still present.

walls. Between pulses, the vacuum system has time to restore the background pressure increased by the pulse gas load to its original value. For a detailed analysis see Chap. 2.3. There are no restraints for beam intensity or background pressure for a single short gas pulse, however, pumping speed will always limit the maximum pulse repetition rate that can be achieved subject to given beam intensity and background pressure requirements. With the low background pressure of pulsed beam experiments, also shock fronts created by the interaction between the expanding gas and the background gas in the expansion chamber tend to be absent. Shocks form only by reflections from chamber walls, but for short pulses, these do not exist until the pulse has fully traversed the chamber.

Assuming a series of ideal 'square' gas pulses with repetition rate ν and pulse duration τ, the reduction of the gas load is given by the duty factor defined as $f = \tau \cdot \nu$ and can easily reach 1/200. The gas consumption of the experiment is reduced in the same way. Pulsed molecular beam sources are mechanical devices. In comparison to steady-state sources these can be used only in a limited temperature range. The fast moving shutter tends to bounce, so that double pulses are often observed. Pulsed valves are subjected to wear, so that the opening characteristic changes over time. Their shutter function may also change with expansion conditions and opening time. Molecular beam properties are very sensitive to the expansion circumstances. Typical minimum opening times of a pulsed beam to reach steady state-conditions within the pulse have been found to be in the range of a few microseconds [54, 55]. This time is also a measure for the length of the transition regions at the beginning and the end of longer pulses. Cluster beams, with their delicate, nonlinear dependence on local beam properties, are even more sensitive to expansion conditions than molecular beams. For them the transition time to steady state conditions is only a lower limit. Moreover, pulse-to-pulse variations, often not relevant in uncondensed beams, can be aggravated by the condensation process. Thus, the higher beam intensity and cluster content of pulsed beams is available only at the price of a lower duty cycle and considerably larger experimental effort. The performance of the nozzle, such as its opening characteristic and mass flow, have to be closely controlled in actual experiments (see Chap. 2.3 and 3.2).

2.2 Experimental Setup

Vacuum System

To perform the experiments a two-chamber molecular-beam apparatus has been built. It takes into account the special requirements of pulsed cluster beams, such as a high pumping capacity to cope with the gas load and a large-volume expansion chamber to store the gas load of each individual pulse before it is pumped away between pulses. The vacuum chamber consists of three modular subunits (Pink Vakuumtechnik) based on ISO-DN250 flanges. A variety of KF40 openings are provided for use as feedthroughs as well as viewports. Two of the units are identical spheres fitted with six-fold crosses and having a volume of about 35 liters each, while the third one is a DN250 cylinder fitted with a four-fold DN160 cross and has a volume of about 17 liters. One sixfold-cross is used as the expansion chamber, and the combined remaining two units as the experimental chamber. The separation of the expansion and the experimental chambers has been established by sandwiching a blind DN250 flange between them. The flange has been fitted with an additional sealing ring as well as a central bore to house the skimmer setup. A schematic drawing of the whole vacuum system is given in Fig. 2.8. The vacuum is maintained with a 1500 l/s turbo molecular pump (Balzers TMH1600) in the expansion chamber and a 520 l/s turbo molecular pump (Balzers TMH520) in the experimental chamber. Both pumps are equipped with an internal second compression stage, which allows for a fore line pressure in the mbar regime that is achieved by oil-free membrane fore line pumps (Vacubrand MD4T). A bypass between the fore line pumps allows for the equal distribution of the gas load, which predominantly stems from the expansion chamber, if valve BP

is open. Together with valves S_1 and S_2 the bypass allows maintenance work at individual fore line pumps without venting the system. The pressure in both vacuum chambers is measured by a combined pirani / cold cathode ion gauge (Balzers Compact Gauge 250) with a working range from 1000 to $5{\cdot}10^{-9}$ mbar. A discussion of the time dependent pressure-measurement when the pulsed beam is switched on is given in Chap. 2.3. The fore line pressure is determined from two pirani gauges (Balzers TPR261). All pressure readings are displayed by TPG252 controller units. The vacuum pumps, as well as the pressure values are monitored by a SPS controller (Siemens Simatic S7-200) which in the event of problems shuts down the system in a controlled manner (e.g. pump failure, power loss)

Gas Load

The maximum gas load for the vacuum system can be calculated from a few system parameters. The required minimum mean free path length implies an upper limit for the pressure in the expansion chamber of 10^{-3} mbar. For steady state beams and a pump speed of 1500 l/s, this corresponds to a gas load of 1.5 mbar l/s or $\approx 3.6{\cdot}10^{19}$ particles/s. For a nozzle diameter of 0.5 mm this flow rate is reached at a He stagnation pressure of ≈25 mbar. Assuming a seeded gas expansion with a dilution of 3 % and a mean cluster size of 1000, the flow of clusters out of the nozzle is in the range of 10^{15}/s. The skimmer typically reduces the gas load by a factor of 1000, leaving 10^{12} clusters/s in the experimental chamber. By pulsing the beam, for example with a repetition rate of 10 Hz and a pulse duration of 300 μs, the instantaneous intensity can be increased by the inverse of the duty factor of 333 corresponding to a stagnation pressure of ≈8 bar. Stagnation pressures larger than 25 bar have been experimentally achieved, increasing the amount of clusters ($\bar{N}$=1000) to 10^{15}/s in the experimental chamber, corresponding to $3{\cdot}10^{11}$ clusters per pulse.

Gas Supply

The creation of mixed as well as seeded cluster beams is based on the expansion of gas mixtures. To allow for flexibility with respect to gas composition, a gas mixing unit has been set up based on a 1 liter pressure reservoir (Whitey). The reservoir, as well as all connecting lines, can be evacuated by means of a 240 l/s turbo molecular pump (Balzers TPU240) coupled with a two-stage rotary-plane fore line pump (Edwards E2M-18). The pressure in this separate vacuum system is again monitored by a PKR250 / TPR261 / TPG252 combination. The reservoir can be filled via inlet ports and a system of valves (see Fig. 2.8). Back streaming can be reduced by evacuating the supply tubes between each individual mixture component. An additional exhaust port allows for the release of residual pressure in the reservoir before it is evacuated. The stagnation pressure at the nozzle can be regulated by means of a one-stage pressure reduction valve (DruVa 0.1-30 bar). All connecting tubes are made of 6 mm stainless steel tubing; all valves are vacuum tight (Nupro BN and DS series). The gas pressure in the reservoir, as well as the chosen stagnation pressure at the nozzle, are monitored by two total pressure gauges (BD Sensors DMP333, DA480 control unit) providing readings of up to 100 bar with ±0.25 % accuracy. The reservoir together with the tubing circuit and the valves are placed into a temperature controlled (T_{max}=400 K) insulated box (see Fig. 2.8). By evacuating the gas mixing unit at elevated temperatures, it can be cleaned of all kinds of residues. This cleaning procedure has been implemented between runs with different gas mixtures. The vacuum chambers as well as the gas mixing unit are supported in a frame structure built from 40mmx40mm aluminum profiles (Item). It provides additional rack space

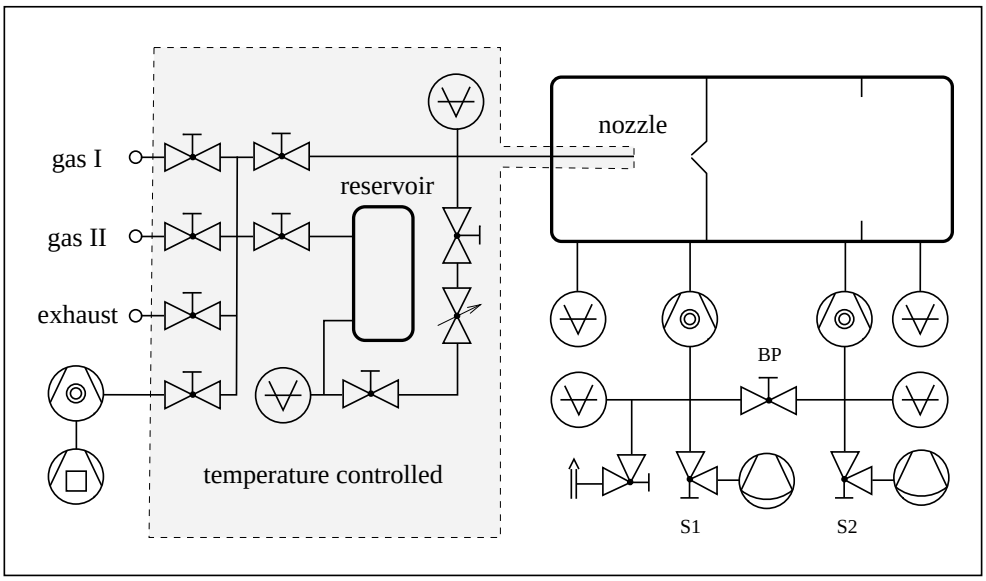

Figure 2.8: Setup of the vacuum system and the gas supply. The shaded region comprises the temperature controlled units which consists of the gas mixing system and the pulsed nozzle. They can be evacuated by a separate pump system (left). To the right, is the differentially pumped two-chamber cluster beam apparatus together with its vacuum circuit.

not only for the pump- and pressure-controllers, but also for additional measurement and data acquisition devices. A system of adjustable feet and castors complete the self-contained mobile system.

Pulsed Nozzle

The pulsed nozzle used to generate the cluster beams is a high speed solenoidal valve (General Valve Series 9, Iota One pulse driver). The principle, taken from fuel injectors in automotive industry, is based on the magnetic force that an energized solenoid exerts on a ferromagnetic plunger. While there is current through the solenoid, the plunger is retracted and opens the nozzle orifice. Otherwise, a system of counteracting springs presses the plunger against the orifice and thus seals it (see Fig. 2.9). To minimize leakage, the plunger tip is made out of a ductile material. In the present experiments Teflon and Kel-F tips have been used. Although Teflon has superior sealing properties, its plasticity results in fast wear and requires frequent replacement. Typical pulse widths used for the cluster beams are in the range of 250-750 μs, typical stagnation pressures between 1 and 20 bar. Different nozzle orifices have been used with diameters between 200 μm and 500 μm. The shape of the nozzle is best described in terms of a simple converging nozzle that leads to the previously described free jet expansion.

The nozzle is mounted in the expansion chamber by means of a XYZ-translation stage, allowing for the positioning of it in front of the skimmer (Beam Dynamics Type II). The latter has a round opening of 1.5 mm diameter and is mounted on a 30 mm long cylinder (see Fig. 2.10). The distance between the skimmer tip and the chamber wall has to be sufficiently large in order to prevent backscattering of the gas pulse front into its tail. The translation stage of the nozzle setup allows for the

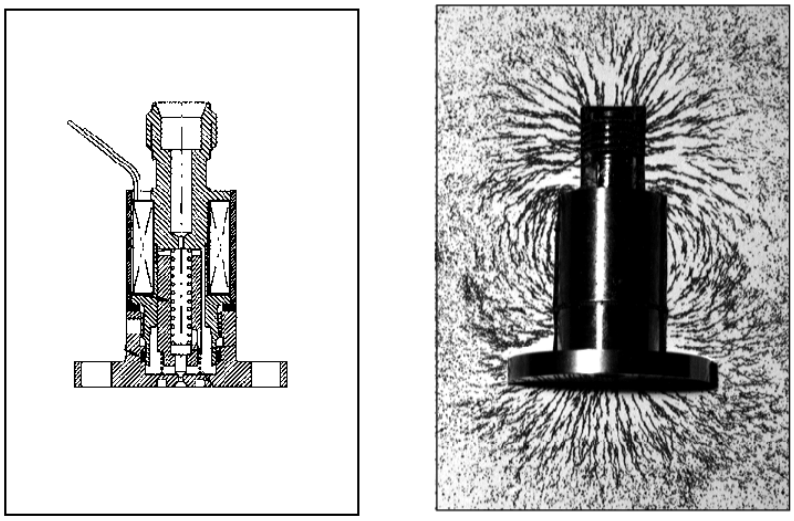

Figure 2.9: Pulsed nozzle. The left panel shows a cross section of the high speed solenoidal valve (General Valve) employed in the experiments. A plunger seals the orifice due to the force exerted on it by a system of springs. Upon opening the nozzle, a concentric solenoid is energized and pulls the plunger back by magnetic forces. The right panel shows the magnetic field which surrounds the energized valve. The field lines have been visualized with the help of iron filings. Although this field influences neither the neutral nor the heavy ionized clusters to a noticeable extent, it has to be taken into account for electron attachment experiments directly in front of the nozzle. The magnetic field strength does not exceed 9 mT anywhere outside of the nozzle housing.

adjustment of the nozzle to skimmer distance. For pulsed beams, the optimal nozzle to skimmer distance is generally larger than in the steady-state situation, where the skimmer has to sample the flow before the shock front forms as a result of the interaction of the expanding gas with the background. Without this restraint larger distances are favorable, because they place the skimmer in a region of lower density and thus reduce skimmer interference. Moreover, they give the pulse more time to complete expansion. The beam intensity in the experimental chamber has an optimum for a nozzle-skimmer distance of 3.5 cm $\pm$0.5 cm.

Nozzle Temperature

As pointed out before, cluster growth strongly depends on the stagnation temperature. Lowering the latter facilitates the condensation of weakly interacting species. Elevated temperatures are necessary to prevent premature condensation in the tubing system of substances with relatively low vapor pressure (water). Control of the expansion temperature is achieved by a simple heat exchanger setup along the last 40 cm of the supply line of the nozzle (see Fig. 2.10). The heat exchange of a flowing medium in a circular pipe is well studied [56]. Here, a gas mixture with temperature T_0 enters a heat exchange pipe of length l_H which can be assumed to have a constant wall temperature T_w. The exit temperature for a pipe of length l_H and diameter d is given by

$$T_{exit} = T_w + (T_0 - T_w) \cdot \exp(-\frac{Nu}{Re \cdot Pr} \cdot \frac{4\,l_h}{d}), \tag{2.22}$$

where gas specific properties enter via the Nusselt number *Nu*, the Prandtl number

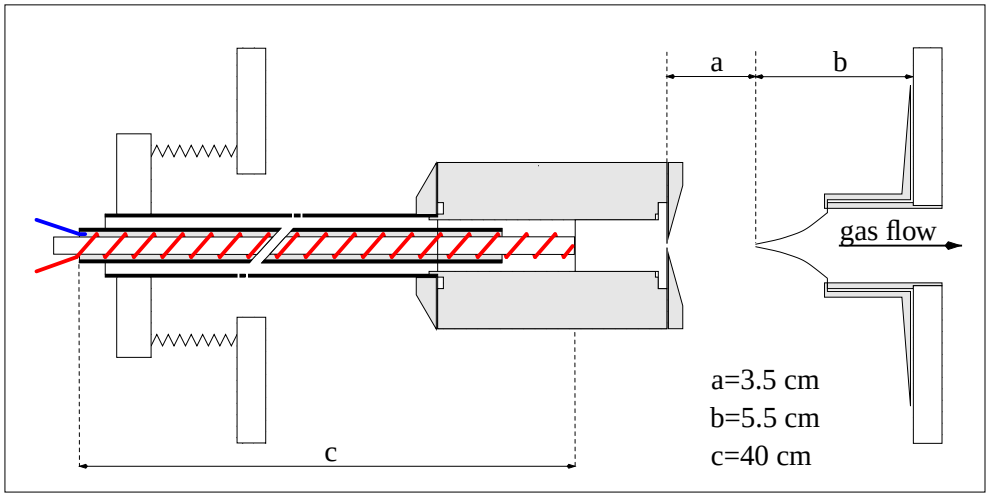

Figure 2.10: Setup of the expansion chamber. The nozzle is mounted on an XYZ-translational stage, to ensure its optimal positioning with respect to the skimmer. The supply line to the nozzle is temperature controlled, allowing for the heating of the nozzle setup in case of condensable vapors, or for cleaning purposes. On the other hand, it allows for the cooling of the expansion gas, which enhances the clustering process of weakly interacting species.

Pr and the Reynolds number *Re*. Within the supply line (d=4 mm) there is a laminar flow with a typical velocity of 1...10 cm/s and typical values for $Pr \approx 1$ and $Nu \approx 4$. Under these conditions the gas reaches wall temperature within a few centimeters. To achieve expansion temperatures below room temperature, the vapor phase above a liquid nitrogen dewar is blown through the guiding tube of the heat exchanger around the nozzle supply line. When close to the nozzle the vapor exits the inner tube and returns in the outer one, which supports the nozzle within the expansion chamber. In this way the nozzle body as well as the nozzle mount are cooled. By using an electromagnetic valve together with an adaptive temperature controller (Eurotherm 900 EPC) to regulate the flow of the coolant in the heat exchanger, stable nozzle temperatures as low as 130 K can be reached. This proved to be sufficient to create large mixed N_2/O_2 clusters. To prevent liquification in the supply lines, the vapor pressure of the gas components at the given nozzle temperature has always to be larger than the respective partial pressure. Safe conditions are given, if the nozzle temperature lies above the critical temperature of all the gas constituents. For heating purposes, an electric heater pipe (Thermocoax, d=1mm) was soldered directly to the supply line of the nozzle with one free end being wrapped around the nozzle body. By resistive heating, temperatures of up to 450 K have been reached. For liquid samples, a small reservoir (10 ml, Whitey) has been inserted into the supply line, in which the carrier gas bubbled through the liquid to ensure optimal saturation. The carrier gas was preheated in the gas reservoir.

Gas Composition

In the case of seeded beam expansions, as well as for mixed clusters, it is essential that the composition of the expanded gas mixture is well defined and constant throughout

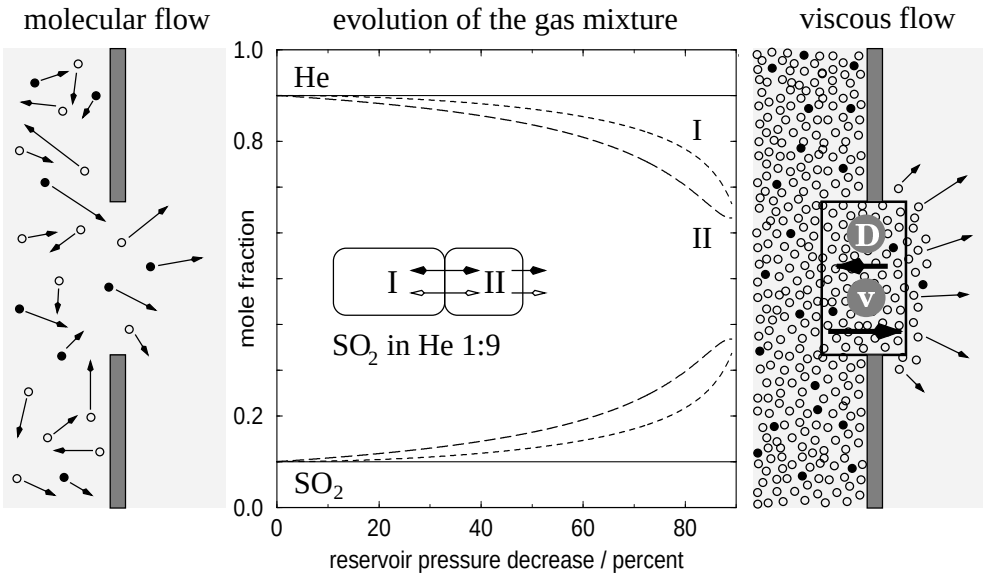

Figure 2.11: Time-dependent partial pressure in the mixing unit. Whereas for molecular flow conditions (left panel) a strong time dependence of the reservoir composition due to the different mean thermal velocities of the mixture constituents is observed, the composition of high pressure gas flow (right panel) remains constant. Generally, the velocity v of a volume element leaving the nozzle is larger than the diffusion velocity D within the gas. Thus, information about the demixing of the gases can not enter the reservoir. The center panel depicts the situation for the two limiting cases based on the gas circuit actually used in the experiments. The gas reservoir I is coupled via a pressure reduction valve to the nozzle supply line (II), from where the gas expands into the vacuum chamber. The solid line gives the high pressure situation, showing no change in composition. The short dashed line represents the demixing in the gas reservoir (I), the long dashed line the demixing in the nozzle supply line (II) for the situation of molecular flow. They have been calculated by solving the respective rate equations. The pressure reduction valve has been incorporated into this model by a time dependent coupling between I and II that keeps the total pressure in II constant.

the experiments. The filling of the gas reservoir with the various mixture components is a highly turbulent process ensuring a high degree of homogeneity of the mixture right from the start. Moreover, typical diffusion velocities at reservoir pressure (max 50 bar, mostly He) lie in the range of mm per minute, which, together with typical reservoir dimensions of 10 cm, smooth out minor inhomogeneities. Measuring the pressure increase connected to the addition of a further component via a capacitive pressure gauge avoids gas specific correction factors. The transfer of the gas mixture through the pressure regulator and the nozzle into the vacuum chamber is discussed in Fig. 2.11. Since the flow velocity in the supply line, as well as through the nozzle, is large compared to typical diffusion velocities, the composition of a gas volume element does not change during the transfer. Therefore, the composition of the gas expanded through the nozzle reflects the situation in the reservoir.

2.3 Calibration of the Particle Number per Pulse

The number of particles introduced into the vacuum system with each pulse is a fundamental reference magnitude for all quantitative measurements, such as of ion yields. Furthermore, by monitoring the particle number per pulse, changes in the expansion conditions (decreasing stagnation pressure, changing performance of the pulsed nozzle due to wear) can also be detected. In the case of continuous sources, the equilibrium working pressure $p_{w,eq}$ in the vacuum chamber allows a straightforward determination of the gas flow into the vacuum system. At the equilibrium working pressure the nozzle supplies the same amount of particles as are being removed out of the vacuum chamber by the pump. In this case, the gas load q is given by $q = p_{w,eq} \cdot S_{eff}$ where S_{eff} represents the effective pump speed of the vacuum pump at the given geometry.

Pulsed Nozzles

With pulsed nozzles, the situation is more complicated, as the background pressure now becomes time dependent. Moreover, in a simple two-chamber setup, as it is used in the present experiments, the gas load found in the second chamber is not only due to the directly transmitted gas pulse, but is also due to the diffuse transport of background gas through the skimmer. Both contributions can be of the same order of magnitude.

For a quantitative model we consider the response of such a system to a single gas pulse or to a periodic sequence of gas pulses. For all practical purposes, the pulse can be represented by a delta function, delivering all particles to the system within negligible time. This separation of time scales is justified if both, the pulse duration and the time to reach a homogeneous gas distribution within the vacuum chamber are short with respect to typical pumping times. Under the present conditions, pulses last from 200 μs to 500 μs, and the time scale to reach a homogenous gas distribution, given by a typical dimension of the vacuum chamber and the thermal particle speed, is of the order of one millisecond. On the other hand, typical pumping time constants lie in the range of several 10 ms to 100 ms.

Single Chamber

In this approximation the injected number of particles ΔN for a single gas pulse can be inferred from the pressure increase Δp at t$\approx$0 connected to each pulse according to the basic equation of the kinetic gas theory

$$p \cdot V = N \cdot k_B \cdot T \rightarrow \Delta N = \frac{V}{k_B \cdot T} \cdot \Delta p, \tag{2.23}$$

where V stands for the volume of the vacuum chamber under consideration and T for the temperature of the chamber walls. As the vacuum pump starts removing the additional particles from the vacuum chamber, pressure decreases again. For a single pulse, the time dependence is given by

$$p_{\text{single}}(t) = p_{bg} + \Delta p \cdot \exp(-k_p t) \tag{2.24}$$

where k_p stands for the pump rate of the vacuum system and p_{bg} for the background pressure without the beam.

Pressure Step Method

The exponential decrease after a single pulse implies that after a fast start, it takes more and more time to remove an ever smaller amount of particles. In the case of periodic gas pulses, not all particles have been removed before the next gas pulse

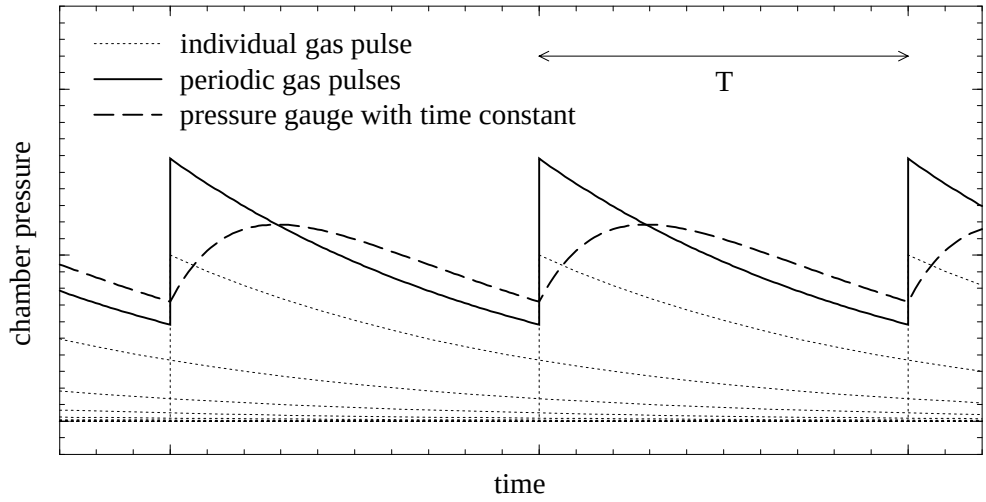

Figure 2.12: Time dependence of the pressure in the vacuum chamber, as produced by an individual pulse (dotted line) or by a periodic chain of pulses (solid line). The repetitive gas supply increases the minimal pressure in the chamber by accumulating the tails of the exponential decay of previous pulses, as well as the peak pressure. Nevertheless, the pressure increase associated with each individual pulse remains unchanged. Typical pressure gauges have a inherent time constant k_m. They do not follow the real time pressure instantaneously but rather smooth out the abrupt changes. A typical gauge response is given by the dashed curve. Values used for the graph are $k_p = 1/T$ for the pump rate and $k_m = 5/T$ for the gauge time constant.

is injected into the chamber. This leads to an accumulation of particles which is governed by the repetition rate as well as the pump rate of the system. For an infinite chain of delta-shaped gas-pulses separated by an interval of T, the time dependence the pressure can be calculated analytically

$$\begin{aligned} p_{rep}(t) &= p_{bg} + \sum_{n=1}^{\infty} \Delta p \cdot \exp(-k_p(t+nT)) = \\ &= p_{bg} + \frac{\Delta p}{1-\exp(-k_p T)} \cdot \exp(-k_p t) \quad (0 < t < T). \end{aligned} \tag{2.25}$$

As is depicted in Fig. 2.12, the periodic gas supply increases the minimum background pressure to $p_{bg} + \Delta p/(\exp(k_p T) - 1)$, and rises the peak pressure to $p_{pb} + \Delta p/(1 - exp(-k_p T))$. Nevertheless, the pressure increase Δp connected to each gas pulse remains unchanged, thus allowing for the calculation of ΔN according to Eq. (2.23).

Coupled Chambers

The time dependent pressure in a second vacuum chamber, which is connected to the expansion chamber by way of a skimmer, consists of two distinct contributions. Firstly, a fixed fraction of the original gas pulse is instantaneously transmitted into the second vacuum chamber. It can therefore be described by Eqs. (2.24) and (2.25). Secondly, an additional contribution stems from the diffusive flow of gas through the connecting skimmer, in between pulses. Due to the large pressure difference between

the chambers and the small amount of gas transmitted by the skimmer from the direct pulse, this diffusive flow has to be taken into account for the second chamber. The diffusive gas exchange through the skimmer is governed by a rate equation

$$\frac{dp_2(t)}{dt} = -k_{p2} \cdot p_2(t) + K(p_1(t) - p_2(t)), \tag{2.26}$$

with K characterizing the coupling between chamber I and II. The value of K can be calculated from the rate of particles colliding with the skimmer orifice of area A and is given by

$$K = \frac{1}{4\,V_{II}}\,A\,\bar{c}, \tag{2.27}$$

where V_{II} represents the volume of chamber II and $\bar{c}$ the mean thermal velocity. Under typical working conditions, the pressure in the expansion chamber is three orders of magnitude larger than the pressure in the second vacuum chamber. Therefore, the back streaming from II into I, given by the term $-K\ p_2(t)$, can be neglected. In this case, the time dependent pressure in chamber II for a periodic chain of pulses is given by

$$\begin{aligned} p_{II}(t) &= \Delta p_{II} \cdot f(k_{p2}) + \frac{K\ \Delta p}{k_{p1} - k_{p2}} \cdot [f(k_{p2}) - f(k_{p1})] \qquad (2.28) \\ f(k_i) &= \frac{\exp(-k_i\ t)}{1 - \exp(-k_i\ T)}. \end{aligned}$$

Taking the limit $T \to \infty$ returns the response of the system to a single gas pulse. Also in the case of additional diffuse gas exchange between the chambers, the pressure rise at t≈0 is connected to the direct gas load Δp_{II} alone. Thus, the number of particles per pulse introduced into chamber I and chamber II, can be obtained from an analysis of the pressure step at t≈0 according to Eq. (2.23). At this time the pulse has distributed homogeneously in the respective chamber but the pumps have not yet removed the gas load.

Prerequisite for this method, however, is a gauge device with a sufficiently fast response time. A suitable device is the *Fast Ionization Gauge* (Beam Dynamics, see also Chap. 3), a pressure gauge based on the Bayard Alpert design, that can resolve rise times down to some microseconds. For the determination of the particle number per pulse, the FIGs are mounted at a position where they are not directly hit by the particle cloud of the gas pulse, and measure the time dependence of the working pressure in chamber I and II. They can be calibrated against a reference pressure gauge under equilibrium conditions, by introducing nitrogen gas into the chamber via an adjustable leak (typical FIG sensitivity: $0.7 \cdot 10^5$ V/mbar at 1 mA Emission), so that their reading can be interpreted in terms of particle number per pulse by applying the above pressure step method. The main uncertainty of this method is the determination of the step height, which is washed out by the time it takes to distribute the gas homogeneously. However, this amounts to an uncertainty below 10 % which is sufficient for all practical purposes.

Average Particle Number per Pulse

Due to the non-negligible influence of the diffuse gas exchange between chamber I and II, the pressure step method is the only straightforward way to determine the

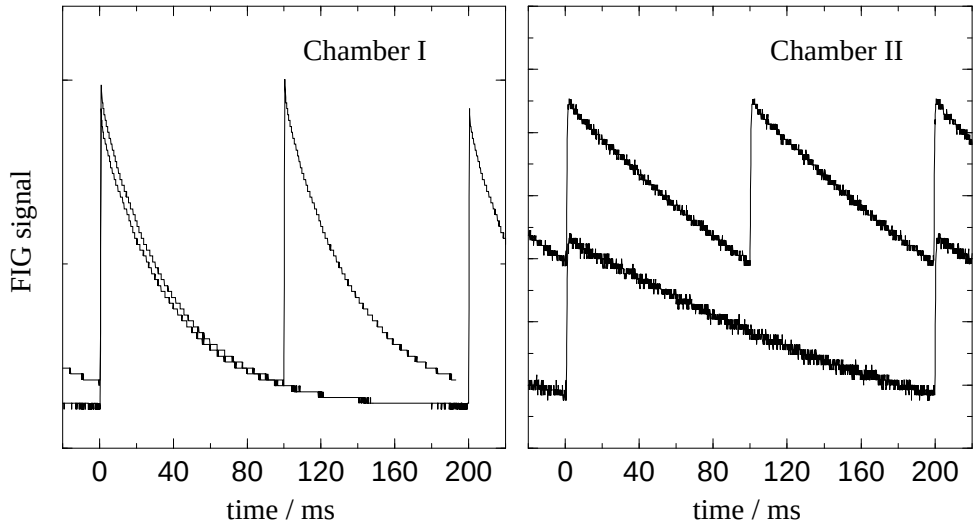

Figure 2.13: Measuring the particle number per pulse in chambers I and II by means of the pressure step method. After proper calibration the FIG readout can be directly interpreted in terms of pressure. This allows for the determination of the particle number via Eq. (2.23) and the known respective chamber volume (Chamber I: 35 l, Chamber II: 52 l). The graphs give the time dependent pressure for two repetition rates (5 Hz, 10 Hz). The higher repetition frequency leads to an increase in background pressure which shifts the respective curve upwards. However, the pressure step associated with each individual pulse remains constant. Fitting the pressure decrease using the appropriate model according to Eqs. (2.25) or (2.28) gives the pump rate of the chamber. For N_2, a pump rate k_{p1}=21 s^{-1} and k_{p2}=4.8 s^{-1} has been determined for chamber I and chamber II, respectively.

particle number per pulse for chamber II. To monitor the *average* particle number per pulse in chamber I, a simpler equilibrium method is possible. Instead of using a very fast pressure gauge to resolve the instantaneous pressure, a slower type that averages out the fast changes is used. A simple model for such a device is given in terms of an RC-time constant. The response $R(t)$ of such a system to a time-dependent excitation $S(t)$ is given by

$$\frac{d}{dt}R(t) = k_m\, S(t) - k_m\, R(t), \tag{2.29}$$

where $1/k_m$ is the relaxation time of the device. This is a first order linear differential equation which can be solved using a propagator method. For a periodic chain of gas pulses, the signal of the pressure gauge in chamber I is given by (see Fig. 2.12)

$$X(t) \propto \frac{\Delta p \cdot k_m}{k_m - k_{p1}} \left[\exp(-k_{p1}\, t) - \left(\frac{\exp(-k_{p1}\, T) - 1}{\exp(-k_m\, T) - 1}\right) \exp(-k_m\, t)\right]. \tag{2.30}$$

With a sufficiently slow measuring device, the reading will remain constant within the accuracy of the device. In this case, Eq. (2.30) can be replaced by its time average, giving

$$\overline{X(t)} = \frac{1}{T} \int_0^T X(t)\; dt = \frac{1}{T}\, \frac{\Delta p}{k_{p1}}. \tag{2.31}$$

This simple relation, which is even independent of the time averaging constant k_m provided k_m is large enough to allow for the replacement of Eq. (2.30) by its mean value, relates the pressure rise above background pressure to the mean average particle number per pulse in Eq. (2.23). The pump rate in the first chamber is easily available by fitting an exponential decay to the FIG pressure readings as shown in Fig. 2.13. Although the averaging does not allow for a pulse-to-pulse analysis, it is helpful to monitor the expansion conditions.
Sofar, only pure gas expansions have been considered. The situation for gas mixtures is more complicated due to differences in ionization cross section as well as different pump rates for the respective mixture components. Most ionization cross sections can be found in literature and the pump speeds for the individual species can be determined experimentally. By considering the different partial pressures individually, an extension of the above model is possible. The pressure step method is ideally suited for the analysis of mixed expansions since the specific pump speeds does not influence the result: At time zero, the pressure increase in chamber I is given by an ensemble of particles that have the same composition as the gas mixture in the reservoir. In order to determine the number of particles in strongly condensed, skimmed beams (chamber II), the analysis of the pressure step has to be made by a mass selective ion gauge (e.g., a quadrupole mass spectrometer) since in this case the composition of the direct contribution does not necessarily represent the situation in the reservoir.

Chapter 3

Molecular Cluster Ions

To facilitate cluster manipulation and cluster detection, it is often necessary to ionize the produced molecular clusters. The Coulomb interaction of charged clusters represents a kind of 'handle' that allows for easy detection, e.g. by directly measuring the neutralization current on some collision surface, and for easy manipulation via electromagnetic fields as employed in mass analysis via pulsed time-of-flight mass spectrometry (see Chapter 4).

Adiabatic vs. Vertical Ionization Potential

Ionization of a preexisting molecular cluster is generally connected to the introduction of excess energy into the system. The minimal energy required for ionization is given by the *adiabatic ionization potential*, which denotes the energy difference between the respective minima of the potential energy hypersurfaces describing the neutral and the charged molecular cluster. The corresponding transition is often connected to substantial configuration changes including rearrangements in the charge-carrying constituent as well as solvation-like rearrangements of the cluster environment induced by the interaction with the core ion. The latter intermolecular configurational changes, including ion-molecule reactions like chemiionization, dimerization or proton transfer [57, see also Chap. 7], can be large. However, typical ionization methods like photoionization, field ionization or electron impact ionization are *vertical.* They do not follow the adiabatic pathway but proceed on a time scale fast compared to the above rearrangements. Governed by Franck-Condon factors, they connect the minimum of the neutral hypersurface to some region of highest transition probability on the cluster ion hypersurface. Therefore the *vertical ionization potential* is generally larger than the adiabatic one, with the energy difference being introduced into the cluster. In the same way, the difference between adiabatic and vertical electron affinity also leads to excited cluster anions.

Fragmentation and Metastable Decay

All surplus energy eventually relaxes into inter- and intramolecular vibration of the cluster, which represents a heat bath for short time energy storage. Often smaller clusters with sizes of up to some ten molecules do not have sufficient degrees of freedom to accommodate the introduced energy and are thus substantially fragmented or even disintegrated immediately after the ionization event (prompt dissociative ionization). A well known example is the Ar system [58, 59] where, due to the large dimerization energy of Ar_2^+, the Ar trimer is completely destroyed upon ionization.
Larger clusters are heated up by the introduced energy and stabilize evaporatively by monomer emission, the rate of which is governed by Eq. (2.17) in the same way as

the hot clusters produced by the accumulation process during adiabatic expansion. In general, energy equilibration proceeds rapidly, so that most of the excitation energy is converted into ejected monomers on a time scale of 1 μs. However, in the case of forbidden electronic transitions, potential barriers, delayed internal ion-molecule reactions governed by rearrangements and slow intermolecular energy transfer, this energy transfer can take place on a longer time scale. Metastable decay has been observed e.g. for nitrogen cluster ions induced by the release of intramolecular vibration quanta into the cluster over an experimental time window of 100 μs. As each quantum is larger than the binding energy of a single N_2, this transfer of a localized excitation leads to the fast ejection of a corresponding amount of monomers [60]. As pointed out in the introduction (Fig. 1.2), the slow energy transfer can be rationalized by the difference of time scale of the fast internal vibration of the strongly bound N_2 molecule and the slow intermolecular vibration.

Fragmentation processes obviously are of central importance and are ubiquitous in cluster ionization processes. They impede quantitative investigations as a function of cluster size, e.g., collisional interaction of electrons and ions with clusters [61] or photoionization cross sections, as the fragmentation process mixes the different channels. Fragmentation can be minimized by using photons close to the ionization threshold or low energy electrons and by using large, initially cold clusters with many internal degrees of freedom. Although fragmentation can never be totally avoided in the ionization of preexisting clusters, it presents no fundamental limitation for the experiments conducted in the present work, as they focus on large clusters and cluster properties that only gradually change with cluster size.

Magic Numbers

A further property of molecular cluster ions, intimately connected to the evaporation process of excited molecular clusters and cluster ions, is the formation of *magic numbers* in the mass spectra of cluster ion distributions (see Fig. 3.1). Magic numbers, basically intensity irregularities in the mass spectra, indicate that clusters of respective sizes are more stable than those of neighboring sizes. The origin of these magic numbers used to be under discussion; i.e., whether to interpret them as being due to special structure and stability of the neutral clusters or to attribute them to properties of the cluster ion [62]. In the case of Van der Waals clusters, the evaporative stabilization after the ionization process dominates the abundance anomalies [63, 64], so that the latter model is applicable.

The presence of magic numbers can be explained in terms of *shell closures*. The pronounced peaks in mass spectra of Na_n clusters [68] have been attributed to closed electronic shells containing 8, 20, 40, 58 or 92 electrons as predicted by the Jellium model. Being bosons, the Na ion cores do not show a shell structure of their own. In the case of Van der Waals clusters, often optimized packing of the constituents can explain the magic numbers in terms of configurations that maximize the number of bonds or minimize the cluster surface. The crystal structure of the bulk is energetically favorable only for large aggregates of several thousand molecules [69, 59]. Icosahedral structures having fivefold symmetries that are forbidden in translationally invariant macroscopic crystals, are preferred for smaller structures. In the process of growing, more and more entities are added to the icosahedral, leading to closed shells for 13, 55, 147, 309 and 561 particles. These configurations represent cluster sizes with enhanced stability.

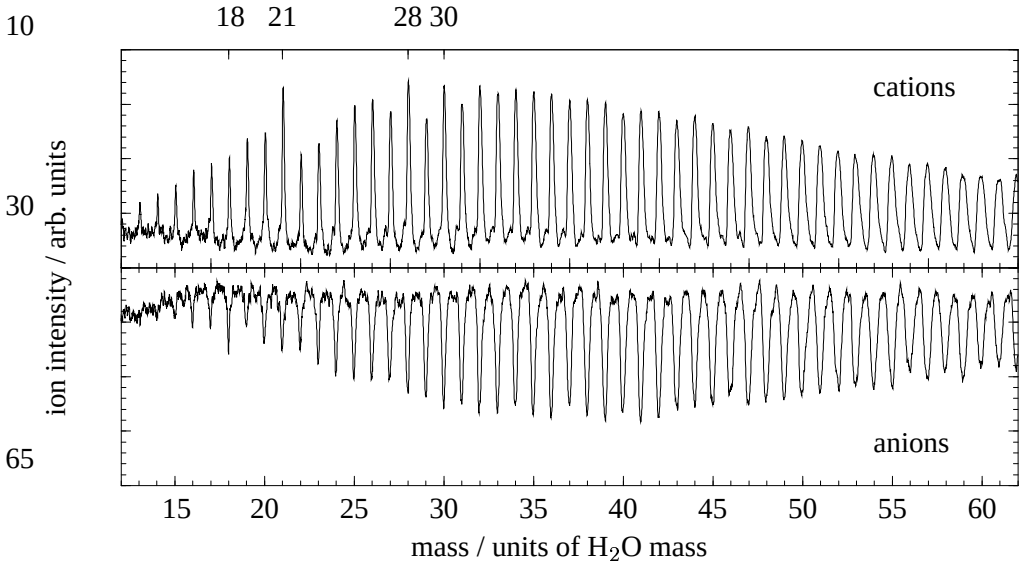

Figure 3.1: Cluster fragment mass spectra of water clusters. The core ions are H_3O^+ and OH^- solvated by water molecules. The spectra have been obtained using the method of cluster fragment mass spectrometry developed in the present work. Neutral water clusters ($\bar{N} = 2 \cdot 10^3$, v=1.7·10^3 m/s) impact on a SiO_x surface held at 690 K. Cluster fragmentation reveals the charges that are present in neutral water clusters due to autoprotolysis. Clearly, the cation spectrum contains magic numbers at 21, 28 and 30 monomers, as is also found upon electron impact ionization of neutral water clusters. In the anion spectrum $(H_2O)_{17}OH^-$ has special stability.

As is evident from Fig. 3.1, magic numbers can not only be observed following established electron impact or photoionization methods but also as a consequence of the cluster fragmentation method proposed in this work. Instead of adding a charge carrier to or removing one from a neutral precursor cluster, a cluster containing a pair of opposite charges is fragmented via a surface collision. Being incorporated into different fragments, the charge carriers become separated. Thus, their mutual shielding, making the precursor cluster neutral, terminates and positively and negatively charged cluster fragments emerge. The creation of geminate ion pairs e.g. via chemical reactions is often easier and more efficient than other options of ionization. The experimental data shown in Fig. 3.1 represent also a proof-of-principle for the new idea outlined in the introduction, namely to 'inspect' charge transfer processes taking place at bulk density in molecular clusters by cluster fragmentation.

Water Mass Spectra

In the case of water clusters (Fig. 3.1) the charge pair is due to autoprotolysis and consists of H_3O^+ and OH^- core ions. In pure, bulk water, this spontaneous proton transfer between two water molecules leads to a concentration of 10^{-7} mol/l of H_3O^+ – the well known pH value – at a temperature of 22^oC. This corresponds to a fraction of $1.8 \cdot 10^{-9}$ protonated water molecules. For a mean cluster size of $\overline{N}$=1000 a fraction of about $2 \cdot 10^{-6}$ clusters should contain a charge pair in first approximation which can be made visible by cluster fragmentation. The emerging

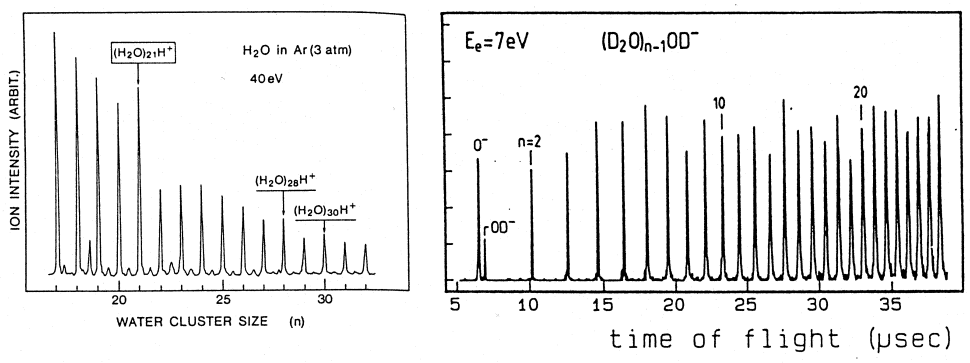

Figure 3.2: Mass spectra of water cluster ions taken from literature. Left: electron-impact ionization of preformed clusters with 40 eV electrons [65]. Spectra with similar intensity irregularities were also observed for near threshold VUV ionization in the same work as well as for cluster ions formed by free-jet expansion of ionized water vapor [66]. Right: Electron attachment with 7 eV electrons [67]. Although completely different ionization mechanisms are involved, the spectra show the same magic numbers with n=18 for $(H_2O)_{n-1}OH^-$ and n=21, 28, 30 for $(H_2O)_{n-1}H_3O^+$.

positive cluster fragments feature magic numbers at 21, 28 and 30. The same values have been observed in standard electron impact mass spectra of water clusters (see Fig. 3.2), where the protonated species $(H_2O)_nH^+$ are formed following a fast intra-cluster ion-molecule reaction [65]. The stable structures $(H_2O)_{21}H^+$ and $(H_2O)_{28}H^+$ are compatible with ion-clathrate (ion-centered cage) configurations, which are special shell structures around a given ionic core. Especially in the case of the smaller structure, the high stability can be explained by a strong Coulombic interaction between the encaged H_3O^+ ion and the surrounding 20 water molecules, which form a deformed pentagonal dodecahedral cage [65]. Previous measurements of the time evolution of these magic numbers show that these structures evolve surprisingly late; in a time window between 4 and 40 μs after electron impact ionization [64]. Although the perturbed clusters immediately start to stabilize themselves by monomer evaporation no magic numbers are formed at early times since in the hot structureless clusters the evaporation rate is not cluster-size dependent. Only upon further cooling, the cluster ion will freeze into more ordered structures and the evaporation rate of clusters with a closed-shell structure will drop appreciably below that of neighboring cluster ions, thus forming magic numbers. A time scale of 10^{-5} s is consistent with Monte Carlo studies [70]. In this way, the temperature of the observed cluster ions can be estimated from the presence or absence of magic numbers. Interestingly, the cationic magic numbers seem to have some flexibility with regard to the nature of the core ion, as the same structure has been found for mixed ammonia/water molecules, where the cage of water molecules includes an NH_4^+ ion [65]. On the other hand, mass spectra of water anions exhibit different magic numbers, the most prominent being $(H_2O)_{17}OH^-$, and thus different cluster ion structures for negative core ions (see Fig. 3.1). This difference can be understood, as the water molecule is not symmetrical with regard to charge inversion. The stable structure at $(H_2O)_{17}OH^-$ has

also been observed in dissociative electron attachment to water clusters with electron energies between 5 and 15 eV [67], although a fundamental different ionization mechanism is at work (see Fig. 3.2). The energetic position of the negative ion states leading to the formation of hydroxygenated cluster ions, as observed in the electron energy dependences of the cross section, are similar to results obtained from dissociative attachment to bare water molecules [71]. The variance, that in the latter mainly H^- is produced compared to the predominate production of $(H_2O)_nOH^-$, can be explained via a fast internal ion-molecule reaction in which the intermediate $(H_2O)_nH^-$ decays rapidly to the observed $(H_2O)_nOH^-$ [72].

Multiply Charged Clusters

Especially in connection with time-of-flight mass analysis (Chap. 4), which is sensitive only to the charge-to-mass ratio, multiply charged cluster ions become a concern. A molecular cluster containing two equal but separate charges is subjected to forces resulting from the attractive interaction between each charge and its environment (dominated by ion dipole or ion-induced dipole forces) and the repulsive interaction between the equal charges within the cluster. Both contributions depend on the specific properties of the cluster . A *critical size* can be defined via the transition from unstable to at least metastable clusters as a function of cluster size. Since experiments normally probe only certain time windows, full thermodynamic stability is not required to observe multiply charged cluster ions.

The electrostatic potential energy of two elementary point charges in vacuum amounts to 1.44 eV at a distance of one nanometer. Therefore, only strongly bound systems like metal and semiconductor clusters can be metastable down to the dimer. For the weakly bound Van der Waals or hydrogen bonded clusters, the critical size is much larger, on the order of several ten molecules. The observed critical sizes can be understood by employing a simple liquid drop model [6, 73] incorporating the surface energy of the cluster and the Coulomb repulsion of like charges. It has been demonstrated [74, 75] that the measured appearance sizes of multiply charged clusters follow the semi-empirical scaling law

$$n_z \propto T_c \cdot v^{1/3} = \text{const}, \tag{3.1}$$

where n_z represents the critical size of a cluster having z charges, v the molecular volume and T_c the critical temperature. The observation of common appearance sizes for $[(N_2)_n]^{2+}$ and $[(N_2)_nN]^{2+}$ [76] indicates that the stability of multiply charged clusters is not affected by the exact nature of the charge carriers. The predicted fixed ratios of the critical sizes for different charge states have been experimentally verified and were found to be $n_2 : n_3 : n_4 \approx 1 : 2 : 4$. For triply charged CO_2 clusters, a particularly asymmetric Coulomb explosion has been experimentally observed [75].

The appearance potential for multiply charged cluster ions is strongly red-shifted with respect to the multiply charged monomer ion and is found to be equal to the respective multiple of the value for the singly charged constituent. Together with their large abundance this confirms that in a multiply charged cluster several singly charged constituents which are the result of sequential, locally separated single ionization processes, are embedded. In the case of electron impact ionization, charges are produced by two subsequent single ionization events of one incoming electron at two different constituents within the cluster (the probability of two incoming electrons

hitting the same cluster is generally low). In photoionization, subsequent ionizations can be induced by the primary photoelectron [77].

Shielding and Total Dipole Moment

A significant deviation of the predicted critical sizes from the experimentally measured values is observed for molecules with large dipole moments. It can be resolved by using a dielectric shielding $\tilde{\epsilon}$ for these clusters, which neglects the contribution of the molecular dipole moment. This hints at the fact that, presumably due to the dominant role of the surface as well as the other charges, the alignment of the solvent molecules around the ions is hindered [75] and thus, shielding remains imperfect at least in smaller clusters with $N \leq 100$. Experiments that determined the total external dipole moment of larger neutral aggregates via the molecular beam electric deflection method in quadrupole fields [78], found that although small clusters of polar molecules, such as the H_2O dimer [79], the $SO_2{\cdot}H_2O$ dimer [80], or the trimer of acetic acid clusters [81] display dipole moments, larger clusters are almost non-polar [80], for example $(H_2O)_n$ with n from 3 to 17 [79]. That molecular clusters do not behave as electrets reflects their tendency to minimize total energy under the boundary condition of finite size. Concerning the dipole moment, the large amount of accessible configurations seem to provide sufficient phase space to realize conformations of vanishing dipole moment even in a finite system. Upon introducing a charge carrier into such a neutral system, the molecular dipole moments start shielding the charge by forming highly ordered micellar structures. In these ordered structures, the dipoles are aligned in comparable directions thus increasing their interaction energy via the repulsion of the dipole tails. Whereas this interaction is carried away in the bulk by consecutive dipole shells, this is not the case in the finite system. Therefore, the fully solvated structure does not necessarily represent the energetically lowest configuration. A tradeoff between solvation and dipole interaction energy determines the quality of shielding in polar clusters.

3.1 Electron Impact Ionization

A large number of methods exist to produce beams of cluster ions (for an overview see [40]); e.g., corona discharges in the expansion chamber, single and multiphoton laser ionization, Penning ionization, charge exchange ionization, sputtering or electrospray techniques. The method of choice largely depends on the special properties of the chosen system: 1+1 resonant two-photon ionization at 193 nm of ammonia clusters allows for the creation of cluster ions with very limited fragmentation [82]. However, a long lived state peculiar to NH_3 seems to be involved. Electron impact ionization is a commonly used method of ionizing molecular clusters as it is almost generally applicable and easy to use. In the present work, cluster ions are created by passing the collimated, fully expanded cluster pulse through an axial electron impact ion source. Depending on the energy of the impacting electrons predominantly cationic or anionic clusters are formed via ejection of a secondary electron or electron attachment, respectively.

Ionization Cross-Section of a Cluster

The ionization process of a molecular Van der Waals cluster is not a collective phenomenon, but can be described to a large extent in terms of an electron interacting with individual molecules of the cluster. Thus, the electron impact ionization of

molecular clusters can rely on a wealth of data accumulated from electron molecule interaction. The latter interaction is commonly described in terms of a cross section, based on a simplified picture of collisions between hard spheres of given diameter. For electrons with energies well above the appearance potential of the respective molecular ion but below 100 eV, the effective area which a molecule exposes to an incoming electron is typically 10^{-15} cm^2. This *total collision cross section* includes all kinds of different interactions: from mere inelastic scattering, which does not impart energy to the internal degrees of freedom of the molecule, via rotational or vibrational excitation to ionization and dissociation. Typical total cross sections for ionization in this energy range lie around 10^{-16} cm^2, roughly one order of magnitude below the total cross section. The number of ions created by a uniform electron beam of density n_e interacting with a thermal gas of density n is given by N_{ion}=$\alpha\, n_e\, n\, \sigma_{ion}$, where α is a constant for a given thermal velocity distribution. Often the electron beam is replaced by an electron bath with a mean velocity and density inside an ionization cage through which the gas passes. In this case α depends also on geometrical factors, as well as on the velocity with which the gas passes through the ionizer.

In a gas containing molecular clusters, the process of ionization can be separated into two distinct steps: first, the incoming particle has to collide with the cluster, upon which the electron interacts with the cluster constituents. Given the high particle density inside the cluster, which is comparable with the values for the respective liquids or solids, the electron frequently interacts. The typical length-scale inside the cluster, calculated from the molecular volume or the Van der Waals binding distance, is 4 Å. This amounts to a geometrical cross section which is on the same order of magnitude as the typical total electron interaction cross section. Thus, the electron inside the cluster is sent on a zig-zag route through the cluster. Whereas an unscattered particle travels a mean distance of 4/3 R through a sphere of radius R, this distance is considerably enlarged by the 'random walk' of the electron through the cluster. With the cross section of ionization being only a factor of 10 below the total cross section, the probability of ionizing one constituent rapidly approaches unity even for moderate cluster sizes, once the cluster has been hit by the electron. This also rationalizes the aforementioned high probability of multiply ionizing a cluster in sequential steps if the electron is endowed with sufficient energy. Since the probability of ionization approaches unity once the electron is inside a sufficiently large cluster, the above outlined two-step ionization process can be approximated by the collision probability of an incoming electron with the cluster alone, thus neglecting all intracluster processes. The respective cross section is given by the geometrical cluster cross section. The radius of a spherical cluster is related to its number of constituents N via $R = R_s\, N^a$ with R_s being the effective radius of a single solvent molecule, as determined from the bulk density. If one neglects all packing effects the exponent a becomes 1/3 just from geometrical considerations. Packing effects result in a somewhat larger a in the range of $a = 0.4 - 0.5$ [83]. So far no closed theory exists to describe the ionization behavior of condensed beams or to compare the ionization probability of clusters of different sizes. Nevertheless, a large number of relative ionization cross sections has been measured [62]. To account for the relative ionization probabilities of clusters of different sizes, simple additive rules have been used for dimers and a scaling parameter of $N^{2/3}$ for larger clusters of size N.

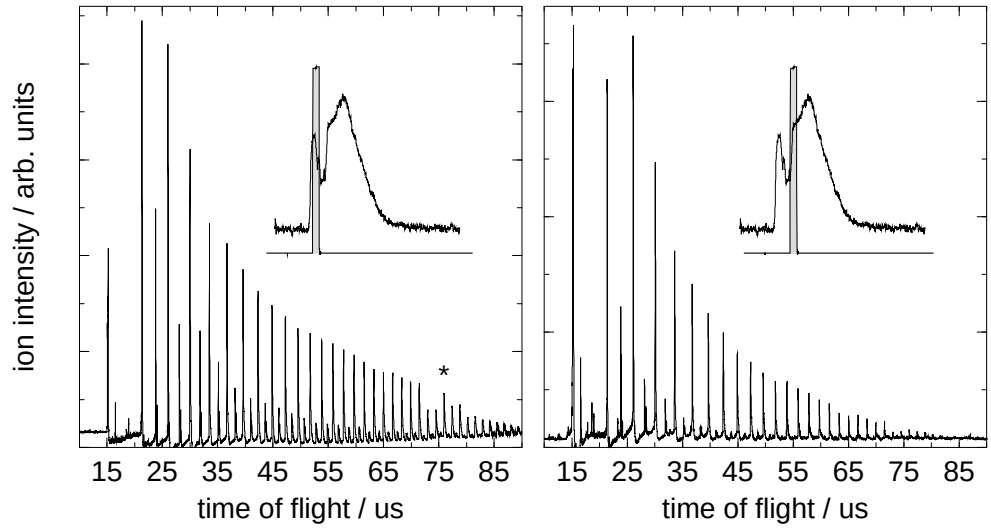

Figure 3.3: Electron impact ionization of oxygen clusters. The two mass spectra reflect the ion compositions of oxygen clusters, as measured with the time-of-flight method, after pulsed ionization (50 eV electrons, 80 μs pulse width) of an unseeded O_2 cluster beam (pulse width 600 μs) emerging from a 0.3 mm nozzle (stagnation pressure 20 bar). The spectra are taken at different positions within the beam (see inset). The amount of dissociative ionization leading to $(O_2)_nO^+$ (progression of smaller peaks interlacing the main series) is considerably larger at the beginning of the pulse (left panel) than when compared to the pulse center (right panel), where larger clusters are to be expected (see Fig. 2.7). This can be rationalized in terms of a *caging* effect of larger clusters, that either prevent dissociation itself or prevent the dissociated atom from escaping the cluster. Simple mass spectrometry can not discern between these two possibilities as they give ions with the same mass. However, cluster fragmentation of the respective cluster ions would disclose the core ions and thus allow for the exploration of such intracluster processes. The mass peak marked by an asterix in the left panel, represents a magic number for a cluster size of 26. As it affects neighboring peaks with a lower mass, it represents a stability of the cluster ion that emerges after evaporative stabilization [50]. A similar stability is also observed for mixed N_2/O_2 clusters.

A semi-empirical approach to the calculation of absolute cross-sections for the single ionization of Van der Waals clusters can be found in [83].

Electron-Cluster Interaction

By moving through the cluster, the impinging electron looses kinetic energy. This energy transfer is related to a manifold of different mechanisms, such as inelastic scattering via vibrational excitation, and eventually leads to the evaporation of cluster constituents. Recent experiments [84] have found a good correlation between microscopic processes and a description in terms of macroscopic *stopping power*, as it is used in models dealing with electronic sputtering of solid material [85]. The high yield of evaporated monomers - one or even two magnitudes larger when compared to electron sputtering of solid surfaces - observed during cluster ionization under conditions of strong cluster excitation, is due to the absence of a bulk heat bath. Heat conduction can not drain absorbed energy out of the excited region as the cluster is a finite, isolated entity. The pure absence of energy dissipation by heat conduction does not necessarily amount to a higher cluster 'temperature' when compared to bulk

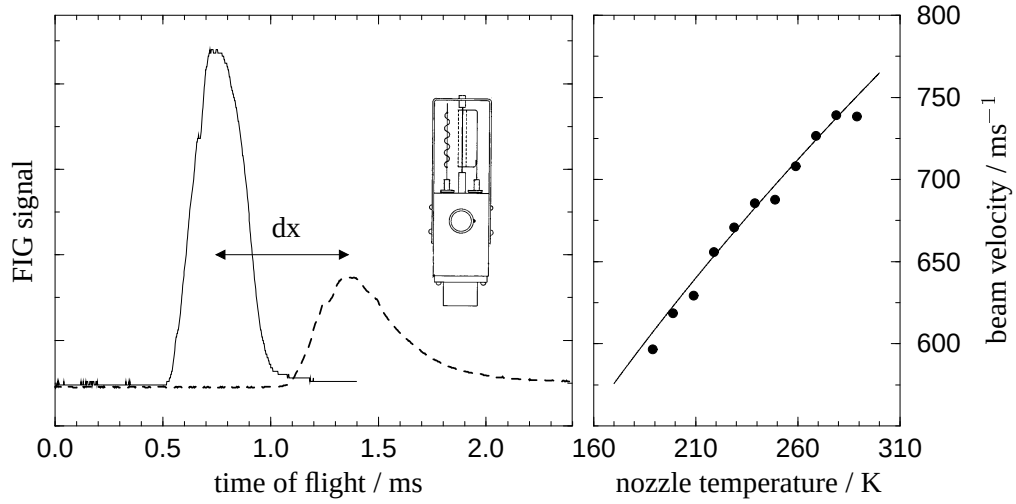

Figure 3.4: Control of pulse shape and determination of the beam velocity. The Fast Ionization Gauge (see inset) allows for the direct monitoring of the density profile of the cluster pulse in the light of total ion yield. By measuring the profile at two different distances from the nozzle (Δx=885mm), the beam velocity can be determined from the time delay. For the present mixture of SO_2/He with X_{He}=0.967 a velocity of 1446 m/s was experimentally determined; this corresponds well with the theoretical value of 1454 m/s. The right panel depicts the dependence of beam velocity on reservoir temperature. The measured velocities of an N_2/O_2 gas mixture conforms well with the theoretical prediction of Eq. (2.12). The main source of error is the measurement of the nozzle temperature. For a discussion of a more detailed beam velocity determination see [14].

volumes exposed to the same energy quantum, since evaporative cooling is also an efficient energy drain, that can be even faster than heat conduction [70, and Eq. (2.17)]. The stopping power can even lead to the capture of the impinging electron or of an electron released by a previous ionization process. Either a cluster anion or a neutral cluster incorporating an ion pair is created. Depending on the mobility of charge carriers inside the cluster, such ion pairs reneutralize or get stabilized. In the latter case they can be made visible by charge separation using the method of collision-induced cluster fragmentation outlined in Chap. 1.

3.2 Gas Pulse Characterization

Pulse Shape and Timing

While greatly decreasing the vacuum pump requirements for cluster beams, the pulsed nozzle technique introduces a complex mechanical device into the system, that needs to be empirically optimized (e.g. sealing pressure of the plunger in the present experiments). Furthermore, it needs real-time monitoring to detect gradual changes in its performance, since they can have profound influence on the highly non-linear process of cluster formation. Moreover, the cluster beam is no longer uniform in time and therefore requires a precise choreography of the experimental procedure. Non-uniformities within the cluster pulses (see Fig. 3.3) introduce a dependence of the

measurements on the particular pulse segment used. Therefore real-time characterization of the individual gas pulses is necessary.

Beam Velocity

As has been pointed out in Chap. 2.1.2, the seeded beam method allows for the adjustment of the beam velocity between 600 and 2400 m/s which corresponds to energies per particle varying from 0.03 eV up to 2.2 eV for the various systems employed in this work. Part of this energy is transferred, by means of a cluster-surface collision, into intracluster excitation, whereupon it influences the fragmentation behavior of the cluster; i.e., whether it rebounds largely intact, whether it fragments into pieces or even shatters down to the monomer (for a discussion of cluster fragmentation see Chap. 5.4.4). Moreover, beam velocity also defines the duration of cluster surface collisions via the advection time (ratio of cluster diameter and beam velocity) and thus the time window for impact induced phenomena. Intracluster processes initiated by surface contact, either by the energy coupled into the cluster or by pick up of a reaction partner, have to take place within this time window, since after the impact the reaction partners are separated by cluster fragmentation.

Fast Ionization Gauge

To perform the respective measurements of pulse shape and beam velocity (Fig. 3.4), a Fast Ionization Gauge (FIG) has been employed. It is essentially a Bayard-Alpert type pressure gauge, that has been optimized to achieve time resolutions on a μs time scale. Electrons emitted from a filament (emission: 5 μA-3 mA) at approximately ground potential are accelerated towards a cylindrical ion cage (d=4 mm, l=24.4 mm) in which they impact-ionize the gas constituents. Due to the small ionization efficiency and the dependence of the ion yield on the velocity of the particles, the FIG is a density detector. Even though it is possible to calibrate the FIG against a pressure gauge using the background pressure, particle densities within condensed molecular beams can not be directly determined: Firstly, because the beam does not extend over the full ionization volume, this would introduce a correction factor, secondly, because the ionization cross section varies with cluster size and thus connects the total ion yield to the cluster size distribution, and finally because heavy cluster ions are only partly detected, with ions that have kinetic energies larger than the ion cage retention energy of 160 eV completely escaping detection (see Fig. 3.3). Although the FIG measures pulse shape in the 'light' of its ionization and detection mechanism, it readily provides important timing information and allows for the monitoring of pulse shape stability. The beam velocity can be determined by measuring the arrival time (center of FWHM) at two different positions along the beam axis (see Fig. 3.4). In the present work, the distance between the two detector positions has typically been 85 mm. Due to the good correlation of measured and theoretically predicted (Chap. 2.1.2) velocities, beam velocity has often been calculated directly from the composition of the expanded gas mixture.

3.3 Cluster Size Measurement: Retarding Field Method

Methods to determine cluster size or cluster size distributions are a key issue for cluster experiments. Size measurements of neutral clusters have been performed based on high energy electron diffraction via the broadening of diffraction peaks with a decreasing number of unit cells in the cluster, and thus, with decreasing cluster size

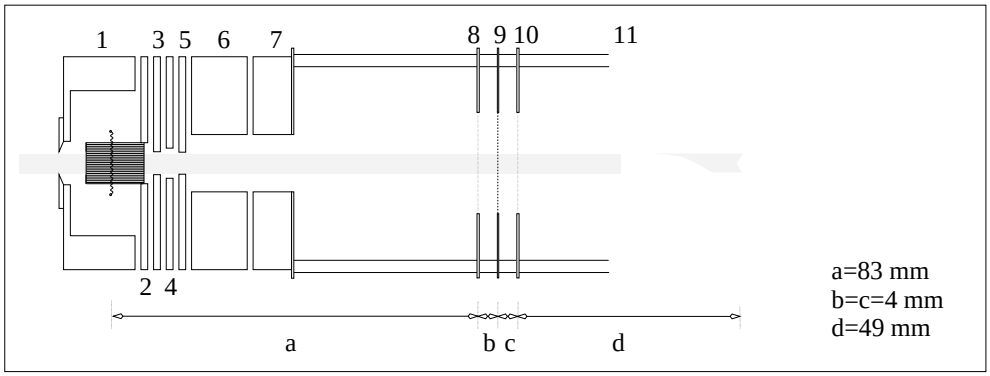

Figure 3.5: Retarding field setup. The fully expanded, skimmed cluster beam is passed through an axial ionizer (electrodes 1-7). Before being collected in a Faraday cup the ions encounter a potential step realized by a system of three grids. Whereas the outer two are grounded (8,10), the central grid (9) is set to a variable potential. Due to their higher kinetic energy, only cluster ions larger than a minimum size can surmount the potential barrier. By varying barrier height the cluster size distribution can be determined. The transmitted cluster ions are detected using a differential amplifier in high impedance mode (Tektronix ADA400A / TDS420A, input $\approx \infty\,\Omega$) via the charging of the Faraday cup capacitance.

[86]. However, a strong dependence on temperature and crystalline structure prevent a general application. Scattering methods are also useful for the size measurements of small neutral clusters [58]. The cluster beam is crossed at right angle by a He beam. Elastically scattered clusters appear according to their different centers of mass at different laboratory scattering angles and at different final velocities. For very large clusters, with diameters larger than 1000 Å which corresponds to clusters of more than 10 million monomers, the method of Rayleigh scattering of laser light has been employed [87].

Method

The cluster size distributions in the present experiments are measured using the retarding field method introduced by Hagena [46, 88, 89]. It makes use of the narrow velocity distributions obtained after adiabatic expansion within a molecular beam (see Chap. 2.1). Since all centerline molecules leaving the nozzle reach approximately the same velocity, the kinetic energy per monomer is equal for each molecular species and the ratio of the kinetic energies for different species is given by their mass ratio. During cluster formation, gas particles assemble into larger entities in which they pool their kinetic energy. Thus, a straightforward relationship exists between cluster size N and the kinetic energy of the cluster which is, in the case of neat clusters, just N times the kinetic energy of the monomer. After suitably ionizing the cluster pulse, its kinetic energy distribution and consequently the size distribution of the created cluster ions can be determined; e.g., by investigating their ability to surmount a potential step of variable height. Of course, changes in mass induced by the ionization process (cluster fragmentation) must be kept in mind.

Experimental Setup

The setup used is given in Fig. 3.5. By passing the fully expanded, skimmed cluster beam through an electron-impact axial beam ionizer (Extranuclear 041-1), predominantly cluster cations or anions can be created depending on the electron impact

energy. Typical values for the SO_2 are 7 eV in the case of anions and 30 eV to produce cations. Electron energies within this region limit fragmentation effects [90] and exclude formation of multiply charged cluster ions via sequential ionization processes. The cluster ions continue towards a Faraday cup (Kimball Physics) connected to an high impedance differential amplifier (Tektronix ADA400A/ TDS420A, one input grounded). The measured signal is the voltage increase due to the charging of the Faraday cup capacity C_F related to the total amount of cluster ions Q collected during each gas pulse according to $\Delta U_{cup} = Q/C_F$ (see Fig. 3.6). Between pulses the signal decays exponentially similarly to the time dependent background pressure (see Chap. 2.3). The time constant τ of the decay allows for the measuring of the capacity of the setup via $\tau = R\,C_F$ where R stands for the input impedance of the amplifier, and consequently for the determination of the amount of collected charges self-consistently out of the measurement. C_F lies in the range of 100 pF and is largely due to the capacity of the BNC line connecting the cup to the amplifier. The potential barrier is realized by a system of three grids. The outer two are both grounded and determine the spatial extention of the decelerating and accelerating region before and behind the central grid. They consist of knitted tungsten meshes (Kimball Physics) with $\approx$ 15 lines / inch that have been spot-welded to a stainless steel rim. The central grid is made from a 70 lines / inch copper mesh (Buckbee) that has been glued to an Invar rim using a conductive glue (Epoxy Technology EPO TEK H35 175 MPLV). The different heat expansion coefficients of copper and Invar help to tighten the mesh after curing the epoxy at elevated temperatures [91]. The potential of the central grid U_R can be varied using a high voltage supply (Stanford Research Systems PS350 0-5 kV, floated at $\pm$250 V) between -240 V and 4.76 kV in the case of cluster cations. The high voltage supply as well as the signal acquisition are controlled by a PC-based Labview program (National Instruments) that obtains retarding field curves as given in Fig. 3.6. With increasing U_R a decreasing amount of cluster ions are able to surmount the barrier due to their size-related kinetic energy, until finally the largest clusters are also reflected by the central grid. The signal height at a given U_R corresponds to the integral amount of cluster ions that are larger than the minimum required size to reach the detector, given by $N_{min} = U_R/E_{pp}$ where E_{pp} stands for the kinetic energy per particle as determined by the beam velocity. By taking the derivative of this curve, the energy distribution of the cluster ions averaged over the pulse is obtained. This energy distribution can be transformed into a size distribution via E_{pp}. As detailed in Fig. 3.6, this method can also be employed to determine local size distributions for the cluster ions at different positions within the gas pulse.

Cluster Size Distributions

Several empirical models describe the measured cluster ion size distributions $h(N)$ e.g. [88, 82]

$$h(N) = \alpha^2\, N\, \exp(-\alpha\, N) \tag{3.2}$$

$$h(N) = \frac{1}{\sqrt{2\pi}\sigma N}\, \exp\left[-\frac{(\ln N - \mu)^2}{2\sigma^2}\right], \tag{3.3}$$

as well as simple Gaussian distributions (see Fig. 3.7). The log-normal distribution of Eq. (3.3) is suited to describe heavily condensed beams [82], since the model which it is based on takes cluster coagulation during the growth process into account. The

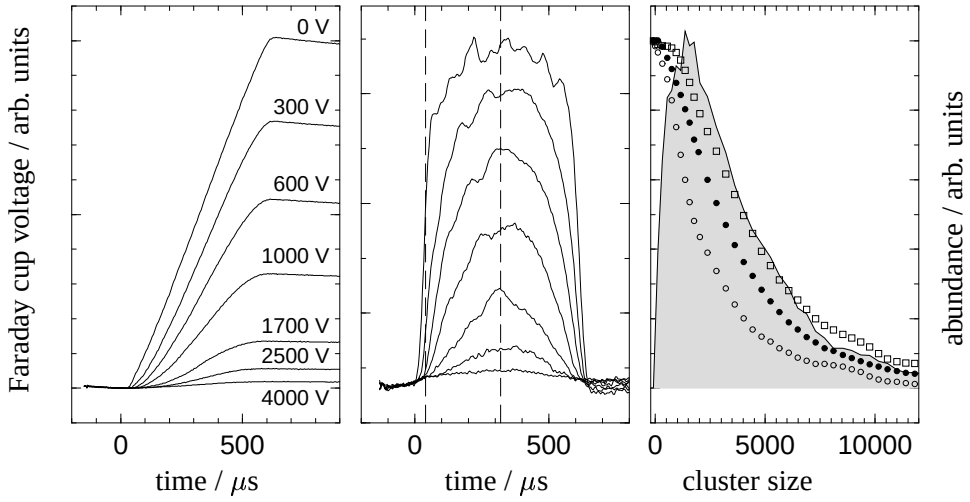

Figure 3.6: Size distribution of NH_3 cluster ions (X_{NH3}=0.0513 in He, stagnation pressure p_d=5.1 bar, nozzle: d=0.5 mm, electron impact energy 30 eV) measured with the retarding field technique. The left panel displays the signal due to the charging of the Faraday cup for several retarding voltages (0 V, 300 V, 600 V, 1000 V, 1700 V, 2500 V and 4000 V). The rise time of the signal is related to the pulse width of the cluster beam (≈500 μs). Due to the high impedance of the voltage amplifier, the plateau value of each curve corresponds to the number of cluster ions, that have been able to surmount the potential barrier in front of the Faraday cup. The exponential decay of the signal at longer times (not shown) allows to calculate the number of cluster ions from the plateau voltage self-consistently. Taking the derivative of the signal curves in the left panel reproduces the cluster pulse in the 'light' of cluster ions being larger than the threshold size (center panel). These curves allow to determine cluster size distributions as function of pulse position: the narrowing pulse width for larger cluster sizes reveals, that they tend to reside towards the pulse center. This effect, however, is much less pronounced for the seeded beam expansions compared to the unseeded ones (see Fig. 2.7). If local cluster size distributions are in the focus of investigation, the ion current curves of the center panel can be determined directly by using a current amplifier (Stanford Research Systems SR570), thus avoiding to take a derivative. The right panel displays the measured cluster size distributions. The x-axis has been rescaled from retarding voltage to cluster size using the kinetic energy per particle as determined from the beam velocity measurement (v=1664 m/s, E_{pp}=0.244 eV). The full circles represent the decay of the measured plateau voltage. The x value for which this curve reaches its half value determines the mean cluster size. Taking the derivative of this curve results in the size distribution of the cluster ions for the whole pulse (shaded curve). For two different positions in the pulse (marked by dashed lines in the center panel) local retarding field curves are displayed (center position: open squares, pulse front: open circles) which emphasize the comparatively high homogeneity of the seeded cluster pulses.

success of the different empirical distribution functions in describing details of the measured curves varies with the system under consideration. Nevertheless, they are advantageous since they approximate the complicated distributions obtained, e.g., by taking the derivative of the retarding field curve or by time-of-flight measurements (see Fig. 2.7). They allow an easy comparison between different expansion condi-

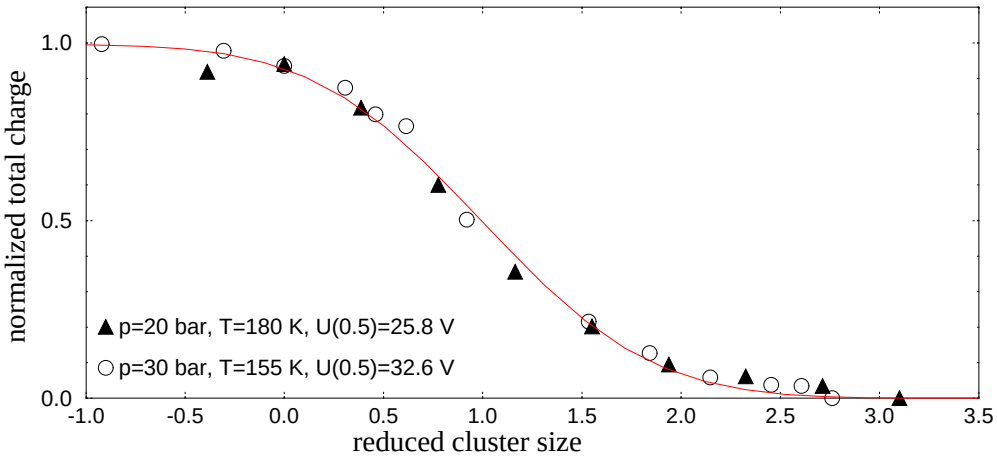

Figure 3.7: Mean cluster $\bar{N}$ size as scaling parameter. Two normalized retarding field curves for N_2/O_2 cluster beams are plotted as function of reduced cluster size $N/\bar{N}$. Although the cluster size distribution is different in the two cases due to different expansion conditions, they coincide in the reduced representation. The solid line represents a fit for a simple Gaussian distribution model.

tions or experiments using the model parameters like α, σ or μ. In this spirit, it is often convenient to characterize a cluster ion distribution by its mean value $\bar{N}$ alone, which coincides with the cluster size for which the retarding field curve reaches its half value (arrows in Fig. 3.8). The mean cluster size $\bar{N}$ is the preferred parameter within which to characterize cluster size distributions in the work presented here, in which only the order of magnitude of the cluster size is important. Mean cluster size also represents a scaling parameter for the retarding field curves [88]. They tend to coincide if the normalized curves are plotted as function of $N/\bar{N}$ (see Fig. 3.7). This emphasizes that it is possible to describe the size distributions by a single parameter, namely the mean cluster size $\bar{N}$, and that other properties, e.g., the width of the distribution, are a function of this parameter. Indeed, it is an established rule of thumb that the width of the distribution is always in the order of $\bar{N}$.

In Fig. 3.8 some mean cluster sizes are given for the size distribution of SO_2 cluster ions produced by electron impact ionization for different stagnation pressures. The figure illustrates the experimental procedure for the empirical adjustment of $\bar{N}$ to the desired value by varying the expansion conditions. As pointed out before, *no* direct correlation exists between the measured size distribution of the cluster ions and the precursing neutral clusters since the transfer function that takes into account, e.g. ionization induced fragmentation, is generally not known. However, they can at least be used as a measure to characterize the neutral cluster size distribution and to monitor changes in the neutral cluster size distribution via the charged counterpart. However, this implies that a measured $\bar{N}$ must always be accompanied by information about the ionization mechanism to allow conclusions to be made on the neutral cluster size distribution. All values for the mean cluster sizes given in the following work are measured using the retarding field method. They have to be understood as a measure for the neutral cluster distribution in the light of electron impact ionization with

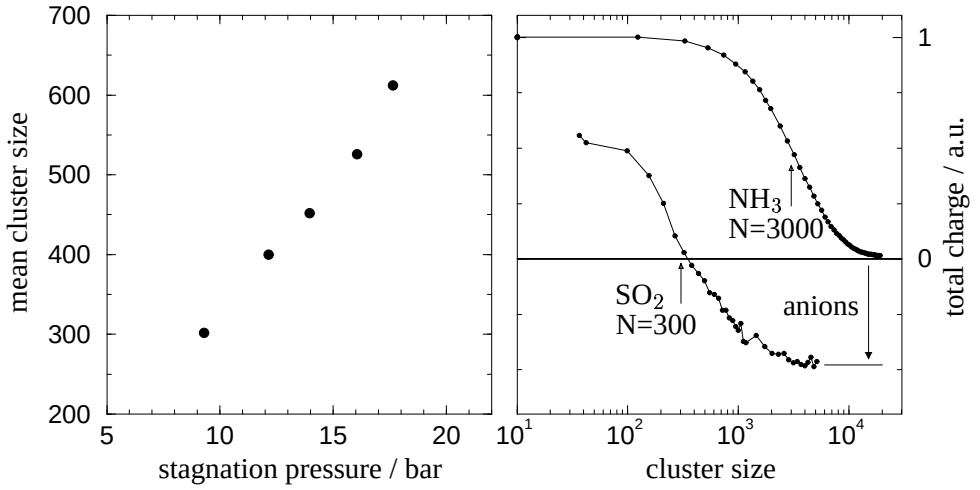

Figure 3.8: Mean cluster size and electron capture: The left panel illustrates the straightforward way to change mean cluster size by varying the stagnation pressure exemplified for a seeded SO_2 cluster beam (X_{SO_2}=0.11 in He, nozzle: d=0.5 mm). The data points reflect the mean sizes of the cluster cations that emerge after electron impact ionization with 30 eV electrons as measured with the retarding field method. Although these mean sizes do not reflect the neutral distribution, they can be taken as measure for the evolution of the mean size of the neutral clusters with stagnation pressure. The right panel shows retarding field curves for a NH_3 cluster beam (X_{NH_3}=0.0513 in He, stagnation pressure p_d=5.1 bar, nozzle: d=0.5 mm, electron impact energy 30 eV) and a SO_2 cluster beam (X_{SO-2}=0.11 in He, stagnation pressure 9.3 bar, nozzle=0.5 mm, electron impact energy 30 eV): the observed shift of the latter curve towards negative total charge yields can be explained in terms of cluster anion formation which is supported by the molecular electron affinity of SO_2. This effect implies abundant formation of large neutral SO_2 clusters incorporating charge pairs formed by ionization of a cluster constituent followed by electron capture in some different cluster region. They provide interesting objects for investigation via the method of cluster fragment mass spectroscopy developed in this work. Moreover, the observed SO_2 cluster anion formation implies a strong discrimination of large cluster cations in the respective cluster size distribution: upon impact ionization large clusters tend to recapture the electron, thus remaining undetected as long as cluster cations are concerned.

typically 30 eV impact energy.

Electron Capture

This important caveat is further illustrated in the right panel of Fig. 3.8 giving the retarding field curve for NH_3 cluster ions and SO_2 cluster ions. Compared to the NH_3 curve, the SO_2 curve seems to be shifted towards negative total charge yields, eventually falling below zero and reaching a negative asymptote. This shift can be explained in terms of cluster anions, for which the potential step in front of the Faraday cup represents no barrier. For electron impact ionization of SO_2 clusters at 30 eV impact energy, there is substantial amount of cluster anion production! At zero retarding voltage, the detector signal consists of the sum of the charges of the cluster anions and a majority of cations. With increasing retarding voltage more and more positively charged cluster ions are rejected, while the cluster anions remain unaffected. For a specific retarding voltage, the measured charge drops to zero. This

implies that the Faraday cup collects equal amounts of cluster cations and anions. With increasing retarding field, finally only cluster anions are able to reach the detector. The negative asymptotic value reached for high retarding voltages corresponds to the integral charge of all cluster anions in the pulse. The anion formation induced by high energy electrons can be understood in terms of the previously stated *stopping power* of the cluster. The electron is decelerated in the cluster until low energy electron attachment becomes possible. The energy absorbed by the cluster is dissipated in the form of monomer evaporation. With typical binding energies of 0.3 eV per particle an electron energy of 30 eV corresponds to the evaporation of a hundred molecules, which is quite feasible for large clusters. The observation that ammonia clusters do not form comparable amounts of cluster anions can be rationalized in terms of the lack of a molecular electron affinity of NH_3. The bulk electron affinity seems to be too weak to stabilize an impacting electron, especially in a cluster heated by the interaction with the electron. Although the mechanism is the same for SO_2 and NH_3, it can not be observed in the latter case since the thermalized electron detaches from the hot cluster. Apart from the obvious implication that due to electron-cluster interactions clusters may loose up to 100 monomers at 30 eV electron energy, there are much deeper consequences exemplified by the SO_2 system. The substantial anion production implies that large clusters tend to capture the impacting electron and thus to form negatively instead of positively charged cluster anions. An even more efficient process should be the recapture of an electron set free by means of ionizing a cluster constituent at some other location within a large cluster. However, this forms neutral clusters which incorporate a charge pair. Therefore, measuring the cluster cation distribution following electron impact largely discriminates against large clusters, which tend to be neutral or to form anions. Therefore, the mean cluster size of $\bar{N}$=300, given in Fig. 3.8, largely underestimates the situation for the size distribution of the neutral SO_2 clusters. Indeed, measuring the cluster size distribution of the SO_2 anion reveals considerably larger values for $\bar{N}$. This decreasing ionization efficiency of large clusters with non-negligible electron affinity due to electron capture processes, seems to have been neglected until now. It can be seen as an extension of a similar behavior observed for ionization cross sections of large molecules [92] through the formation of intermediate charge pairs. In the context of *cluster fragment mass spectroscopy* developed in this work, the high fraction of neutral SO_2 clusters that should incorporate a geminate ion pair after electron impact ionization are of interest. After extracting all ions out of the cluster beam, these ion pairs can be investigated after fragmenting the cluster via a surface collision, e.g., to study recombination processes. The tenor of this chapter, dealing largely with the involved yet unsuccessful attempts to determine neutral cluster size distributions, validates the approach taken in the present work; i.e., it is not the sizes-dependencies during the step-wise growth of the cluster which represent the focus, but the cluster is taken as a microscopic test tube, whose dimensions are large when compared to the incorporated systems. While it is only the order of magnitude of the cluster size which is interesting in this context, it is the gas phase character of the cluster, combined with its high internal density, which makes it such an advantageous means of investigation.

Chapter 4

Time-of-Flight Mass Spectrometry of Molecular Cluster Ions

The following chapter introduces time-of-flight (TOF) mass spectrometry as the fundamental method of detection and analysis employed throughout the experiments presented in this work. It allows for the determination of the charge-to-mass ratio of the primary cluster ions as well as of the charged products set free by the collision-induced fragmentation of the cluster upon surface impact. Whereas the methods described in Chapter 3 provide integral information such as the envelope of the cluster ion size distribution or the overall pulse shape, time-of-flight measurements provide insight at the level of individual ions. The first TOF mass spectrometer was described in the 1940s [93, 94]. Meanwhile, its design has been considerably improved; e.g., by Wiley and McLaren [95] who introduced the two-stage accelerator, by Mamyrin [96] who added an energy focusing reflector stage, as well as by Wagner and Schröder [97] who developed a space-resolved extraction volume. Besides the high ion transmission of the TOF mass spectrometer and its straightforward construction, the possibility of obtaining whole mass spectra with a repetition rate in the ten kilohertz range is of advantage. Arrival time, on the other hand, generally scales with the square root of the mass m. Consequently mass resolution is limited, since the distance between two masses m and $m+1$ decreases with increasing m and eventually falls below the experimental time resolution or the width of the individual mass peaks. Nevertheless mass resolutions $m/\Delta m$ of some 10,000 [98] have been achieved. This chapter develops the theory behind TOF mass spectrometry as far as it is necessary to describe the two-stage mass spectrometer used in the present work. Emphasis is given to the relevance of a large extraction volume for the CIMS technique. Finally, the experimental setup is described.

4.1 Time-of-Flight Mass Spectrometry

Method

The idea behind TOF mass spectrometry can best be pictured in terms of a 'race' between particles having the same amount of kinetic energy E_{kin}. Since for a given E_{kin} the square of the velocity v decreases rapidly with increasing mass m, it takes heavier particles more time t to cover a certain distance than lighter ones. Due to

their different velocity two particles of neighboring masses separate spatially during their way to the detector. Their mutual distance $\Delta x = (1 - \sqrt{m_1/m_2}) \cdot L$ increases with the traveled length L and is converted at the detector into a time difference $\Delta t = \Delta x/v$, where v represents the velocity of the heavier particle. Whereas Δt is via v dependent on the value of the supplied kinetic energy, the spatial separation is not. Two equi-energetic particles realize the same separation during a given distance independent of the value of E_{kin}. The same is true for two ions of different mass subjected to constant acceleration in an external electric field: In this case, the spatial separation is given by $\Delta x = (1 - m_1/m_2) \cdot L$. Due to the linear dependence on m_1/m_2, the realized separations under acceleration are larger than for ballistic movement. All this implies that TOF mass spectrometers should generally be long, that the amount of supplied kinetic energy plays a minor role and that accelerated movement should be preferred.

Peak Broadening

Although correct, the above considerations neglect peak broadening mechanisms that counteract the spatial separation of the ion bunches with different mass, namely the influence of the initial space and velocity distribution of the particles under investigation. The standard procedure to create particles with almost equal kinetic energy is to ionize them and place the created ions close to an equipotential plane of an electric field. The start of the race is determined either by creating ions only at given instances in time (e.g. by laser ionization) directly within a static electric field (*pulsed ionization*), or by switching the electric field (*pulsed extraction*). The electric force accelerates the ions and thereby fully converts potential energy into kinetic energy. However, due to such factors as the finite width of the laser focus as well as a ubiquitous thermal velocity distribution, sometimes influenced by additional energy sources like Coulomb explosion of multiply charged ions, the produced ensemble of ions always exhibits a space and velocity distribution around some mean value, that deteriorates the achievable mass resolution.

Duopole or Acceleration Region

A single acceleration stage (see Fig. 4.1) already represents a TOF mass spectrometer, which in this case is called a *duopole*. Since it supplies the kinetic energy necessary for mass separation, it is also an indispensable part of every TOF setup. The equation for the arrival time at the detector, also called the *dispersion relation* of the system, is given by

$$t = \sqrt{\frac{2\,m}{q}}\,\frac{1}{E_1}\,\left(\sqrt{\frac{m\,v_0^2}{2\,q} + x\,E_1} - v_0\sqrt{\frac{m}{2\,q}}\right), \tag{4.1}$$

where E_1 stands for the applied electric field, x for the position in the acceleration stage as measured from the attractive electrode (see Fig. 4.2), q for the particle charge and v_0 for the signed initial ion velocity. The latter is often conveniently replaced by an equivalent voltage U_0 defined via $q\,U_0 = \frac{1}{2}\,m\,v_0^2$. The ideal mass resolution of the duopole, which neglects initial velocity and space distribution, is limited only by the experimental time resolution Δt_{det} of the detection unit. For a duopole with an effective flight length x=1 m, an electric field of 1 kV/m and Δt_{det} of 50 ns, masses up to $m_{max} = 2000$ u can in principle be resolved. An upper limit for the peak broadening due to variations in the initial kinetic energy is given by the *turnaround time* $t_T = \sqrt{8\,m\,U_0/(q\,E_1^2)}$ [95] of ions with a velocity component opposite to the acceleration direction. The maximum resolvable mass is that for which t_T equals the

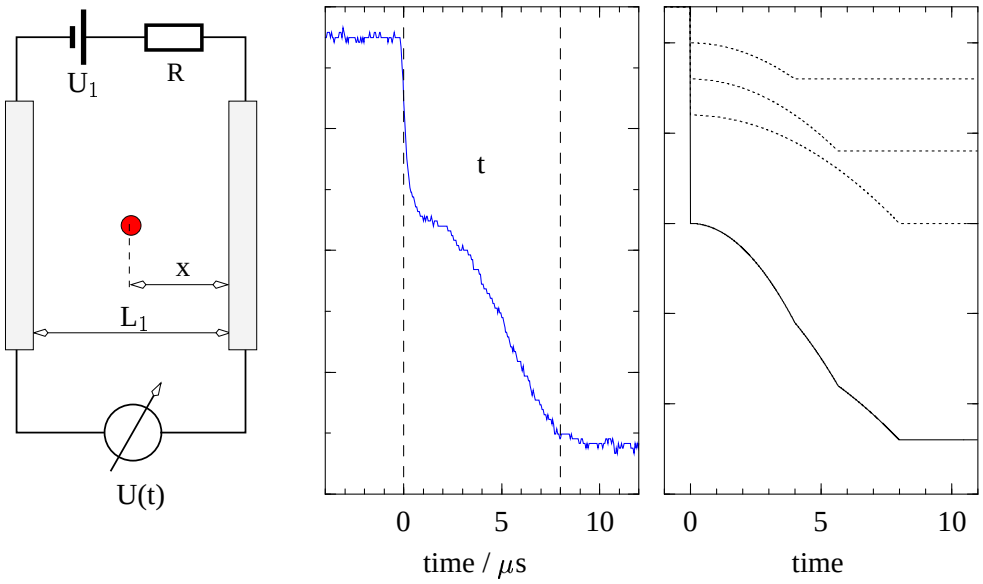

Figure 4.1: The plate capacitor as simple TOF mass spectrometer. The left panel depicts a schematic setup of the duopole-TOF. Ions are created at position x in front of the attracting plate of the capacitor arrangement which contains an electric field $E_1 = U_1/L_1$. The movement of the ions within the capacitor generates a displacement current which can be measured directly via the time dependent potential $U(t)$ and which reflects the accelerated movement of the ions through the capacitor (center panel: laser-created NO ions). The first step in the signal stems from the fast electrons. Whereas the total signal height is a constant, the ratio between ion signal and electron signal depends on the position x, thus allowing for precise position measurements; e.g., of a laser focus. The total amount of charge Q can be quantitatively calculated from the potential drop via $\Delta U = Q/C$. The capacitance of the arrangement is contained in the time constant $\tau = RC$ of the slow recharging (not shown) of the capacitor by the power supply through the resistor R. This method to quantitatively measure charge, which was developed for absolute determination of laser-ionization cross sections [99], will be employed in Chaps. 4.8 and 5. Ion mass is contained in the curvature of the parabolic signal or the arrival time at the plate. A calculated signal for a mixture of ions (mass ratio 1:2:4, abundance 1:2:3) is presented in the right panel. For high resolution mass spectroscopy, one plate of the capacitor can be exchanged for an MCP electron multiplier which is sensitive only to the arrival times. However, due to its various detection efficiencies for ions of different mass and different type, quantitative determination of the total charge is generally not possible in such a setup.

time between adjacent peaks. For a thermal energy of 0.025 eV, the resolution of the above system deteriorates to a modest $m_{max} = 50$ u. Since m_{max} scales in this case with $\sqrt{x\,E_1/U_0}$, the resolution depends only on the potential $U_x = x\,E_1$ at the ion origin. For a spatial ion spread of Δx around the ideal initial position x, the maximum resolvable mass, for which peak width becomes equal to peak separation, scales with $x/\Delta x$ and reaches $m_{max} = 500$ u for Δx=1 mm under the above conditions. Being independent of the applied electric field, the influence of the spatial ion spread can only be reduced by long flight distances. Since at the same time the potential U_x at the

ion origin has to be kept constant (energy resolution!), space resolution of the duopole is also limited by the experimentally available potentials. Due to the linear increase of space resolution with L but the square root dependence of energy resolution on U_x, the duopole is generally limited by its energy resolution. The relative importance of energy and spatial peak broadening mechanisms, which both contribute to the final peak width, is given by

$$\frac{\Delta t_{energy}}{\Delta t_{space}} = 2\,\frac{x}{\Delta x}\,\sqrt{\frac{U_0}{U_x}}. \tag{4.2}$$

Thus, the ideal duopole setup works at high acceleration fields and with long flight distances in order to minimize the influence of the initial velocity and space distribution. Laser ionization with its small ionization volume and molecular beam techniques with their low thermal energy spread allow for the further minimization of the influence of the peak broadening mechanisms. Since the ions are continously accelerated in the duopole, it is well suited to the monitoring of metastable decay processes as well as to the obtaining of information about the spatial distributions of the generated ions.

Two-Stage TOF

The detrimental influence of the initial velocity distribution observed in a simple duopole can be decreased by adding a drift stage, in which the ions propagate ballistically. The dispersion relation of such a system is given by:

$$t = \sqrt{\frac{2\,m}{q}}\,\left(\frac{1}{E_1}\,\left[\sqrt{U_0 + x\,E_1} - v_0\,\sqrt{\frac{m}{2\,q}}\right] + \frac{L_3}{2\,\sqrt{x\,E_1 + U_0}}\right), \tag{4.3}$$

which is the sum of Eq. (4.1) and a term describing the unaccelerated movement over the drift length L_3 in which the energy gained in the duopole and the initial kinetic energy U_0 enter additively. The acceleration stage converts an undirected thermal movement into a directed one by turning around ions moving against the field gradient. Ions with equal mass but opposite initial velocity are injected into the drift region with equal total energy but with a time delay that corresponds to the turnaround time of the ion. The maximum resolvable mass, due to the velocity distribution, is in this case proportional to $(1 + L_3/(2\,x))\,\sqrt{U_x/U_0}$. The use of long drift lengths allows for the improvement of mass resolution. This can be rationalized because acceleration to high kinetic energies reduces the effective width of the velocity distribution; if a particle separates itself from a particle at rest due to a kinetic energy of $q\,U_0$ their separation velocity at an energy level $U \gg U_0$ will be reduced to a value of $2\,\sqrt{U/U_0}$. A separation velocity of 220 m/s for a mass 100 u particle having some thermal energy will be reduced to 0.55 m/s after acceleration to 1 kV. In the duopole, on the other hand, ions have a relatively low kinetic energy during most of their flight time, so that most of the peak spread is accumulated right at the beginning of the acceleration.

The additional degree of freedom of the two-stage TOF mass spectrometer, namely the ratio of the length x and L_3, can also be used to reduce the influence of an initial ion spread on the achievable mass resolution. By requiring the first derivative of the dispersion relation with respect to x (see Eq. (4.3)) to vanish at the center of the ion distribution, it is achievable that ions in the vicinity of this point all arrive at the detector at the same time (*first order space focusing*). This is the case for $L_3 = 2 \cdot x$, for which the larger distance is compensated for by a higher starting potential. The

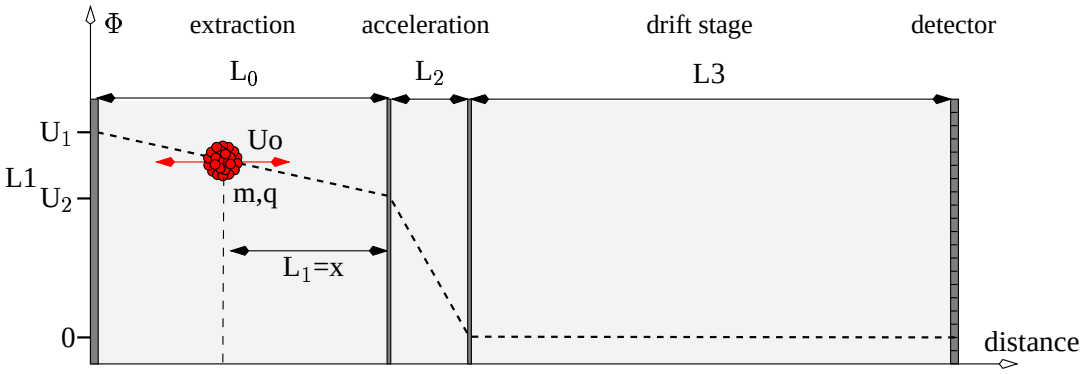

Figure 4.2: The three-stage TOF mass spectrometer. Proposed by Wiley and McLaren [95], it consists, with the extraction region and the acceleration region, of two duopole stages combined with a field free drift region. The dashed curve depicts the course of the electric potential throughout the setup. Compared to the two-stage TOF it provides a total of three free parameters, which not only allow for the establishment of first order space focusing but also for a flexible handling of the dimensions, which helps to minimize the influence of the kinetic energy spread, to realize an extended extraction volume or to achieve higher order space focusing.

fixed length L_3 implies that space focusing and minimization of the influence of an initial velocity spread are requirements that can not be fulfilled at the same time. However, the fulfillment of the space focusing condition is critical in a two-stage setup. Whereas the spatial width of an ion packet remains constant in the duopole stage, it changes in the drift region, as the acceleration stage supplies different kinetic energies to ions starting from different positions. The ion packet contracts up to the space focus, after which its starts expanding linearly with flight time. The limiting resolution achievable in the two stage TOF MS for $L_3 \rightarrow \infty$ is simply given by $x/\Delta x$ as in this case the influence of an initial energy distribution can be neglected.

The above considerations make it desirable to minimize the influence of an initial energy spread while keeping the space focusing condition for the following reason: for the same flight length and final kinetic energy the flight time of the ions in an accelerated field is twice the time of a drift region. Thus, the length ratio for first order space focusing implies that the ions spend 50 % of their total flight time in the acceleration region at low kinetic energies. By introducing a further free parameter, the length of the drift stage can be increased with respect to the length of the acceleration stage while keeping first order space focusing. By using an electric field in the second stage, the additional degree of freedom could be realized, making it a two stage duopole. However, in order to keep a separate drift region with its advantages concerning kinetic energy spread, the two stage TOF is generally extended by introducing an additional, entire duopole stage, thus making it a three-stage setup with two additional degrees of freedom, namely the length of the second acceleration stage as well as the ratio of the electric field strength with regard to the first stage (see Fig. 4.2).

Wiley-McLaren TOF

The dispersion relation of the three-stage TOF, commonly called the Wiley-McLaren

TOF [95], is given by

$$\begin{aligned} t &= \sqrt{\frac{2\,m}{q}}\left[\frac{1}{E_1}\left(\sqrt{U_0 + x\,E_1} - v_0\sqrt{\frac{m}{2\,q}}\right) + \right. \\ &+ \frac{1}{E_2}\left(\sqrt{U_0 + x\,E_1 + L_2\,E_2} - \sqrt{U_0 + x\,E_1}\right) + \\ &+ \left.\frac{L_3}{2\sqrt{U_0 + x\,E_1 + L_2\,E_2}}\right]. \end{aligned} \tag{4.4}$$

First order space focusing requires a vanishing space derivative dt/dx of the dispersion relation at the ion origin. The obtained condition correlates the ratio of the applied electric fields with the length dimensions of the TOF stages; for a given combination of x, L_2, and L_3 a fixed ratio of E_1/E_2 is required [95, 100]. The flexibility in choosing the length dimensions, can be used to minimize the turnaround time in acceleration by maximizing the prevailing electric extraction field. This is achieved by small values for x as well as L_2 [95] or by maximizing the total flight time $t(x)$. The latter two conditions are equivalent, since the time of flight in accelerated stages is always shorter than in comparable drift regions. In this case, the resolution depends strongly on the extension of the ionization volume [95]. This is acceptable in the case of laser ionization, where the spatial extent of the ionization volume is small.

4.2 Large, Pulsed Extraction Volumes

For the present work a different optimization scheme which sacrifices overall resolution in favor of large extraction volumes has been used for the three-stage TOF mass spectrometer, in order to adjust it to the requirements of the spatially extended CIMS ion source: Charged cluster fragments are produced during the collision-induced fragmentation of a cluster containing a cation/anion pair. They originate from all points of the interaction area of the cluster beam with the target and are emitted into a large space angle (see Chap. 5.4.4). Therefore, a large part of the nearby TOF extraction volume is filled with ions. Since only the identity of the ions and not the details of the scattering process are of interest in the present context, such an integration over a large volume is appropriate and increases overall sensitivity.

The three-stage Wiley-MacLaren setup is well suited for the realization of large extraction volumes; by adjusting its length dimensions, it allows for the design of a 'flat' dispersion relation (see Fig. 4.3) that allocates equal arrival times to ions starting from different positions. First order space focusing can always be maintained by choosing a corresponding ratio of the two extraction fields. The aim of the dimensional optimization is either to achieve a second order space focusing ($d^2t/d^2x = 0$) at some point within the desired volume or to minimize the difference in arrival time for two points within the extraction volume [95, 100, 101]. As depicted in Fig. 4.3, extraction volumes with an axial length of several centimeters can be realized. The lower mass resolution of such a setup, which is mainly connected to the larger fraction of time that the ions spend in the acceleration stage due to their large distances x from the first grid, represents a minor limitation for the CIMS technique which

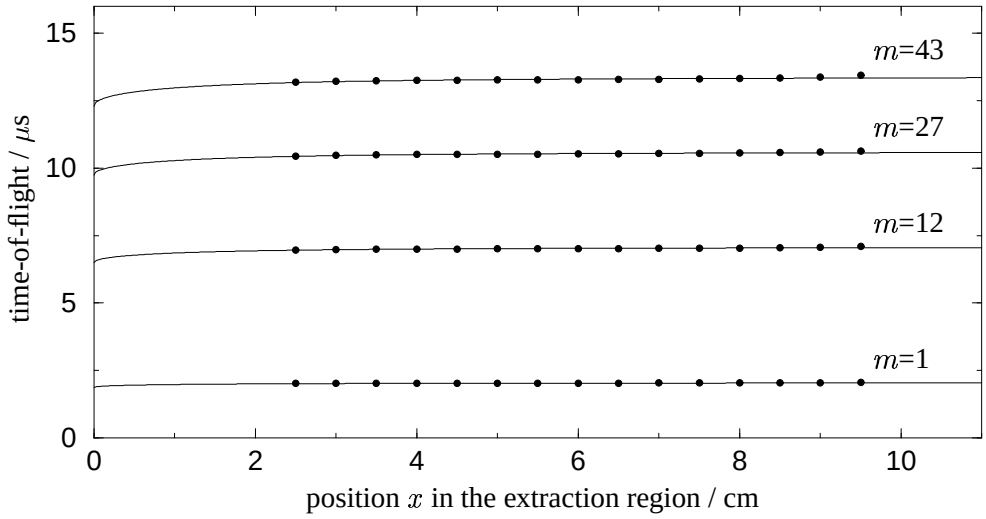

Figure 4.3: The TOF dispersion relation of large extraction volumes. By laser ionization (266nm, 4th harmonic of a Nd:Yag picosecond laser) of, e.g., hydrocarbons, the flight time of ions can be measured at given locations of the acceleration region. By moving the laser focus along the spectrometer axis (for the parameters of the used axial TOF see Chap. 4.3), the entire dispersion relation of the mass spectrometer can be recorded. The full circles in the graph give the measured times of flight for different masses. As predicted by the theory (black lines), it is possible to realize a flat dispersion relation over an extended region, which in the present case comprises more than 8 cm.

extracts most of the information from small, well resolved cluster fragments. Optimized mass resolutions can still reach values of around 2000 for extractions volumes with Δx=10 cm [101].
Large separations of the field generating electrodes of the first acceleration stage are the consequence of large extraction volumes. This results in difficulties with respect to homogeneity of the respective electric field: As depicted in the center panel of Fig. 4.4, the equipotential planes within the duopole stage are considerably distorted from the ideal plate capacitor situation. This is due to the penetration of the ground potential of the surrounding metal parts. The effect is especially pronounced in the first acceleration stage, as it generally employs elevated potentials. An upper limit of the field distortion can be obtained from the penetration depth of a given potential V, which is taken to be the higher of the electrode potentials, into the space enclosed by two grounded plates. The asymptotic decay of the potential is given by [103]

$$\Phi(x,y) \rightarrow \frac{4\,V}{\pi}\ \exp(-\pi\,y/a)\ \sin(\pi\,x/a) \tag{4.5}$$

where a stands for the plate separation, x for the distance from one of the plates and y for the distance from the plate border. To limit the deviations at the center line of the TOF spectrometer to within 1 % of the ideal field, the ratio of diameter to distance of the plates has to be in the order of 3, for deviations smaller than 1/1000, the ratio has to be between 4 and 5. For plate separations in the order of 10 cm, space limitations in the vacuum chamber generally preclude such large-diameter electrodes.

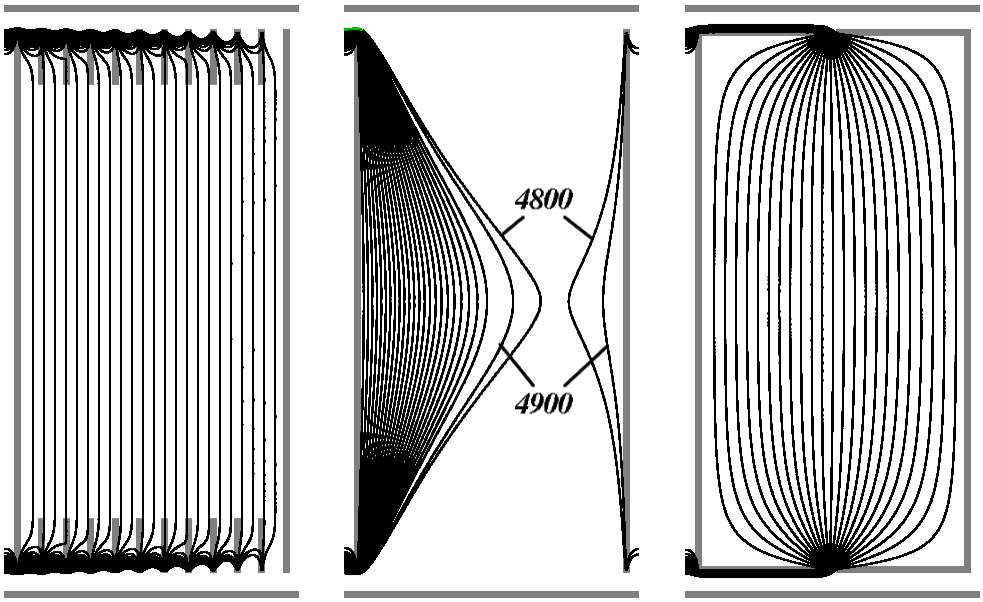

Figure 4.4: Homogeneity of the electric field in extended extraction regions. The panels depict a cross-section of an extraction region (circular electrodes, diameter/distance=2:1) of a TOF mass spectrometer with large separation of the first duopole electrodes. The thin lines give the equipotential planes as numerically calculated at separations of 100 V by the Simion [102] program for typical electrode voltages V_1=7444 V, V_2=5000 V. The thick horizontal lines represent grounded parts of the surrounding apparatus. The center panel illustrates the major problem of large electrode separations: Due to the penetration of the surrounding ground potential into the extraction region, the gradient of the electrostatic potential becomes inhomogeneous, even falling below the value of the electrodes. The left panel gives the established solution: A series of guard electrodes, which are set to potentials corresponding to their position by means of a resistive voltage divider, restore the homogeneous electric fields even for small diameter to distance ratios. However, especially with pulsed, high potential TOF mass-spectrometers, the time constant $\tau = RC$, introduced by the combination of voltage divider resistance and electrode capacitance, limits the response. The right panel offers a new approach for the realization of homogenous potential gradients over extended regions: Field homogeneity around the TOF axis can also be restored by using "pot-shaped" electrodes. Although inhomogeneous in the border sections, the smaller potential difference between the ideal value and the realized ones, decays fast as the central region is approached. Since this setup employs only capacitive elements, no power is consumed once the electrodes are brought to their potential and no passive time constant τ is introduced into the system.

Guard Electrodes

The left panel of Fig. 4.4 illustrates the established solution for creating homogenous potential gradients for large extraction values [105, 101, for example], namely to enclose the ion region by a number of typically equidistant guard electrodes. By setting these shielding rings to potentials that equal the ideal values at the respective position, a homogenous extraction field for diameter to distance ratios in the order of unity is achieved. Disadvantages of this setup are the somewhat complicated construction and the critical influence of the voltage divider, which supplies the guard electrode, on the homogeneity of the obtained electric field. Moreover, in connection with pulsed extraction techniques, its time constant $\tau = RC$, resulting from the re-

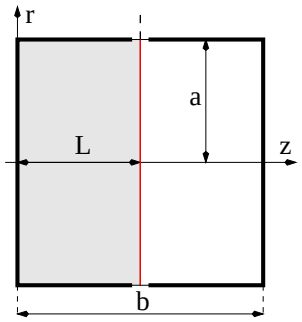

Solution of the Laplace equation
in cylindrical coordinates
$\Phi(r, \phi, z) = R(r)\, Q(\phi)\, Z(z)$

$$V = \sum_{m=1}^{\infty} \frac{2\, V_0}{x_m J_1(x_m) \sinh(x_m L/a)} \sinh(x_m \frac{z}{a}) J_0(x_m \frac{r}{a})$$

Figure 4.5: The electrostatic potential in an acceleration stage formed by pot-shaped electrodes. For the setup shown, symmetry considerations require the electrostatic potential to take the mean value of the electrode potentials along the central plane normal to the TOF MS axis. This allows for the individual consideration of each electrode (e.g. shaded region). By adding a constant potential, the single electrode problem is transformed into the case of a closed cylinder with the potential at the side and the bottom surfaces being zero while its top has a given potential V_0. The analytical solution for the potential V inside the cylinder is given by the above infinite sum [104], with x_m being the m-th root of the zero-order Bessel function J_0. The complete description of the extraction region is obtained by superposition of the single electrode solutions for the given boundary conditions. Due to the slow convergence of the above sum, calculations have been performed by the numerical SIMION program [102].

sistive voltage divider and the electrode capacities, can limit the achievable switching time of the extraction region. Realizing a smaller τ by reducing the divider resistance, is quickly limited by the availability of adequate high-current switches as well as the high power consumption at high potentials. Storing the necessary energy would require large supporting capacitors, since especially in cluster mass spectrometry, the extraction fields have to be maintained until the heaviest cluster of interest has left the extraction region. The latter can take in the order of ten microseconds.

Pot Electrodes

During the course of the present work, an alternative approach was developed that seems to be well suited for pulsed extraction techniques. It avoids guard rings and voltage dividers while only moderately increasing the diameter to distance ratio. A well-behaved, symmetric electrical field that approximates the ideal homogenous potential gradient very well in the regions around the TOF axis (see Fig. 4.6) can be achieved by employing pot-shaped electrodes (right panel of Fig. 4.4). The horizontal walls of the electrodes shield the interior of the extraction region from the penetration of external electric fields. Since the potential difference between the electrodes is generally smaller than the difference between any of the electrodes and ground potential, this already decreases the field distortions. The symmetry plane in the middle of the electrodes, which carries the correct value for the potential, effectively cuts the plate separation in half and thus reduces the penetration depth of the perturbations from the horizontal electrode parts further (see Eq. (4.5)). Additionally, since the perturbation, introduced by the deviation of the constant horizontal electrode potential from the ideal potential, increases linearly for each electrode, starting from zero at the respective electrode position, the penetration depth is further reduced compared to a constant perturbation that extends over the whole electrode separation. A major

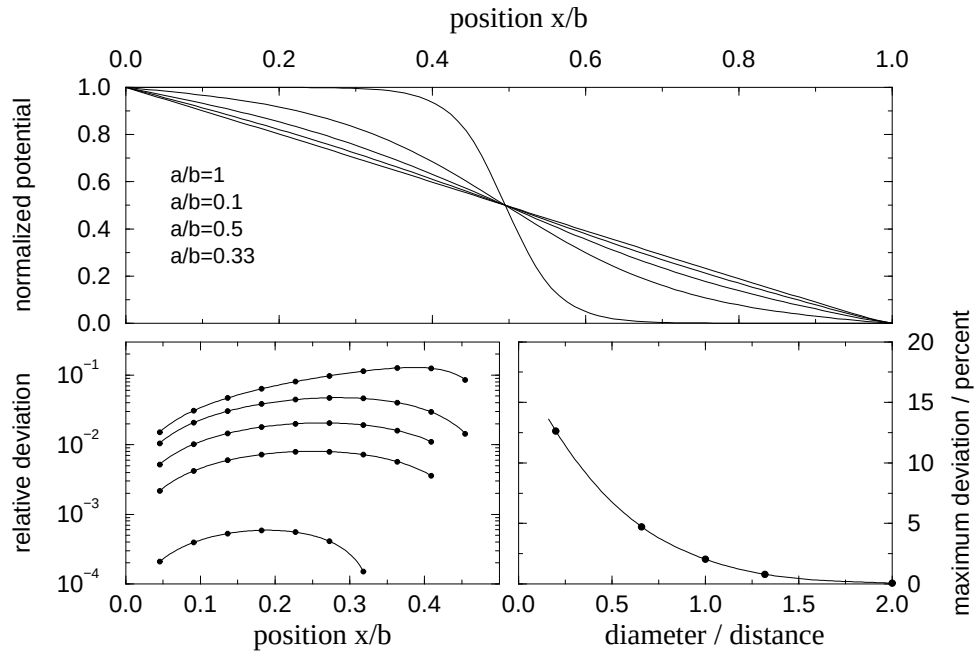

Figure 4.6: Field homogeneity in acceleration stages realized with pot-shaped electrodes. The upper panel gives the normalized potential along the axis of the acceleration stage for pot-shaped electrodes with various ratios of radius a to plate separation b. As depicted in the lower panels, the deviations from the ideal course of the potential are a rapidly decreasing function of the ratio of plate diameter to plate separation. For a ratio of 2:1, the ideal gradient is reproduced within better than a thousandth part. All the above calculations have been performed using the SIMION program [102].

advantage of this setup is, that once the electric potential of the electrodes is chosen, its overall shape is fully determined and can be described analytically (see Fig. 4.5). It is only determined by the easily controllable electrode geometry and not by more involved parameters like the resistance of voltage dividers or the position of many guard electrodes. Since only capacitive elements are involved, this setup allows for fast switching with minimal power consumption. As illustrated in Fig. 4.6, the linearity of the potential gradient along the axis of the extraction stage is influenced by the ratio of plate diameter to plate separation. With a diameter to distance ratio of 1:1, deviations from the ideal situation lie in the percent regime, while with ratios of 2:1 the ideal potential gradient is reproduced to better than a thousandth part.

4.3 Experimental Setup

Two different, interchangeable TOF mass spectrometers were employed in the experimental chamber. Both are based on a large extraction volume design and operate in the pulsed mode, which allows for the analysis of ions that have not been formed directly within the extraction volume, but which drift into the TOF mass spectrometer while the electrodes are at ground potential. The switching of the electrodes is done via two high voltage push-pull switches (Behlke GHTS60, GHTS100) that achieved

Axial TOF			
a	11 cm	b	3 cm
c	98.0 cm	d	19.4 cm
e	20.8 cm	f	1.0 cm
g	4.8 cm	h	0.5 cm
i	5.1 cm		

detector: channeltron

Perpendicular TOF			
a	4.2 cm	b	1.0 cm
c	40.8 cm	d	3.7 cm
e	8.0 cm	f	1.4 cm
g	0.7 cm	h	1.0 cm
i	2.0 cm		

detector: multi-channel plate

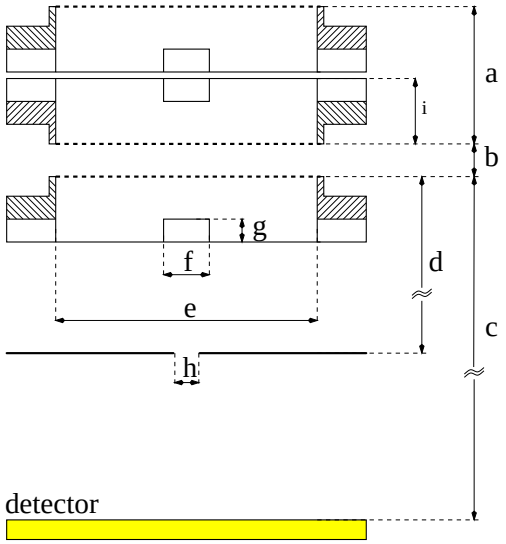

Figure 4.7: The dimensions of the TOF mass spectrometers employed.

rise times within some 10 ns. They are connected to high voltage power supplies that provide voltage between either 0-6.5 kV or 0-12 kV (FUG HCN 35-6500, HCN14-12000), depending on the required energy range for the cluster ions.

Axial TOF

For the analysis of the primary cluster beam, an axial TOF has been set up (for its dimensions see Fig. 4.7), which concentrically encloses the cluster beam. This design has been chosen to allow an easy, unbiased analysis of large clusters: Cluster formation by way of adiabatic expansion of seeded or unseeded gases (see Chap. 2) produces aggregates with a considerable velocity; in the 1 km/s regime. Together with the long flight time of heavy clusters in a TOF mass spectrometer, the initial cluster velocity introduces a radial velocity component for perpendicular extraction. A perpendicularly extracted heavy cluster would hit the detector plane 10 cm off axis due to its ballistic movement during its 100 μs flight time. To ensure detection, either detectors with large sensitive area or additional deflecting electrodes [101, 105] that compensate the radial movement of a certain fraction of the cluster ion distribution, have to be employed. For the axial extraction scheme employed here, the initial velocity of the clusters only influences the arrival time of the respective species at the detector. Since after adiabatic expansion all clusters have an equal initial velocity regardless of their size, the overall spectrum is shifted to earlier arrival times in first order approximation:

$$t(x, Uo) \approx t(x, Uo = 0) - \sqrt{\frac{2\,m}{q}} \frac{1}{E_1} \sqrt{Uo}. \tag{4.6}$$

Moreover, no peak broadening due to the turnaround time is to be expected, since all ions already move towards the detector. The electrodes (aluminum and stainless steel construction) for the first acceleration stage have the newly developed pot-shaped geometry, which allows for a plate separation of 11 cm. As illustrated in Fig. 4.3, the useful extraction region comprises ≈8 cm. On the axis, the electrodes have a circular hole with a diameter of 0.8 cm in order to admit the molecular beam, and respec-

tively, the created ions. The first electrode is situated 19.2 cm downstream of the nozzle and 15.6 cm after the skimmer which connects the expansion and the experimental chamber. To allow for laser ionization throughout the whole extraction region, the electrodes have been fitted with slits parallel to the TOF axis. Alternatively, the cluster beam can be ionized by an electron impact axial beam ionizer (Extranuclear Mod 41-1). The center of the ionization volume of the latter was situated 6 cm in front of the first TOF electrode. In conjunction with a pulse generator (HP 214B) ionization can be performed using electron pulses with a width down to 10 μs. As illustrated in Fig. 4.8, this setup not only provides an easy-to-handle source of positive as well as negative ions, but allows, by a combination of pulsed ionization and delayed extraction, for the suppression of the content of small clusters and thus for the analysis of larger cluster ions with enhanced detector sensitivity (see Fig. 4.8).

Quantitative Detection

The axial TOF features a hybrid detector which consists of a channeltron combined with a simple collector electrode (see inset in Fig. 4.8). This setup has been chosen with regards to the well known problems concerning quantitative detection of large cluster ions. Conventionally, the detection of clusters as charged ions involves the use of a secondary electron multiplier at some point in the detection scheme. They combine the fast nanosecond response time, crucial for mass resolved TOF measurements, with a high sensitivity, which allows for the detection of individual ions in the low mass regime with almost unit probability. Upon the impact of the ion on the detector, the initial secondary electron can be emitted from the solid either in form of a *potential secondary electron* or a *kinetic secondary electron* [106]. In the first mechanism, the impinging ion is neutralized as it approaches the surface and the energy released is used to emit an electron from the solid. In the second, the kinetic energy of the ion is converted into electron excitation within the solid, which allows some of the excited electrons to diffuse towards the surface and to escape from the substrate. While the second mechanism is dominant under typical conditions, the first, which is not appropriate for negative ion detection, plays a role at low velocities and for multiple charged ions, since it requires the ionization energy of the impinging ion to be at least twice the work function of the solid. Generally, the yield of secondary electrons increases with ion velocity, starting from a velocity threshold for the emission of kinetic secondary electrons in the order of $4.5 \cdot 10^4$ m/s for small metal cluster ions [107]. However, in TOF mass spectrometry, heavier particles impinge on the detector with lower velocity. This implies a decreasing secondary electron yield with increasing cluster size. On the other hand, for a given velocity, the secondary electron yield is found to be proportional to cluster size (addition law) [107, 108]. These opposite trends lead to an intermediate maximum followed by a decrease in detection efficiency for large clusters, which makes quantitative measurements of cluster ion distributions difficult. Instead of the established approach, which consists in substantial post acceleration of the cluster ions (up to 100 kV), the envelope of the size distributions of the cluster ions was determined in a straightforward but quantitative way. For the retarding field method, a combination of a collector electrode and high impedance differential amplifier has already been used to quantitatively determine amounts of charge down to a thousand elementary charges (see Chap. 3.3) via the relation $\Delta U = C\,Q$, where C has been self-consistently determined from the slow recharging of the capacitance through the known resistance R. As shown

in Fig. 4.8, this principle can be applied to the detection of TOF mass spectra. The enclosure of the channeltron detector by the collector electrode allows for separate measurement with both detectors, performed under similar conditions. The discrepancies between the measured size distributions manifest quite clearly the decreasing detection efficiency of SEV detectors with increasing cluster size. The mass resolved channeltron spectra are ideal for providing individual mass analysis in the low mass range, however, they are completely inadequate for the determination of the overall size distribution of the cluster ions. For the latter purpose, the direct charge measurement is ideal, especially for the analysis of the primary beam with its abundant charges. This method is not based on secondary electron emission but on charge neutralization. For the latter, unity probability can be achieved by employing biased electrodes (to avoid the escape of secondary electrons) as well as multi-collision collectors (e.g., a stack of razor blades). Although it does not provide individual mass resolution, it is fast enough (see rise time of the electrode signal due to the impinging monomers) to represent the accumulated charge without distortion, which allows for the obtainment of quantitative size distributions by taking the time derivative of the measured curves.

Perpendicular TOF

For the analysis of small cluster fragments, especially the positive and negative cluster fragments created during the surface-collision of the primary cluster beam (see Fig. 5.1), a second TOF mass spectrometer (for the dimensions see Fig. 4.7) that extracts ions perpendicular to the beam axis has been employed. The pot-shaped electrodes consist of aluminum rings, to which copper meshes (Buckbee Mears, 70 lines/ inch) have been attached using a conductive glue (see Chap. 3.3). The primary beam passes through the center of the extraction region via two slits in the electrodes and is accessible to laser ionization via a pair of perpendicular openings in the electrodes. This geometry also allows for the analysis of the incoming cluster beam by laser- or electron-impact ionization. The axis of the perpendicular TOF and the beam axis intersect each other 22 cm downstream from the skimmer. The perpendicular TOF was fitted with a standard multichannel plate electron multiplier for the detection of the impinging ions. Contrary to the common setup, the front face of the channel plate was grounded at the sacrifice of an additional post acceleration stage. The back side of the MCP and its collector anode were consequently at high potential (typ. 2 kV) and the ion signal was fed into a fast preamplifier (EG&G Ortec 9306) by capacitive coupling. This detection scheme was employed with regards to the mass spectrometry of bipolar cluster fragments. By simply changing the polarity of the voltages applied to the acceleration stages, positive as well as negative cluster ions could be detected with an unchanged detector. Since the CIMS method extracts information mainly from the well resolved small cluster fragments, the loss of detection efficiency in the high mass region connected to the lack of an post-acceleration stage is tolerable. Depending on the collision parameters, the cluster fragments are on average a factor of 10 to 100 times smaller than the precursor cluster, even starting with the bare core ion. Additionally, by employing high extraction voltages, some of the high mass sensitivity can be restored. Typical ion energies employed in the perpendicular TOF lie in the range of 3 kV - 6 kV. An upper limit is given not only by the fast switches that apply the voltage to the extractor, but also by considerations regarding field detachment of weakly bound electrons in cluster anions.

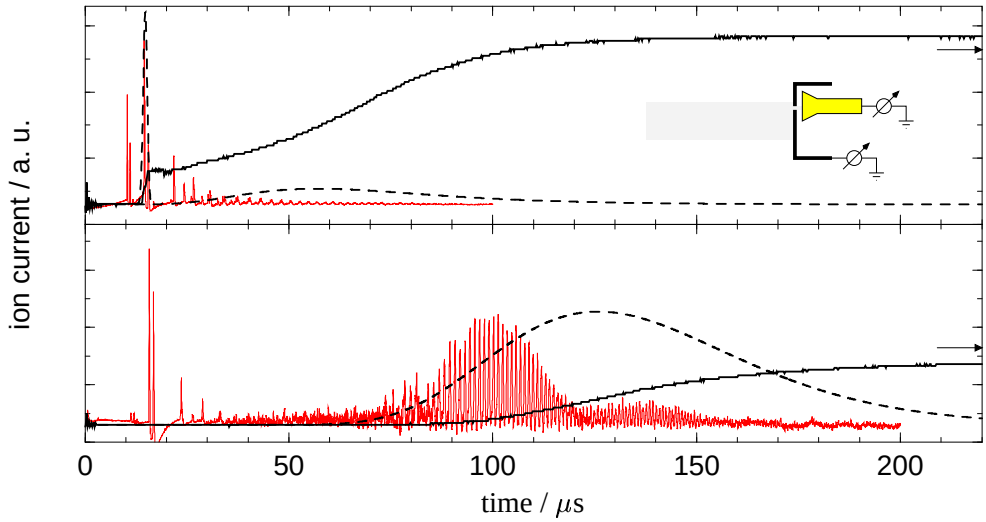

Figure 4.8: Delayed extraction and quantitative measurement of cluster ion distributions. The panels show TOF mass spectra for mixed clusters of N_2 / O_2 (nozzle diameter 0.3 mm, stagnation pressure 10 bar, nozzle temperature 270 K) recorded by the axial TOF mass spectrometer. The ions were created via the axial ionizer, which precedes the TOF setup, with an 80 μs electron pulse with 50 eV energy at a source potential of 50 eV. Before entering the extraction region, the ions have to cover a distance of 6 cm, which takes them varying amounts of time according to their mass. This explains why the upper spectrum, which was recorded 60 μs after the start of ionization, is dominated by the fast monomers. The bottom spectrum, recorded after a delay of 160 μs, at a time when monomers have already left the extraction region, shows a distribution of large clusters. This technique, basically a TOF-TOF coupling, can be employed to specifically analyze the large clusters in a distribution at a detection sensitivity which would damage the detector in the presence of abundant monomers. The first pair of peaks, situated around 10 μs, corresponds to dissociatively ionized N^+ and O^+. Again, they correlate with small clusters and almost vanish in the presence of large clusters. Since all monomer ions directly created by the ionization have left the extraction region at that time, the molecular cluster ions in the bottom panel must be fragments of the large clusters. Instead of the channeltron detector, mass spectra can be directly recorded by way of a collector electrode situated at the same position. The full lines give the corresponding pile up of charge as measured with a high impedance differential amplifier (Tektronix, ADA400A). Although this method does not provide individual peak resolution, it quantitatively describes the overall envelope of the cluster ion distribution. The dashed curves give the corresponding distributions as obtained from a model based on the log-normal distribution. The obvious discrepancy between the channeltron and the collector spectrum can be explained in terms of the already established fast decrease of detection efficiency of SEV detectors for slow, massive ions.

Mass Calibration

Generally, a TOF mass spectrometer measures the arrival time of ions at the detector. With the help of the respective dispersion relation, which can always be written in the form $t = t_0 + k\sqrt{m}$ where t_0 and k are apparatus specific constants, this information in the time domain can be converted into a mass spectrum via a simple axis transformation. To preserve the quantitative information about the collected charge,

that is contained in the peak area, the signal height has to be corrected according to

$$\int_0^\infty f(t)\,dt = \int_0^\infty g(m)\,dm \;\Rightarrow\; g(m) = f(t)\frac{dt}{dm} = f(t)\frac{k}{2\sqrt{m}} = f(t)\frac{k^2}{2\,(t-t_0)}, \tag{4.7}$$

which has been derived via the condition that the total amount of particles detected in the time domain has to be the same as contained in the mass spectrum.

Chapter 5

Charge Separation in Polar Molecule Clusters - The Clusterelectric Effect

Introduction

In this chapter, cluster impact mass spectrometry will be applied for the investigation of the hitherto unexplained charge generation process observed during cluster-surface collisions of water as well as sulphur dioxide clusters. This phenomenon represents a prototype process for the CIMS technique. While cluster-surface collision is an essential part of the phenomenon, the focus of investigation is on the nature of the process for charge generation. Is it a spontaneous intra-cluster process, an impact driven intra-cluster reaction or a cluster-surface charge transfer? The mass analysis of the charge carriers produced during surface impact will shed light on the responsible mechanism. In a series of experiments described hereafter, evidence is given, that the observed phenomenon is not restricted to sulphur dioxide or water, but seems present in the whole class of polar molecule clusters. The CIMS mass analysis of the emerging ions for the SO_2 system, reveals that ubiquitous easy-to-ionize surface adsorbates, mostly in the form of alkali atoms, play a key role. A detailed microscopic mechanism for the charge generation process is proposed and its individual aspects are discussed.

5.1 Overview

It has been a puzzling observation that neutral molecular clusters of H_2O [90, 109, 110, 111] and SO_2 [112, 14, 113] efficiently break up into positively and negatively charged fragments upon low energy impact on essentially any solid surface. This charge separation takes place, despite the initial kinetic energy of each cluster constituent being smaller (up to 25 times) than the required ionization energy of a single cluster molecule. Therefore a direct, collision-induced ionization of individual molecules can not account for the observed charge generation.

Water Clusters

In a series of papers [109, 110, 111], Vostrikov and co-workers investigated this phenomena by scattering water clusters of different mean sizes $\overline{N}$ with a velocity of 1300 m/s on a variety of surfaces including metals, semiconductors and dielectrics.

The generation of free charge carriers that rebound from the surface, have been observed for all of the investigated surfaces; e.g., for gold, steel, titanium nitride, graphite, duraluminium, gallium doped germanium, fiberglass laminate as well as a fullerene covered surface. This hints at an underlying mechanism that is indifferent to the electronic structure of the collision target. Nevertheless, the target material influences the absolute value as well as the ratio of the observed amounts of positive and negative charge with the negative ions showing the more pronounced variations [109, 110]. Retarding field measurements of the emerging ions performed by Vostrikov and co-workers [109, 110] revealed that the charge carriers have considerable energy. Therefore, they either have to emerge with hyperthermal velocity or are endowed with considerable mass; e.g., by consisting of several molecules. For an angle of incidence of 70 degrees, positive as well as negative ions are preferentially emitted in the tangential direction in accordance with neutral scattering [109, 110]. While the energy of the positive ions diminished with a decreasing scattered angle, the kinetic energy of the negative charge carriers was found to increase reaching a maximum at negative reflection angles. For normal incidence, the amount of scattered negative ions is considerable smaller than of the positive ions. However, at large angle of incidence the amounts can become comparable for certain target materials; e.g., for gold [109]. Magnetic deflection measurements also identified a contribution of free-electrons in the negative current [109]. The total amount of charged fragments of either polarity, showed a strong dependence on incident scattering angle, with a maximum at 70 ± 5 degrees with respect to the surface normal. The ionization probability per cluster for cluster-surface collision is cluster size dependent and increases to an optimum angle of incidence from 10^{-7} for a beam with average cluster size $\bar{N}$=300 molecules to 10^{-4} for $\bar{N}$=1500 [110]. A lower size limit for the observed charge separation has been found to be $\bar{N}$=40 [110]. The impact of water monomers under comparable conditions has not been reported to produce charges. The absence of charge separation in analogous experiments with $(CO_2)_n$ and $(N_2O)_n$ clusters [110] led the authors to a water-specific explanation of the observed phenomena in terms of an autoprotolysis reaction. While the threshold energy for polar dissociative ionization of a single water molecule is in the order of 17 eV, this reaction is known to have a much lower activation energy of E_a=0.58 eV in the condensed phase, due to the high energy of hydration of both the proton and the hydroxyl group. It occurs spontaneously due to thermal OH overtone excitation [114, 115]. Because the observed charge separation efficiency per single water molecule was orders of magnitude larger than expected for the cold water clusters ($T\approx180$ K), it is argued that the formation of ion pairs is enhanced by vibrational excitation of the water molecules during the cluster-surface collision [109, 111]. The authors claim to have observed this mechanism in molecular dynamics simulations of small H_2O clusters (N=32, 64), which collide with a surface at velocities of 1, 3.4 and 10 km/s under normal incidence [111]. For a given impact energy, ion pairs have been found to form more efficiently for larger clusters. Therefore, they propose that the larger cluster size used in the experiments compensate for the considerably higher velocities used in the molecular dynamics calculations. However, whether an efficient excitation of intramolecular vibrations really does take place under the slow, grazing collisions of the experiments remains to be shown. Since the ion pairs observed in the molecular dynamics sim-

ulation rapidly recombined (within $5{\cdot}10^{-13}$s), the surface has to actively participate in the ion separation via asymmetric ion neutralization. The target-dependence of the charge yields, and the measured currents to the target at the scattering of water clusters without an external electric field, support this reasoning. The increase of the ion yield for tangential impact of water clusters is explained by enhance charge pair generation via the breaking of adsorption bonds that have been formed during the cluster-surface contact [111]. The observation of free electrons among the negative charge carriers is attributed to Auger emission from the target due to neutralization of the positive charge [109].

Sulphur Dioxide Clusters

A new facet to the cluster-impact induced charge separation emerged when Schröder and co-workers reported [14, 112, 113] the observation of comparable amounts of positive and negative charged cluster fragments created during the low-energy impact ($\approx$ 0.5 eV / molecule) of sulphur dioxide clusters on gold, graphite, silicon, and sodium chloride single crystal surfaces as well as on polycrystalline quartz, sapphire, copper and molybdenum. Although the observed phenomenon largely resembled the reported behavior of water clusters, it can not be explained by an autoprotolysis model as outlined above, since bulk SO_2 does not exhibit an ionic auto-dissociation [116]. Further analysis [14] revealed that the highest charge yield was produced by the gold surface and its yield increased exponentially with surface temperature. While raising the substrate temperature from 110 K to 900 K a signal increase of $\approx$3 was observed [14]. The authors interpreted the temperature dependence in terms of a decreasing adsorbate coverage of the target. This is consistent with the decrease of charge yield with exposure time of the target to the beam compared the comparatively stable ion yields at high surface temperature [14]. The condition of the surface influenced the ratio of the negative and positive charge yields. While freshly prepared gold crystals induce equal amounts of positive and negative charges, it has been found that the positive ion yield decreases faster with time than the negative one. This has been connected to a changing re-neutralization probability with increasing adsorbate coverage of the surface [14]. Charge pair production has generally been observed only for fast SO_2 (v$\approx$1.3 km/s) clusters as achieved by seeded expansion with helium or hydrogen carrier gas and not with slower clusters from pure SO_2 or SO_2/Ar mixtures, and the ion yield decreased with increasing angle of incidence [112, 14]. Both hints at an energy barrier for the production of free charges. From the fact that the ion signal did not correlate with the amount of SO_2 monomers or trimers in the cluster beam, the authors concluded, in accordance with the findings of Vostrikov *et al*, that there is a minimum cluster size for the process to take place. The importance of large clusters for the observed charge separation is emphasized by the non-linear increase of the ion yield with the stagnation pressure [14]. The seed gases He, Ar, Kr alone did not produce detectable amounts of charges, although clusters have been detected [14]. Retarding field measurements in [14] and more detailed in [113], confirmed that the ions emerging after the scattering process have kinetic energies in the range of 1 eV to 10 eV and consist of various ensembles with possibly different mass and velocity distributions. To explain their observations, the authors proposed an intra-cluster mechanism motivated by the observed equal amount of opposite charges and the robustness of the phenomena with respect to different collision surfaces. To surmount the energy barrier of $\approx$ 6 eV [113] for the charge transfer between SO_2 molecules

inside the cluster, an efficient energy focusing of collective kinetic energy into individual excitations is invoked; e.g., by means of the sudden compression of the cluster during surface impact leading to either direct thermal excitation by the shock wave [14] or a piezoelectrically induced charge transfer [14, 113]. The latter can result from the compression induced deformation of individual SO_2 molecules or the displacement of crystal planes in local orientational anisotropies (short range order in liquids) [113]. As this intracluster model relies only on the molecular dipole moment of the clustered species, it could also explain the observations for water clusters. It does not invoke collision-induced excitations of intramolecular vibrations which are unlikely at low impact velocities (see Chap. 1).

Influence of the Surface

However, the recent findings of Petterson and co-workers [90] about H_2O clusters ($\bar{N}$ up to 3700, v=1.3 km/s, angle of incidence 70 degrees), convincingly rule out a charge generation mechanism in the water system that relies on the above *intracluster* mechanisms alone. The authors observed oppositely charged ions emerge from a freshly cleaved, untreated graphite surface at 298 K. The signal from the negatively charged particles has been found to be a factor of 2.5 larger than for positively charged particles. Again, retarding field measurements revealed that the rebounding ions had considerable kinetic energy when leaving the surface, and therefore most likely represent large cluster fragments. Yet, after a heating cycle during the preparation process of the graphite surface, no further room temperature signal was observed. From the view point of internal autoprotolysis as well as the internal piezoelectric model this is a completely unexpected behavior and indicates that the charge pair generation in the low velocity regime using untreated, almost arbitrary surfaces *does* involve some special property of the surface which is irreversibly destroyed by elevated temperatures.

For prepared graphite surfaces and high surface temperatures in the range of 950-1450 K, the authors discover a different regime of charge carrier formation characterized by Arrhenius activation energies of 0.52 eV for the positive and 3.1 eV for the negative ions [90]. In this case, they interpret the anion formation by electron transfer from the hot graphite surface to large water clusters that have already developed an electron affinity in the range of 1.4 eV [90]. Moreover, they tentatively explain the formation of positive cluster fragments, in analogy to Vostrikov *et al.*, by an autoprotolysis reaction in the cluster during surface contact followed by subsequent removal of the OH^- ion by the surface via an unidentified mechanism. In this regime, the kinetic energy of the negative particles is larger than for the positive ones and both are smaller than in the case of the untreated surface. For a surface temperature of 1370 K, the negative charge generation was found to have a stronger pressure dependence than positive ions. A minimum mean cluster size of $\bar{N}$=440 has been established for this case.

While the observation of free positive and negative charge carriers during low-energy cluster-surface collision at high surface temperature can at least be partly understood in terms of a direct cluster-surface charge transfer model [90], the charge separation observed for untreated surfaces at room temperature remains completely unexplained. Room temperature excludes an efficient charge transfer between the cluster and the surface and the influence of a heat sensitive surface property rules out the internal autoprotolysis model as does the observation of collision-induced charge sep-

aration in the sulphur dioxide system. The lack of an explanation combined with the universality of room temperature charge separation process with regard to the used collision surfaces, makes it a challenging phenomenon. The aim of the following chapters is to introduce and experimentally prove a microscopic mechanism which has a general applicability beyond the water or sulphur dioxide system. The main experimental technique used to elucidate the details of the observed phenomenon has been Cluster Impact Mass Spectrometry (CIMS).

5.2 Dipole Moment - The Origin of Charge Separation

The similarity between the room-temperature charge separation phenomena during low-energy cluster surface collisions of water clusters [90, 109, 110, 111] and sulphur dioxide clusters [112, 14, 113] hints at the possibility of a common microscopic mechanism. Due to the findings above, such a common explanation can not rely on intracluster processes alone, but must at some point incorporate the collision surface. The influence of the surface has to be a very general one, since charge separation is observed on almost arbitrary surfaces, but it also has to be very susceptible with regard to surface temperature. A working hypothesis in the present work has therefore been that surface adsorbates are involved in the charge-generation process. On the other hand, some common property of the water and the sulphur dioxide system has to enter into the mechanism if a common explanation exists at all. The above findings; i.e., that clusters of CO_2 and rare gases do not exhibit the effect, hint at the relevance of a molecular dipole moment for a common charge generation mechanism. This was taken as a second working hypothesis. However, this is contradictory to previous experiments in which clusters of N_2O do not show the effect [110] although N_2O exhibits a weak dipole moment of 0.161 debye.

In the process of unveiling the microscopic process of the observed phenomenon, these working hypotheses have been tested in a two step approach. The relevance of a molecular dipole moment has been investigated in a series of screening experiments involving molecular clusters built from a variety of substances with and without a molecular dipole moment as well as with a different electron affinity. To understand the surface influence, the positive and negative ions created during the cluster-surface collisions have been subjected to a mass spectrometric analysis employing the CIMS technique. If surface adsorbates are involved in the microscopic mechanism, they have to show up in the respective mass spectra. In any case, the exact identification of the previously unknown nature of the ions created during the cluster-surface collision should shed light on the microscopic mechanism, as it allows for the discrimination between pure electron transfer processes and dissociative ionization mechanisms; e.g., between $(H_2O)_n^-$ and $(H_2O)_nOH^-$.

Experimental Setup

The typical CIMS setup that allowed for these investigations is depicted in Fig. 5.1. To perform the cluster-surface collisions, the previously described two chamber cluster beam apparatus was fitted with a retractable target in the second chamber. It perpendicularly intersects the beam, 300 mm downstream from the nozzle and consists of a mount assembled from standard stainless steel parts (Kimball Physics, eV parts) that allowed for the use of a variety of target materials; e.g., SiO_x from silicon

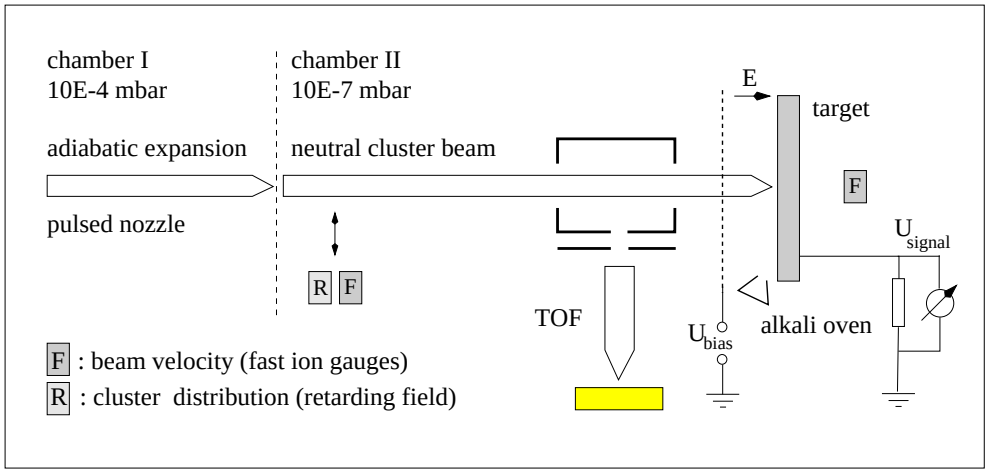

Figure 5.1: Experimental setup for the CIMS analysis of the fragment ions emerging after the low-energy cluster-surface collision of molecular clusters. For this purpose, the two chamber cluster beam apparatus has be fitted with a combined collision and charge collector electrode as well as with a TOF mass spectrometer.

wafers, electrolytically deposited gold on steel or stainless steel itself. By means of a mica-isolated heating element (Telemeter HM6807, 38.1 mm diameter) attached to the back surface, the target material could be heated up to 800 K. The target temperature has been monitored by a type K (chromel/alumel) thermoelement. To measure the total yield of positive or negative charges per pulse, a plate capacitor arrangement is formed by the target and a grid (knitted tungsten mesh, $\approx$ 15 lines / inch) which is placed 10 mm in front of it. For this kind of experiment, the target is grounded via a high impedance differential amplifier (Tektronix TDS410, ADA400A, one input grounded, high impedance mode). By applying a sufficiently high potential (typically between -250 V and $+250$ V) to the grid via a high voltage supply (Stanford Research Systems PS350, 0-5 kV, floated at -250 V with respect to the target), one polarity of the emerging ions is pushed against the target while the other is attracted towards the grid. The latter ions pass the grid and are lost into the vacuum chamber where they do not further influence the measurement process. At the surface, the neutralization of the other ion polarity leads to an decrease of the target potential ΔU (typically mV regime) that is measured by the differential amplifier. Using the target capacitance, which can be determined self-consistently from the slow exponential discharging of the target through the impedance of the differential amplifier (see Chap. 3.3), the deposited charge can be calculated via the fundamental equation of capacitance C=Q/ΔU. The grid potential as well as the signal acquisition process is controlled by a PC-based Labview program (National Instruments). By measuring the ion yield as a function of grid voltage, the energy distribution of the created ions can be determined [110, 14, 113] quite similar to the cluster size distribution determination which uses the retarding field method.

To allow for the spiking of the collision surface with neutral alkali atoms during the course of the following experiments, alkali metal dispensers (*SAES GETTERS*) are

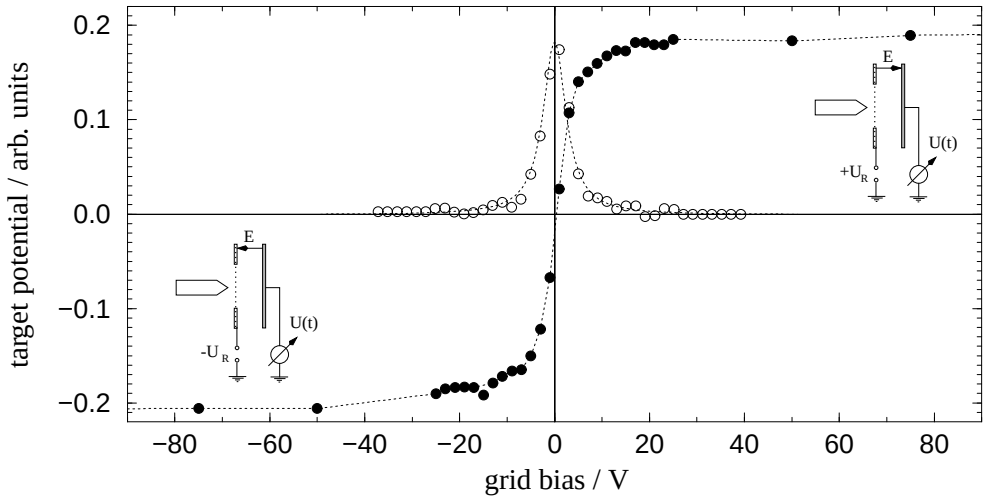

Figure 5.2: Integral charge measurement. SO_2 clusters ($\bar{N}$=60 at 30 eV electron impact ionization) impinging on SiO_x target doped with In with a velocity of 1.3E3 m/s (0.58 eV per particle). The generated charge is measured via the discharging of a plate capacitor setup formed by the target and a bias grid in front of it. Depending on the applied bias potential (see insets) either positive or negative charges are neutralized on the target, with the opposite charge carriers leaving the setup undetected. By varying the bias potential, a retarding field measurement can be performed (full circles). The derivative of the latter (empty circles) represents the energy distribution along the surface normal of the emerging ions.

fitted close to the target, with a distance between oven and beam axis of ≈1.5 cm. The ovens are based on a mixture of an alkali metal chromate (Me_2CrO_4 with Me=Na, Cs) with the alloy Zr84%-Al16% used as reducing agent. This also prevents contamination of the alkali metal vapor by absorbing chemically active gases, predominately hydrogen, produced during the reduction reaction. The mixture is held within a metal container with a trapezoidal cross-section and an exit slit for the alkali vapor. In order to release the alkali metal the dispenser is resistively heated. Evaporation is achieved between 550^{o}C and 850^{o}C (corresponding to heating currents between 4.5 A and 7.5 A). Each working temperature corresponds to a well defined evaporation rate. The alkali metal evaporation can typically be sustained for a period of 20 minutes.

Role of the Dipole Moment

To test the conjecture, that a molecular dipole moment is involved in the microscopic charge generation process, screening experiments have been performed with clusters built from polar as well as unpolar molecules. The clusters were created by means of adiabatic expansion of a gas mixture which contained the respective species and helium as a carrier gas in a ratio of typically 1:10. In the case of acetonitrile, which is a liquid under normal conditions, the carrier gas was bubbled through the substance (see Chap. 2.2). The seeded beam technique has been used to account for the experimental finding that a threshold velocity for the charge generation of SO_2 clusters exists [14, 112]. It is therefore desirable to raise the beam velocity above the value of the pure substance. Since the investigated phenomenon is a cluster effect with a minimum size threshold [14, 110], the cluster size of the tested substance has

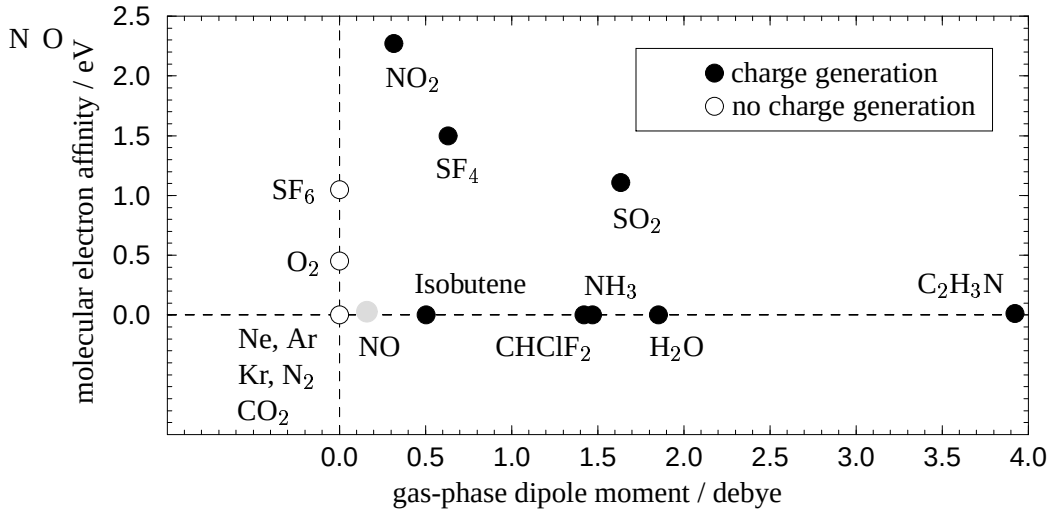

Figure 5.3: Screening experiments. To determine the influence of the molecular dipole moment, clusters built from different molecules have been tested for their capability to create free charge carriers upon low-energy surface collision: empty circles denote that for this species, no charge generation has been observed experimentally. Substances represented by full circles at least show the production free ions of one polarity. The grey circle for NO indicates that weak charge production has been observed in the first chamber alone, where the beam intensity is a factor ≈1000 higher than in the second chamber. While charge production clearly correlates with the molecular dipole moment, the molecular electron affinity, which should be crucial if surface-molecule electron transfer is involved, does not have a major influence.

been varied by raising the stagnation pressure of the gas mixture behind the nozzle in steps until either charge generation is observed, or the maximum pressure (≈25 bar) is reached. Detection limit for the charge generation process is typically 10^4 charges/pulse, which is approximately 1 % of the SO_2 signal under 'normal' experimental conditions. While surface impact of SO_2 clusters has been found to generate almost equal amounts of charges [14], a great variability in the relative amount of positive and negative charges is reported for water clusters [90, 109, 110]. To account for this, the detection of at least one polarity of free charge carriers was taken as the signature of the effect. Fig. 5.2 gives an example of the performed measurements for the SO_2 system. Moreover, by seeding SO_2 in Ne, He and H_2 and applying various reservoir pressures, neutral clusters are produced with variable average sizes $\overline{N}$ and velocities v. From the corresponding set of data (v=750 ms^{-1}... 1.75 10^3 ms^{-1}, $\overline{N}$=0...750) a threshold velocity close to 10^3 ms^{-1} ($\overline{N}$≈300) is deduced and a minimum average cluster size of about $\overline{N}$=20 (v≈1.2 10^3 ms^{-1}). For the case of water, similar thresholds have been reported [109, 110]. The impact of a beam of individual SO_2 molecules at comparable velocities does not produce any charges.

Fig. 5.3 summarizes the experimental findings. The respective substances are represented by circles according to their molecular dipole moment and their molecular electron affinity. Since all mechanisms that involve charge transfer processes from

the surface to the cluster should strongly depend on the electron affinity of the cluster in general as well as the respective molecular electron affinity. Using various target setups and target materials (metals, insulators), the measurements have been performed over an extended period of time. More detailed investigations concerning the group SO_2, SF_4, NH_3 and H_2O will be presented in the following chapters. While substances that led to the generation of free charge carriers upon low energy surface-impact of the respective clusters are represented by a full circle, those not showing the effect are marked by a empty circle. There is a clear separation into two groups. In contrast to clusters from polar molecules like H_2O, SO_2, NO, NH_3, NO_2, SF_4, CH_3CH, $CHClF_2$, and isobutene, clusters from molecules which have no permanent dipole moment like O_2, N_2, CO_2, SF_6, and the noble gas atoms Ne, Xe, Kr did not produce a detectable amount of charge upon surface impact. The grey shaded circle representing NO reflects a very weak charge production. It was only observed in the expansion chamber, where the beam intensity is a factor $\approx$1000 higher than in the second chamber. The above findings emphasize that the microscopic process of the observed effect requires the existence of a permanent molecular dipole moment.
The molecular electron affinity on the other hand, seems to have no significant influence on the charge generation process itself since it is observed with comparable strength for SO_2 as well as NH_3. However, the molecular electron affinity particularly influences the amount of free negative charge carriers. While the impact of SO_2 clusters gives rise to comparable amounts of free positive and negative charge carriers, there is a strong variability, with respect to the experimental conditions, in the amount of free negative charge carriers detected for clusters from species without molecular electron affinity e.g. H_2O or NH_3. As will be confirmed in the next chapter, this can be taken as a indication that at some point during the microscopic charge generation process, a free electron is created that can be securely stabilized via a molecular electron affinity. Otherwise, as has been observed for water clusters, it can be lost into the collision target or detach from the cluster to form a free electron (also [109]).
For an exemplary investigation of the nature of the generated charge carriers by mass spectrometry, SO_2 turned out to be the ideal molecule for the following reasons: it is chemically stable, lacks complications due to hydrogen bonding and autodissociation [116] and clusters are readily produced at room temperature. In contrast to the very low electron affinities (EA) of small NH_3 or H_2O clusters [117], the EA of a single SO_2 molecule is already about 1 eV [118], which greatly facilitates the formation of stable cluster anions.

5.3 Mass Analysis of the Fragment Ions

TOF Setup

The mass spectrometric analysis of the positive and negative charge carriers created during cluster-surface collision is performed by the perpendicular TOF mass spectrometer described in detail in Chap. 4.3. The distance between the TOF axis and the collision surface is 7.5 cm. Before it encounters the collision surface, the neutral cluster beam passes through the extraction volume (extraction plates grounded) by way of two openings (see Fig. 5.1). After passing the grid in front of the target,

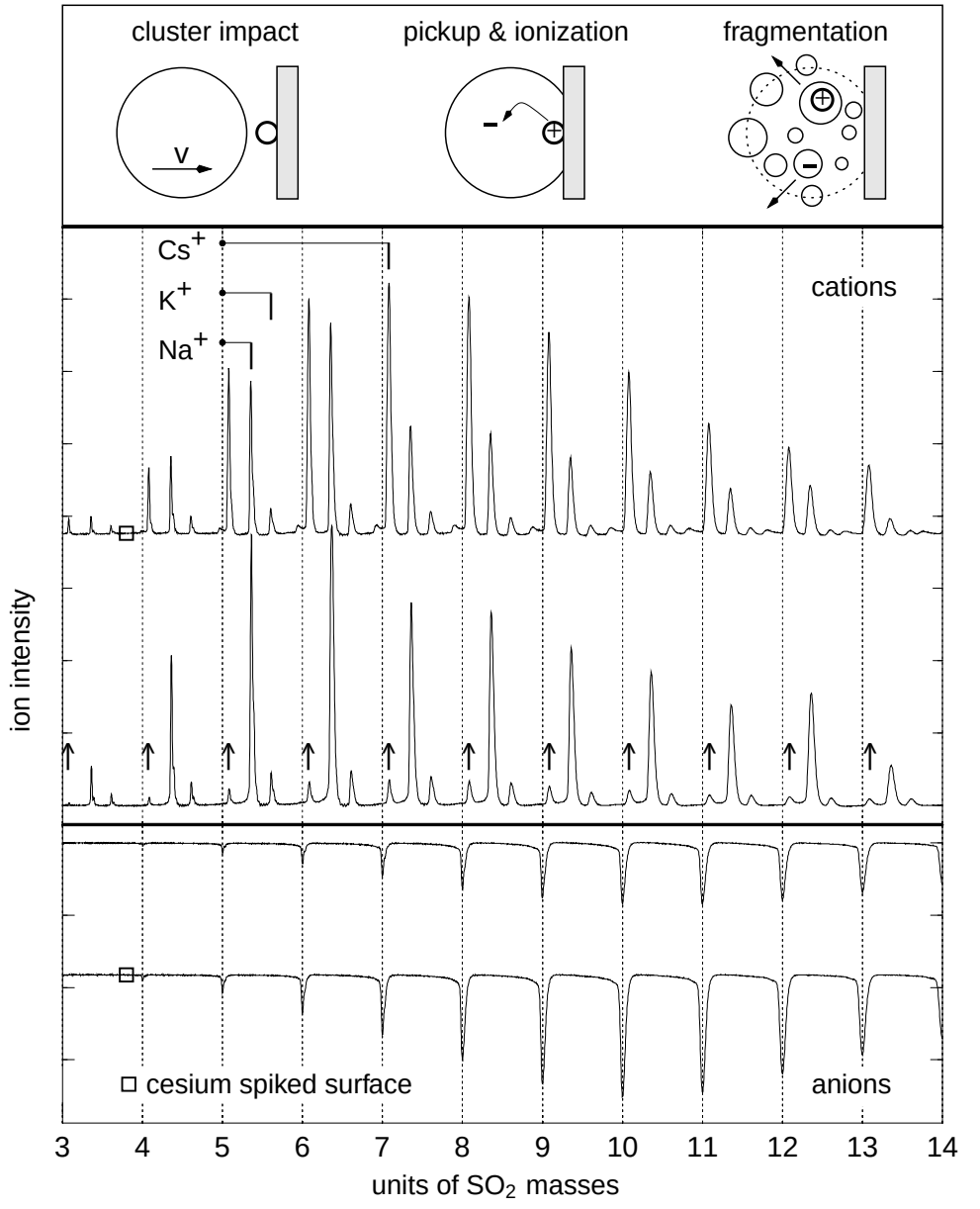

Figure 5.4: Central and lower panel: Mass spectra of positive and negative SO_2 cluster fragments (incident velocity 1.2 km/s, energy per particle 0.48 eV, mean cluster size 500) from impact on electrolyte gold on steel at 600 K. The mass scale is given in units of SO_2 masses. The cluster cations all carry an additional alkali atom. These atoms originate from a ubiquitous surface contamination and were picked up from the surface during the course of cluster impact. Spiking the surface with Cs increases the yield of the corresponding $Cs^+(SO_2)_n$ progression (marked by arrows) and the overall anion yield. Upper panel: Schematic representation of the proposed microscopic charge generation mechanism.

the cluster pulse impinges perpendicularly on the collision surface, which is for this type of measurement directly connected to ground. Due to the broad angular distribution of the generated charge carriers, a fraction of them retraces the beam path and ballistically enters the extraction volume of the perpendicular TOF. By switching on the extraction field between the TOF electrodes these ions can be mass analyzed. Depending on the polarity of the extraction voltage, positive or negative ions are investigated. The grid in front of the target allows for the enhancement of the fraction of the charge carriers that enter the mass spectrometer. By positively biassing it in the case of mass analysis of negative ions and negatively for positive ones, the respective ions are adiabatically transferred from the target into the extraction region of the TOF mass spectrometer. While the ballistic ion drift only allows for the analysis of ions emitted in the direction close to the surface normal, the ion transfer provides the possibility for the analysis of ions emitted more tangentially since the corresponding electric field 'narrows' the emission cone of the ions. Due to the spatial separation of ion source (target) and detection (TOF), the analyzed ions represent a subset of the generated ions, namely ions which all reach the extraction volume at the moment when the extraction field is switched on. This condition can be fulfilled by different tuples of flight distance, velocity, emission angle and creation time (finite cluster pulse width). Since the desired information, namely the identity of the created free charge carriers, is contained in the presence or absence of individual peaks in the mass spectrum and only to a lesser extent in the peak height distribution, this partial averaging over the ion distribution plays a minor role in the present context.

Mass Spectra

Fig. 5.4 presents a mass analysis of the free charge carriers generated by the low-energy impact (incident velocity 1.2 km/s, energy per particle 0.48 eV) of sulphur dioxide clusters (mean cluster size $\overline{N} = 500$) on electrolyte gold on steel. In order to desorb weakly bound molecular adsorbates from the background gas, the target is maintained at a temperature of 600 K. However, this temperature is not yet high enough to induce substantial electron emission from the surface ($k_B T$=0.05 eV). It is also well below the critical temperature range of between 900 K and 1400 K, that irreversibly destroys the room-temperature effect [90]. While the center panel gives mass spectra obtained for the positive free charge carriers, the negative ion spectra are contained in the bottom panel. To represent the ion polarity directly within the spectra, the general convention adopted has been that positive ion intensity rises in the direction of the positive ordinate, while the negative ion intensity increases in the direction of the negative ordinate. The spectra have been transformed from the time to the mass domain (see Chap. 4.3) with the mass of a SO_2 molecule as the fundamental mass unit.

Both, the positive and negative spectra exhibit pronounced progressions, each of which consists of a characteristic pattern that is shifted by multiples of the mass of a single SO_2 molecule over the whole mass range. This periodicity in the monomer mass is a standard feature of cluster distributions (see e.g. Fig. 2.5 or Fig. 2.6). Thus, the overall structure of the spectra immediately reveals that the free charge carriers are indeed cluster fragments, containing several monomers of the precursor cluster. For the first time, this solves the ambiguity of previous measurements of the ion energy which used a retarding field technique [109, 90, 113]. It was not possible to directly discriminate whether the substantial energy of the observed ions is connected

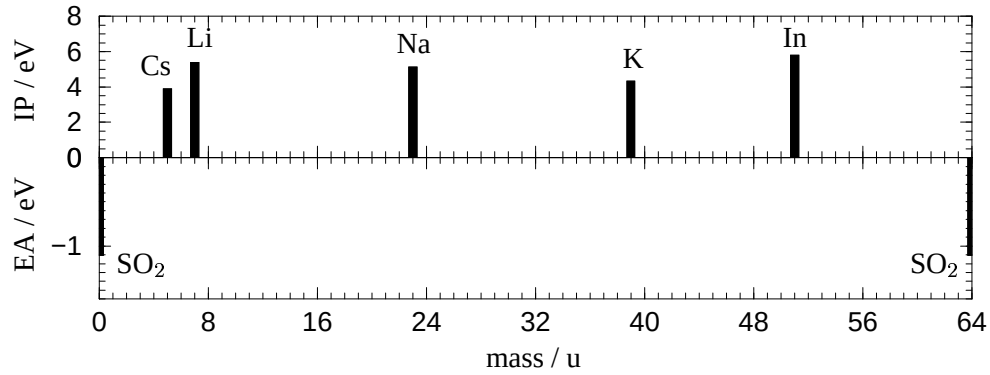

Figure 5.5: Unit cell of the SO_2 mass spectra. In cluster impact mass spectroscopy the fundamental information about the process is generally contained in the mass range spanned by one molecule of the clustered species. The upper panel gives the core ions observed for the positive SO_2 cluster fragments. The vertical axis is taken to be the ionization potential of the respective species. While Li, Na, and K appear at their natural masses, Cs and In are folded back into the unit cell (the spectra containing In and Li follow in the next chapter). The bottom panel gives the negative core ions of the SO_2 cluster fragments with their molecular electron affinity; only SO_2^- is contained in the spectra of Fig. 5.4.

to their massive, composite character or due to the high velocity of bare ions emitted during the cluster-surface interaction. Obviously, the former is the case.

Core Ions

The negative spectra in Fig. 5.4 exhibit a single feature, namely $(SO_2)_n^-$. This indicates that the microscopic charge generation process transfers an electron, which is stabilized via the molecular electron affinity of SO_2. At least for the sulphur dioxide system charge transfer via ions, e.g., in the form of O^- or S^- or via a hypothetical transfer reaction like $2\,SO_2 \rightleftharpoons SO^{2+}+SO_3^{2-}$ [116], does not take place.

Cations of the form $(SO_2)_n^+$ that would correspond to the detected anions are not observed in the positive spectra of Fig. 5.4. This excludes a direct collision induced electron transfer between the cluster constituents. Instead, as shown by the assignment, the positively charged cluster fragments all carry an alkali metal cation, in the case of Fig. 5.4 Na^+, K^+, and Cs^+. In the experiments described in the following chapters Li^+ and In^+ have also been observed.

CIMS Unit Cell

Fig. 5.5 summarizes the experimental findings using the concept of the CIMS unit cell. In Cluster Impact Mass Spectroscopy the fundamental information about the process is generally contained in the identity of the core ions. After collision-induced cluster fragmentation these core ions are still surrounded to various extents by monomers of the precursor cluster, which gives rise to the characteristic progressions in the spectra. The desired information is therefore provided with great redundancy and can already be obtained by analyzing the small part of the mass spectrum that is spanned by the mass of one molecule of the clustered species; e.g., 64 u in the present case. The upper panel contains the core cations observed for the SO_2 system. The vertical axis shows the ionization potential of the respective species. While Li, Na, and K appear at their natural masses, Cs and In are folded back into the unit cell by subtracting one SO_2 unit in the case of In and two units in the case of Cs. The

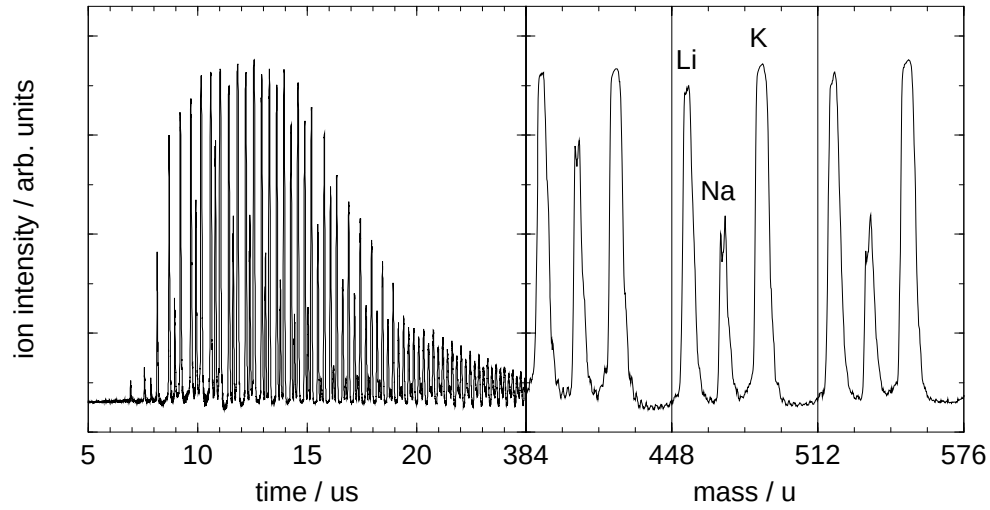

Figure 5.6: Surface adsorbates which induce the charge separation: I. Mass spectrum of the positive cluster fragments emitted during the collision of SO_2 clusters (impact velocity 1.36 km/s, energy per particle 0.61 eV, mean cluster size $\bar{N}$=240 at 30 eV electron impact ionization) on stainless steel at 430^{o}C. The mass peaks in the right panel can be attributed to SO_2 cluster fragments carrying the alkali ions Li, Na and K.

Cs peak observed in the same n-th cell together with the K peak has the composition $(SO_2)_{n-2}\,Cs^+$ while the latter corresponds to $(SO_2)_n\,K^+$. The bottom panel gives the negative core ions of the SO_2 cluster fragments with their molecular electron affinity (only SO_2^- is contained in the spectra of Fig. 5.4). It is important to notice that the peak position for one species within the CIMS unit cell depends on the used clustered molecules. While potassium appears at 39 u in the unit cell for SO_2 and SF_4, it is folded back to mass 5 u or 3 u in the case of ammonia or water, respectively. On the other hand, lithium and caesium coincide at mass 7 u in the water system, while they correlate with mass 7 u and 14 u in ammonia.

The correlated observation of SO_2^- anions with alkali cations in Fig. 5.4, together with the comparable amount of charge carriers with opposite polarity, indicates that the precursor to the observed charge separation process is a neutral alkali atom that gets ionized during the cluster-surface collision. Under the present experimental conditions, the only source of such neutral alkali atoms can be the collision target, where they would have to reside in the form of ubiquitous surface contaminations. To test this conjecture the surface has been spiked with neutral Cs atoms from the oven source. As can be seen from Fig. 5.4, the additional Cs atoms cause a pronounced increase in the corresponding $Cs^+(SO_2)_n$ (arrow marked) as well as in all $(SO_2)_n^-$ peaks along with an equal increase of the total amount of positive and negative charges. This observation further confirms that easy-to ionize surface adsorbates, like alkali atoms, play a crucial role in the charge generation process during low-energy surface collisions of sulphur dioxide clusters.

Metal Adsorbates

In support of this, Figs. 5.6 and 5.7 give mass spectra exhibiting fragment ions with Li, Na, K as well as Cs core ions. The above findings indicate that the observed

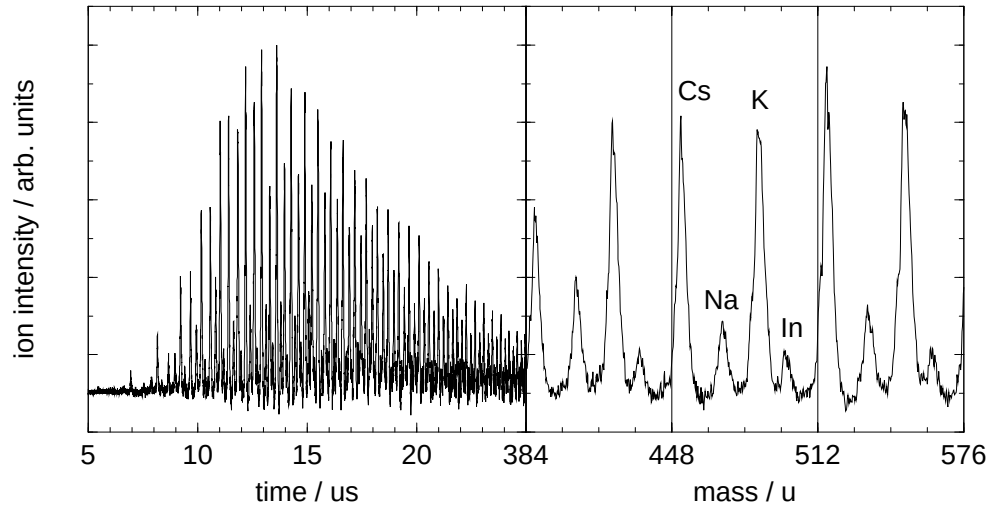

Figure 5.7: Surface adsorbates which induce the charge separation: II. Mass spectra of the positive cluster fragments emitted during the collision of SO_2 clusters (impact velocity 1.3 km/s, energy per particle 0.58 eV, mean cluster size $\bar{N}$=60 at 30 eV electron impact ionization) on SiO_x doped with Cs / In at 200^{o}C. The mass peaks in the right panel can be attributed to SO_2 cluster fragments carrying the alkali ions Na, K, Cs. Moreover, cations carrying the non-alkali ion In^+ can be observed.

charge generation is not connected to the special properties of one, single element, but can be induced by alkali atoms in general. In an attempt to broaden the class of inducing surface adsorbates further, a SiO_x surface has been loaded with indium atoms by mechanically rubbing this ductile metal against the target surface. Subsequently taken mass spectra of the charged cluster fragments, using SO_2 clusters, indeed revealed the presence of mass peaks at the position of $(SO_2)_n In^+$ (see Fig. 5.7). Therefore, charge generation upon low energy impact of sulphur dioxide clusters is not restricted to alkali metals, but can be induced by a more general group of elements. The observation of indium induced charge separation also suggests that the microscopic mechanism at work is not directly connected to the electronic structure of the surface adsorbate. While the electron configuration of the alkali metals can be described in the form [rare gas]ns^1 (e.g., for sodium via [Ne]$3s^1$), the electron configuration of indium is [Kr]$5s^2 4d^{10} 5p$. Therefore, charge separation is not restricted to unpaired valence electrons residing in a diffuse s-orbital.

The suitability of other metal atoms to induce charge separation during cluster impact has been tested by resistively heating a steel loop mounted close to the target surface until it burnt out. In this way the collision surface was loaded with the various metal atoms contained in the steel alloy. An *ex situ* surface analysis (see Fig. 5.8) using a combination of an electron microscope and a x-ray fluorescence spectrometer, confirmed the presence of Fe ([Ar]$4s^2 3d^6$), Ni ([Ar]$4s^2 3d^8$), Mn ([Ar]$4s^2 3d^5$), as well as Cr ([Ar]$4s^1 3d^5$) on the surface. However, upon impact of SO_2 clusters no cluster fragments which carried core ions corresponding to Fe, Ni, Mn, or Cr were observed. The mass spectra have been dominated by cations in the form $(SO_2)_n K^+$ which are

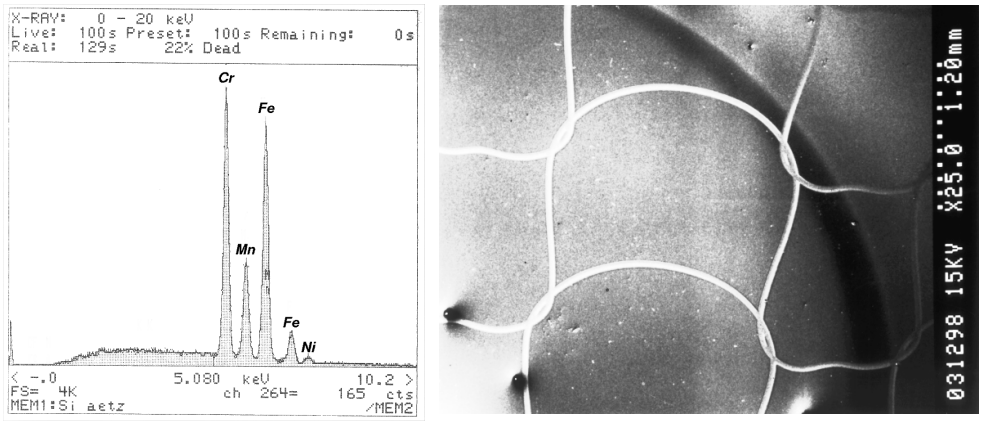

Figure 5.8: Surface adsorbates that do not induce charge separation. In order to deposit a variety of metal atom adsorbates, a stainless steel wire was resistively heated in front of a SiO_x surface until it burnt out. Although *ex situ* analysis by x-ray fluorescence revealed the presence of Cr, Mn, Fe and Ni on the surface (see left panel), these metals have not been observed in the form of charged ions within cluster fragments of SO_2 clusters (impact velocity 1.39 km/s, energy per particle 0.64 eV). Nevertheless, due to K adsorbates which have also been evaporated out of the wire, strong peaks are detected. The electron microscope picture on the right side emphasizes the pick up model. The surface adsorbates layer is altered by the interaction with the impinging cluster beam (beam border in the upper right half). The grid structure on the surface is due to the 'shadow' of the bias grid. It locally blocks the cluster beam so that at the respective position of the surface, the cluster impact induced charge generation process can not take place.

due to potassium atoms that already evaporated from the heated wire loop at modest temperatures. Thus, under the present experimental conditions, Fe, Ni, Mn, and Cr do *not* lead to charged cluster fragments. The case for Cr, which has an electron configuration of [Ar]$4s^1 3d^5$, emphasizes that an unpaired s^1 electron is not a sufficient requirement for an adsorbate that induces charged cluster fragments.

Salt-like Adsorbates

To further clarify the relevant properties of the adsorbates, a SiO_x target was covered with NaCl crystals by evaporating a few milliliters of saturated salt solution dripped on the collision surface. Charge generation upon impact of SO_2 clusters as well as SF_4 clusters was observed under these circumstances. The mass spectra of SF_4 revealed charged cluster fragments that bear the signature of neutral alkali atoms; namely $(SF_4)_n Na^+$ combined with cluster anions which for the SF_4 system, due to ion molecule reaction of SF_4^-, are generally given by SF_5^- (see Chap. 7). However, no anions in the form of $(SF_4)_n Cl^-$ or $(SO_2)_n Cl^-$ have been observed. The high electron affinity of the chlorine anion (3.61 eV), which exceeds that of fluorine (3.4 eV) or bromine (3.36 eV), ensures the observability of picked up chloride anions in the spectra, even if the electron is delocalized from the chloride anion during impact in the same way as the alkali valence electron (contrary to the alkali cation, a neutral chlorine atom would not become stabilized by the surrounding polar molecules). That the electron does indeed settle at the site of highest binding energy is illustrated in Chap. 7 in the case of bromine traces in sulfur tetroxide clusters as well as for SO_2 molecules incorporated into NH_3 clusters. The absence of chloride anions as core

ions of the negatively charged cluster fragments, indicates therefore, that crystalline, ionic salts, do not induce lead to free charge carriers following cluster impact. Since comparable amounts of Na^+ and Cl^- carrying cluster fragments have not been observed, either the direct pickup of ionic Na^+ and Cl^- does not take place, or picked up NaCl molecules do not get separated inside the cluster during the cluster-impact time window. This implies that the well known dissolution of salts by bulk polar solvents, does not proceed under conditions of cluster-surface collisions, probably because the interaction time of $\leq$1 ps is too short.

5.4 Microscopic Model

For the explanation of the experimental observation, the following microscopic process is proposed. The key to charge separation is the pickup of a neutral (but readily ionized) adatom during surface impact of the sulphur dioxide cluster, followed by the delocalization of the adatom's valence electron within the cluster and the subsequent collision-induced fragmentation of the cluster into charged pieces. The latter process separates the geminate ion pair which has been created inside the cluster and thus makes them observable by destroying their mutual shielding. The energy to overcome the Coulomb attraction between the ions is supplied by the kinetic energy of the fragments that enclose the charge carriers (inertial charge separation). This explanation makes the low-energy charge generation during cluster-surface collision the prototype of a chemical reaction that can be investigated by the CIMS method.

The work presented here has already established that charge generation during low-energy surface collisions is a phenomenon that is not only connected to water or sulphur dioxide clusters but seems to pertain to the whole class of clusters built from polar molecules (see Chap. 5.2). To determine whether the microscopic reaction mechanism proposed above represents the universal explanation for this phenomenon, fragment mass spectra have also been taken for clusters of H_2O, NH_3 and SF_4. In the respective spectra, which are presented in more detail in Chap. 7, the signature of the above model, namely cationic cluster fragments carrying alkali ions, has been observed again, as well as a general increase in the amount of generated charge with the alkali coverage of the surface. Within the limit of the investigated number of systems, the proposed microscopic mechanism seems to be the general explanation of the phenomenon.

Pebblestone

The key elements of the proposed mechanism for the observed charge separation are neutral alkali atoms that reside in the form of adsorbates at the collision surface. Although by depositing additional alkali atoms at the surface (see Fig. 5.4) the amount of generated charges can be substantially increased, the effect of charge generation is also easily observed on completely untreated surfaces. This experimental observation indicates that alkali atoms represent ubiquitous surface contaminations. This general persistence of neutral alkali atoms on surfaces is also indicated by surface analyses applying post-ionization of sputtered neutral particles [119]. Although surprising, ubiquitous alkali surface adsorbates can for the first time consistently explain the astounding indifference of the charge generation process regarding the electronic nature of the target [14, 90, 109, 113, this work]. To test the limits of this finding, a rather

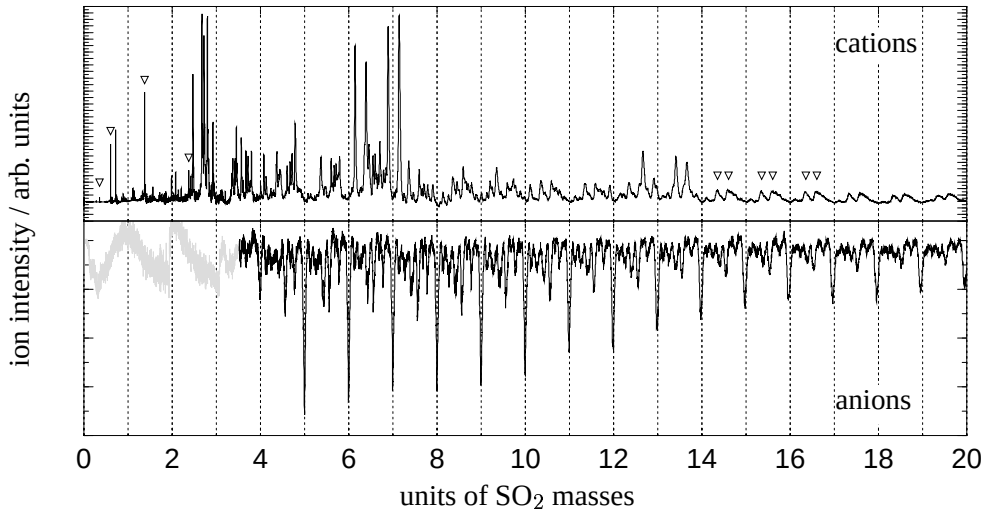

Figure 5.9: Spectra of the charged cluster fragments emerging during impact of SO_2 Clusters (impact velocity 1.38 km/s, energy/particle 0.63 eV, stagnation pressure 10 bar, nozzle orifice=0.5 mm) impinging on a randomly selected, untreated pebbelstone. Besides a very rich structure that indicates a great variety of picked up surface adsorbates, the signature of the proposed mechanism is again present, namely the SO_2 anions together with alkali cations (marked).

unconventional experiment was performed. A randomly selected pebblestone from the embankment of the nearby river Isar was used without pretreatment as a target. Special care was taken to ensure that the cluster beam only interacted with the pebble stone. The observed spectra (see Fig. 5.9) were very rich in structure. Nevertheless, they exhibited the characteristic signature of the proposed mechanism, namely SO_2 anions and fragments carrying alkali cations (marked). Although the resolution of the employed mass spectrometer does not allow for a reliable identification of the large number of additional peaks, it appears that simultaneous co-pickup of additional neutral adsorbates from the surfaces occurs. These remain spectators inside the charged cluster fragment or become charged themselves as a result of ion-molecule reactions induced by the electron or the alkali cation (see Chap. 7). Similar rich patterns have also been observed from freshly mounted targets held at room temperature. The additional pickup of arbitrary adsorbates points to the surface analytical potential of cluster-surface collisions, which, in the presence of alkali metal atoms, provides the picked up adsorbates already in a charged, easy-to-analyze manner. The observation of the proposed charge generation mechanism in the above experiment emphasizes the ubiquitousness of alkali atoms on arbitrary surfaces (charge production has also been observed on a dried oak leave).

Efficiency

Although sodium and potassium are quite abundant in the composition of the Earth's crust (they rank as number seven and eight [120]) the general observation of charge separation from arbitrary surfaces is surprising, and has to at least partly find an explanation in a high efficiency of the charging process: Under typical experimental conditions, a SO_2 cluster pulse is created via adiabatic expansion of a mixture of 5%

SO_2 in He with a stagnation pressure of 10 bar through a nozzle of diameter 0.5 mm. This corresponds to a total flux $\approx 10^{21}$ s^{-1} SO_2 molecules out of the nozzle. Assuming a reduction by the skimmer in the order of 10^{-4}, a mean cluster size of 1000 and a pulse duration of 300 μs, the number of clusters that collide with the surface is given by 10^{10} per pulse. Each cluster samples an area of the surface that equals approximately its cross section ($\approx 10^{-17}$ m^2). With the beam cross section being 1 cm^2 at the collision surface each cluster pulse samples approximately a fraction of 10^{-3} of the interaction area. The typical increase of the target potential with each cluster pulse is given by 1 mV for untreated surfaces. With the capacity of the target setup of $\approx$100 pF this corresponds to an amount of 10^6 charges per pulse from the sampled area. Taking the charge creation efficiency η, which comprises a) the pickup probability if a cluster collides with an alkali adsorbate, b) the charge separation probability inside the cluster with which the neutral atom is stripped of its valence electron by the polar cluster constituents and c) the probability that the collision-induced cluster fragmentation separates the oppositely charged core ions, to be equal to one the observed amount of charges of 10^9 ions/cm^2 corresponds to a surface coverage of 10^{-6} mono-layers of alkali adsorbates. Assuming lower values for η would require a higher surface coverage. This allows for the bracketing of the real charging efficiency of a single cluster, upon impact with an alkali metal adsorbate, by a lower limit. Taking 0.1 mono-layers as an already improbable high surface coverage for alkali metal atoms on untreated surfaces, the fundamental charging efficiency has to be between 10^{-5} and one. Dosing the surface with alkali metal atoms, e.g., Cs from an oven source, strongly increases the observed amount of charges reaching the 1 V range for the charging of the target per pulse corresponding to 10^9 charges. With the number of impacting clusters being of the order of 10^{10}, this corresponds to a charging efficiency well in the percent range per cluster. On the other hand, the charging efficiency per cluster can not be larger than the fundamental charging efficiency η times the number of alkali atoms residing on a surface area that equals the cluster cross section. For clusters of 1000 monomers, the latter factor has to be smaller than 100 so that a better lower threshold for the fundamental charging efficiency can be given. η has to be in the range of [10^{-3},1]. Although the cluster beam intensity can be measured quite accurately (see Chap. 2.3), a better value for the charging efficiency requires a detailed knowledge of the adsorbate coverage, which under our particular experimental conditions is not available. Moreover, the exact value for η is likely to be a function of various experimental parameters among which are the impact velocity of the cluster, the value of the molecular dipole moment of the cluster constituents, the ionization potential of the picked up adsorbate as well as the binding energy of the adsorbate to the supporting surface. Nevertheless, a fundamental charging efficiency η around 10^{-3} is remarkably high given the complex nature of the microscopic process.

The Clusterelectric Effect

Owing to the wide applicability of the proposed mechanism to clustered species and employed collision surface, its high efficiency and the ease of observation of the robust charge signals without requiring sophisticated signal amplification and acquisition equipment, it obtained the laboratory name *"clusterelectric effect"* (CEE), which will be utilized in the subsequent sections as shorthand for the complex microscopic mechanism. The following sections provide a more detailed discussion of the individual steps that make up the clusterelectric effect, namely the pickup of a

surface adsorbate, the charge delocalization of the alkali valence electron inside the polar molecule cluster as well as the inertial charge separation process by the collision induced cluster fragmentation. This subdivision shall not imply that the steps take place in a separated sequential manner. The overall time scale during which the process takes place is in the order of 1 ps and is given by the advection time of the cluster. With typical diameters in the range of 10 Å and impact velocities in the order of 1000 m/s the cluster would completely enter the surface within 1 ps. Since the low energies employed in the present experiments do not lead to substantial implantation but are too high for intact reflection, the cluster has to fragment on this time scale. Fragmentation, however, terminates the charge separation process. The three steps therefore all take place concomitantly, representing only aspects of the effect.

5.4.1 Alkali Surface Adsorbates

The above experimental findings naturally raise some questions concerning the chemical state of alkali atoms at the collision surface and their seemingly ubiquitous presence. The latter finds an explanation in the large abundance of the elements sodium and potassium in general. They total 4 percent of the Earth's crust atoms [120], and therefore should in principle make up a fraction of roughly $4 \cdot 10^{-2}$ monolayers (ML) of each representative surface in the form of various compounds. In the form of their oxides, Na_2O and K_2O, they contribute 7 percent to the average composition of igneous rocks, 4.5 percent to shale and 4 percent to sediments. Even in lime stone they represent 0.3 percent [121]. Due to their lower binding energy (Na: ΔH_{vap}=1.0 eV, K: ΔH_{vap}=0.82 eV) with respect to other metals (Fe: ΔH_{vap}=3.5 eV, Cu: ΔH_{vap}=3.2 eV) their presence in metals and metal alloys is generally reduced to trace concentrations by evaporation during the formation process [122]. Nevertheless, as a consequence of their correspondingly low surface energy they segregate onto the surface of metals and oxides, and thus enlarge their concentration with respect to the bulk [123]. The general persistence of neutral alkali atoms on surfaces is well known from surface analysis applying post-ionization of sputtered neutral particles [119]. A major source of Na and K are the respective ions solvated in water. The oceans represent huge deposits of solvated NaCl ($\approx$ 30 kg/m^{-3}). While Na ions, due to a higher solubility of the sodium salts as well as higher affinity of potassium to alumino-silicates, dominate over K ions in natural solutions, the latter has a higher abundance in the biosphere [124]. Solvated alkali ions represent a major source of alkali contaminations on natural surfaces which come into contact with water. While at high concentrations, the respective crystalline salts form upon evaporation of the water solvent, low concentrations lead to contaminations that are dominated by the adsorbate-surface interaction. Especially in the case of metal surfaces, the formed adsorbate-surface complex has the same nature for ionic or neutral precursor alkali atoms. The same can be expected for arbitrary surfaces after some 'relaxation time'. Therefore, the following discussion of the chemical nature of the alkali atom adsorbed on a surface neglects the electronic history of the alkali and focuses on the interaction within the surface-adsorbate complex in electronic equilibrium.

Metal Substrates

The interaction of alkali atoms with well defined single crystal metal surfaces [125, 126] has been studied. Upon adsorption, the s level of the alkali atom broadens and

shifts. Concomitantly, the alkali valence electron is partially transferred into the substrate, leaving the alkali atom with a positive partial charge [127, 128]. A theoretical study of K adsorbed on a Pt(111) cluster [129] finds that a single adsorbed alkali atom has a bond length of 2.8 Å and an binding energy of 1.86 eV. Several almost isoenergetic binding sites and the absence of activation barriers make the adsorbate very mobile on the surface. The effective charge of the adsorbed K-atom is 0.6 electrons. The corresponding charge transfer to the surface not only reduces the size of the alkali atom from the neutral radius of 2.27 Å [124] to $\approx$ 1 Å, but also leads to the formation of a surface dipole of 9.6 debye [129]. Typical binding energies for alkali adsorbates on metal surfaces lie in the range of 2-3 eV [130] and the induced surface dipole moments vary considerably between 2 debye (Na/W(110)) and 17 debye (Cs/W(110)) [131]. The charge distributions of the surface-adsorbate complex, as well as its optical properties (e.g. regarding second harmonic generation) can be predicted theoretically via density functional calculations for an adsorbate/jellium model [132].

Work Function

A prominent effect of alkali metal adsorbtion on metal surfaces is the decrease of the substrate work function [131]. At low coverages ($<$ 0.5 ML) the work function decreases mostly linearly with increasing coverage. At $\approx$ 0.5 ML a shallow minimum is reached, after which the work function increases again experiences a slight increase, until for a coverage of $\approx$ 1 ML it approaches the value of the respective bulk alkali metal. This general behavior on metal as well as semiconductor surfaces is explained in terms of the surface dipole connected with the adsorption of an alkali atom. It is oriented antiparallel to that of the substrate surface dipole layer and thus reduces the energy required for an electron to leave the substrate. In the simple dipole model, the increase of the work function with coverages larger than $\approx$0.5 ML is attributed to a mutual depolarization of the repulsively interacting adsorbate-dipoles with increasing surface density. A smaller fraction of the alkali valence electron is transferred to the substrate so that the adsorbate dipole diminishes. With increasing coverage, the electron densities of the alkali adsorbates finally overlap and form a metal-like adsorbate. The described decrease of the substrate work function upon alkali metal adsorption can not explain the typical features of the clusterelectric effect. While the latter is a 'cluster effect' with a lower size threshold, a mechanism based on a reduced work function should also give negative ions upon the impact of single molecules that have a sufficient electron affinity. However, charge generation has not been observed for the impact of individual SO_2 molecules (EA: 1.1 eV). On the other hand, it is conceivable, that clusters are needed also in the case of surface-cluster electron transfer, if a too small molecular EA has to be enhanced by solvation effects in larger clusters, to induce a detectable signal. This possibility seems to be unlikely, since the clusterelectric effect is observed on arbitrary surfaces. By exchanging metallic with dielectric surfaces the work function changes considerably. On the other hand, cluster size can compensate for this change only to a limited amount since cluster electron affinity is always bounded by the bulk value. Additionally, the correlated observation of comparable amounts of positive as well as negative charges for the SO_2 system for various collision surfaces, and the observation of fragment anions of ammonia, which itself has no molecular electron affinity, upon doping with SO_2 molecules (see Chap. 7) contradicts a model based on the work function decrease

upon surface adsorption of alkali atoms.

Adsorbate Interaction

The presence of a sub-monolayer of coadsorbed alkali metal atoms significantly influences properties of coadsorbed molecules e.g. their sticking probability, their adsorption site and geometry as well as their dissociation probability [133]. These effects can largely be attributed to the electrostatic interactions between the adsorbates based on the surface dipole induced by the alkali adatom. The electrostatic potential of the alkali surface dipole is rapidly screened close to the surface by a conducting substrate, but further out it falls off slower and will asymptotically fall off as a free dipole field. The lateral range of the perturbation of the substrate surface electronic structure is in on the order of 10 Å [131]. Electronegative molecules like O_2, N_2, CO and NO are found to be more stable, often in side-on bonded configuration [134], and to dissociate more easily on surfaces precovered by alkali metals [135]. The lowering of the dissociation activation energy can be explained in terms of an increased electron density in anti-binding orbitals of the adsorbed molecules which is induced by the electrostatic interaction with the adsorbed alkali atom. Alkali doped surfaces therefore play an important role in heterogenous catalysis [133]. The strength of the electrostatic interaction is illustrated by the reorientation of ammonia adsorbates upon alkali coadsorption. While NH_3 normally binds with the N atom towards the surface and the hydrogen atoms pointing away like an umbrella, ESDIAD measurements [136] reveal that in the presence of a fractional monolayer of alkali atoms, ammonia adsorbs in a tilted configuration with one hydrogen pointing along the surface normal. Moreover, water molecules have been found to completely turn around upon interaction with adsorbed alkali atoms [137]. These two examples hint at the strong interaction of adsorbed alkali atoms with molecules having a permanent dipole moment.

Surface Compounds

The violent reaction of bulk alkali metals towards oxidation, suggests a similar behavior for alkali adsorbates. However, alkali chemistry on (metal) surfaces exhibits a more complex behavior due to the coverage dependent charge transfer between alkali-adsorbate and surface as well as the competition between the adsorbate-adsorbate interaction with the surface-adsorbate interaction. Adsorbed alkali multilayers with metal-like electronic structure indeed show bulk-like behavior and readily react with water and oxygen [138]. While for the multilayers the adsorption energy approaches the sublimation energy of the bulk, low coverage alkali adsorbates exhibit higher binding energies. For potassium on Ru(001) the bond strength decreases from 2.82 eV at low coverages to 1.1 eV at saturation of the monolayer [139]. In the low-coverage regime, the alkali s valence electrons are strongly involved in the bond formation with the substrate surface and thereby loose their free electron character. This is reflected in a different chemical behavior: While sub-monolayer alkali coverages promote the adsorption of oxygen [138], no compound formation between alkali and oxygen is found at low coverages ($<$0.25 ML for K on Ru(001)), instead, adsorption of atomic oxygen on the alkali modified ruthenium surface is observed [139]. While for the co-adsorbtion of CN with multilayer K on Pd surfaces the formation of ionic K^+CN^- was found identical to that of the crystalline bulk, sub-monolayer (0.25 ML) coverage of K led to a 'covalently' bound KCN chemisorbed species [140]. The formation of bound compounds of two coadsorbed species is generally only observed above certain coverage values, when the bonding strength of both adspecies with the

substrate is weakened enough [138, 141]. The ubiquitous alkali surface contaminations, relevant in the present experiments, are well in the sub-monolayer regime (at least for the untreated surfaces) so that their chemistry is likely to be determined by the adsorbate substrate interaction.

Adsorption on Graphite

While graphite is technically a semi-metal, the behavior of K, Rb, and Cs on the basal plane of graphite is very similar to that on metals [125]. A special property of the alkali/graphite system is the possibility to form intercalates. Alkali atoms can diffuse between the graphene layers [133]. Intercalation of K occurs at room temperature [142]. At low temperatures (83 K) potassium remains at the surface and is bound by 1.3 eV [143]. The Na-graphite bond is weaker compared to the heavier alkalis, which is also reflected in its lesser solubility as a graphite intercalate [144].

Adsorption on Oxides and Salts

The adsorption of alkali atoms on oxidic surfaces has recently been reviewed [145, 130]. Adsorption of alkali metals on low bandgap insulators results in a charge transfer to the substrate at low coverages. For the system TiO_2 (E_{gap}=3.1 eV) charge transfer leads to the reduction of the oxidation state of the substrate surface metal cations ($Ti^{4+} \rightarrow Ti^{3+}$). In this case the alkali atoms have a strong cationic character. They induce a surface dipole moment of 6 debye and have a binding energy of $>$2.2 eV [146]. Thermal desorption measurements of K and Cs on TiO_2 [146, 147] have confirmed the relatively strong binding by the observation of neutral alkali desorption up to temperatures of 800 K. Theoretical calculations [148] predict a decreasing charge transfer from the alkali to the substrate for increasing band gap, which results in a weak binding energy for smooth, stoichiometric wide-bandgap oxides. This is in accordance with findings for Na on MgO(100) [149]. Higher adsorption energies are found for faceted MgO surfaces, which indicates the importance of defects for the strength of the adsorption bond [150]. Thus, for wide-bandgap material, especially under natural conditions, the binding and the charge transfer from the alkali to the substrate is controlled mainly by the presence of surface defects. Investigations of the system Na/Cr_2O_3(0001) [151] found that sub-monolayers of Na desorb thermally within a temperature range of $\approx$ 400 K to $>$ 800 K. For the adsorbtion of Cs on thin SiO_2/Si structures a charge transfer from the alkali into the interface has been observed with the resulting build up of a dipole field [152]. Thermal desorption measurements [130] revealed a range of binding energies centered around 1.8 eV/particle. Introducing surface defects by ion bombardment leads to higher binding energies [130]. Indium, which also induces the clusterelectric effect, has been found to inject less charge into the SiO_2/Si interface upon adsorption [152] and therefore has a much smaller surface dipole. Thermal desorption measurements for alkalis from oxide surfaces found a majority of neutral alkalis as desorption products, although the adsorbed alkali has an ionic character [130]. Thus, the low-energy desorption pathway for an alkali ion is to pick up an electron from the substrate and to desorb as a neutral. Alkalis desorb as ions only at higher temperatures ($>$ 1200 K). The observed accumulation and desorption of neutral alkali metal atoms on the surface of salt crystals following irradiation with energetic photons or electrons has been explained in terms of diffusion of bulk defects and excitations (induced by the irradiation) to the surface [153, 154]. For large band-gaps (e.g. NaCl: E_{gap}=24 eV) there is no charge transfer towards the bulk and consequently the neutral alkali atoms have small binding energies. Due to their low binding energy, neutral alkali metals

tend to decorate defects on the surface and to cluster into three dimensional compounds. This behavior has actually been used to create supported clusters of alkali metals by Volmer-Weber growth from deposited alkalis on LiF and SiO_2 substrates [155, 156]. In this case, adsorption energy to the substrate is lower than the alkali-alkali bond and therefore is smaller than $\approx$ 1 eV in the absence of defects. Thermal desorption measurements reveal an activation energy of 3 eV for Na^+ and 2 eV for neutral NaCl molecules for the desorption from NaCl crystals [157]. Investigations of an iron oxide catalyst containing 5% of potassium oxide [158] found desorption of neutral alkali atoms with activation energies in the range of 1.45 eV between 900 K and 1000 K.
In summary, the alkali atoms, especially sodium and potassium, represent a very abundant class of elements. While the bulk material exhibits a high reactivity, trace concentrations of alkali metals on surfaces are generally less reactive, with their chemistry being dominated by the alkali substrate interaction. The alkali is generally chemisorbed on the surface. A partial transfer of the valence electron towards the substrate is most prominent with metal surfaces but decreases with increasing band gaps. The binding energy correspondingly decreases. The partial charge transfer leads to the formation of a surface dipole, which allows the alkali to interact strongly with molecules having a permanent dipole moment. On dielectrics, the bond is often determined by surface defects. The typical binding energies lie within the range of 1 eV to 2 eV. Even from oxidic alkali compounds, neutral alkali atoms can be desorbed with this binding energy. Although the alkali metal partially transfers its electron to the substrate, the lowest energy desorption channel is neutral on most substrates.

5.4.2 The Pickup Process

The initial step in the proposed microscopic mechanism for the clusterelectric effect is the pickup of a neutral alkali metal atom during surface collision. In this context, the term neutral refers to the signature of equal amounts of positive and negative charges observed during the CEE of SO_2 and SF_4, which indicates that the alkali cation and the electron enter the impinging cluster in a concerted way, most likely in the form of a neutral alkali atom. Naturally, the present experiments can not provide information about the electronic state of the alkali atom at the surface, which could have a partial ionic character due to strong surface-adsorbate interaction. The proposed neutral pickup is in agreement with thermal desorption experiments [130, 158], which found it to be the lowest energy channel.
A pickup-induced clusterelectric effect implies a change in the surface density of the respective adsorbates. This is illustrated by the electron microscope picture of the collision target, that has been used in the experiments with a Cr, Fe, Ni and Mn dosed surface (see Fig. 5.8). The thick adsorbate layer on the surface, that was deposited by the burn out of the stainless steel wire, has been clearly influenced by the interaction with the cluster beam. The curved structure in the upper right corner can be attributed to the rim of the circular cluster beam. The measured diameter of 8 mm corresponds well to the expected beam diameter at the target. To the left of the rim the target has been exposed to intensive cluster impact. A most prominent feature is the grid-like structure superimposed over the picture, predominantly in the region interacting with

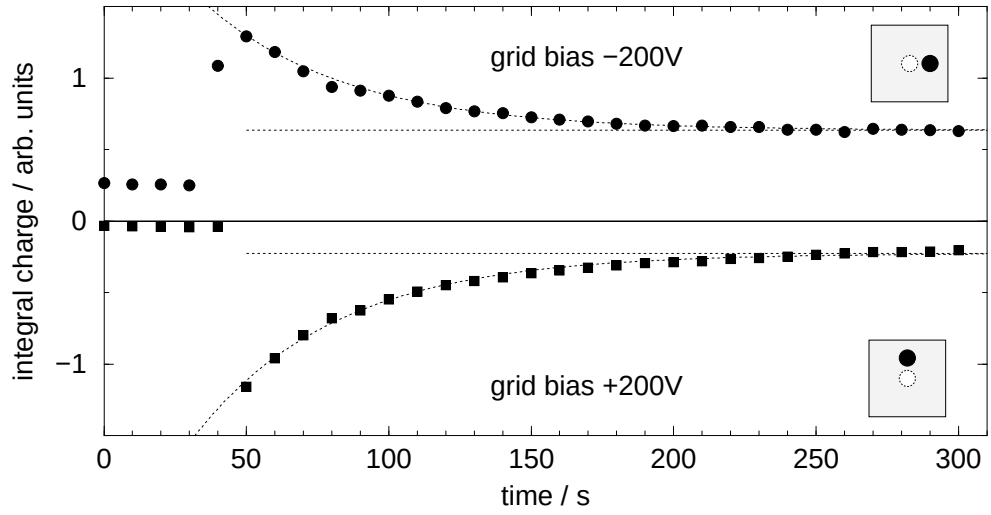

Figure 5.10: Time-dependence of the charge separation signal. The two curves represent the integral amount of charges that were collected on the target (grid bias ± 200 V) due to SF_4 clusters (impact velocity 1.32 km/s, energy per particle 1 eV, mean cluster size $\bar{N}$=75 at 30 eV electron impact ionization) impinging on a Cs dosed SiO_x surface at room temperature. The curves were sequentially measured. After 40 s, the beam location on the target was moved (see inset) by translating the latter by 5 mm perpendicularly to the beam axis. The same exponential decay is with a time constant of 0.02 s^{-1} was observed for both polarities.

the cluster beam. It corresponds to the 'shadow' of the bias grid in front of the target setup which partially blocks the incoming cluster beam and thus prevents sampling of certain target areas by the beam. The markedly different properties of these areas, as compared to areas with cluster impact, is tentatively explained in terms of the ablation process connected with the clusterelectric effect. In the shadow of the bias grid, the initially homogenous adsorbate layer is not ablated. The facile formation of these structures, which have a width of 100 μm, already points to the lithographic potential of the clusterelectric effect (see Chap. 8). A visual inspection of other alkali dosed SiO_2 targets, found a clean SiO_2 reflection in the area in contact with the cluster beam as well as areas protected from the alkali vapor as opposed to the alkali-induced milky overlayer in the other regions. That the clusterelectric effect is indeed connected to an ablation process of surface adsorbates is further illustrated in Fig. 5.10. Sulphur tetrafluoride clusters impinge on a SiO_2 surface that has been dosed with Cs atoms. The figure shows the time dependent charge signal as measured with the differential amplifier. After some ten seconds interaction time, the cluster beam is directed onto a different spot on the surface and the following signal decay is recorded. For both polarities, a similar time constant of 0.02 s^{-1} is recorded which can be explained in terms of an ablation of alkali adsorbates caused by the clusterelectric effect: In this experiment approximately 10^{11} SF_4 clusters with an average size of 10^2 impinge on the surface. Each cluster samples an area that equals approximately its cross section; i.e., $2{\cdot}10^{-18}$ m^2 in the present case. Neglecting overlap of the sampled areas within each pulse, this amounts to an sampled area A_s of $2{\cdot}10^{-7}$ m^2 for each gas pulse.

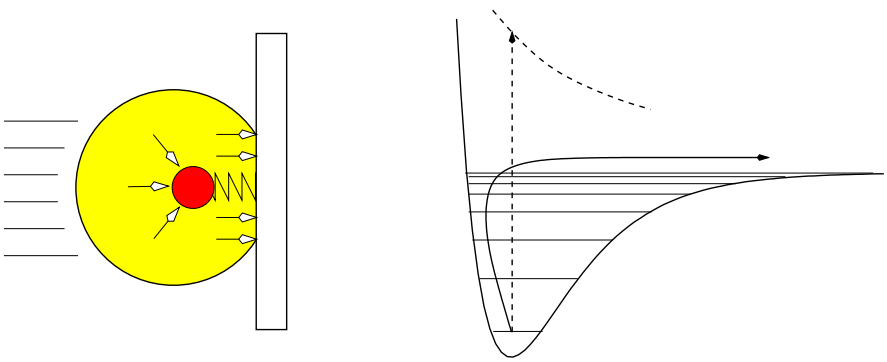

Figure 5.11: Cluster-impact induced desorption. The left panel gives a very schematic picture of the desorption mechanism. During surface contact, the impinging cluster covers the bonded adsorbate (dark sphere). Several collisions (white arrows) of cluster constituents with the adsorbate, transfer energy into the adsorbate bond. Additionally, the bond can be excited by the collisional excitation of low lying electronic surface states. The excited bond breaks and the adsorbate desorbs into the cluster. The right panel illustrates the mechanism using an energy diagram. Before the cluster impact the adsorbate is bonded in a potential well due to physisorption or chemisorption. The collisional energy transfer excites the vibrational levels of the bond until dissociation is possible. The dotted line, representing an excited dissociative state, hints at the possibility of electronic excitations with increasing impact energy.

Assuming a general efficiency β for the pick up process, the change of the number of alkali atoms per unit time within the beam cross section A_{beam} is given by

$$\frac{dN}{dt} = -\beta \frac{A_{\mathrm{s}}\,\nu}{A_{\mathrm{beam}}} + \text{diffusion}, \tag{5.1}$$

where ν is the pulse repetition rate and the term 'diffusion' accounts for diffusional changes in the surface density of the alkali adsorbates. Neglecting the latter, an exponential decay is obtained. The order of magnitude of the theoretically predicted time constant for the present conditions $(\beta\, A_{\mathrm{s}}\, \nu)/A_{\mathrm{beam}} = \beta \cdot 0.04$ coincides well with the experimentally obtained decay rate, and predicts an efficiency β in the order of several 10 percent. It lies within the previously estimated limits for the overall efficiency α of the clusterelectric effect, $10^{-3} < \alpha < 1$. In spite of the rather good agreement between observed and theoretically predicted decay rate, the time constant might be influenced by a variety of different processes. Further experiments should investigate the influence of oxidation of the alkali adsorbates, or the aggregation of a high surface coverage of alkali adsorbates into supported clusters like in [155].

Alkali Desorption

While the findings presented in Fig. 5.8 and Fig. 5.10 strongly support the pickup of an alkali metal atom during surface-collision of the cluster, they do not identify the exact nature of the Cluster-Impact-Induced Desorption process. Various mechanisms for alkali desorption from surfaces are documented in the literature. Besides the aforementioned thermal desorption process, the photoinduced (PSD) and electron impact induced (ESD) desorption of neutral alkali atoms from halide crystals [154, 159], graphite [143] and especially from thin oxidic surfaces [130, 160, 161] have been studied. In both cases, the desorption mechanism is based on a re-neutralization of

the partially charged alkali adsorbate which occurs due to the transfer of electron density to the substrate. In the case of halides, the required electron is provided by a diffusing bulk defect in the form of an F center (an electron replacing an halogen anion) that has been created upon photo- or electron irradiation [162]. Due to the low binding energy at the halide crystal surface (large band gap material), the neutral alkali atoms desorb thermally. The PSD desorption of alkali atoms from graphite (threshold photon energy 3.1 eV) [143] and Cr_2O_3 [163] is proposed to follow a resonant scattering of photo-induced, hot substrate electrons into the alkali resonance [143]. The latter is antibonding with respect to the adsorbate-substrate bond, so that the resulting repulsion between alkali atom and substrate can lead to desorption. The filling of the resonance corresponds to a vertical transition to the repulsive wall of the weakly-bound covalent state, like the ion-to-covalent transitions in alkali-halide molecules (see Fig. 5.11). Thus, it can be understood in terms of the Menzel-Gomer-Redhad model [164], with the difference, that the repulsive state is formed due to the trapping of a hot electron in an unstable repulsive state and not via the primary excitation of the adsorbate-substrate complex. The *re-neutralization mechanism* is corroborated by the fact, that photo-induced desorption ceases for high alkali coverage when the alkali adsorbates achieve a metal-like, neutral state[143]. Hot electrons also play a major role in photoinduced processes between adsorbates and metal surfaces. While the lifetime of adsorbate resonances is generally very short ($<$ 2 fs) due to the rapid electronic quenching by the metal substrate, a long-lived resonance ($\approx$11 fs, photon energy 3.1 eV) has recently been observed for the Cs/Cu(111) system [165], which led to desorption of neutral caesium [166]. Electron stimulated desorption experiments for neutral alkali atoms from thin oxidized tungsten and molybdenum surfaces [161, 167] as well as from a thin SiO_2 layer ($\approx$100 Å) [130] found threshold energies of 25 eV [161, 167]. In this case the re-neutralizing electron stems from a Auger-process induced by a $2s$ core-level ionization of the oxygen anion in the oxide layer. The Auger stabilization can lead to a positive oxygen ion as well as a neutralized alkali atom. If the oxygen ion recaptures electrons from the substrate within the lifetime of the neutral alkali atom, the repulsion due to the overlap between the valence orbitals of the O^- and the alkali atom can induce neutral desorption. This is consistent with the observed hyperthermal velocities of the alkali atoms (0.1-0.5 eV) which decrease from Cs to Li [167] due to the decreasing difference between ionic and atomic radius. The strongly reduced desorption of neutral alkali atoms from silicided tungsten [167] indicates that the high energetic Si Auger electrons ($\approx$90 eV) are to energetic for the effective alkali re-neutralization. Experiments using PSD as well as ESD techniques [160] with thick SiO_2 films ($\approx$ 10 nm) found a considerable lower energy threshold in the order of 4 eV for desorption of neutral sodium atoms. The threshold is explained in terms of re-neutralization through electronic excitations from SiO_2 surface states (presumed to be formed by the trapping of the Na valence electron upon adsorption) or, from SiO_2 defect states.

Desorption Mechanism

To account for the observed indifference of the CEE with respect to the electronic structure of the target material, a general pickup mechanism which must not draw on specific substrate properties has to be developed. It has to be able to desorb neutral species from the surface, over a wide range of binding energies that range from a few tenth of an eV to more than 2 eV. In this respect it is an advantage that the con-

stituents of the cluster are particles with masses comparable to the adsorbate mass. This also allows for direct impulsive energy transfer during collisions, while photons and electrons under typical conditions can only deposit their energy in the form of electronic excitations, which can be very high in energy. The 25 eV threshold for electron-induced desorption for the alkali/SiO_2 system, which has a binding energy around 2 eV, illustrates this. The direct impulsive excitation, on the other hand, can induce desorption along the minimum energy reaction coordinate, much like the thermal processes.

Two possible microscopic mechanisms that would lead to the desorption of neutral alkali atoms during the cluster-surface collision are schematically depicted in the left panel of Fig. 5.11. It depicts the cluster (grey sphere) at the moment of surface impact. The cluster interacts with the surface as well as with adsorbates (small dark sphere) residing on the impact area by means of collisions of cluster constituents (white arrows). Energy is transferred into the surface. It has already been demonstrated [168] that low-velocity impact ($v \approx 1600$ m/s) of molecular clusters built from CCl_4, CH_3CN or benzene on metal surfaces can lead to electron emission ('exo-electrons'), which has been explained in terms of a localized heating of the first few substrate surface layers. With respect to the CEE, the situation is even more favorable. The excitation of the surface electrons during impact does not have to reach the vacuum level. Desorption can already take place when excited charge carriers re-neutralize adsorbed alkali atoms similar to the photon-stimulated desorption of alkali from graphite [143]. This mechanism can be generalized to non-metals, where instead of a free-electron gas, defect states and surface states are which have been populated by the partial electron transfer following alkali adsorption, are excited. In the case of polar molecule clusters required for the CEE, the interaction of the impinging cluster with the electronic surface states can be enhanced by the dipole field of its constituents; e.g, in the form of Stark level shifting (see *Adsorbate Interaction* in Chap. 5.4.1).

Moreover, there are direct collisions between the adsorbate and the cluster constituents during cluster-surface impact. For example, there are in the order of 10 such collisions in a cluster of size 1000, as estimated from the column-density above the adsorbate. Moreover, since alkali adsorbates often form a surface dipole, the interaction between the adsorbate and the polar cluster constituents as mediated via the Coulomb fields, has an increased cross section when compared to the situation for two nonpolar collision partners. These collisions can transfer energy directly to the adsorbate and vibrationally excite the adsorbate-surface bond in this way. This is schematically illustrated in the right panel of Fig. 5.11. The adsorbate-surface bond is approximated by a Morse potential, neglecting all specific substrate details like physisorbed precursor states. Its vibrational population depends on the surface temperature. During cluster-impact, the adsorbate is exposed to a series of collisions. The impulsive energy transfer can excite vibrational quanta of the adsorbate-surface bond: by climbing the vibrational ladder the adsorbate bond is excited to such a level, that it eventually breaks and the adsorbate desorbs into the cluster. This mechanism resembles the way a basket ball lying on the ground is picked up by patting it a few times. However, while for the latter the exact timing of the perturbation ensures that energy flows only to the basket ball, the time sequence of collisions inside the

cluster is presumably random. Thus, there also exist collisions which de-excite the adsorbate-surface bond. The energy flow into the adsorbate bond, therefore has the character of a diffusional process. While the energy flow into intramolecular degrees of freedom has received considerable theoretical treatment for systems incorporated into clusters heated by high-energy surface collisions [21, 15, 13], the activation of weak adsorbate-surface bonds during low-velocity cluster impact, has to date not been comprehensively researched[1]. In the case of large energy transfer, or preceding thermal excitement of the bond, a single collision may already suffice to induce dissociation. The elastic energy transfer per collision can be estimated from kinematic considerations: for the central collision of two masses m_1 and m_2 with the latter initially at rest, the energy transfer is governed by the ratio of the masses

$$\frac{\Delta E}{E_o} = \frac{4\, m_1 \,/\, m_2}{(1 + m_1 \,/\, m_2)^2}. \tag{5.2}$$

In the present experiments the initial energy per particle has been in the range of 0.25 eV (ammonia) to 1 eV (sulphur tetrafluoride) and the mass ratio m_1/m_2 varied between 0.13 for the system ammonia/caesium, to 0.81 for the system sulphur tetrafluoride/caesium and 15.4 for the system sulphur tetrafluoride / lithium. For a given cluster constituent, the ratio of the energy transfer to a CEE inducing adsorbate like Li, Na, K and Cs is given by 0.82, 0.98, 0.85 and 0.4 for ammonia, by 0.36, 0.77, 0.94 and 0.87 for sulphur dioxide and finally by 0.23, 0.58, 0.78 and 0.99 for sulphur tetrafluoride. Thus, the energy transfer is generally high, save for the most disparate pairs. Although the model of central collisions is a strong idealization with respect to the real collision processes, the obtained energy transfer ratio nevertheless also governs the flow of energy under realistic conditions. An important caveat with respect to the basket ball pickup is given in terms of the separation of time scales. Excitation of the adsorbate-surface bond can only proceed efficiently during cluster-surface collision if its strength is such, that the perturbation presented by the collisions with the cluster constituents are faster or on the same time scale as the characteristic surface-adsorbate vibration. This is generally the case for binding strengths up to 1 eV, which are comparable with the intermolecular bond within the impacting cluster. Thus, while the pickup by vibrational bond excitation is independent of the surface, it seems to be applicable only to the more weakly bound species. For the more tightly bound species, a not a yet specified mechanism, maybe connected to the electric dipole field of the impacting cluster constituents, might lead to a kind of 'bond-softening', followed by vibrational bond excitation and desorption.

Cluster-Induced Desorption

The mechanisms for cluster-induced desorption developed above seem to be unrelated to a specific cluster property. Adsorbate desorption, as induced by re-neutralization or vibrational excitation of the adsorbate-surface bond, is also in principle possible via the impact of a single, higher-energetic particle. In fact, surface sputtering is a standard surface analysis method. However, during sputtering of the surface with single particles, surface adsorbates are transferred into the gas-phase as individual particles, while the cluster-induced desorption goes hand in hand with incorporation

[1] A deeper insight into surface-pickup processes would have broad application in areas apart from the CEE, e.g., concerning the fragmentationless transfer of large molecules into the gas phase by means of cluster-surface collisions.

of the adsorbate into the cluster, where it can get solvated and cooled or even react. Moreover, in the case of large molecules it should be of advantage that the energy supply is not point-like, but extended over the whole cluster cross-section. This simultaneity of surface-desorption and cluster incorporation makes this form of pickup useful for such things as the incorporation of a reaction partner into a cluster at a given time during a CIMS experiment.

5.4.3 Charge Delocalization

Within the proposed model for the CEE, the surface pickup of an easy-to-ionize adsorbate is followed by its instantaneous ionization within the polar molecule cluster. This results in the formation of a geminate ion pair. The nature of the ionization mechanism will be discussed in more detail in Chap. 6. To become separated during impact induced cluster fragmentation, the ion pair has to separate whilst inside the cluster, since neighboring cluster constituents are likely to end up in the same cluster fragment. In this case, the cation/anion pair would shield each other, and consequently would not be detected. The respective migration process of the charge carriers inside the cluster is discussed here.

Cation Mobility

The CEE leads to the formation of a geminate ion pair consisting of a metal cation and a quasi-free electron. In this context, the adsorbates can be considered as potential electrolytes which form ions due to the interaction with the polar solvent. This allows for the application of much of the established knowledge concerning ideally diluted electrolytes. The spatial separation of the geminate ion pair can be considered as a diffusion process of two interacting particles, driven by the thermal movement of the solvent and hindered by their mutual attraction. Neglecting the latter, an order of magnitude estimate for the cation movement can be obtained from the diffusion coefficient of the respective ions at infinite dilution in aqueous solution (see Tab. 5.1). Via the Einstein-Smoluchowski equation $D = d^2/(2\tau)$, the diffusion coefficient D can be correlated to a characteristic jump time τ using a typical jump length d that equals the intermolecula distance. For the alkali cations it is in the order of some ten picoseconds (Na^+: τ=33 ps). Even if one takes into account an increased diffusion coefficient due to an elevated 'temperature' in the impact heated front of the colliding cluster, a diffusion of the metal cations within the cluster, on the picosecond time scale of cluster impact, seems improbable. This corroborates the observation, that dissolution of salts, namely NaCl, does not take place on the time scale of cluster impact. Even if the cluster-induced desorption process incorporated NaCl entities into the cluster, they would not separate fast enough within the cluster to become disjunct during cluster fragmentation. Only if salt molecules had been introduced into the cluster (e.g., by means of gas phase pick up) sufficiently early prior to cluster fragmentation, should cluster fragments carrying the respective salt ions should become observable.

Proton Mobility

A comparison of the diffusion coefficient for solvated ions like Na^+ and Cl^- with the hydrated excess proton in water (see Tab. 5.1) reveals a remarkably high mobility of the latter, which can be rationalized by the Grotthuss mechanism [170] of structural diffusion. In this model, the proton diffuses not via hydrodynamic Stokes diffusion of a rigid complex, but via migration of a structural defect due to a continual inter-

Ion	D in 10^{-5} cm^{2}s^{-1}	Ion	D in 10^{-5} cm^{2}s^{-1}	Ion	D in 10^{-5} cm^{2}s^{-1}
H^+	9.311	Na^+	1.334	Cs^+	2.056
Li^+	1.029	K^+	1.957	Cl^-	2.032

Table 5.1: Diffusion coefficients D for various ions at infinite dilution in aqueous solution at 25^{o}C [169]. Compared to the ions given, the proton features a considerable higher mobility.

conversion between covalent and hydrogen bonds. The proton randomly hops from molecule to molecule propelled by the hydrogen cleavage in front of it and the bond formation behind it. Recent ab initio calculations [171] stress the quantum nature of the proton which represents a delocalized defect in the hydrogen-bonded network of water molecules. Since the Grotthuss mechanism involves re-orientations of the water structure, it exhibits a temperature dependence and it was found to cease below 190 K [172]. In an impact-heated cluster, however, the proton should exhibit sufficient mobility that a proton transfer reaction within the cluster leads to charged cluster fragments. This allows this large class of reactions to be investigated with the CIMS method. Besides water, other protonic solvents like ammonia could provide a reference time scale.

Electron Mobility

The ionization process of the picked up adsorbate yields a quasi-free electron as counterpart to the metal cation. The interaction of electrons with polar solvents has been studied in great detail [173, 174, 175, 176, 177, 178]. On long time scales, the electron may finally be stabilized as a molecular anion, or, in the absence of a molecular electron affinity, it may be captured in a potential well formed by neighboring molecules of the liquid. In clusters of finite size, often a minimum number of solvent molecules is necessary to form such an electron trap. Experiments have found N_{min} to be 2 for H_2O, D_2O, HCl and $C_2H_4(OH)_2$ whereas for NH_3 an unexpected high N_{min} of 35 has been observed [179, 180, 181]. For ammonia a strong yet unexplained isotope effect has also been observer with N_{min} being 41 for ND_3. Theoretical treatments [182] exploring the nature of the excess charge distribution based on quantum path integral simulations, found that water cluster anions smaller than N=32 are surface bound whereas those larger than N=64 are volume bound, explaining the deviations observed for small water cluster anions. Small ammonia cluster anions do not support stable electronic surface states. This explains the late onset of stable ammonia cluster anions, as internally bound states exist only for n>30. In an initial step, a fast electron injected into a molecular cluster is thermalized by means of inelastic collisions with solvent molecules until its kinetic energy is brought to the average of the environment. For liquid water this step takes about 20 fs. In the absence of a molecular affinity, the electron localizes in a preexisting trap on a time scale of $\approx$200 fs [177], where it forms a 'wet electron' which can be considered as an excited state of the solvated electron [177]. In this two-state model, the wet-to-solvated electron transition proceeds via an internal conversion [183] and is connected to librations or translations of the surrounding water molecules [173, 177, 175, 176] on a time scale of between 200 fs and 1 ps. The high mobility of the quasi-free electron inside the liquid is illustrated by the small recombination of electron-cation pairs observed following photo-excitation of neat water, which indicates, that the two species

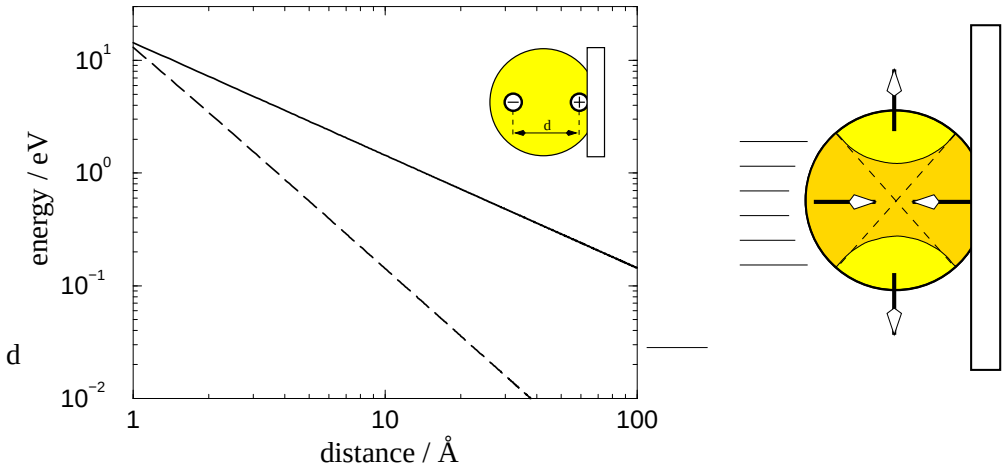

Figure 5.12: Left panel: Coulomb attraction of the ion pair at distance d without dielectric shielding (full line). The dotted line gives the energy required to further increase the distance by 1 Å. Right panel: Schematic picture of the fragmentation process of larger clusters, induced by cluster-surface collision. The cluster is compressed as its back part is still moving on whereas its front has already been reflected. Sideways movement of cluster material is the consequence which leads to impulsive fragmentation.

separate from each other [173]. In the case of electron stabilization via the formation of a molecular anion, resonant charge exchange can occur, as has been observed for cations in He clusters [184] with a diffusional time constant on the picosecond time scale. There is a fundamental difference in the solvation of the electron and an ion. The high mobility of the quasi-free electron allows it to sample the liquid for preeexisting traps in which it settles and relaxes to the ground state of a solvated electron. Here, the solvation process is only connected to small solvent rearrangements. The slower resonant charge transfer between anions, will not always settle for the optimum site so that its solvation is connected to larger rearrangements in the local solvent structure. However, in both cases, the electron has sufficient mobility to separate from its cation by diffusion through the cluster even in the short time scale of cluster impact. In a completely cooled down cluster the charge is no longer mobile. To leave its location it would have to provide the polarization energy, which could be as high as 1 eV, while hopping to another place. The localization sets the vibrational as well as polarization energy free. Localization typically takes place on a time scale of a picosecond.

Ion-Pair Interaction

So far, the separation between the electron and the cation has been treated as a diffusional process neglecting the mutual attraction which counteracts the separation. In Fig. 5.12, the Coulomb attraction for a geminate ion pair as a function of separation distance, is plotted without the influence of dielectric shielding. To take the latter into account, only the electronic part of the respective substance should be used, since the presence of multiple solvation centers combined with the finite cluster size hinders the optimal orientation of the molecular dipoles of the cluster constituents (see Chap. 3). Additionally, under the cluster impact conditions, the energy introduced into the cluster should destroy ordered solvent structures. As can be seen, the mutual attraction at a typical intermolecular distance of 3 Å is still in the order of some

eV. The dashed line gives the energy necessary to further increase the separation of the ion pair by one Å. Diffusional processes can be the driving force for separation within the cluster, if the energy required for each jump, is smaller than the available thermal energy. This is only the case for distances of several Å. This implies that the ionization process itself should include a non-negligible initial charge separation, which can increase further by diffusion.

5.4.4 Cluster Fragmentation and Inertial Charge Separation

The collision induced fragmentation of molecular clusters presents the essential step in Cluster Impact Mass Spectrometry that transfers the contents of the 'test tube', in the form of individual particles or small cluster fragments, into the gas phase, whereupon they are straightforwardly and unambiguously mass analyzed. As part of the Clusterelectric Effect, it serves to separate the geminate ion pair created inside the impacting cluster and thus reveals the exact nature of the charge transfer process induced by the interaction of a picked up surface adsorbate and the cluster constituents as solvent.
Several theoretical [16, 185, 186] as well as experimental [187, 188, 189] investigations of cluster-surface collisions exist in the literature. In an idealized picture, the front of the cluster is reflected upon impact and starts interacting with its back part which is still approaching the surface. The ensuing collisions between the cluster constituents drive the transfer of the kinetic energy contained in the center-of-mass movement of the cluster into internal degrees of freedom. For normal incidence, a zero order estimate for the duration of the cluster-surface collision is given by the advection time, i.e. the ratio of cluster diameter and impact velocity [190]. As pointed out in Chap. 1, the resulting time scale is a crucial determinate for into which internal degrees of freedom the injected energy flows. Numerical simulations [191] of the impact of a mixed Ar / Ne cluster of size N=111 on a rigid surface with an impact velocity between 100 m/s and 700 m/s – corresponding to impact energies per monomer between 0.05 and 1.6 times the binding energy per monomer – find an overall efficiency for this transfer between 0.8 and 0.95. Although energy transfer into the surface has been neglected in this model, the 'thermalization' of the originally directed energy by the cluster-surface collision is remarkably high. The main reason for this behavior has been identified [17] to be the random orientation of the interatomic distances in a molecular cluster. The two limiting cases for the fate of such an impact-heated cluster are obvious: at very low impact velocities, the clusters recoils 'hot' but essentially intact, stabilizing itself by evaporation of monomers on longer time scales. Very high impact velocities, on the other hand, lead intuitively to complete disintegration of the cluster. For example, a theoretical simulation of argon clusters (N=111, binding energy 0.065 eV/atom) impacting on a flat model surface [187] found almost intact rebounding of the cluster at a translational energy of 0.025 eV, strong monomer evaporation combined with a surviving cluster core between 0.05 and 0.1 eV and almost complete destruction of the cluster at 0.5 eV. The major parameter that governs the outcome of cluster-surface collisions is the ratio of total impact energy and total cluster binding energy. In addition to this, there is the monomer evaporation rate. The thermalization process allows for a temperature to be

assigned to the impact heated cluster, which, with the binding energy per monomer as parameter, governs the stabilization of the cluster according to Eq. (2.17). While for a given cluster size the evaporation rate depends only on the total amount of absorbed energy, an increase of impact velocity does not only increase the amount of injected energy but at the same time also the rate of energy transfer. With decreasing impact duration, monomer evaporation becomes less and less efficient.

Shattering In the regime of high-energy cluster-surface collisions, characterized by a ratio of impact energy to total binding energy well above unity, a new 'stabilization' mechanism in terms of complete, instantaneous fragmentation of the impact heated cluster takes over from evaporative cooling. This has recently been experimentally and theoretically described [192, 189, 193, 194]. A very sharp transition between the two regimes has been discovered and explained in terms of a competition between two entropic effects. The large entropy related to the many possible configurations of a large cluster, stabilizes energy in the intact cluster. It accommodates the additional energy provided by the surface collision by isomerization to configurations with fewer intermolecular bonds. On the other hand, the entropy connected to the translational motion of individual particles favors the disintegration of the cluster. Each contribution is exponentially large, so that at the point where the two effects are balanced, small changes in the collision parameters can result in large variations of the probabilities of the two outcomes [15]. Only when the absorbed energy would be sufficient to evaporate a substantial amount of monomers in a concerted manner, namely when it surmounts considerably the total intermolecular binding energy, does the translational entropy win and shattering occurs [193]. Moreover, the high-energy impact of an Ar_{561} cluster on a sodium chloride surface at a velocity of 3000 m/s [16] was found to develop a internal shock wave which formed a transient medium with extreme density, pressure and temperature within the cluster. The formation of such a shock wave has been studied for Kr clusters scattered from a Pt surface at total incident energies between 10-10^6 eV [185, 19]. In this context of high-energy collisions the surface itself can no longer be considered to be an idealized means to inject energy into the cluster since it actively takes in the processes. Cluster impact can lead to substantial surface damage [16] or surface reactions; e.g., the hyperthermal impact of alkali fluoride clusters on silicon led to the formation of surface fluoride species [195].

Rebound At very low impact energies, the cluster rebounds almost intact but hot. Even if there is no substantial evaporation during the picosecond time scale of the collision, the cluster stabilizes itself during the microsecond timescale of the detection process, whereupon it decreases considerably in size. After scattering, the size of the remaining cluster is found to increase with initial size and with surface temperature, while it decreases with incident velocity [196, 197]. For large impact angles with respect to the surface normal, the cluster was found to slide along the surface for tens of nanometers [197]. During the gliding motion the cluster is further heated by energy transfer from the surface and it starts to decompose by monomer evaporation. When the cluster reaches a certain temperature, $\approx$950 K for water clusters [198], extensive fragmentation (see Eq. (2.17)) forces the remaining large cluster to leave the surface. The dynamics of cluster-surface scattering in the energy regime between intact rebound and shattering has been described in terms of a dynamic zone structure model

	SO_2	SF_4	NH_3	H_2O	Ar
T_b / K	236.1	232.7	239.8	373.2	87.29
$\Delta H_{vap}(T_b)$ / eV	0.258	0.274	0.242	0.421	0.0666
E_{coll} / eV	0.56	0.95	0.15	0.16	0.35

Table 5.2: Comparison of the binding energy per monomer and the collision energy per monomer. Collection of the standard boiling point T_b, the enthalpy of evaporation at the boiling point and the collision energy per particle of a cluster impacting on a surface with a velocity of 1.3 km/s, which is typical for seeded beam expansions.

[190]. The first zone comprises the cluster constituents with surface contact which undergo thermal equilibration at the surface. They may experience a repeated trapping/desorption process before they recollide with the cluster and participate in slowing it down via momentum transfer. A second zone is defined by particles that get compressed between the surface-bound layer and the approaching constituents from above. This zone heats up to T_{eff} and starts evaporating monomers. The achievable temperature depends on cluster stability and varies between 140 K for Ar clusters [190], 600 K for ethanol clusters [199], between 300 K and 600 K for ammonia [200] and 950 K for H_2O clusters [198] as obtained from the angular distribution of the evaporated monomers. The evaporation takes place in thermal equilibrium with the intermolecular degrees of freedom of the cluster. When all normal kinetic energy has been dissipated into evaporation, there might still be a fraction of the incident cluster left -zone 3- which has been slowed down to zero normal velocity before it reaches the surface. While it leaves the surface with only a small amount of momentum in the normal direction, the tangential velocity component has not been changed, so that it is scattered in near grazing direction [201, 202, 191]. In general, the process resembles the Leidenfrost phenomenon, according to which the rate of vaporization of a liquid droplet on a sufficiently hot plate is efficiently reduced by the formation of an isolating vapor layer. However, in the case of cluster-surface collisions, the energy for the evaporation of the constituents stems from the normal component of the kinetic energy of the incident cluster [190]. Within this model, the size of the remaining core cluster can be estimated from an energy balance between the injected energy and the energy dissipated by monomer evaporation. For an idealized flat, rigid surface with zero trapping probability one obtains [190]:

$$n = \frac{N[\,3\,k_B\,T_{\text{eff}} + 2E_a - (1 - c_{nt})\,m\,v_0^2\,\cos^2\Theta]}{2E_a}, \tag{5.3}$$

where $3\,k_B\,T_{\text{eff}}$ stands for the energy stored in the excited internal degrees of freedom of the cluster, E_a for the energy necessary to remove one constituent, m for the constituent mass, N for the size of the impinging cluster, Θ for the incidence angle of the cluster, v_0 for the initial cluster velocity and n for the size of the surviving cluster relic. Additionally, c_{nt} has been introduced to account for the coupling of normal to tangential kinetic energy within the compressed cluster (see Fig. 5.12).

Cluster Fragmentation

With the help of Tab. 5.2, the present experiments can be discussed with respect to shattering or rebounding dynamics. It presents the impact energies per cluster constituent for several of the investigated systems under typical experimental conditions,

which are also representative of CIMS in general. Additionally it provides the enthalpy of evaporation. While there is considerable difference between the binding energy of the monomer and the enthalpy of evaporation for bulk substances due to the reduced number of neighbors for surface constituents, the binding energy per monomer of small to intermediate clusters is very well approximated by the enthalpy of vaporization, since a considerable fraction of the constituents resides at the strongly curved surface. It becomes evident, that only the heavy systems like SO_2 or SF_4 accumulate sufficient energy in the seeded expansion to reach the onset of the shattering regime. The same is true for Ar, in this case due to its weak intermolecular binding. For these three cases sufficient energy is provided, even taking into account the energy transfer to the surface, to completely destroy the cluster. For ammonia the impact energy corresponds to 60 % of the binding energy per monomer and for the hydrogen-bonded water only 40 % are provided by the impact energy. The dynamic zone model from Eq. (5.3) can be applied to ammonia and water under normal incidence impact using the parameters c_{nt}=0.35 [190], $\mathrm{E}_a=\Delta H_{\mathrm{vap}}(T_b)$, $T_{\mathrm{vib}}(\mathrm{H_2O})$=950 K [198], $T_{\mathrm{vib}}(\mathrm{NH_3})$=600 K [200]. It predicts no evaporation of the water clusters during the surface collision and around 10 % evaporation for the ammonia clusters. Since both molecules are relatively light-weight, the seeded beam technique can accelerate them to impact velocities in the range of 1700 m/s. In this case the above model predicts 10% instantaneous evaporation for the water clusters and 40 % for ammonia. Even though the latter two system only marginally disintegrate during surface-impact, there is considerable evaporation on the microsecond time scale of detection. To cool down from 950 K to 300 K — the evaporation rate at this temperature corresponds with 10^6 to the inverse detection time scale (Eq. (2.17))— a water cluster has to evaporate an additional 20 % of its constituents. The prediction of the dynamic zone model that the tightly bound, light-weight ammonia and water systems disintegrate only moderately during surface-collision whereupon they stabilize via monomer evaporation, seems to be inconsistent with the observed charge separation in the context of the CEE. Since neutral monomers are generally more weakly bound than the incorporated ion, evaporation would always proceed via the neutral channel. The geminate ion pair would not get separated and would elude detection due to its mutual shielding[2]. However, the above model does not take into account the highly asymmetric perturbation introduced into the cluster by surface impact. With the front of the cluster rebounding from the surface and the back part of it still approaching the target, the only direction of relief for the compressed interior of the cluster is sideways. This situation is depicted schematically in the right panel of Fig. 5.12. During impact, the cluster thus forms an oblate overstructure on the target which can spontaneously segregate into several substructures following the rupture of relatively few bonds. This cleaving would be highly unlikely for more spherically shaped clusters as is obvious from the analogy of macroscopic liquid drop models. This ‘fragmentation’ has indeed been observed in theoretical

[2] As will be discussed in Chapter 7, the delocalized electron detaches easily from the impact heated ammonia and water clusters due to their lack of a molecular electron affinity. In this case the positive cations are observable even without cluster fragmentation. However, by doping the ammonia clusters with an electron scavenger (Chap. 7), the electron is stabilized within the cluster. The above discussion pertains to this case.

simulations [203] of water cluster surface-collisions starting from velocities of 1300 m/s. The transition from pure evaporation to fragmentation during surface impact has also been described for the mixed clusters of Ar / Ne [191] starting from impact energies of 80% of the monomer binding energies.

In the present experiments, the disintegration dynamics of the impacting cluster lies between the regime dominated by intact rebound followed by monomer evaporation on the one hand, and the complete shattering of the cluster on the other hand. This is consistent with the overall structure of the observed mass spectra for the scattered charge carriers. They reveal cluster fragment ions of intermediate size amounting to roughly 10 % of the size of the impinging clusters. For systems that already reach into the shattering regime, these structures can be explained in terms of an enhanced binding energy between cluster constituents and the incorporated ion. Even when the shattering for the neutral interaction strength is reached, the ion cores retain their stronger bound environment. Since the size of the observed 'solvation' shell should correlate to the solvation energy of the respective core ions, this opens up an interesting field for future work, namely the interpretation of the variation of the solvent shell size in terms of solvation energy data available from equilibrium measurements from high pressure mass spectrometers [204]. Due to the deformation during surface contact, systems closer to the evaporative regime fragment into several entities, which subsequently stabilize by monomer evaporation. With respect to the CIMS method, the selection of the solvent molecule as well as of the impact energy allows for the variation the cluster fragmentation dynamic between these two prototype behaviors. When robust charge transfer reactions are investigated often deformation-induced fragmentation followed by evaporative stabilization is already sufficient. In the case of investigations concerning the dynamics of a process, the instantaneous disintegration of the cluster upon surface collision is necessary and thus, higher impact energies or weaker bound solvent clusters are required. In this context it should be noted, that by seeding water in hydrogen instead of helium, the direct disintegration of water clusters should be possible.

Inertial Charge Separation

So far, collision-induced cluster fragmentation has been described as a means to spill out the contents of the molecular 'test tube' for mass spectrometric investigation. With respect to charged reaction products of the CEE, a further aspect becomes important. The separation of a mutually attracting geminate ion pair requires additional energy as opposed to neutral products. The left panel of Fig. 5.12 gives the unshielded Coulomb interaction energy of a geminate ion pair for various separations inside the cluster. They typically amount to energies around one eV. Due to cluster fragmentation, the dipole chains that shield the Coulomb interaction inside the cluster get ruptured and surface charges are formed on the entities surrounding the core ions, so that the total Coulomb interaction between the cluster fragments carrying the ions corresponds to the unshielded value. However, by increasing their mutual distance within the cluster, the total Coulomb energy is strongly decreased as opposed to the time of charge pair generation. While temporal charge transfer in gas-phase collision pairs can often be inferred only indirectly (e.g. via the scattering behavior of the collision partners [18]), since there is not enough energy available to separate the charged products, this is different in the case of CIMS measurements. Although the kinetic energy per particle, especially after the surface collision, is also gener-

ally lower than the necessary amount, charge separation can be achieved by energy pooling between the cluster constituents surrounding the core ions. It is the inertial movement of the cluster fragments (Inertial Charge Separation), that provides the necessary energy. Assuming a Coulomb interaction of 1 eV and the above impact conditions for a SO_2 cluster especially with respect to the efficiency of 0.35 for the conversion of normal translational energy into tangential one, a fragment consisting of three SO_2 molecules could already separate the geminate ion pair.

Chapter 6

Fast Electron Transfer Mechanism

The key to the observed charge separation is the pickup of an alkali atom during the cluster-surface collision. This chapter focuses on the mechanism that subsequently delocalizes the alkali valence electron within the molecular cluster, which is the essential step to allow for charge separation during the impact-induced cluster fragmentation. As will become evident from a survey on previous investigations of solvated metal atoms, the delocalization of alkali valence electrons in polar solvents is a known effect which confirms this aspect of the proposed CEE mechanism. However, while previous equilibrium studies show that the formation of a cation/anion pair is energetically favorable, it is hardly possible that solvent rearrangements can establish this equilibrium under cluster-impact conditions. To reconcile the observed charge separation with the limited time window given by the advection time of the cluster, a new, fast electron transfer mechanism is proposed which is based on field-induced charge transfer.

6.1 Electron Delocalization in Bulk Polar Solvents

Liquid Ammonia

As early as 1863 a blue discoloring was observed upon dissolution of elemental alkali metals in liquid ammonia [124]. This was explained in terms of spontaneous ionization of the alkali atom inside the solvent which leads to the formation of a solvated cation and a quasi-free electron. Since ammonia does not exhibit a molecular electron affinity, the electron is stabilized in a solvent cavity with a radius of 300-340 pm which is formed by rearrangements in the solvent [178]. The electron and the cation are screened individually by the surrounding dielectric medium. The Coulomb energy of the ionization process is compensated by the reorganization of polar solvent molecules around the two-center charge distribution. The spectroscopic properties of such a solution are governed by the interaction of the electron with the solvent molecules and are almost independent of the alkali cation [205, 178]. Its broad absorption spectrum has a maximum at $\approx$1500 nm and extends into the visible, which results in the observed blue color. The cavity model for electron stabilization is consistent with the observed decrease in solution density compared to pure liquid ammonia. Solutions of alkali metals in ammonia are strong reducing agents. They can induce hydrogen atom abstraction in protonic compounds. The alkali/ammonia so-

lutions are generally unstable on a time scale of hours; e.g., with respect to imide formation: $M+NH_3 \rightarrow MNH_2 + \frac{1}{2}H_2$. Spontaneous ionization and the formation of solvated electrons in liquid ammonia has also been observed for the heavy group II elements Ca, Sr, and Ba as well as the lanthanides europium and ytterbium [124]. They all share a low metal lattice energy, a low ionization potential as well as a high solvation energy.

Other Solvents

Alkali metal dissolution with concomitant formation of free electrons has also been observed for aliphatic amine and in hexamethylphosphortriamid $P(NMe_2)_3$. Furthermore, heavy alkalis like K, Rb and Cs also solvate with spontaneous ionization in tetrahydrofuran (molecular dipole moment: 1.63 debye), ethylenglycoldimethylether and other polyethers [124]. Like ammonia, they do not exhibit a molecular electron affinity, so that ionization is accompanied by the formation of solvated electrons. While the characteristic discoloring associated with the solvated electrons indicates a successful charge separation inside the solvent and has focused much interest on the phenomenon, the driving force behind the ionization process as such are the dielectric properties of the solvent. The solvation process of ions via the re-orientation of dipolar solvent molecules or the polarization of surrounding solvent molecules makes the presence of a cation/electron pair more energetically favorable than a neutral atom incorporated into the solvent. Based on this, solvent induced ionization should be a very general phenomenon, even in systems where the formation of solvated electrons is not observed. The CEE measurements performed using sulphur dioxide clusters are an illustration of this. Here, the stabilization of the electron is achieved via the molecular electron affinity of SO_2. The interaction of alkali atoms with liquid water [206, 207, 208], which will be treated in more detail in Chap. 7, is another example. While the spontaneous ionization of the sodium atom seems to be the fundamental step, much like the case of ammonia, a chemical reaction is initiated in the presence of several alkali atoms leading to the well-known hydroxyd formation. Thus, there is another class of solvents, in which the spontaneous ionization is disguised by chemical reactions.

6.2 Solvated Metal Atoms - Observations in Clusters

Alkali Metals

Experimental and theoretical studies of the solvation of alkali metal atoms in polar solvents have been performed with regards to their size-dependent spectroscopic properties, especially their photoionization threshold (IP), in a variety of clusters including water, ammonia and acetonitrile [209]. For example, the IPs of clusters having the composition $Me(H_2O)_n$ with Me=Li [210, 211], Na [212, 213, 208] and Cs [214] as well as $Me(NH_3)_n$ with Me=Li [210, 215], Na [208, 216, 217] and Cs [214] have been investigated by photoionization mass spectrometry (see Fig. 6.1). The compounds have been formed by means of adiabatic expansion of the solvents combined with either a pickup oven-source or with a laser-ablation source for the metal atoms. In the water system, the IP was found to decrease rapidly with the addition of up to four water molecules to the metal atom, beyond which the IP forms a plateau for larger cluster sizes. The value of the latter compares well with the bulk value extrapolation of the vertical detachment energies (VDE) of $(H_2O)_n^-$ of 3.3 eV [218]. In

the case of ammonia as solvent, the IPs have been found to decrease monotonically with increasing cluster size in the observed size window. Again, the extrapolated bulk limit also coincides very well with the VDE limit of 1.45 eV [117] for $(NH_3)_n^-$. For both systems, the results have been found to depend on the chosen alkali atom only for the first few solvation steps, while for larger aggregates with $n \geq 4$, the size dependent IPs for the different alkali atoms converge to a common function which is characteristic for the solvent only. This behavior is interpreted in terms of the formation of an ion-pair state [219] consisting of a solvated alkali cation and a solvated electron which is not strongly dependent on its counter ion. The energy for charge separation, which in the gas phase is approximately 5 eV, has to be provided by the interaction of the solvent molecules with the metal atom and the formation of solvation shells. The difference between ammonia and water as solvents is attributed to the existence of surface states in the case of water, which are already available at small cluster sizes [220], whereas ammonia only forms internal bound states for the solvated electron [5]. The proposed electron transfer from alkali atom to the solvent has been supported by theoretical calculations [221, 222, 219].

Besides ammonia and water, acetonitrile has been investigated as a solvent for Li, Na [225] and Cs [214]. Acetonitrile has a dipole moment of 3.92 debye, which is much larger than that of ammonia and water and has been found to be able to directly stabilize an electron in a dipole bound state [226]. For Cs, a lower IP for compounds with 2 and 3 solvent molecules compared to solvent clusters with n from 4 to 6 has been found [214]. The IP then reaches a plateau for more than 12 solvent molecules at a value of 2.4 eV (see Fig. 6.1). The minimum of the IP has also been observed for the sodium and lithium system for three solvent molecules from where the IP increases and reaches a plateau of ≈3.1 eV and ≈3.5 eV respectively, for six to eight solvent molecules. While the behavior of the IP in small aggregates is proposed to be influenced by the strong dipole interactions of the solvent constituents and its influence on the solvent shell, the general decrease is tentatively explained in terms of an electron transfer to the solvent with the stabilization of the electron by the molecular dipole moment [225].

Group III Metals

A recent set of papers [227, 228, 224] investigated the group III metals Al, Ga, and In embedded in clusters of ammonia. The complexes have been created by laser ablation of a metal target (KrF excimer laser) and subsequent cooling of the vaporized material by means of adiabatic expansion within a mixture of NH_3 and He. Wavelength-dependent one-photon-photoionization mass spectra have been obtained for $Al(NH_3)_n$ with n up to 13, as well as for $Ga(NH_3)_n$ and $In(NH_3)_n$ with n up to 3. They indicate a decreasing cluster IP as the number of ammonia molecules in the cluster increases. The single-ammonia compounds $Al(NH_3)$, $Ga(NH_3)$ and $In(NH_3)$ [227] already exhibit a strong redshift of the IP with respect to the bare metal atoms, which is rationalized via the strong interaction of the ammonia electron lone pair with the metal ion. The IP decreases further with subsequent addition of ammonia monomers. For the $Al(NH_3)_n$ system [224] distinct regions in the cluster-size dependence of the IP are identified. The largest decrease that takes place is up to three solvent molecules. Here, a strong Lewis-acid Lewis-base like interaction between the metal and the ammonia molecule takes place [224]. The system can still be described by a one-center state having the electron very near the metal atom. The less

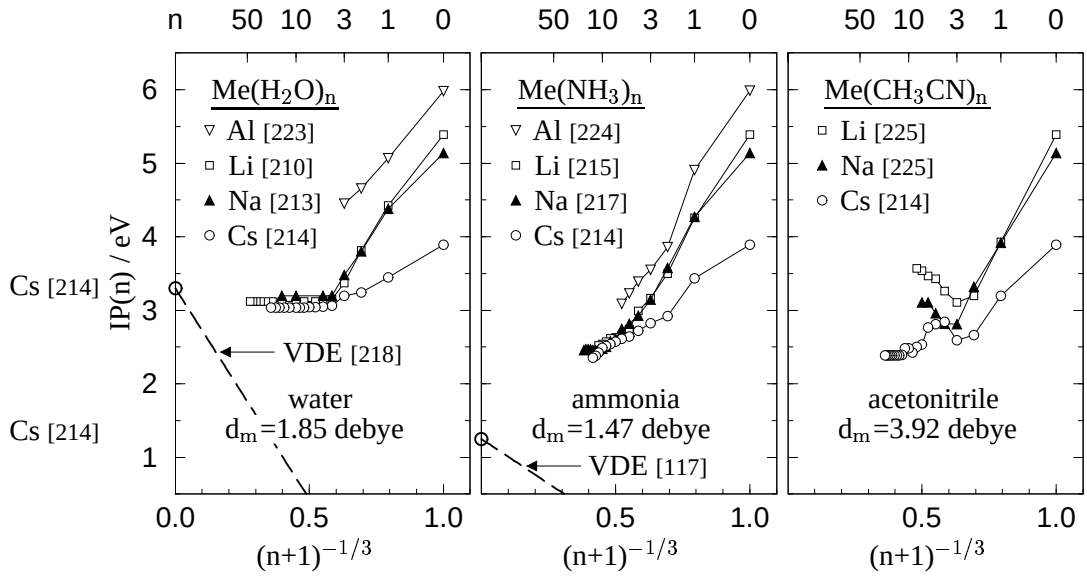

Figure 6.1: Size dependent photoionization thresholds for solvated metal atoms taken from the literature. Left panel: For alkali-water clusters the IP rapidly approaches a constant value which is independent of the specific species and closely coincides with the bulk limit of the vertical detachment energy (VDE) for solvated electrons in water clusters. Center panel: For the ammonia system, the photoionization thresholds for the presented metal atoms monotonically approach a common asymptotic value which again coincides with the bulk limit of the measured VDE. When compared to the water system, convergence is slower and can be understood from the lack of bound surface-states for small ammonia clusters [182]. Right panel: The pronounced variations with cluster size for the acetonitrile system indicate the importance of solvent structure for the ionization potential, which is in this case subject to two strong influences: the solvent-metal interaction as well as the solvent-solvent interaction of the highly polar cluster constituents.

rapid IP decrease for $n \geq 3$ suggests that the valence electron begins to delocalize forming a Rydberg-like surface state which, between $4 \leq n \leq 8$, is being squeezed out of the orbit close to the metal ion into an orbit where its density is predominately associated with ammonia hydrogens. Then, with increasing cluster size, a gradual electron solvation takes place. The further weak decrease of the IP, which again extrapolates [224] to the VDE bulk limit of negatively charged ammonia clusters, is consistent with a two-center model [219] which describes the valence electron by an orbital localized far away from the cationic core. An ion pair state is formed, in which both, the Al^+ and the electron, are surrounded by ammonia molecules. Theoretical *ab initio* investigation of the $Al(NH_3)_n$ system by means of density functional theory (GAUSSIAN) [228, 224] confirmed the experimental results by showing that the radial probability of the Al valence electron becomes more diffuse as the number of ammonia molecules around it increase from zero to four. Comparison of the measured IPs for Na, Cs and Al clustered with ammonia as a function of n [228], reveals a marked dependence of the IP on the element only for small n, whereas for $n > 5$ they extrapolate to the same value. These results also confirm that for group

III metals clustered with ammonia, complete solvation of the valence electron takes place for large cluster sizes. This is in accordance with the finding that indium is inducing the CEE.

6.3 Fast Electron Transfer: Field-Ionization by Point-Charges

Equilibrium

As indicated above, alkali as well as group III metals tend to give away their valence electron if they are surrounded by polar molecules like ammonia or water, be it in a macroscopic solution or in a cluster of sufficient size. In this context, it is not the observed decrease of the photoionization threshold of small metal-atom/solvent compounds alone that indicates the electron solvation, since the stronger solvent/metal-cation bonds compared to the solvent/atom interaction generally reduce the ionization potential. Experimental proof can be found by directly observing the solvated electrons made visible by the discoloring of the bulk solutions, in the observed asymptotic behavior of the IP which for water and ammonia reaches the VDE bulk limits for solvated electrons, as well as the independence of the IP from the specific nature of the alkali atom for large sizes of the solvent cluster. Thus, in these solvents it is energetically more favorable to form a two-center, separately solvated ion-pair state as opposed to the solvation of a neutral metal atom. Under equilibrium conditions, this preferred state is reached via reorganization of the solvent molecules. The experimental observation of this delocalization in metal-doped solvent clusters indicates that the microsecond time scale between the doping of the cluster and the measurement of the cluster ionization potential is sufficient to reach the energetically most favored state. In these experiments the doping of the cluster generally took place in a region of high particle density of the adiabatic expansion, either via concomitant laser ablation [227, 225] or via a pickup oven-source close to the nozzle [217]. Therefore, the clusters are still hot with respect to internal excitations and readily accommodate the introduced alkali atom.

Solvent Structure

The solvent structures corresponding to the equilibrium structures around metal atoms have been theoretically investigated; e.g., for the systems $Na(H_2O)_n$ with $n = 1 - 6$ [229] and $Na(NH_3)_n$ with $n = 1 - 6$ [230] by using *ab initio* molecular orbital methods. In a recent work the geometry of $Li(H_2O)_n$ with $n = 1 - 6, 8$ [222] was found to correlate well for $n \geq 4$ with the solvation structure of the respective cation. This further confirms the two-center ionic state. The delicate relation between the electronic structure of the solute and the geometric structure of the solvent, is illustrated by the experimental as well as theoretical studies of the alkali/acetonitrile system [225, 214]. Due to the strong dipole-dipole interaction of the acetonitrile molecules, a second boundary condition is introduced (see Fig. 6.1). Besides optimizing the solute-metal interactions, the system also tries to minimize also the solvent-solvent interaction energy. This leads to structural rearrangements with increasing cluster size. With the changing geometric structure of the solvent shell, the electronic structure of the solute also changes. This is reflected in the fluctuation of the cluster IP as a function of the cluster size, which is markedly different from the situation in less interacting solvents like water and ammonia.

Due to the difference in the time scale between electron and solvent movement, and also in the inertial masses connected to such movements, the electrons generally follow the movement of the solvent molecules much like the Born-Oppenheimer approximation. In a cold environment the preferred direction of movement of the solvent molecules at a given instance of time depends on the current electronic structure of the solute. After a time increment of Δt the solvent molecules will have changed their position. At the same moment, the electronic structure of the solute rearranges to the new solvation geometry. These steps reiterate, disturbed by thermal fluctuations, until a solvent structure is reached that minimizes overall energy.

Far From Equilibrium

Enter the problem with the Clusterelectric Effect. Here, the metal solute is brought into contact with the polar molecule cluster during a cluster-surface collision. Under typical experimental conditions the impact has a duration in the order of one picosecond, as estimated from the advection time of the cluster. This is shorter than, or at most comparable, to electron solvation times [174]. Within this short time window, the alkali adsorbate has to be picked up, its electron has to delocalize and the formed geminate ion pair has to become spatially separated by cluster fragmentation. Furthermore, the impact heated cluster is highly excited, which is reflected in strong fluctuations in the relative orientation of the cluster constituents. The thermal movement of the cluster constituents counteracts the formation of a well defined solvent structure around the picked up surface adsorbate. Compared to the high amounts of energy injected into the cluster during surface impact, the local minimum in configuration space that corresponds to the solvated adsorbate is too shallow to influence the movement of the cluster constituents. Experimental proof of this conjecture is represented inthe absence of magic numbers in hot cluster ions as discussed in Chapt. 3. Furthermore, the experimental observation that both SO_2 (EA $\approx$ 1 eV, dipole moment 1.6 debye) and NH_3 (EA $\approx$ 0 eV, 1.3 debye) exhibit a strong clusterelectric effect, although their ability to stabilize an electron is very different due to the vanishing electron affinity in the case of ammonia, indicates that the delocalization of the electron proceeds independently of subsequent ion or electron solvation processes. Since neither the short time window for the electron transfer to the cluster nor the energy-rich environment of the picked up adsorbate seems to allow for the formation of solvate structures that would make electron transfer reaction to the surrounding cluster energetically favorable, an new electron transfer mechanism is proposed, which relies primarily on the direct interaction of the alkali atom with individual cluster constituents instead of relying on collective structures.

ET Model

Motivated by the observed fundamental importance of a molecular dipole moment for the CEE, the electron delocalization mechanism is based on the interaction of the solute with the partial point charges associated with the molecular dipole moment of the cluster constituents. The character of the proposed model is that of a field-ionization-mechanism which has been successfully applied in field-emission microscopy as well as to the ionization processes in the focus of strong laser beams. They all consider the electron to be bound in a superposition of Coulomb core potentials and an external disturbance e.g. a static electric field. A prominent example is the so called Barrier Suppression Ionization (BSI) model which was suggested by Codling *et al.* in the late 1980s [231], after which it was improved and rationalized by Bandrauk *et al.* [232, 233] and analytically treated by Schröder *et al.* [234]. Ionization takes place

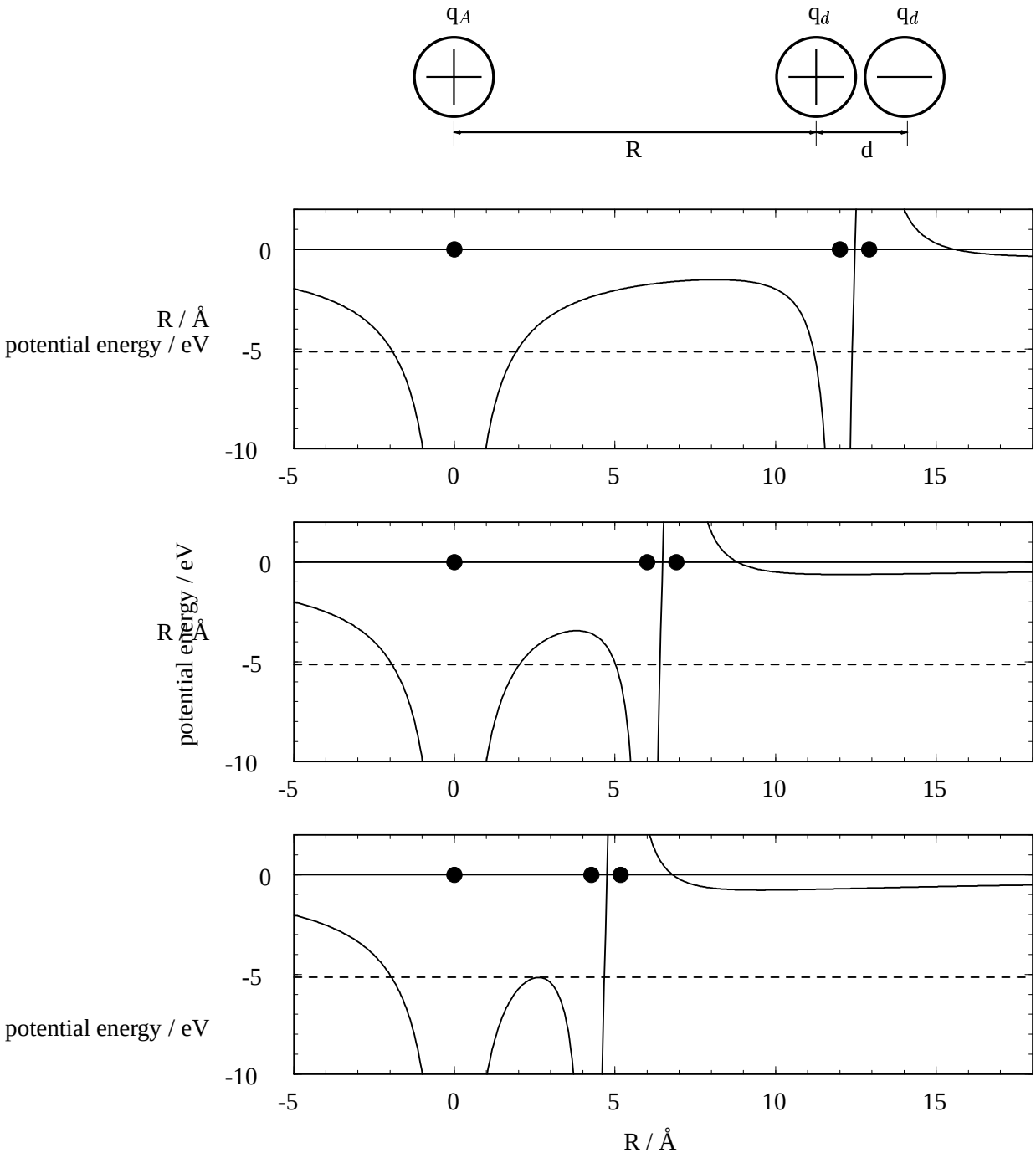

Figure 6.2: Point-charge induced electron transfer mechanism. A HF molecule approaches a sodium atom and delocalizes its valence electron. Parameters: q_A=0.68, q_d=0.449, d=0.917. The barrier falls below the valence electron level of sodium for R=4.26 Å.

when the external perturbation deforms the ion core potential to such an extent that the electron becomes quasi-free and escapes into the accessible half-space.
The proposed model is restricted to the single-active-electron approximation, which is moving in a one dimensional potential of the cation core. The perturbation is represented by a dipole field approaching the adsorbate along the model axis having the most favorable orientation. The corresponding electrostatic potential experienced by the electron is given by

$$V(x) = -\frac{e}{4\pi\epsilon_0}\left(\frac{q_A}{|x|} + \frac{q_d}{|R-x|} - \frac{q_d}{|R+d-x|}\right), \tag{6.1}$$

where R stands for the distance between the picked up adsorbate and the positive partial charge of the approaching dipole. The parameters q_d and d represent the absolute value of the partial point charges which set up the dipole field (see Fig. 6.2) and their mutual separation. Together with the effective core charge q_A of the adsorbate cation, these parameters allow for the adaptation of the model to the employed systems. To simulate a sodium atom with atomic radius of 1.896 Å and an ionization potential of 5.138 eV a q_A value of 0.68 can be calculated from the Coulomb law. The polar molecule is modeled via dipole moment and bond length. For HF, with a dipole moment of 1.96 debye and a bond length of 0.917 Å, the respective model parameters are d=0.917 Å and q_d=0.449. With respect to the choice of the molecular dipole moment, it is interesting to note that the absolute value changes in passing from the gas to the liquid phase. A recent *ab initio* calculation [235] for water found that the dipole moment increases from the gas phase value of 1.85 debye to ≈3 debye which is explained in terms of self-consistent mutual polarization effects in the condensed phase. The dipole moments of clustered molecules are generally expected to lie between the gas and the liquid phase.
Fig. 6.2 depicts three stages during the approach of a HF molecule towards a picked up sodium atom. At a distance of R=12 Å the potential wells of the sodium atom (left black circle) and the HF molecule (right black pair of circles) remain almost undistorted. The sodium valence electron is localized at the sodium core with a binding energy of -5.14 eV which corresponds to the sodium ionization potential (dashed line). At a distance of 6 Å the interaction of the positive partial charge with the sodium atom starts to decrease the barrier between the atom and the approaching polar molecule. Stark shifting of the electronic levels has been neglected in this schematic model. Upon further decreasing the mutual distance R down to 4.26 Å, the barrier between atom and molecule finally falls below the level of the sodium valence electron and allows it to move freely between the two entities. This is the first step to electron delocalization within the cluster. The electrostatic repulsion between the sodium core and the dipole in this configuration, and thus the necessary impact energy to reach this point, amounts to 0.2 eV, which can be readily provided via the single-particle impact energy during cluster surface collision, namely via an impact velocity of 1500 m/s. This value already represents an upper limit to the necessary impact energy since the valence electron is still present during the approach of the dipole molecule, so that it shields part of the repulsion. Direct electron delocalization through the impact of a polar molecule onto an easy-to-ionize species therefore seems to be a reasonable explanation for the processes observed in the context of the

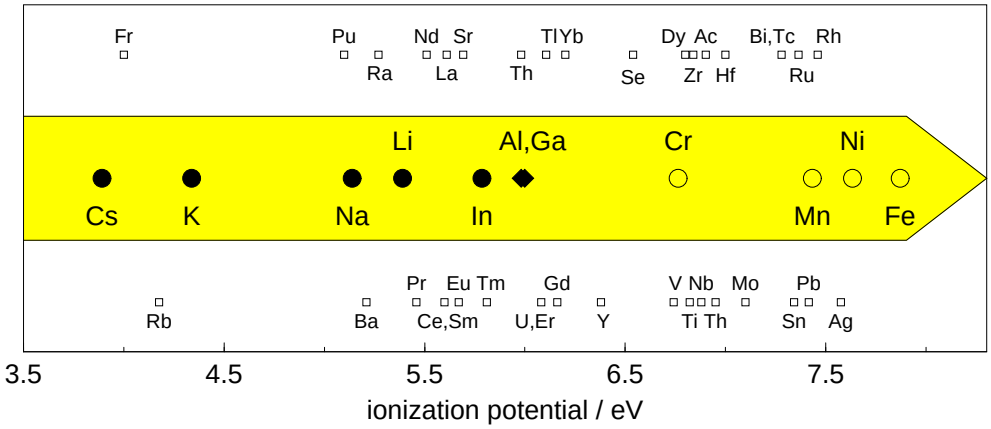

Figure 6.3: The role of the ionization potential. In the present work, adsorbates from elements represented by full circles have been found to induce the clusterelectric effect. Al and Ga (black diamonds) have been added to the list because photoelectron spectra of these metals embedded in polar solvent clusters indicate an electron delocalization [227, 228, 224, see Chap. 6.2]. Empty circles denote adsorbates for which the effect has not been observed under the present experimental conditions. The schematic representation hints at an upper limit for the ionization potential of the surface adsorbate which lies between 6 eV and 6.8 eV. The exact position is likely to depend on experimental parameters like impact velocity, dipole moment and cluster size. Empty squares indicate the positions of easy-to-ionize elements with ionization potentials within the scope of the clusterelectric effect, which should be tested in future work.

Clusterelectric Effect. Since the field-ionization like mechanism, which is based on the partial point charges associated with polar molecules, proceeds barrierless during individual collisions, it is not impeded by the short time scale of cluster-surface collisions, nor by the thermally hot cluster environment at this moment.

The important parameters of the point-charge induced electron transfer model are the molecular dipole moment, the impact energy and the ionization potential of the solute species. Fig. 6.3 presents a selection of easy-to-ionize solute systems ordered according to their IP. Full circles represent the surface adsorbates that have been found to induce the CEE under the present experimental conditions, while empty circles represent the species that did not lead to the production of free charge carriers. The substance with the highest IP that has been successfully tested is indium (IP=5.78 eV). The model proposed here predicts, however, that this range should be extendable to higher values if either larger impact energies or molecules with large dipole moments are employed. An interesting question pertains also to the relevance of this mechanism in the bulk liquid where the processes are commonly described in terms of an equilibrium rate equation. While the formation of ordered solvent structures facilitates the electron transfer and reduces the necessary energy, it seems feasible that the point charge mechanism ultimately initiates the electron transfer via the omnipresent fluctuations in the polar environment [236].

As has been discussed in Chap. 5.4.3, charge separation within the impact heated cluster is a prerequisite for successful separation of the geminate ion pair via clus- *Electron Transport*

ter fragmentation. It has been noted that diffusional processes of the electron or the proton are impeded by the Coulomb attraction of the respective counter ion. The ionization process has therefore already been required to generate the ions at some distance, that allows for further diffusion via the available thermal energies. The point-charge based electron transfer mechanism provides such a possibility. For example, an electron stabilized in the vicinity of its cation can be remobilized by the same process as was the case with alkali ionization. Since electron affinities generally lie below the ionization potential, collisions lower in energy already suffice for this purpose. Fig. 6.4 illustrates another, non-sequential mechanism. During the cluster-collision, not only a single cluster constituent and the picked-up solute approach each other to such extent that their respective potential wells are distorted, but this is a feature that pertains to the whole impacting cluster. The interaction of the whole set of cluster constituents may lead to the formation of an unobstructed potential valley which becomes accessible to the liberated valence electron. While the topology of this valley is rapidly changing due to the colliding cluster constituents, it would allow the electron to instantaneously delocalize over the whole cluster. The figure gives a snapshot for a two dimensional HF cluster containing 21 randomly oriented monomers. The black line denotes a potential value corresponding to the binding energy of the sodium valence electron. Upon one-dimensional compression by a factor of two (lower panel) these regions merge and would allow a present electron to enlarge its accessible locations.

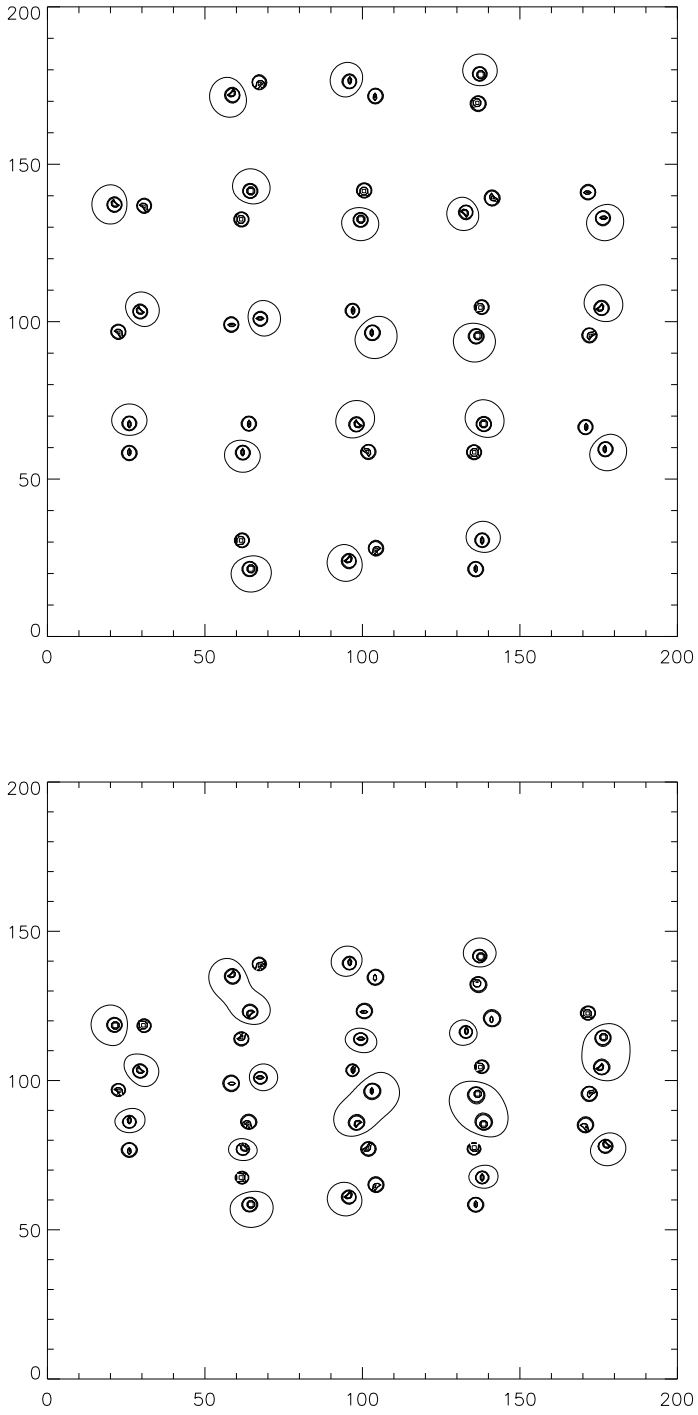

Figure 6.4: Schematic representation of the merging of potentials during cluster impact. For the polar species the properties of HCl have been used. The solid line gives the equipotential line of the ionization potential of Na. Whereas in the uncompressed cluster the latter potential is only reached in isolated areas around the positive partial charge of the dipoles, the situation in the compressed cluster changes: the areas combine, allowing a liberated electron to leave its place of creation.

Chapter 7

The Clusterelectric Effect in Disguise

As illustrated in the present work, the phenomenon of cluster-impact induced charge generation is not restricted to the previously known examples of water and sulphur dioxide, but seems to pertain to the group of polar molecule clusters in general. However, it remains to be shown that the proposed Clusterelectric Effect is the universal microscopic mechanism for this enlarged class of systems. To test this hypothesis, the charged cluster fragments emerging after the surface-collision of sulphur tetrafluoride, ammonia and water clusters have been mass analyzed. The experimental findings fit into the framework of the proposed mechanism. Moreover, the selected systems presented here all show an additional aspect of the CEE, and thus emphasizes the richness of the effect.

7.1 The SF_4 System: Ion-Molecule Reactions

From the view point of the CEE mechanism, sulphur dioxide and sulphur tetrafluoride are similar molecules. Sulphur tetrafluoride has an electron affinity of 1.5 eV and a dipole moment of 0.632 debye, which is somewhat smaller than the 1.63 debye of sulphur dioxide. However, its greater mass normally leads to higher impact energies so that it should be as efficient in the solute ionization as sulphur dioxide. Fig. 7.1 illustrates that surface impact of SF_4 clusters leads to the generation of bi-polar charged cluster fragments in comparable quantities. Moreover, spiking the surface with Cs atoms from an oven source leads to an increase in the overall quantity of both polarities.

Mass analysis of the charged cluster fragments reveals Cs cations as core ions for the positive charge carriers in accordance with the findings from the integral charge measurement. However, the corresponding SF_4^- anions are not observed. Instead, progressions with core ions of SF_5^- and Br^- are present. The origin of the bromine has been related to trace impurities within the used SF_4 gas. Due to its high polarizability, it is preferentially built into the cluster much similar to the discussed example of oxygen accumulation in N_2/O_2 mixed clusters (see Chap. 2.1.4). The formation of bromine anions and their appearance as core ions in the SF_4 progressions illustrates

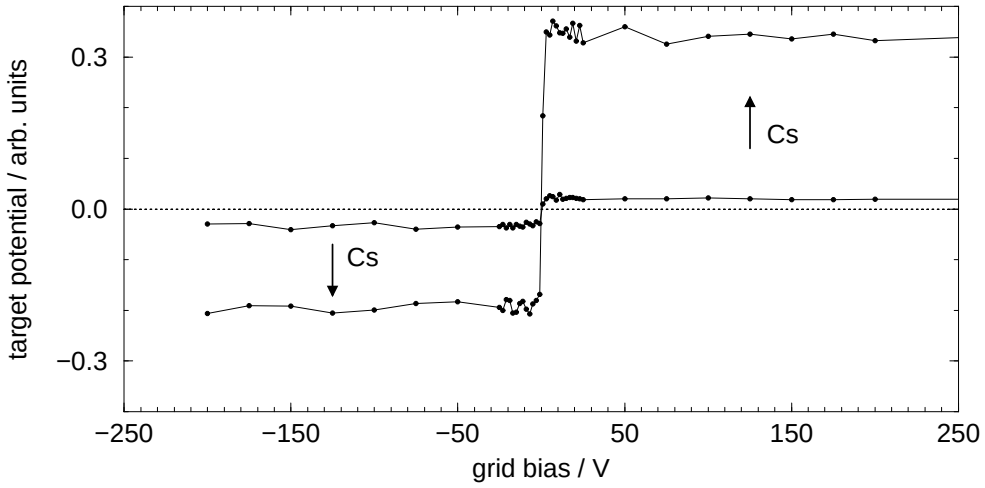

Figure 7.1: Integral charge separation signal of SF_4. The clusters of average size N=125 impinge on the SiO_x surface held at room temperature with a velocity of 1.2 km/s equivalent to an energy per particle of 0.8 eV. The two curves were taken before and after dosing the surface with Cesium.

the high mobility of the electron within the cluster which samples the cluster for the site of highest binding energy. Bromine has, with 3.36 eV, a considerably higher electron affinity than SF_4 or SF_5. The formation of the SF_5^- core ions is interpreted in terms of an electron induced ion-molecule reaction

$$e^- + \mathrm{SF}_4 + \mathrm{SF}_4 \rightleftharpoons \mathrm{SF}_4^- + \mathrm{SF}_4 \rightleftharpoons \mathrm{SF}_3 \uparrow + \mathrm{SF}_5^- . \tag{7.1}$$

In general, the small fluorine anion has similarities to the proton. From this point of view, the fluorine anion transfer observed following the electron attachment resembles the established proton transfer reactions wich occur upon ionization of water or ammonia clusters and which lead to the protonated species [237, 238].

7.2 The NH_3 System: Missing Electron Affinity

The spontaneous formation of solvated electrons was discovered in the liquid ammonia system. While its molecular dipole moment is with 1.47 debye comparable to the one of sulphur dioxide, it lacks a molecular electron affinity. As has been discussed in Chap. 5.4.3, electrons can be stabilized in the volume of ammonia clusters, starting from a cluster size of 35, via shallow potential wells formed by surrounding molecules. With increasing cluster size the electron affinity finally reaches a value of 1.45 eV as measured via the vertical detachment energy [117]. Fig. 7.3 presents integral charge measurements for ammonia clusters of mean size 10^3 impinging at a speed of 1.6 km/s on an untreated SiO_x target held at 573 K. The full circles give the measured charge as function of the bias grid. While SF_4 and SO_2 give rise to comparable amounts of charged fragments, there seems to emerge only one polarity of *free* charge carriers in the ammonia system. The open circles give the derivative

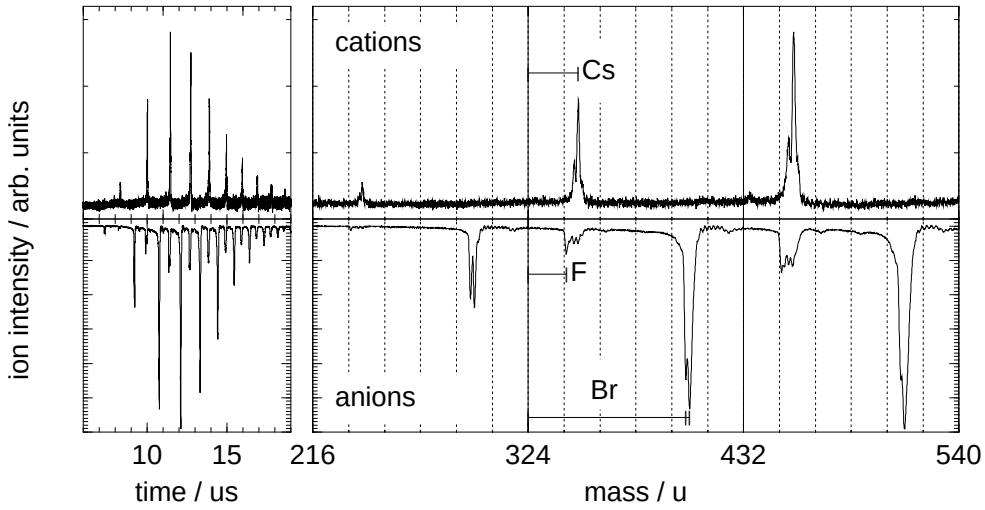

Figure 7.2: Spectra of SF_4 clusters of average size 10^2 impinging on an SiO_x surface held at room temperature and which has been doesed with Cs atoms with a velocity of 1.2 km/s (0.79 eV/particle). The cationic spectrum shows $(SF_4)_4Cs^+$ peaks. The anionic spectrum is dominated by bromine structures like $(SF_4)_4Br^-$. Additionally, a progression of $(SF_4)_nF^-$ is observed.

of the integral charge curve. It correlates directly to the energy distribution of the charge cluster fragments. Assuming a residual kinetic energy of 20% per rebounding particle, a mean kinetic energy of 23 eV corresponds to a cluster fragment size of 500. The observation of relatively lage cluster fragments is consistent with the high binding energy of ammonia. The initial impact energy of 0.23 eV per particle is not sufficient to drive the cluster into the shattering regime (see Chap. 5.4.4). The impact-heated cluster mainly stabilizes by way of monomer evaporation. The determination of the charge amount of one polarity is based on the discharge of a capacitor setup formed by the target and the bias grid. With a high negative bias voltage, negatively charge fragments are forced to move against the surface where they neutralize. Positive fragments, on the other hand are accelerated away from the target and remain undetected. Therefore, the signal corresponding to negative grid voltages can be attributed to the negative ions. On the other hand, for high positive bias voltages, positive charge carriers are reneutralized at the target, while the negative ones are extracted and remain undetected. Thus, the measurement seems to indicate a unipolar charge generation process consisting of negative charge carriers. Especially with regards to the vanishing molecular electron affinity of ammonia, this is rather surprising. However, another explanation exists in the form of the production of a geminate ion pair via the CEE which is followed by the rapid transfer of the delocalized electron into the target substrate. While in this case the integral charge measurement remains unaltered for high negative voltages, the positive bias voltage would give the observed zero signal since the positive charge neutralizes the corresponding negative charge which is already present in the target substrate.

To test the latter conjecture, a cluster size dependence of the integral charge signals

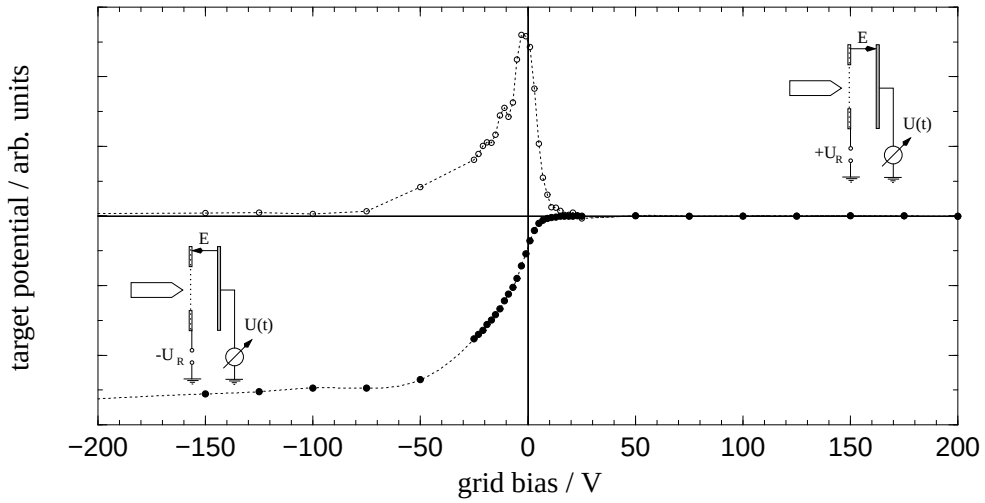

Figure 7.3: Integral charge signal from NH_3 clusters ($\bar{N}=10^3$ at 30 eV electron-impact ionization) impinging on a SiO_x surface held at 573 K with velocity of 1.6 km/s (0.23 eV per particle). The full circles represent the total charge measurement as a function of the bias voltage. The open circles give the derivative of the total charge measurement which correlates to the kinetic energy distribution in the direction of the surface normal.

has been measured and is depicted in Fig. 7.4. By varying the stagnation pressure, the cluster size as well as the amount of clusters increases. Although much smaller, a positive signal part can also be observed. By taking the ratio of both curves, the increase which is caused by the growing gas load with higher expansion pressures is divided out. The right panel presents the ratio of the respective charge amounts as a function of stagnation pressure. Although weaker, the positive signal is found to grow much faster with cluster size than the negative signal part. This is consistent with the hypothesis that the weakly bound electrons are predominantly lost into the substrate. With increasing size, the cluster can stabilize the electron more efficiently.

The working hypothesis which concerns the loss of the weakly bound CEE electrons from the impact-heated ammonia clusters predicts that it should be possible to stabilize the electron within the cluster by doping the latter with an electron scavenger. Fig. 7.5 presents the results for a pickup experiment. The long dashed lines give the amount of positive (left panel) as well as negative (right panel) charges as generated by a single pulse. After approximately 230 μs the pulse (width 400 μs) starts interacting with the target. While there is considerable production of positive free charge carriers (left), almost no negatively charged cluster fragments are observed. In a second run (solid lines), the expansion chamber was converted into a simple pick-up chamber [239, 240] by raising the background pressure by 10^{-3} mbar via the dosage of SO_2 through a needle valve. While the positive signal remains uninfluenced, the negative increases considerably. This is interpreted in terms of stabilization of the electron within the ammonia cluster via the molecular electron affinity of sulphur dioxide and also corroborates that in the case of ammonia the CEE mechanism is at

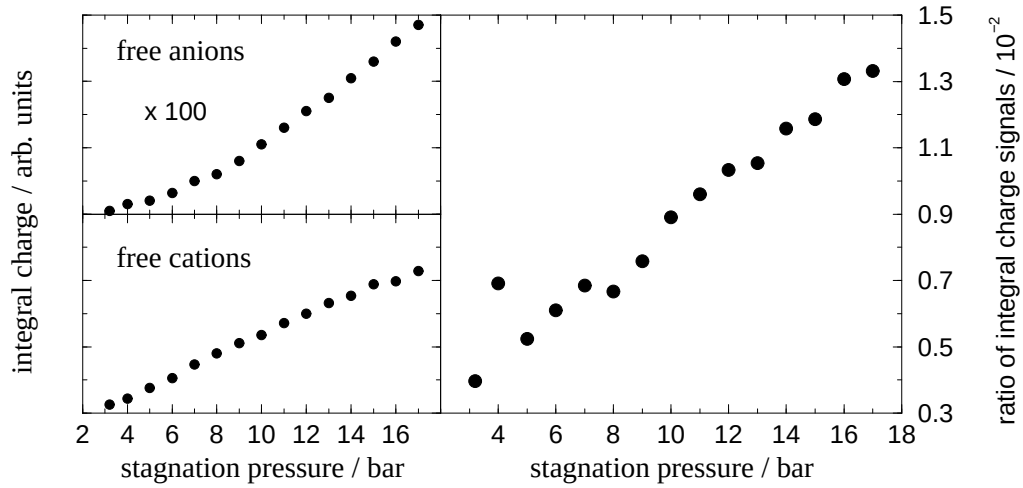

Figure 7.4: Integral charge yield of NH_3 clusters (v=1.6 km/s, 0.23 eV / particle) as a function of stagnation pressure. The left panels give the increase of the respective charge signal with stagnation pressure which itself correlates to the mean cluster size. Right panel: the ratio of the left curves, which is independent of the increase in gas load, reveals that the positive signal part grows much faster with cluster size than the negative part.

work, however, disguised by the loss of the generated electrons to the target substrate. To further establish that the CEE mechanism is valid for the ammonia system, a mass spectrometric analysis of the charged fragments emerging after surface impact has been performed. Fig. 7.6 presents the results for the ammonia clusters of size $2 \cdot 10^3$ impinging with a speed of 1.7 km/s on a SiO_x target. By dosing the surface with Na atoms from a oven source, the corresponding $Na^+(NH_3)_n$ progression is observed in accordance with the CEE mechanism. Additionally, a sequence of the form $NH_4^+(NH_3)_n$ is observed. Since the negative spectra do not exhibit a corresponding negative peak like $NH_2^-(NH_3)_n$,or $OH^-(NH_3)_n$, the positive progression can not be attributed to a proton transfer reaction between two ammonia molecules, similar to the water autoprotolysis, or a reaction with a picked up water molecule. The origin of the protonated ammonia progression is tentatively explained in terms of an ion-molecule conversion reaction:

$$Na^+ + NH_3 + NH_3 \quad \rightleftharpoons \quad NaNH_2 \uparrow + NH_4^+$$

Moreover, the protonated ammonia progression is well known from laser- or electron-impact ionization experiments [237, 241, 242] with ammonia clusters, in which it is explained in terms of a fast ion-molecule reaction between the unprotonated ammonia cation with neighboring ammonia molecules, followed by the ejection of a neutral NH_2. Negative spectra have only been observed upon the doping of the ammonia clusters with SO_2 as an electron scavenger.

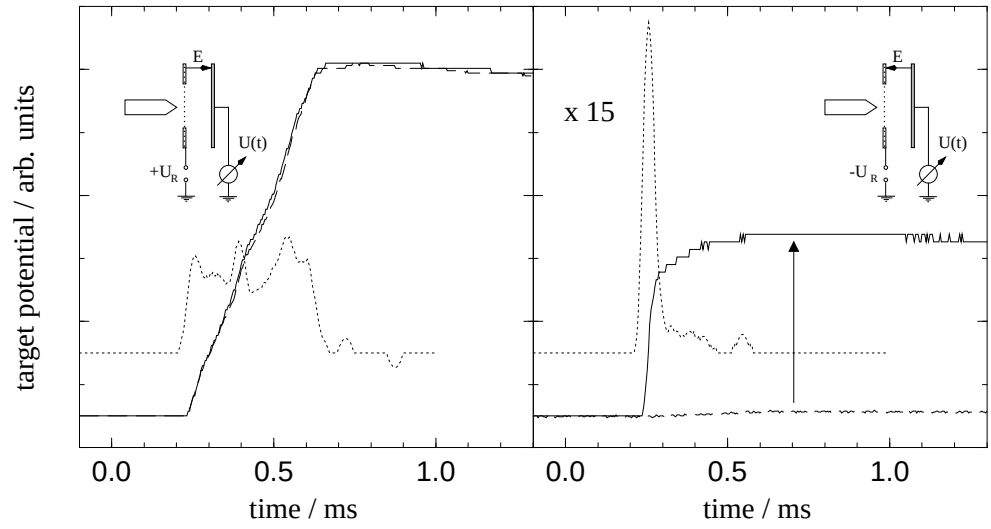

Figure 7.5: Integral charge signal from NH_3 clusters impinging with a velocity of 1.6 km/s on an unspiked SiO_x surface. The almost undetectable signal from the negative carriers increases considerably if the clusters are doped with SO_2 molecules via a pickup mechanism. However, the signal of the positive carriers does not show this behavior. The dotted line gives the derivative of the signal, representing the charging current. Whereas for positive clusters, the shape of the charging signal resembles the pulse shape, indicating that charges are created during the whole cluster pulse, the negative charging current is strongly peaked at the pulse front. The front of the cluster pulse absorbs the SO_2 background molecules completely, so that the trailing part of the pulse is not doped with the electron scavengers. This also demonstrates how dense cluster beams can function as 'brooms'.

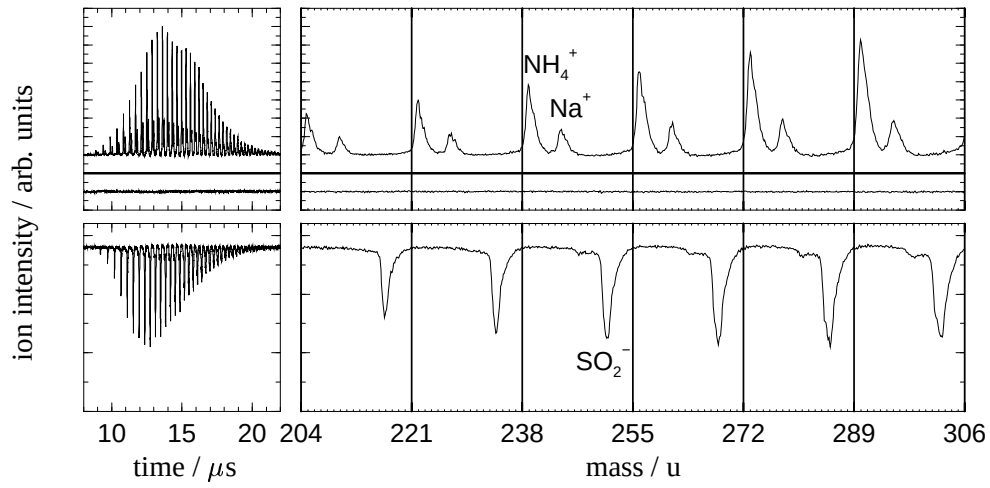

Figure 7.6: Spectra of positive and negative ions generated during the impact of NH_3 clusters ($N=2 \cdot 10^3$, v=1.7 km/s) on SiO_x at 350 K. To observe negative ion spectra (lower panel), the expansion chamber has been filled with SO_2 up to a base pressure of 10^{-3} mbar (lower panel).

7.3 The H_2O System: Autoprotolysis

The CIMS spectrum of water clusters on an untreated surface has already been discussed in Chap. 3, particularly with respect to the direct observation of the autoprotolysis reaction and the magic numbers contained in the spectra. Here, the focus lies on water as a polar species that can induce the CEE. The right panel of Fig. 7.7 presents integral charge measurements for water clusters impinging on SiO_x at 690 K. Positive and negative charge carriers are observed for the untreated surface. Upon spiking the surface with sodium, the amount of positive charge carriers significantly increases, while the total negative charge yield remains almost unchanged. The mass analysis of the charged cluster fragments (left and center panels) reveals the mechanism behind this behavior. The signals from the unspiked surface stem from a intra-cluster autoprotolysis reaction that leads to the formation of H_3O^+ and OH^- core ions (see Chap. 3). The increase of the positive charge yield with the spiking of the surface with sodium atoms, as well as the observation of the corresponding $Na^+(H_2O)_n$ progressions in the mass spectra of the positive cluster fragments, can be interpreted in terms of the CEE: Sodium surface adsorbate get picked up during the cluster surface collision, whereupon the interaction with the polar water molecules strips the alkali of its valence electron. Finally, cluster fragmentation separates the geminate charge pair consisting of a alkali cation an a 'wet' electron. The absence of the corresponding $(H_2O)^-$ peaks in the anion spectra can be explained by a predominant loss of the wet electron into the surface: like ammonia, water has no molecular electron affinity to stabilize the alkali valence electron. The intermolecular dipole cages are to shallow to stabilize the electron within the impact heated cluster.

An interesting aspect of the spectra reported in Fig. 7.7 is the absence of NaOH formation: the text book reaction of solid sodium with liquid water leads to the formation of solvated Na^+ and OH^- ions as well as to molecular hydrogen. If sodium hydroxide can form on the picosecond time scale of cluster impact, cluster fragmentation should be able to separated the sodium cation from the OH^- core ion, so that the respective progressions should become observable in the cluster fragment spectra. Yet, if hydroxide formation is a slow process which occurs only later in the cluster fragments, it would not be observed. However, since the hydroxide formation involves the alkali valence electron, which is lost with high probability into the surface during the collision, the latter channel is unlikely. According to this, the dosing of the surface with Na atoms should lead to a comparable increase of the $Na^+(H_2O)_n$ and $OH^-(H_2O)_n$ progressions. However, Fig. 7.7 shows, that the increase in the first is not accompanied by a rise in the generated anions. This implies that single solvated alkali atoms in water do not induce the formation of sodium hydroxide on the time scale of cluster impact. This observation is consistent with previous experiments, e.g. [243, 212, 213] and most recently by Buck *et al.* [207, 206], which did not observe a significant NaOH formation upon single collision interaction of Na with water molecules, of Na atoms with water clusters or, of Na clusters ($n \leq 21$) with water clusters ($n \leq 40$), respectively. The size dependent IP measurements by Schulz *et al.* [212, 213] (see Chap. 6) confirm that even on a microsecond time scale and under equilibrium conditions, solvated electrons are present in the alkali/water clusters, which implies that hydroxide formation is at least not an ultrafast reaction.

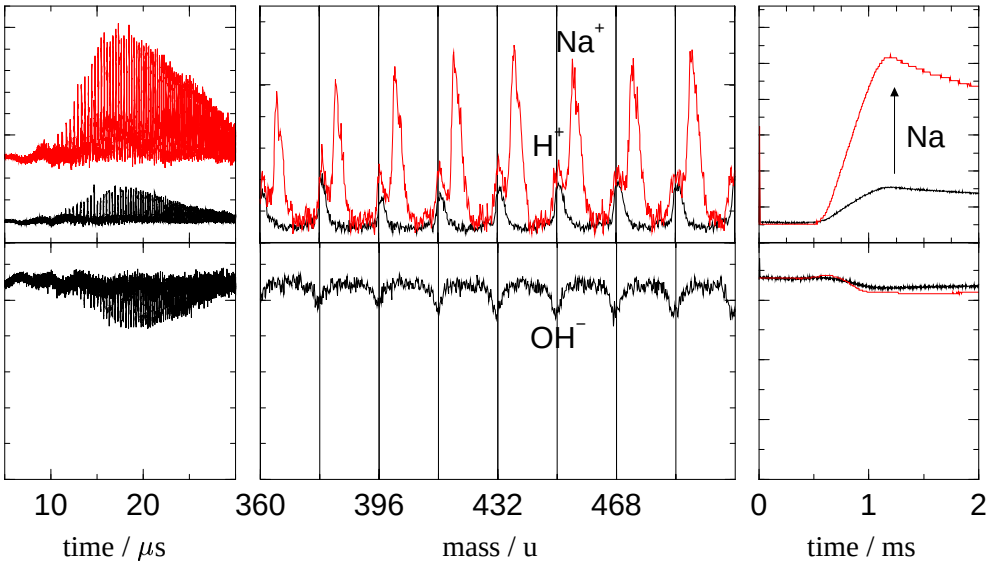

Figure 7.7: Cation and anion spectra of H_2O ($\bar{N}$=2 · 10^3, v=1.7 km/s) impinging on SiO_x at 690 K. Without dosing the surface with Na, the spectrum clearly shows the signature of autoprotolysis. After adding Na to the surface additional $Na^+(H_2O)_n$ peaks emerge. The lack of corresponding $(H_2O)_n^-$ peaks can be explained in terms of the negligible molecular electron affinity of the water system. The impact heated cluster fragments are too hot to stabilize the free electrons via the shallow dipole bound states.

In the work of [207], exclusively $Na^+(H_2O)_n$ progressions have been observed following photoionization (308 nm / 355 nm). On the other hand, formation of sodium hydroxide has been observed in multiple sodium-water cluster collisions [206] for which a two step reaction mechanism is proposed: in a first collision between a sodium atom with a water cluster, solvated sodium atoms of the form $Na(H_2O)_n$ are formed. These react in a second collision with a Na_2 dimer to products of the form $Na(NaOH)_2(H_2O)_m$ which are detected by a combination of photo-ionization and TOF analysis [206]. The importance of the first solvated sodium atom is corroborated by recent theoretical studies of the direct reaction Na_2+2H_2O→$(NaOH)_2$+H_2 [244]. They find a reaction barrier of 1.28 -1.56 eV for this exothermic reaction ($\Delta H \approx -1.9$ eV), which is explained in terms of the equilibrium configuration of the educt complex being far away from the transition state. It is unlikely that such high activation barriers can be surmounted in a finite water cluster with a monomer evaporation energy below 0.5 eV. The solvated sodium precursor is proposed to change the configuration of the water cluster in direction of the transition state for the subsequent reaction with the sodium dimer [206]. That the second collision has to take place with a sodium dimer, manifests itself in the observation that only even numbers of NaOH entities are formed. Correspondingly, a hydrogen molecule is the most likely neutral reaction product which leaves the cluster and eludes detection. However, due the experimental limitation that in the cited works the ionization potential of the unobserved $(NaOH)_n(H_2O)_m$ clusters is likely to be higher than the applied pho-

ton energies, a systematic discrimination against this species can not be excluded. Future CIMS measurements, which are independent of the respective cluster ionization potential, should allow to test the aforementioned sequential model: Water clusters pick up sodium monomers, dimers and trimers before they collide with the fragmentation surface. Depending on the presence or absence of sodium hydroxide formation for the chosen sodium cluster size, either $Na^+(H_2O)_n$ progressions should occur correlated with the respective $OH^-(H_2O)_n$ sequence or, the former with some $(H_2O)_n^-$ (surface neutralization of the solvated electron!) should be observed. As proposed in [206], the experiments could be repeated with water clusters pre-loaded with single alkali atoms. The reaction time scale of hydroxide formation could be tested with a CIMS pickup experiment. With defined alkali surface adsorbates ranging from the sub-monolayer to the multilayer it seems feasible to control the number of alkali atoms incorporated into the cluster. If hydroxide formation proceeds on the picosecond time scale its signature should become observable in the charged cluster fragment spectra if a sufficient amount of alkalis is incorporated into the cluster.

Chapter 8

Applications

This is only the beginning of an understanding of the complex dynamic details involved in the clusterelectric effect. But already, the observed phenomenon promises to be a new and very efficient addition to known ionization or electrification mechanisms and has a series of potential applications (see Fig. 8.1).

8.1 Applications of the Clusterelectric Effect[1]

Trace Analysis

The combination of the high efficiency of the individual pickup and ionization step for alkali adsorbates, with the high density of clusters in beam sources allows for the very sensitive detection of easy-to-ionize surface adsorbates: under the present conditions typically 10^{14} SO_2 clusters of mean size 1000 leave the nozzle per pulse. Assuming a beam divergence of 45^o, this corresponds to a flux of 10^{12} clusters/cm^2 in a realistic working distance of 5 cm. With each cluster sampling an area of roughly 10^{-13} cm^2, 10 % of the collision surface is scanned during each pulse. The minimum detectable surface coverage depends on the size of the sampled area, the CEE efficiency and the sensitivity of the ion detection system. Assuming that 10 ions per pulse can be detected comfortably by an ion counting detector and a CEE efficiency of 10^{-3} corresponding to the lower estimated value for alkali adsorbates, 10^4 alkali atoms would be required to reside on the area sampled with each cluster pulse. For a beam diameter of 1 cm^2 this corresponds to a detectable threshold coverage of 10^{-10} monolayers. To obtain space-resolved information it is often desirable to confine the beam spot on the surface: within an area of 10μm x 10μm, still 10^{-4} monolayers of alkali contaminations can be detected. This compares quite favorably to other surface analysis methods like Auger electron spectroscopy which have a detection limit in the range of 10^{-3} monolayers [245]. The high sensitivity of the CEE may find its application in the characterization of high-purity materials used for e.g., the semiconductor industry. A further application in which sensitive measurement of surface concentrations of alkali metals is necessary is given by the detection of radioactive decay products: e.g., ^{22}Na ($T_{1/2}$=2.6 y), ^{40}K ($T_{1/2}$=1.3 10^9 y) , ^{134}Cs ($T_{1/2}$=2.1

[1] some of the ideas presented in this section have been published in form of a patent application: C. Gebhardt and H. Schröder, *Verfahren und Vorrichtung zur Clusterfragmentation*, Deutsche Patentanmeldung Nr. 199 34 173.7 (21.07.99)

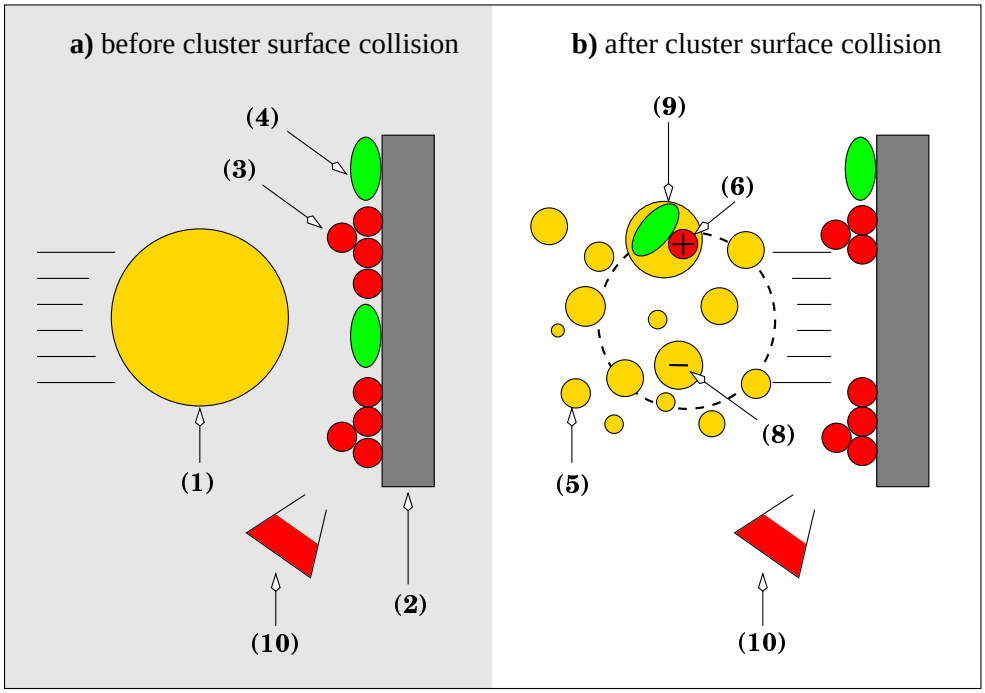

Figure 8.1: Applications of the Clusterelectric Effect: A cluster of polar molecules (1) approaches a target surface (2) with hyperthermal velocity typically in the range between 1 km/s and 2 km/s (left panel). The surface is covered to some extent with adsorbates: besides the CEE inducing species (3) characterized by a low ionization potential, additional adsorbates (4) may reside on the surface. The adsorbate coverage may be controlled by some suitable source (10). After the surface collision (right panel) the cluster fragments into pieces (5). Due to the cluster-surface interaction adsorbates can be picked up which are transferred into the cluster fragments (6,9). In the case of easy-to-ionize species this process can be accompanied by a valence electron delocalization within the cluster upon which some emerging fragments carry a charge (6,8). Due to the highly efficient pickup and charging mechanism, the clusterelectric effect is a candidate for the trace analysis of, e.g., ubiquitous alkali metal traces on surfaces. As it is combined with particle removal, it can be employed to clean surfaces or to lithographically structure alkali overlayers. By dosing the collision surface with alkali atoms, large amounts of charges can be generated. While the creation of heavy anions and cations in the form of charged cluster fragments is of interest in respect to ion propulsion, the efficient charging of impacting clusters may contribute to the analysis of atmospheric aerosols or be applied in cluster ion sources in general. The concomitant pickup of neutral molecules during the CEE might help to transfer large molecules into the gas phase and convert them into easy-analyzable ions.

y) and ^{137}Cs ($T_{1/2}$=30 y). For these alkali isotopes the CEE combines pickup with ionization and thus allows straight forward mass spectrometry. With the proposed validity of the CEE ionization mechanism for all species with low ionization potential, this method would be sensitive to a much larger group of radionuclides (see Fig. 6.3) including francium, radium, strontium and notably also plutonium.

Surface Cleaning and Lithography

The interaction of the impinging clusters with the surface leads to the pickup of adsorbed species. That there is substantial removal of material from the adsorbate layer

has been indicated by Fig. 5.8 and Fig. 5.10: for the above mentioned cluster flux of 10^{12} $s^{-1}cm^{-2}$ established 5 cm downstream of the nozzle and the observed charging efficiency per cluster of 10 percent in the presence of high adsorbate coverages, 10^{-4} monolayers per pulse are removed. At a repetition rate of 10 Hz, the unskimmed cluster beam would remove an amount of 10^{-9} mole/s of the surface adsorbates. By shaping the beam with a skimmer, or in a more elaborate way, using a transmission mask, alkali adsorbate can be removed from localized areas. While the structures presented in Fig. 5.8 have a typical dimension of 100 μm, the achievable resolution is much smaller. Being limited mainly by the size of the cluster source and the geometry of the arrangement, a typical setup (nozzle diameter 0.5 mm, source-mask distance 5 cm, mask-target distance 1 mm) should be capable of producing structures in the order of 1 μm. Resolution can be increased with higher source-mask distances, however, at the cost of cluster flux. As illustration for a potential application, the space-resolved enhanced oxidation of silicon surfaces shall be mentioned: In the course of semiconductor development there is a need for thin, defect free SiO_2 layers, which are grown at lower temperatures than usual (1400 K) [246]. A possible solution is the coadsorption of alkali metal atoms which catalyze the reaction. In the sub-monolayer region they facilitate dissociative adsorbtion, while in the multilayer regime the alkali metals are believed to function like a sponge that forms oxides of various compositions. Upon annealing to 900 K, oxygen is transferred to the substrate and the alkali atoms desorb [246]. In combination with an alkali layer shaped by the CEE, this would allow for the growth of thin SiO_2 μm structures at low temperatures.

Ion Source

While it is characteristic of the CEE that it can be observed on almost any substrate, the amount of charge produced can be strongly increased by deliberately dosing the collision surface with alkali adsorbates. With the full cluster beam of 10^{14} clusters per pulse impinging on an alkali treated surface, a total charge of 10^{-6} C is expected to emerge (10 percent charging efficiency per cluster in the high coverage regime) corresponding to an ion current in the order of mA during the pulse duration of typically 300 μs. Since positive and negative charge carriers are created in comparable amounts, space charge does not play a significant role: the charge cloud equals more a cold 'plasma' with its volume elements each being approximately neutral. Only upon separation in external fields does the mutual repulsion of like charges come into play. The high charging efficiency per cluster (10^{-1} in comparison with 10^{-4} for typical electron impact sources) makes the CEE an ideal multipurpose ion-source, that provides charged clusters of polar molecules. While the positively charged clusters which carry an additional alkali cation are of interest for solvation studies, the negatively charged clusters are 'clean' in the sense that they have only an additional electron. The latter can be photo-detached, so that the CEE can also be used to provide mass selected or high energetic neutral clusters. With respect to spectroscopic investigations or fluorescence imaging, it has the special advantage that it is a 'dark' ion source: contrary to the hot filament of electron impact ionizers, no light is emitted. Moreover, *Chapter* 4 illustrated that the detection of large clusters via secondary electron multipliers faces the problem of decreasing secondary electron yield with increasing cluster size. In the case of polar molecule clusters, the use of an alkali doped conversion surface would efficiently provide charged cluster fragments of reduced size for straightforward detection. The basic idea behind the CEE as an ion source

consists of a two step mechanism for the production of free charge carriers. First, a cation-anion pair is generated which gets separated by cluster fragmentation in a second step. Charge pair generation can be very efficient, for example during a chemical reaction, and has a lower energy threshold compared to a one step mechanism like photo-ionization. The mutual Coulomb interaction is surmounted efficiently by the unspecific cluster fragmentation. This idea can be generalized beyond the system of alkali atoms in polar molecule clusters.

Ion Propulsion

The CEE mass spectra presented here reveal fragment sizes large than 100 molecules. The high ion mass as well as the high charging efficiency per cluster appeal to the field of ion propulsion. The thrust T of a rocket is defined as $T = \dot{m}\ u$ with $\dot{m}$ being the rate of change of rocket mass by exhaust of the propellant and u the exhaust velocity relative to the rocket. At constant u and neglecting gravitational influences, the velocity increment Δv achieved by the ejection of Δm of the initial mass m_0 is given by $\Delta v = u\ \ln(m_0/(m_0 - \Delta m))$. Clearly, it is necessary for u to be comparable with Δv if a significant fraction of the original mass is to be brought to the final velocity. The maximum exhaust velocity from combustion thrusters is about 4500 m/s [247]. To obtain higher exhaust velocities of $\Delta v > 6 \cdot 10^4$ m/s desired for long time missions, electrostatic propulsion systems have been developed wherein the propellant is accelerated by direct application of electric forces to ionized particles. Practical sources are the cesium-tungsten contact source (j_{max}=0.01-0.02 A/cm^2, ion creation energy 500-700 eV) and the electron bombardment source (j_{max}=0.005-0.01 A/cm^2, ion creation energy 300-600 eV). During 1997 two communication satellites equipped with Xe ion propulsion systems were launched . They produced about 18 mN of thrust (Δm=7 10^{-4} g/s = 3.2 10^{18} atoms/s, ionization probability 0.7, u_e=5 10^4 m/s, acceleration potential 1.2 kV, ion creation energy 1000 eV/ion) at a power consumption of 500 W which is primarily needed for system heating (1100^{0}C) and cooling. A CEE based ion propulsion system would be similar to the contact source. However, efficiency is not limited by the Cs desorption flux from the hot tungsten surface, but rather by the supply of neutral alkali atoms to the active area of the collision target which needs less energy. From a 1 cm^2 orifice of a potassium oven at 340^{o}C an atom flux of 4.5 10^{20} atoms/s can be obtained and then converted into ions. This is the thrust limiting step because the cluster flux density has no practical limits. On the other hand each cluster can only be effective for a single collision whereupon most of its material is lost unionized. According to present knowledge, 0.5 percent of the exhaust mass can be ionized at high coverages. It remains to be shown whether this deficiency is overcompensated for by obvious advantages such as very low ion creation energy, no space charge limitations, positive and negative charge carriers, variable mass to charge ratios and high impulsive thrust.

Aerosol Detection

Instead of analyzing a substrate surface, the CEE on alkali treated collision targets can be applied to characterize the impinging cluster. The alkali pickup by polar molecule clusters efficiently leads to charged fragments which can be mass analyzed in a straightforward manner. A natural occurrence of such polar molecule clusters are the ubiquitous aerosols of the atmosphere, the composition of which, besides their content of polar water molecules, is in the focus of atmospheric chemistry [248]. Charge generation has previously been observed during the passage of rocket-born electrostatic particle-detectors through Noctilucent Clouds [249], an atmospheric structure

that typically forms at an altitude of 83 km. This is interpreted as the signature of ice particles impinging with velocities of 800 m/s on the detector [111]. The new insight provided by the CEE into the relevant charge generation mechanism, allows for the development of improved detectors for atmospheric submicron ice particles, which should facilitate a direct composition analysis. Additionally, by providing bi-polar cluster fragment spectra different aspects of the cluster composition are emphasized: while the positive mass spectra -due to the relative immobility of the alkali cation in the cluster- will reflect the statistic composition of the cluster, the negative spectra -since water molecules have no molecular electron affinity- tend to emphasize cluster constituents with electron affinity, where the highly mobile electron preferentially resides (see Chap. 7). An interesting aspect of Noctilucent Clouds and regions of so called Polar Mesospheric Summer Echoes (PMSE) structures, which also appear in an altitude of 83-90 km, is the large deviation from the expected electron density and mean ion mass [250] which has been observed and which is not yet fully understood. However, a layer of neutral sodium is known to exist in an altitude between 70 km and 110 km with densities between 10^2 cm^{-3} and 10^{-4} cm^{-3} peaking around 90 km [251]. This coincidence between the observation of charge carriers with the presence of water clusters and sodium strongly hints at the CEE as a potential mechanism. Interestingly, the existence of sodium and potassium in the tenuous ($p < 10^{-10}$ mbar) atmospheres of the Moon and Mercury has also been established [252, 253]. The presence of the polar molecules SO_2 or water has been detected for a variety of celestial bodies among which are Venus, Callisto, Europa and with 98 % most prominent the Jupiter moon Io [254]. Apart from that, the CEE has to be taken into account as a source of spurious signals during the operation of rocket-borne or aircraft-borne mass spectrometers. How far the lower impact velocity on the respective sampling systems is compensated by cluster size remains to be shown.

Atmospheric Electrification

Moreover, the clusterelectric effect might have possible implications concerning natural electrification processes. The accepted mechanisms for the creation of ions and electrons in the atmosphere are cosmic rays and radioactive decay at the Earth's surface [255]. The experimental results presented here suggest that alkali atoms should also be considered as a source of charge carriers, in particular at significant aerosol concentrations after, e.g., volcanic eruptions. The electrification might occur as follows: a hydrometeor picks up one or several alkali atoms upon collision with an aerosol and increases its intrinsic conductivity through the formation of solvated cations and electrons. This enables one of the many possible cloud charging mechanisms [256] to become effective, or the hydrometeor may directly burst into charged pieces.

Neutral Pickup

A further application is contained in the rich spectra observed for the CEE on untreated, freshly mounted surfaces, namely in the tendency of the impinging cluster to incorporate arbitrary surface adsorbates. In combination with alkali adsorbates, this can lead to a transfer of the co-picked up species into the gas-phase within ionic cluster fragments. It is worthwhile exploring this observation in more detail, as it can contribute to the long-standing problem of transferring large molecules into the gas-phase. The proposed mechanism of cluster-induced desorption combined with alkali-induced charging can complement existing methods like Electrospray or MALDI. Since large molecules generally have some functional group with electron

affinity, the formation of the respective gas phase anions can be enhanced by employing clusters built from polar molecules without molecular electron affinity, like water or ammonia. In this case, the electron, injected into the cluster as consequence of the concomitant alkali pickup, settles preferentially with the molecule of interest. In this case it would also be possible to evaporate a large number of the solvent molecules in the cluster fragments by appropriately chosen impact conditions, so that the molecular ion is transferred almost bare into the gas phase, as it has been observed here for the alkali cations. At the same time, the evaporation of the solvent shell drains energy out of the system, so that the remaining molecular ions are cold with respect to internal excitations.

8.2 Implications of Cluster Impact Mass Spectrometry

The Clusterelectric Effect (CEE) and the concept of Cluster Impact Mass Spectrometry (CIMS) in general, represent not only a rich subject for scientific research in themselves but may also be applied as a means of investigation.

Cluster Ions

While the present study is centered on large clusters for which size dependencies play a minor role, cluster size effects are a general focus of current research. An ion source based on the CEE allows the generation of intense size-selected beams of polar molecule cluster with variable energy. Two relevant scientific fields have already been identified in the introduction: on the one hand there are high-energy cluster-surface collisions which open up the way to a new regime of chemistry under extreme conditions. Studies with monodisperse clusters allow for the separation of the cluster-size effect from the influence of the collision energy [21]. On the other hand, there is the interaction of strong laser fields with molecular clusters which provide bulk density directly to the laser focus. Work with size-selected clusters would test the ionization mechanism based on electron impact ionization induced by field-ionization electrons that move coherently in the external field [29]. Additionally, the CIMS method lends itself naturally to the investigation of ionization processes inside molecular clusters. The surprisingly high yield of SO_2 cluster anions upon electron impact ionization with 30 eV electrons, in Chap. 3.3, indicates an efficient recapturing process of secondary electrons set free by the primary ionization event. This would lead to the formation of neutral clusters that contain cation/anion pairs. Such a process in clusters with high electron affinity would be relevant to all cluster size determinations involving positive ion formation. A CIMS experiment involving a SF_6 cluster beam (no CEE), out of which all cluster ions have been extracted following electron impact ionization, could prove this mechanism. The seemingly neutral cluster should break up into charged fragments upon surface collision.

Solvation and Catalysis

The positively charged cluster fragments generated during the CEE all carry an alkali cation. They are therefore of interest with respect to studies of the solvation of metal cations [9, 10]. The charged cluster fragments allow mass selection and thus to work with monodisperse solvation structures, which is important for spectroscopic analysis. The study of successively larger clusters containing ions mimics the solvation process in solution and provides a microscopic view of the solvation structure and dynamics. Moreover, a strong reactivity enhancement was observed between neutrals

clustered on metal cations [257]. For example, the rate constant for the homogenous gas phase reaction of N_2O_5 with NO to form N_2O_4 and NO_2 is increased by at least seven orders of magnitude when bound to a sodium ion and in excess of nine orders of magnitude in the case of Li^+ [257]. The clusterelectric effect allows for a straight forward creation of such metal ion doped clusters to study these ion-catalytic effects in more detail. A first example in this direction is the observed ion-molecule reactions of the alkali cation in SF_4 clusters. Generally, the composition of clusters with respect to the reaction educts can be influenced by adiabatic expansion of gas mixtures as pointed out in Chap. 2.1.4. In this context, the CIMS method, which makes reaction products visible, opens up a new approach to ion-induced chemistry.

Dissolution

As has been the tenor of the present work, CIMS is the method of choice to inspect chemical processes inside molecular clusters, especially if they lead to the formation of intracluster cation-anion pairs. The most fundamental of such processes is the dissolution of a salt in a solvent. Although the macroscopic phenomenon belongs to every-day experiences, the microscopic processes are not yet understood [258]. The CIMS method allows for new insight in this interesting field. By loading solvent clusters with salt molecules, a successful solvation would become manifest from the presence of charged cluster fragments upon fragmentation which carry the respective core ions. The seeded beam technique allows to influence the important parameter of cluster temperature for this kind of experiments. Moreover, by varying the time between pickup and fragmentation, dynamic aspects of the dissolution process could also be investigated.

Reaction

Chemical reactions that lead to the formation of cation/anion pairs can also be readily investigated by the CIMS method. Among these are proton transfer reactions which play a cardinal role in a number of chemically as well as biologically relevant processes, of which, however, many details remain to be clarified [259]. As experimental proof-of-principle the excited-state proton transfer reaction of 1-naphthol to a surrounding water or ammonia cluster is suggested. This has already been studied in detail using spectroscopic methods [12, 259, 260]. The CIMS investigation would allow to directly monitor the ionic reaction products via the charged fragments set free by the collision-induced disintegration of the molecular test tube. Another important field of investigation to which the CIMS technique can contribute is ion-molecule reactions. In Chap. 7, the mass spectra of the SF_4 system revealed the signature of ion-molecule reactions induced by the cation as well as the electron injected into the cluster in the course of the CEE. In a bulk-like cluster environment the interaction of SF_4^- with SF_4 is observed to result in the formation of SF_5^-. The generalization of this comprises the interaction of electrons or ions with molecular clusters to investigate ion-molecule half-reactions [72] at bulk density. While in this case the cluster is generally charged and can in principle be analyzed directly, its fragmentation during CIMS clarifies the exact nature of the incorporated charge carriers, which otherwise might be obscured when both reaction partners remain inside the cluster (isobaric processes). Moreover, by applying CIMS to molecular clusters ionized directly via electron impact ionization or photo-ionization, the result of ion-molecule reactions can be studied without the influence of a relative angular momentum between the reaction partners, which in the case of collision complexes, can influence the decay kinetics of the complex as well as the dispersion of excess energy among the products

[72].

Coherent Control

Recent progress concerning the experimental availability of shaped femtosecond laser pulses [261, 262] as well as with regard to the theoretical basis of coherent chemical control [263] presents a step in the direction of the longstanding desire to steer the outcome of chemical reactions on-the-fly by means of vibrational excitation of the reactive coordinates on the ground-state potential surface. While coherent control of small gas phase molecules is presently worked on [261, 262, 264] the ultimate challenge remains to transfer this technique to large molecules or even the condensed state. Here, coherent control has to defeat the rapid de-phasing times. A model system to explore coherent control in such a complex environment is proposed to be intermolecular proton transfer that can readily be investigated at bulk density by the combination of molecular test tubes with the CIMS technique. An interesting candidate, which combines conceptual simplicity with high fundamental importance, is the autoprotolysis reaction of bulk water, as induced by vibrational overtone excitation [114].

Chapter 9

Summary and Outlook

The motivation behind this work is the desire to obtain direct insight into the physical and chemical processes of bulk liquids, in particular charge transfer or charge separation processes in a polar solvent. This class of processes are fundamental to our every day experience, nevertheless they still lack complete understanding, not least with respect to their inherent dynamics. Typical examples are electron transfer reactions like the spontaneous ionization of alkali atoms in liquid ammonia, proton transfer reactions as exemplified in the autoprotolysis reaction of bulk water, and solvation phenomena like the dissolution of sodium chloride in a solvent. Direct observation of these processes has up to now been impeded by the contrast between the high particle density which defines these bulk processes and the need to do analysis on a single particle level.

The central idea presented in this work is to employ molecular clusters as 'test tubes' in which the above processes can be initiated at bulk density, and to inspect the result by disintegrating the cluster via a low-energy cluster-surface collision. The fragmentation of the cluster causes the contents of the 'test tube' to spill out and it transfers the reaction products into the gas phase in the form of single molecules or small-sized aggregates that allow for straightforward and unambiguous analysis in a mass spectrometer. Of central importance is the unique division between strong intramolecular and weaker intermolecular binding energy regimes which occurs in molecular clusters. By coupling energy into the cluster via a low-energy surface collision, the weak intermolecular bonds can be ruptured without activating the strong intramolecular ones, so that the chemical nature of the cluster constituents is not changed. Whilst in general, mass spectrometric analysis requires suitable post-ionization of the released cluster content, the aforementioned processes all result in charged products which can be directly analyzed.

For the experimental analysis of bulk processes via collision-induced fragmentation of molecular clusters – termed Cluster Impact Mass Spectrometry (CIMS) – a molecular beam apparatus which is capable of producing and characterizing molecular clusters including mixed species containing different reactants, was constructed. The analysis stage consists of a collision target, on which alkali metal adsorbates can be deposited, and a home-built large-extraction-volume time-of-flight spectrometer. The latter allows for bi-polar as well as quantitative ion detection. During the course of the work, a new design for the TOF spectrometer electrodes was developed, the com-

position of mixed clusters has been investigated and modeled, and electron-recapture processes during the ionization of molecular clusters were discovered.

A proof-of-principle demonstration of the CIMS method is given in terms of the first direct observation of autoprotolysis in a water cluster. The main result of the present work consists of the elucidation of the microscopic mechanism behind the hitherto unexplained charge generation which occurs during the low-energy cluster-surface collision of water as well as sulphur dioxide clusters. CIMS measurements revealed an electron-transfer reaction between a reactant picked up during the cluster-surface collision and the cluster constituents. Backed by evidence from experiments with different clusters of e.g. sulphur dioxide, water, ammonia and sulphur tetrafluoride, in combination with alkali and indium surface adsorbates, this mechanism (termed the 'Clusterelectric Effect' (CEE)) is recognized as a new electrification mechanism that in general pertains to systems consisting of polar molecule clusters and easy-to-ionize surface adsorbates. The mechanism itself is modeled via three fundamental steps that take place in a concerted way during the picosecond time scale of the cluster-surface collision. During impact, the surface adsorbate is picked up by the cluster (1), due to the interaction with the polar cluster constituents it looses its valence electron (2) and the thereby formed geminate ion pair is separated by the collision-induced cluster fragmentation (3). The proposed mechanism of Cluster-Induced Desorption of the adsorbate is based on the impulsive interaction of the cluster constituents with the collision surface as well as with the adsorbate directly. The coincidence of desorption with the presence of the cluster at the surface leads to an efficient incorporation of the alkali atom into the cluster. Delocalization of e.g. alkali valence electrons in polar solvents, is generally known from previous equilibrium investigations of the bulk as well as of clusters. However, the rapid time scale of the cluster-surface collision, as well as the perturbation induced by the impact, precludes the formation of an equilibrium solvation structure around the picked up species. To explain the observed ion pair formation within the cluster, a fast electron transfer mechanism is proposed that is based on field ionization by the partial point charges connected to the polar cluster constituents. The separation of the geminate charge pair takes place if they are embedded on different cluster fragments. The energy to overcome the mutual Coulomb interaction and to form the free charge carriers is provided – in the form of Inertial Charge Separation – via the kinetic energy of the respective cluster fragment. Experimental evidence is given that the incorporated charge carriers can induce a variety of ion-molecule reactions in the surrounding solvent, for example, the electron-induced fluoride transfer between clustered SF_4 molecules. This indicates the possibility to investigate ion-molecule reactions or electron-induced reactions using a combination of alkali atom pickup and CIMS.

Outlook

With the Clusterelectric Effect, a new electrification mechanism has been discovered, which not only explains the previously observed charge generation for low energy cluster-surface collisions of water and sulphur dioxide clusters, but has a much broader relevance. In the present work, its microscopic mechanism has been revealed and has been shaped into a graphic model. Special emphasis has been given to explore the various aspects of this amazing, zero-order phenomenon to identify fields of further, fruitful work. Although the proposed Clusterelectric Effect seems to allow a consistent explanation of the experimental observations, each of the three aspects of

the proposed model, namely the adsorbate pickup, the charge delocalization and the cluster fragmentation, deserves a more detailed investigation. I hope that the present work can be an incentive as well as a guiding line for further investigations of the complex details involved in the Clusterelectric Effect.

Appendix A

Reprint of *Nature* 400 544-547 (1999)

letters to nature

We first compare the size dependence of the bandgap E_g, as extracted from the tunnelling data, with the nanocrystal sizing curve (Fig. 3a). The sizing curve (open diamond data points) was obtained by correlating the average nanocrystal size (that is, radius r), measured using transmission electron microscopy (TEM), with the excitonic bandgap of the same sample[9,24]. To compare these data with the tunnelling results, we have added a correction term, $1.8e^2/r$, to compensate for the electron–hole excitonic Coulomb interaction which is absent in the tunnelling data[4] (here e is the electron charge). Agreement is good for the larger nanocrystal radii, with increasing deviation for smaller nanocrystals. The deviation occurs because the TEM sizing curve provides a lower limit to the nanocrystal radius due to its insensitivity to the (possibly amorphous) surface layer. On the other hand, the size extracted from the STM topographic images is overestimated because of the tip–nanocrystal convolution effect[20]. These differences should be more pronounced for the small sizes, as is indeed observed.

Next, in Fig. 3b, we compare the size dependence of the higher strongly allowed optical transitions with the level spacings measured by tunnelling spectroscopy. We plot excited level spacings versus the observed bandgap for both PLE and tunnelling spectra, thus eliminating the problem of QD size estimation discussed above. The two lower data sets (II) in Fig. 3b compare the difference between the first strong excited optical transition and the bandgap from PLE (E3–E1 in ref. 9), with the separation $\Delta_{VB} = 2_{VB} - 1_{VB}$ in the tunnelling data (open and filled squares, respectively). The excellent correlation observed enables us to assign this first excited transition in the PLE to a $2_{VB} - 1S_e$ excitation, as shown schematically in the inset of Fig. 3. Strong optical transitions are allowed only between electron and hole states with the same envelope-function symmetry. We thus infer that the envelope function for state 2_{VB} should have s character and this state can be directly identified as the $2S_{3/2}$ valence band level[9].

Another important comparison is depicted by the higher pair of curves in Fig. 3b (set III). The second strong excited optical transition relative to the bandgap (E5–E1 in ref. 9) is plotted along with the spacing $\Delta_{CB} = 1P_e - S_e$ from the tunnelling spectra. Again, excellent correlation is observed, which allows us to assign this peak in the PLE to the 1_{VB}–$1P_e$ transition (Fig. 3, inset). The top-most valence band level, 1_{VB}, should thus have some p character for this transition to be allowed. From this, and considering that the bandgap optical transition 1_{VB}–$1S_e$ is also allowed, we conclude that 1_{VB} has mixed s and p character. It is not clear at present whether there is an intrinsic mixing[22] or degeneracy between different states having s and p characteristics[9]. Scanning tunnelling spectroscopy experiments in a magnetic field may resolve this issue.

The good correlation between optical transitions and the spacing of levels observed in the tunnelling spectra indicates that the charging did not have a significant effect on the QD level structure. The tunnelling I–V curves are thus well described as an algebraic sum of single electron charging energies and the QD level spacings. □

Received 10 March; accepted 4 June 1999.

1. Alivisatos, A. P. Semiconductor clusters, nanocrystals, and quantum dots. *Science* **271**, 933–937 (1996).
2. Kastner, M. A. Artificial atoms. *Phys. Today* **46**, 24–31 (1993).
3. Ashoori, R. C. Electrons in artificial atoms. *Nature* **379**, 413–419 (1996).
4. Brus, L. E. Electron-electron and electron-hole interaction in small semiconductor crystallites. The size dependence of the lowest excited electronic state. *J. Chem. Phys.* **80**, 4403–4409 (1984).
5. Norris, D. J., Sacra, A., Murray, C. B. & Bawendi, M. G. Measurement of the size dependent hole spectrum in CdSe quantum dots. *Phys. Rev. Lett.* **72**, 2612–2615 (1994).
6. Leon, M., Petroff, P. M., Leonard, D. & Fafard, S. Spatially resolved visible luminescence of self-assembled semiconductor quantum dots. *Science* **267**, 1966–1968 (1995).
7. Gammon, D., Snow, E. S., Shanabrook, B. V., Katzer, D. S. & Park, D. Homogenous linewidths in the optical spectrum of a single gallium arsenide quantum dot. *Science* **273**, 87–90 (1996).
8. Empedocles, S. A., Norris, D. J. & Bawendi, M. G. Photoluminescence spectroscopy of single CdSe nanocrystallite quantum dots. *Phys. Rev. Lett.* **77**, 3873–3876 (1996).
9. Banin, U. *et al.* Size dependent electronic level structure of InAs nanocrystal quantum dots: Test of multiband effective mass theory. *J. Chem. Phys.* **109**, 2306–2309 (1998).
10. Herzberg, G. *Atomic Spectra and Atomic Structure* Ch. 3 (Prentice-Hall, New York, 1937).
11. Guzelian, A. A., Banin, U., Kadavanich, A. V., Peng, X. & Alivisatos, A. P. Colloidal chemical synthesis and characterization of InAs nanocrystal quantum dots. *Appl. Phys. Lett.* **69**, 1432–1434 (1996).
12. Mucic, R. C., Storhoff, J. J., Lestinger, R. L. & Mirkin, C. A. A DNA-based method for rationally assembling nanoparticles into macroscopic materials. *Nature* **382**, 607–609 (1996).
13. Alivisatos, A. P. *et al.* Organization of nanocrystal molecules using DNA. *Nature* **382**, 609–611 (1996).
14. Colvin, V. L., Schlamp, M. C. & Alivisatos, A. P. Light-emitting diodes made from cadmium selenide nanocrystals and a semiconductor polymer. *Nature* **370**, 354–357 (1994).
15. Klein, D. L., Roth, R., Lim, A. K. L., Alivisatos, A. P. & McEuen, P. L. A single electron transistor made from a cadmium selenide nanocrystal. *Nature* **389**, 699–701 (1997).
16. Colvin, V. L., Goldstein, A. N. & Alivisatos, A. P. Semiconductor nanocrystals covalently bound to metal surface with self-assembled monolayers. *J. Am. Chem. Soc.* **114**, 5221–5230 (1992).
17. Grabert, H. & Devoret, M. H. (eds) *Single Charge Tunneling* (Plenum, New York, 1992).
18. Alperson, B., Cohen, S., Rubinstein, I. & Hodes, G. Room-temperature conductance spectroscopy of CdSe quantum dots using a scanning force microscope. *Phys. Rev. B* **52**, R17017–R17020 (1995).
19. Porath, D., Levi, Y., Tarabia, M. & Millo, O. Tunneling spectroscopy of a single C_{60} molecule in the presence of charging effects. *Phys. Rev. B* **56**, 9829–9833 (1997).
20. Wiesendanger, R. *Scanning Probe Microscopy and Spectroscopy* (Cambridge Univ. Press, 1994).
21. Ekimov, A. I. *et al.* Absorption and intensity-dependent photoluminescence measurements on CdSe quantum dots: assignment of the first electronic transitions. *J. Opt. Soc. Am. B* **10**, 100–107 (1993).
22. Fu, H. & Zunger, A. Excitons in InP quantum dots. *Phys. Rev. B* **57**, R15064–R15067 (1998).
23. Bertram, D., Micic, O. I. & Nozik, A. J. Excited state spectroscopy of InP quantum dots. *Phys. Rev. B* **57**, R4265–R4268 (1998).
24. Banin, U., Lee, J. C., Guzelian, A. A., Kadavanich, A. V. & Alivisatos, A. P. Exchange interaction in InAs nanocrystal quantum dots. *Superlattices Microstruct.* **22**, 559–567 (1997).
25. Alperson, B., Hodes, G., Rubinstein, I., Porath, D. & Millo, D. Energy level tunneling spectroscopy and single electron charging in individual CdSe quantum dots. *Appl. Phys. Lett.* (in the press).

Acknowledgements. We thank B. Alperson, G. Hodes and I. Rubinstein for discussions. This work was supported in part by the Israeli Academy of Sciences and Humanities. U.B. acknowledges the support of an Alon fellowship.

Correspondence and requests for materials should be addressed to O.M. (milode@vms.huji.ac.il).

Surface impact ionization of polar-molecule clusters through pickup of alkali atoms

C. R. Gebhardt, H. Schröder & K.-L. Kompa

Max-Planck-Institut für Quantenoptik, Hans-Kopfermann-Strasse 1, 85748 Garching, Germany

The observation that clusters of neutral H_2O (refs 1–4) or SO_2 (ref. 5) molecules, on impact with essentially any solid surface, can decay efficiently into positively and negatively charged fragments has defied explanation, not least because the kinetic energy per molecule can be much smaller than the molecular ionization potentials. Here we present a microscopic model of the charging mechanism, based on a mass analysis of charged SO_2 cluster fragments, which appears to be applicable to polar-molecule clusters more generally. Our mass spectra reveal that all positively charged fragments carry an alkali ion (sodium, potassium or caesium), whereas the negative fragments are simply $(SO_2)_n^-$. The yields of both charged species are comparable, and can be enhanced significantly by pre-treating the sample surface with additional alkali atoms. The key to charge separation in the clusters therefore appears to be the pickup of a neutral (but readily ionized) adatom during impact, followed by delocalization of the adatom's valence electron within the cluster and the subsequent collision-induced fragmentation of the cluster into charged pieces. This process could be of practical use in, for example, charge-pair generation and surface analysis; it may also be relevant to atmospheric ionization processes.

We performed the experiments in a conventional two-chamber molecular-beam apparatus (background pressure, 10^{-7} mbar). Clusters are produced by condensation in a seeded free-jet expansion through a pulsed nozzle (diameter 0.5 mm, typical pulse width 400 μs, stagnation pressure up to 20 bar). The cluster size distribution is measured with the retarding field technique[6] employing 30-eV electron impact ionization. The target is mounted in the second chamber perpendicularly to the beam axis, 300 mm downstream from the nozzle. We estimate that a fraction of 2×10^{-4} of the uncondensed particles leaving the nozzle arrive at the surface where

the beam diameter is 8 mm. Most experiments are performed on the SiO_x surface of commercial silicon wafers or on gold (deposited by electrolysis on steel) at a temperature between 400 K and 600 K; that is, under conditions where weakly bound molecular adsorbates have already desorbed. The surface can be pre-treated with alkali-metal atoms by means of an oven source. A plate capacitor arrangement, formed by the target and a grid placed 10 mm in front of it, allows us to measure the total yield of positive and negative charges per pulse. The grid is also used to transfer fragment ions into the detection volume of our pulsed Wiley-McLaren-type time-of-flight mass spectrometer, which has been further optimized for a large extraction volume[7]. The front face of its microchannel plate detector was grounded to ensure that positive and negative ions impinge with the same energy.

Screening experiments have been performed for a variety of clusters striking metallic, as well as insulating, targets. No charge separation is observed for clusters formed by the non-polar molecules O_2, N_2, CO_2, SF_6, and the noble gases Ne, Xe, Kr. In contrast, clusters of H_2O, SO_2, NO, NH_3, NO_2, SF_4, CH_3CN, $CHClF_2$ and isobutene all break into positively and negatively charged fragments on striking the target. This emphasizes that the existence of a permanent molecular dipole moment is required. We chose to examine the SO_2 molecule because it is chemically stable, it lacks complications due to hydrogen bonding and autodissociation[8] and clusters are readily produced at room temperature. In contrast to the very low electron affinities of small NH_3 or H_2O clusters[9], the electron affinity of a single SO_2 molecule is ~1 eV (ref. 10), which greatly facilitates the formation of stable anion clusters.

By seeding SO_2 in Ne, He and H_2 and applying various reservoir pressures, neutral clusters are produced with variable average sizes $\bar{N}$ and velocities v. From the investigated parameter ranges (v = 750–1,750 m s^{-1}, $\bar{N}$ = 1–750) we deduce a threshold velocity close to 10^3 m s^{-1} ($\bar{N} \approx 300$), and a minimum average cluster size of about $\bar{N} = 20$ ($v \approx 1.2 \times 10^3$ m s^{-1}). Comparable thresholds have been reported[1,2] for clusters of water molecules. The impact of a beam of individual SO_2 molecules ($v \approx 1.2 \times 10^3$ m s^{-1}) does not produce any detectable charges.

The four mass spectra of SO_2 cluster fragments, which are partially displayed in Fig. 1, illustrate our explanation of the way in which the impact of a cluster on a surface can lead to the production of positively and negatively charged cluster fragments. The spectra of negatively charged species exhibit a single feature, namely $(SO_2)_n^-$. The corresponding cations, $(SO_2)_n^+$ were never observed. Instead, as shown by the assignment, the cations all carry one alkali-metal ion, in this case Na, K or Cs; we have also observed Li. Moreover, pre-treating the surface with, for example, Cs atoms causes a pronounced increase of the corresponding $Cs^+(SO_2)_n$ peaks (marked with arrows); it also produces an increase of all the $(SO_2)_n^-$ peaks, along with an equal increase of the total amount of positive and negative charges. Further treatment of the surface finally leads to a charging efficiency of several per cent per cluster striking the surface. This strong charge-separation signal only gradually disappears after the Cs source has been turned off. This indicates that possible pickup of isolated alkali-metal atoms from the vapour phase is not important, and illustrates the connection between pickup and removal of alkali adatoms from the surface.

We have also measured fragment mass spectra for H_2O, NH_3 and SF_4. Again, cations carrying an alkali ion are observed, thus confirming the proposed explanation. In the case of NH_3 and SF_4, we also find indications of intracluster ion–molecule reactions; for H_2O clusters, we find the signature of autoprotolysis. For systems with negligible molecular electron affinity, like water and NH_3, no (or only weak) negative spectra could be recorded. In such systems,

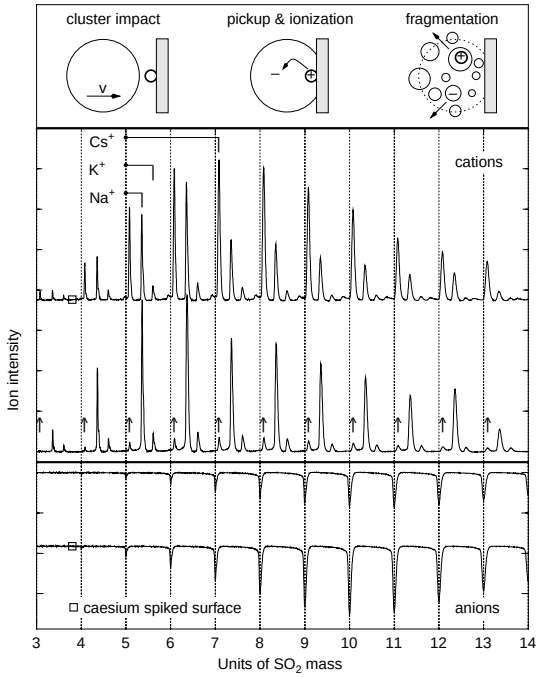

Figure 1 Spectra of positive and negative SO_2 cluster fragments. The clusters have an incident velocity of 1.2×10^3 m s^{-1}, a mean cluster size of 500, and strike a sample consisting of electrolytic gold on steel at 600 K. The mass scale is given in units of SO_2 mass. The cluster cations all carry an additional alkali-metal ion. These atoms originate from a ubiquitous surface contamination and were picked up from the surface during the course of cluster impact (top). Pre-treating (spiking) the surface with Cs increases the yield of the corresponding $Cs^+(SO_2)_n$ progression (marked by arrows) and the overall anion yield.

letters to nature

the shallow Coulomb traps inside our agitated cluster fragments are unable to stabilize the delocalized electron. Hence, the electrons may become detached from the cluster or disappear into the surface. To test this argument, we doped NH_3 clusters with a potential electron scavenger by adding SO_2 as background gas into the nozzle chamber, whereby a pronounced anion spectrum could be recorded. However, reactive intracluster contributions can not be excluded.

Using SO_2 clusters the richest spectrum was observed from a randomly selected pebble, which was used as target without pretreatment. The observation of surface impact ionization in this case shows the ubiquity of alkali-metal atoms on surfaces. Although we are not able to reliably identify the large number of additional peaks, it appears that simultaneous co-pickup of additional neutral species from the surface occurs. Similar rich patterns have been observed from freshly mounted targets held at room temperature. This points to the surface-analytical potential of the surface impact ionization of clusters, which is strictly non-destructive because only adsorbates are picked up.

We also tested the ability of other metal atoms to induce surface impact ionization of clusters by doping the surface via a resistively heated steel loop mounted close to the target. Although *ex situ* surface analysis confirmed the presence of Fe, Ni, Mn and Cr, the observed strong signal was caused exclusively by K and Na atoms. However, an indium-loaded surface seemed indeed to produce the corresponding $(SO_2)_n{}^{115}In^+$ ions, thus indicating that the metal atom needs to have a low ionization potential, rather than the special s^1 electron configuration found in the alkali-metal atoms.

To learn more about the pickup process, the surface was covered with NaCl. Neither strong $Na^+(SO_2)_n$ peaks nor any Cl^- carrying anions could be observed. This shows that dissolution of salts does not occur on the timescale of cluster impact, and confirms that atoms in their neutral state are inducing the ionization of fragmenting clusters. In other words, oxidation proceeds much faster than cluster breakup. The general persistence of neutral alkali atoms on surfaces—though surprising—is known from surface analyses applying post-ionization of sputtered neutral particles[11].

Metal-atom-doped clusters in the gas phase have frequently been studied[12–15]. Direct electron delocalization in polar molecular clusters analogous to the liquid phase has been demonstrated for alkali atoms (ref. 16 and references therein; ref. 17), as well as group III metal atoms (ref. 28). Also, accurate molecular dynamics simulations of small solvated structures are available[18–20]. However, these investigations consider only the equilibrium state reached on a long timescale. Information about the early dynamics of valence-electron delocalization in polar environments has not been available up to now. In the case of surface impact ionization, delocalization has to proceed in the short time window between the cluster–surface contact and the impact-induced fragmentation of the cluster. This window is of the order of the advection time (cluster diameter/cluster velocity), that is, only about one picosecond under our experimental conditions: this is even shorter than (or at most comparable to) electron solvation times[21,22]. Furthermore, we note that SO_2 (electron affinity ~1 eV, dipole moment ~1.6 debye) and NH_3 (≈0 eV, 1.3 debye) clusters show strong surface impact ionization, although their ability to stabilize an electron is very different[23]. From these arguments we conclude that the delocalization of the electron proceeds without a barrier and independently of subsequent ion or electron solvation processes. We propose that the Coulomb fields of the partial point charges associated with the polar environment causes electron delocalization, in a process quite similar to field ionization.

The cluster clearly remains neutral until the collision-induced fragmentation induces the spatial separation of the charge carriers. The energy to overcome the mutual Coulomb attraction is supplied by the kinetic energy of the fragments (inertial charge separation). This concept of examining ion pair formation in neutral clusters through impact fragmentation promises to be useful in the investigation of chemical reactions inside clusters, or cluster-size-dependent solvation of salts. In the context of our experiments, the necessity of cluster fragmentation to make charge separation observable rationalizes the existence of a threshold velocity. Also, the existence of a minimum cluster size seems to be quite natural, because a single molecule can neither pick up an atom nor delocalize an electron.

Cluster fragmentation is an issue of general interest[24,25]. Owing to the varying mean cluster size $\bar{N}$ within the pulse, we found very small fragments ($n \approx 6$) at the beginning but up to $n \approx 100$ towards the end of the supersonic pulse. This indicates a clear trend: large clusters burst into large fragments.

The effect we report here promises to be a new and very efficient addition to the known ionization or electrification mechanisms. We expect that it could be applied in a wide variety of situations; for example, generation of heavy anion plasmas, efficient detection of mesospheric cloud particles, ion propulsion systems, creation of size-selected cluster ions for spectroscopy, or detection and removal of alkali-metal atom contamination from surfaces even in extremely low concentrations.

We note a possible implication of our results for natural electrification processes. The accepted mechanisms for the creation of ions and electrons in the atmosphere are cosmic rays and radioactive decay at the Earth's surface[26]. Our experimental results suggest that alkali atoms should also be considered as a source of charge carriers, in particular at significant aerosol concentrations. The electrification might occur as follows: a hydrometeor picks up one or several alkali-metal atoms on collision with an aerosol, and increases its intrinsic conductivity through the formation of solvated cations and electrons. This enables one of the many possible cloud-charging mechanisms[27] to become effective, or the hydrometeor may directly burst into charged pieces. □

Received 22 March; accepted 22 June 1999.

1. Vostrikov, A. A., Dubov, D. Yu. & Predtechenskiy, M. R. Ionization of water clusters by surface collision. *Chem. Phys. Lett.* **139,** 124–128 (1987).
2. Vostrikov, A. A. & Dubov, D. Yu. Surface induced ionization of neutral water clusters. *Z. Phys. D* **20,** 61–63 (1991).
3. Vostrikov, A. A. *et al.* Ionization of water clusters by collision with surface. *Z. Phys. D* **40,** 542–545 (1997).
4. Andersson, P. U. & Pettersson, J. B. C. Ionization of water clusters by collisions with graphite surfaces. *Z. Phys. D* **41,** 57–62 (1997).
5. Christen, W., Kompa, K.-L., Schröder, H. & Stülpnagel, H. Ionization of SO_2-clusters by scattering from surfaces. *Ber. Bunsenges. Phys. Chem.* **96,** 1197–1200 (1992).
6. Hagena, O. F. & Obert, W. Cluster formation in expanding supersonic jets: effect of pressure, temperature, nozzle size and test gas. *J. Chem. Phys.* **56,** 1793–1802 (1972).
7. Chandezon, F., Huber, B. & Ristori, C. A new-regime Wiley-McLaren time-of-flight mass spectrometer. *Rev. Sci. Instrum.* **65,** 3344–3353 (1994).
8. *Gmelin Handbuch* Schwefel, Ergänzungsband 3, 226 (Springer, Berlin, 1980).
9. Lee, G. H. *et al.* Negative ion photoelectron spectroscopy of solvated electron cluster anions, $(H_2O)_n^-$ and $(NH_3)_n^-$. *Z. Phys. D* **20,** 9–12 (1991).
10. Rothe, E. W., Tang, S. Y. & Reck, P. G. Measurement of electron affinities of O_3, SO_2, and SO_3 by collisional ionization. *J. Chem. Phys.* **62,** 3829–3831 (1975).
11. Becker, C. H. & Gillen, K. T. Surface analysis of contaminated GaAs: Comparison of new laser-based techniques with SIMS. *J. Vac. Sci. Technol. A* **3,** 1347–1349 (1985).
12. Tang, I. N., Lian, M. S. & Castleman, A. W. Jr Mass spectrometric study of gas-phase clustering reactions: Hydration of the monovalent strontium ion. *J. Chem. Phys.* **65,** 4022–4027 (1976).
13. Donnelly, S. G. & Farrar, J. M. Size-dependent photodissociation cross sections for $Sr^+(NH_3)_n$, n = 3–6 Rydberg state formation and electron transfer. *J. Chem. Phys.* **98,** 5450–5459 (1993).
14. Weinheimer, C. J. & Lisy, J. M. Vibrational and unimolecular dissociation of mixed solvent cluster ions: $Na^+((CH_3)_2CO)_n(CH_3OH)_m$. *Chem. Phys.* **239,** 357–368 (1998).
15. Ohshimo, K., Tsunoyama, H., Yamakita, Y., Misaizu, F. & Ohno, K. Photoionization and density functional study of clusters of alkali metal atoms solvated with acetonitrile molecules, $M(CH_3CN)_n$ (M = Li and Na). *Chem. Phys. Lett.* **301,** 356–364 (1999).
16. Takasu, R., Misaizu, F., Hashimoto, K. & Fuke, K. Microscopic solvation process of alkali atoms in finite clusters: photoelectron and photoionization studies of $M(NH_3)_n$ and $M(H_2O)_n$ (M = Li, Li^-, Ma^-). *J. Phys. Chem. A* **101,** 3078–3087 (1997).
17. Hertel, I. V., Hüglin, C., Nitsch, C. & Schulz, C. P. Photoionization of $Na(NH_3)_n$ and $Na(H_2O)_n$ clusters: a step towards the liquid phase? *Phys. Rev. Lett.* **67,** 1767–1770 (1991).
18. Barnett, R. N. & Landman, U. Hydration of sodium in water clusters. *Phys. Rev. Lett.* **70,** 1775–1778 (1993).
19. Kim, K. S. *et al.* The nature of a wet electron. *Phys. Rev. Lett.* **76,** 956–959 (1996).
20. Feller, D., Glendening, E. D., Kendall, R. A. & Peterson, K. A. An extended basis set *ab initio* study of $Li^+(H_2O)_n$, n = 1–6. *J. Chem. Phys.* **100,** 4981–4997 (1994).
21. Mosyak, A. A., Prezhdo, O. V. & Rossky, P. J. Solvation dynamics of an excess electron in methanol and water. *J. Chem. Phys.* **109,** 6390–6395 (1998).
22. Rips, I. Electron solvation dynamics in polar liquids. *Chem. Phys. Lett.* **245,** 79–84 (1995).
23. Jortner, J. Cluster size effects. *Z. Phys. D* **24,** 247–275 (1992).
24. Christen, W., Even, U., Raz, T. & Levine, R. D. Collisional energy loss in cluster surface impact: Experimental, model, and simulation studies of some relevant factors. *J. Chem. Phys.* **108,** 10262–10273 (1998).
25. Svanberg, M., Ming, L., Markovic, N. & Pettersson, J. B. C. Collision dynamics of large water clusters.

J. Chem. Phys. **108**, 5888–5897 (1998).
26. MacGorman, D. R. & Rust, W. D. *The Electrical Nature of Storms* 32 (Oxford Univ. Press, New York, 1998).
27. Pruppacher, H. R. & Klett, J. D. *Microphysics of Clouds and Precipitation* 813–814 (Kluwer Academic, Dordrecht, 1996).
28. Di Palma, T. M., Latini, A., Satta, M. & Giardini Guidoni, A. Molecular beam studies of ammonia clustered with metals produced by pulsed laser reactive ablation. *Int. J. Mass Spectrom.* **179/180**, 319–326 (1998).

Acknowledgements. We thank R. D. Levine for discussions, and H.-J. Schmidtke for contributions to the early stage of this work.

Correspondence and requests for material should be addressed to H.S. (e-mail: hms@mpq.mpg.de).

Triple-isotope composition of atmospheric oxygen as a tracer of biosphere productivity

Boaz Luz*, Eugeni Barkan*, Michael L. Bender†, Mark H. Thiemens‡ & Kristie A. Boering§

* *The Institute of Earth Sciences, The Hebrew University of Jerusalem, Jerusalem 91904, Israel*
† *Department of Geosciences, Princeton University, Princeton, New Jersey 08544, USA*
‡ *Department of Chemistry, University of California, San Diego, La Jolla, California 92093, USA*
§ *Departments of Chemistry and of Geology and Geophysics, University of California, Berkeley, California 94720-1460, USA*

Oxygen has three naturally occurring isotopes, of mass numbers 16, 17 and 18. Their ratio in atmospheric O_2 depends primarily on the isotopic composition of photosynthetically produced O_2 from terrestrial and aquatic plants[1–3], and on isotopic fractionation due to respiration[4]. These processes fractionate isotopes in a mass-dependent way, such that ^{17}O enrichment would be approximately half of the ^{18}O enrichment relative to ^{16}O. But some photochemical reactions in the stratosphere give rise to a mass-independent isotope fractionation, producing approximately equal ^{17}O and ^{18}O enrichments in stratospheric ozone[5] and carbon dioxide[6,7], and consequently driving an atmospheric O_2 isotope anomaly. Here we present an experimentally based estimate of the size of the $^{17}O/^{16}O$ anomaly in tropospheric O_2, and argue that it largely reflects the influences of biospheric cycling and stratospheric photochemical processes. We propose that because the biosphere removes the isotopically anomalous stratosphere-derived O_2 by respiration, and replaces it with isotopically 'normal' oxygen by photosynthesis, the magnitude of the tropospheric ^{17}O anomaly can be used as a tracer of global biosphere production. We use measurements of the triple-isotope composition of O_2 trapped in bubbles in polar ice to estimate global biosphere productivity at various times over the past 82,000 years. In a second application, we use the isotopic signature of oxygen dissolved in aquatic systems to estimate gross primary production on broad time and space scales.

The magnitude of the ^{17}O anomaly in the present atmosphere can be estimated by comparing $\delta^{17}O$ and $\delta^{18}O$ of ambient air O_2 (represented by the HLA standard; see Methods) with O_2 that was not affected by stratospheric processes. To make the latter, we built two airtight terrariums in which O_2 was consumed and replaced biologically. Ultraviolet radiation that could lead to mass-independent fractionation was absent. The terrariums contained *Philodendron* plants, soil and natural water. In both terrariums, O_2 production and consumption occurred via the higher plants as well as via bacteria and algae. Illumination was changed during the experiment with the aim of varying the ratio of photosynthesis to respiration, thereby inducing a wide range of $\delta^{18}O$ and $\delta^{17}O$ values.

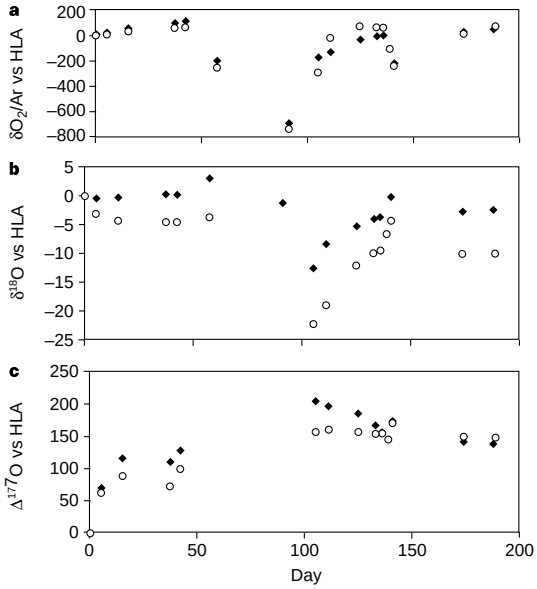

Figure 1 Removal of the atmospheric ^{17}O anomaly by biological cycling. Shown are variations of $\delta O_2/Ar$ (**a**) $\delta^{18}O$ (**b**) and $\Delta^{17}O$ (**c**) in the terrarium experiment. Data points: diamonds, terrarium PK; circles, terrarium PDS. Horizontal scale: days from the beginning of the experiment. Light: continuous illumination, days 1–42; room light, days 43–90; 10 h light, 14 h dark, days 91–136 and days 142–198; dark, days 137–141.

After several turnovers, anomalous ambient air O_2 had been removed by respiration and replaced with normally fractionated O_2, and steady state was attained. Subsequent illumination changes significantly affected O_2 concentration (measured as $\delta O_2/Ar$; see Methods) and $\delta^{18}O$ but not the ^{17}O anomaly (Fig. 1). The $\delta^{18}O$ versus $\delta^{17}O$ trend for data points for which the anomaly was at steady state plot on a nearly perfect straight line ($R^2 = 0.99999$) with a slope of 0.5211 (± 0.0005), as expected for mass-dependent fractionation[8] (data not shown). The intercept of the regression line is $0.155 \pm 0.008‰$ or 155 ± 8 in units of per meg (see Methods). Based on this analysis, we defined the $\Delta^{17}O$ anomaly as the deviation from normal mass-dependent fractionation ($\Delta^{17}O = \delta^{17}O - 0.521\delta^{18}O$); in the case of the terrarium experiment, $\Delta^{17}O$ is equal to the intercept value of the regression line. HLA was the preferred standard for high-precision measurements in our study. However, as a reference for $\Delta^{17}O$ it is admittedly confusing, because it has anomalous isotopic composition. An air sample with no photosynthetic O_2 added will have a $\Delta^{17}O = 0$ with respect to HLA, and a sample of biologically equilibrated O_2 will have a $\Delta^{17}O = +155$ per meg with respect to HLA. In this treatment, ocean and meteoric waters are defined as normal with $\Delta^{17}O = 155$ per meg. A comparison of the isotopic composition of ocean water (represented by V-SMOW) to air O_2 ($\delta^{18}O = -22.960‰$ and $\delta^{17}O = -11.778‰$)[6], supports our conclusions that air bears a mass-independent signature. The $\Delta^{17}O$ of V-SMOW is calculated as 184 per meg [$\Delta^{17}O = (-11.778 - 0.521 \times 22.96)\,1{,}000$]. In this calculation, the derived anomaly is very sensitive to the slope term (0.521), and thus the small difference between 184 and 155 per meg may not be significant.

Importantly, the terrarium experiment cannot represent all Earth-surface processes affecting $\Delta^{17}O$. For example, the range of isotopic variations in global meteoric waters is much greater than in

Bibliography

[1] A.W. Castleman and R.G. Keesee. Gas-phase clusters: Spanning the states of matter. *Science*, 241:36–42, 1988.

[2] P.A. Montano, G.K. Shenoy, E.E. Alp, W. Schulze, and J. Urban. Structure of copper microclusters isolated in solid argon. *Phys. Rev. Lett.*, 56:2076–2079, 1988.

[3] M. Seidl, K.-H. Meiwes-Broer, and M. Brack. Finite-size effects in ionization potentials and electron affinities of simple metal clusters. *J. Chem. Phys.*, 95:1295–1303, 1991.

[4] J. Jortner. Cluster size effects. *Z. Phys. D*, 24:247–275, 1992.

[5] M.P.J. van Staveren, H.B. Brom, L.J. de Jong, and Y. Ishii. Energetics of charged small metal particles. *Phys. Rev. B*, 35:7749–7751, 1987.

[6] D. Kreisle, O. Echt, M. Knapp, E. Recknagel, K. Leiter, T.D. Märk, J.J. Sàenz, and J.M. Soler. Dissociation channels for multiply charged clusters. *Phys. Rev. Lett.*, 36:1551–1554, 1986.

[7] E.K. Parks, B.H. Weiller, P.S. Bechthold, W.F. Hoffmann, G.C. Niemann, L.G. Pobo, and S.J. Riley. Chemical probes of metal cluster structure: Reactions of iron clusters with hydrogen, ammonia and water. *J. Chem. Phys.*, 88:1622–1632, 1988.

[8] C.E. Klots. The evaporative ensemble. *Z. Phys. D*, 5:83–89, 1987.

[9] S.G. Donnelly and J.M. Farrar. Size-dependent photodissociation cross sections for $Sr^+(NH_3)_n$, n=3-6: Rydberg state formation and electron transfer. *J. Chem. Phys.*, 98:5450–5459, 1993.

[10] C. J. Weinheimer and J. M. Lisy. Vibrational and unimolecular dissociation of mixed solvent cluster ions: $Na^+((CH_3)_2CO)_n(CH_3OH)_m$. *Chem. Phys.*, 239:357–368, 1998.

[11] B.D. Kay, V. Hermann, and A.W. Castleman Jr. Studies of gas-phase clusters. *Chem. Phys. Lett.*, 80:469–474, 1981.

[12] O. Cheshnovsky and S. Leutwyler. Excited-state proton transfer in neutral microsolvent clusters: α-Naphthol$\cdot(NH_3)_n$. *Chem. Phys. Lett.*, 121:1–8, 1985.

[13] I. Schek, T. Raz, R.D. Levine, and J. Jortner. Cluster impact chemistry. *J. Chem. Phys.*, 101:8596–8605, 1994.

[14] W. Christen. *Kurzzeitdynamik elektronischer Wechselwirkung von Molekülen und Clustern mit Festkörperoberflächen*. PhD thesis, Ludwigs-Maximilians-Universität München, 1996.

[15] T. Raz. *Cluster-Surface Collsions.* PhD thesis, Hebrew University, Israel, 1996.

[16] C.L. Cleveland and U. Landman. Dynamics of cluster-surface collisions. *Science*, 257:355–361, 1992.

[17] T. Raz and R.D. Levine. Fast translational thermalization of extreme disequilibrium induced by cluster impact. *Chem. Phys.*, 213:263–275, 1996.

[18] R.D. Levine and R.B. Bernstein. *Molecular reaction dynamics and chemical reactivity.* Oxford University, New York, 1987.

[19] I. Schek and J. Jortner. Microshock wave propagation in molecular clusters. *J. Chem. Phys.*, 104:4337–4342, 1996.

[20] T. Raz and R.D. Levine. Four-center reactions: A computational study of collisional activation, concerted bond switching, and collisional stabilization in impact heated clusters. *J. Phys. Chem.*, 99:7495–7506, 1995.

[21] T. Raz, I. Schek, M. Ben-Nun, U. Even, J. Jortner, and R.D. Levine. Dissociation dynamics of diatomic molecules embedded in impact heated rare gas clusters. *J. Chem. Phys.*, 101:8606–8619, 1994.

[22] T. Raz and R.D. Levine. Four-center reactions induced by cluster impact. *J. Am. Chem. Soc.*, 116:11167–11168, 1994.

[23] T. Raz and R.D. Levine. Concerted vs. sequential four-center reactions: A computational study of high-energy dynamics. *J. Phys. Chem.*, 99:13713–13715, 1995.

[24] T. Raz and R.D. Levine. Kinematic model for four-center, AB+CD, reactions. *Chem. Phys. Lett.*, 226:47–55, 1994.

[25] T. Raz and R.D. Levine. On the burning of air. *Chem. Phys. Lett.*, 246:405–412, 1995.

[26] W. Christen and U. Even. Cluster impact chemistry. *J. Phys. Chem. A*, 102:9420–9426, 1999.

[27] B. Gompf, R. Günther, G. Nick, R. Pecha, and W. Eisenmenger. Resolving sonoluminescence pulse width with time-correlated single photon counting. *Phys. Rev. Lett.*, 79:1405–1408, 1997.

[28] D. Lohse, M.P. Brenner, T.F. Dupont, S. Hilgenfeldt, and B. Johnston. Sonoluminescing air bubbles rectify argon. *Phys. Rev. Lett.*, 78:1359–1362, 1997.

[29] T. Ditmire, J.W.G Tisch, E. Springate, M.B. Mason, N. Hay, R.A. Smith, J. Marangos, and M.H.R. Hutchinson. High-energy ions produced in explosions of superheated atomic clusters. *Nature*, 386:54–56, 1997.

[30] T. Ditmire, J. Zweiback, V.P. Yanovsky, T.E. Cowan, G. Hays, and K.B. Wharton. Nuclear fusion from explosions of femtosecond laser-heated deuterium clusters. *Nature*, 398:489–492, 1999.

[31] A. McPherson, T.S. Luk, B.D. Thompson, A.B. Borisov, K. Boyen, and C.K. Rhodes. Multiphoton-induced X-ray emission at 4-5 keV from Xe atoms with multiple core vacancies. *Nature*, 370:631–634, 1994.

[32] C.R. Gebhardt and H. Schröder. Verfahren und Vorrichtung zur Clusterfragmentation. *Deutsche Patentanmeldung Nr 199 34 173.7*, 1999.

[33] C.R. Gebhardt, H. Schröder, and K.L. Kompa. Surface impact ionization of polar-molecule clusters through pickup of alkali atoms. *Nature*, 400:544–547, 1999.

[34] H. Haberland and K.H. Bowen. Solvated electron clusters. In H. Haberland, editor, *Clusters of atoms and molecules*, volume II of *Springer Series in Chemical Physics*. Springer, Berlin, 1994.

[35] S.B. Ryali and J.B. Fenn. Clustering in free jets - aggregation by dispersion. *Ber. Bunsenges. Phys. Chem*, 88:245–253, 1984.

[36] D.R. Miller. Free jet sources. In G. Scoles et al, editor, *Atomic and Molecular Beam Methods*, volume 1, chapter 2, pages 14–53. Oxford University Press, 1988.

[37] H.R. Murphy and D.R. Miller. Effects of nozzle geometry on kinetics in free-jet expansions. *J. Phys. Chem.*, 88:4474–4478, 1984.

[38] J.J. Breen, K. Kilgore, K. Stephan, R. Hofmann-Sievert, B.D. Kay, R.G. Keesee, T.D. Märk, and A.W. Castleman Jr. The use of similarity profiles in studying cluster formation in molecular beams: evidence for the role of pre-existing dimers. *Chem. Phys.*, 91:305–313, 1984.

[39] W. Demtröder and H.-J. Foth. Molekülspektroskopie in kalten Düsenstrahlen. *Phys. Bl.*, 43:7–13, 1987.

[40] M. Kappes and S. Leutwhyler. Molecular beams of clusters. In G. Scoles et al, editor, *Atomic and Molecular Beam Methods*, volume 1, chapter 15, pages 380–415. Oxford University Press, 1988.

[41] A.C. Zettlemoyer. *Nucleation Phenomena.* Wiley, New York, 1977.

[42] G.D. Stein. Cluster beam sources - Predictions and limitations of the nucleation theory. *Surf. Sci.*, 156:44–56, 1985.

[43] D. Lippmann, W.C. Schieve, and C. Canestaro. Clustering time-dependance in molecular dynamics -A kinetic model. *J. Chem. Phys.*, 81:4969–4974, 1984.

[44] O.F. Hagena. Nucleation and growth of clusters in expanding nozzle flows. *Surf. Sci.*, 106:101–116, 1981.

[45] O.F. Hagena. Condensation in free jets: Comparison of rare gases and metals. *Z. Phys. D*, 4:291–299, 1987.

[46] O.F. Hagena and W. Obert. Cluster formation in expanding supersonic jets: Effect of pressure, temperature, nozzle size and test gas. *J. Chem. Phys*, 56:1793–1802, 1972.

[47] J. Farges, M.F. de Feraudy, B. Raoult, and G. Torchet. Noncrystalline structure of argon clusters. I. Polyicosahedral structure of Ar_N clusters, 20<N<50. *J. Chem. Phys.*, 78:5067, 1983.

[48] P.C. Engelking. Determination of cluster binding energy from evaporative lifetime and average kinetic release. *J. Chem. Phys.*, 87:936–940, 1987.

[49] J.W. Brady, J.D. Doll, and D.L. Thompson. Cluster dynamics: A classical trajectory study of $A_n^* \rightarrow A_{n-1}$+A. *J. Chem. Phys.*, 74:1026–1028, 1981.

[50] C.E. Klots. Evaporative cooling. *J. Chem. Phys.*, 83:5854–5860, 1985.

[51] A. Laaksonen, M. Kulmala, and P.E. Wagner. On the cluster compositions in the classical binary nucleation theory. *J. Chem. Phys.*, 99:6832–6835, 1993.

[52] O.F. Hagena. Molekularstrahlerzeugung mit Düsen im Impulsbetrieb. *Z. Angew. Physik*, 16:183–187, 1963.

[53] W. Gentry and C. Giese. Ten-microsecond pulsed molecular beam source and a fast ionization detector. *Rev. Sci. Instrum.*, 49:595–600, 1978.

[54] K.L. Saenger and J.B. Fenn. On the time required to reach fully developed flow in pulsed supersonic free jets. *J. Chem. Phys.*, 79:6043–6045, 1983.

[55] G. Hall, K. Liu, M.J. McAuliffe, C.F. Giese, and W.R. Gentry. State-to-state vibrational excitation of I_2 in collisions with He. *J. Chem. Phys.*, 81:5577–5585, 1984.

[56] K. Schwier. Wärmeübergang im horizontalen Rohr bei laminarer Strömung und seine Beeinflußung durch freie Konvektion und durch die Temperaturabhängigkeit der Stoffwert. Fortschr.-Ber. VDI-Z. Reihe 6 Nr. 6, VDI, 1965.

[57] C.Y. Ng. Molecular beam photoionization studies of molecules and clusters. *Adv. Chem. Phys.*, 52:263–362, 1983.

[58] U. Buck. Scattering analysis of cluster beams: Formation and fragmentation of small Ar_n clusters. *Phys. Rev. Lett.*, 52:109–112, 1984.

[59] J. Jortner. Level structure and dynamics of clusters. *Ber. Bunsenges. Phys. Chem*, 88:188–201, 1983.

[60] T. Leisner, O. Echt, O. Kandler, Y. Xue-Jian, and E. Recknagel. Quantized losses from charged nitrogen clusters. *Z. Phys. D*, 12:283–284, 1989.

[61] T.D. Märk. Cluster ions: Production, detection and stability. *Int. J. Mass Spectrom. Ion Processes*, 79:1–59, 1987.

[62] T.D. Märk and A.W. Castleman Jr. Experimental studies on cluster ions. *Adv. Atom. Mol. Phys.*, 20:65–172, 1985.

[63] T.D. Märk and P. Scheier. Production and stability of neon cluster ions up to Ne_{90}^{+}. *Chem. Phys. Lett.*, 137:245–249, 1987.

[64] O. Echt, D. Kreisle, M. Knapp, and E. Recknagel. Evolution of 'magic numbers' in mass spectra of water clusters. *Chem. Phys. Lett*, 108:401–407, 1984.

[65] U. Nagashima, H. Shinohara, N. Nishi, and H. Tanaka. Enhanced stability of ion-clathrate structures for magic number water clusters. *J. Chem. Phys.*, 84:209–214, 1986.

[66] H.R. Carlon and C.S. Harden. Mass-spectrometry of ion-induced water clusters - an explanation of the infrared continuum absorption. *Appl. Opt.*, 1980.

[67] M. Knapp, O. Echt, D. Kreisle, and E. Recknagel. Electron attachment to water clusters under collision-free conditions. *J. Phys. Chem.*, 91:2601–2607, 1987.

[68] W.A. de Heer, W.D. Knight, M.Y. Chou, and M.L. Cohen. Electronic shell structure of of metal clusters. *Solid State Phys.*, 40:94–181, 1987.

[69] M.R. Hoare. Structure and dynamics of simple microclusters. *Adv. Chem. Phys.*, 40:49–135, 1979.

[70] J.M. Soler, J.J. Saenz, and N. Garcia. The effect of ionizaton on magic numbers of rare-gas clusters. *Chem. Phys. Lett.*, 109:71–75, 1984.

[71] L.G. Christophorou, editor. *Electron-Molecule Interactions and their Application*, volume 1, chapter 6, pages 522–526. Academic Press, 1984.

[72] C.E. Klots and R.N. Compton. Electron attachment to van der Waals polymers of water. *J. Chem. Phys*, 69:1644–1647, 1978.

[73] R. Casero, J.J. Sàenz, and J.M. Soler. Coulomb fragmentation of doubly ionized molecular clusters. *Phys. Rev. A*, 37:1401–1405, 1988.

[74] T.D. Märk, P. Scheier, M. Lezius, G. Walder, and A. Stamatovic. Multiply charged cluster ions of Ar, Kr, Xe, N_2, O_2, CO_2, SO_2 and NH_3: Production mechanism, appearance size and appearance energy. *Z. Phys. D*, 12:279–281, 1989.

[75] O. Echt, D. Kreisle, E. Recknagel, J.J. Sàenz, R. Casero, and J.M. Soler. Dissociation channels of multiply charged van der Waals clusters. *Phys. Rev. A*, 38:3236–3248, 1988.

[76] P. Scheier, A. Stamatovic, and T.D. Märk. Production and properties of singly, doubly and triply charged N_2 clusters. *J. Chem. Phys.*, 88:4289–4293, 1988.

[77] C. Bréchignac, M. Broyer, Ph. Cahuzac, G. Delacretaz, P. Labastie, and L. Wöste. Single-photon double ionization of mercury clusters using synchrotron radiation. *Chem. Phys. Lett.*, 133:45–48, 1987.

[78] W.E. Falconer, A. Büchler, J.L. Stauffer, and W. Klemperer. Molecular structure of XeF_6 and IF_7. *J. Chem. Phys.*, 48:312–318, 1968.

[79] B.D. Kay and A.W. Castleman Jr. Molecular beam electric deflection study of the hydrogen-bonded clusters $(H_2)_n$, $(CH_3OH)_n$ and $(C_2H_5OH)_n$. *J. Phys. Chem.*, 89:4867–4868, 1985.

[80] A.W. Castleman Jr. and B.D. Kay. Evidence for the fragmentation of clusters upon electron impact ionization from electric deflection experiments. *Int. J. Mass Spectrom. Ion Proc.*, 66:217–222, 1985.

[81] R.G. Keesee, R. Sievert, and A.W. Castleman Jr. Mass spectral and electric deflection study of acetic acid clusters and sulfur trioxide/water clusters. *Ber. Bunsenges. Phys. Chem.*, 88:273–274, 1984.

[82] U. Buck, R. Krohne, and S. Schütte. Vibrational excitation of ammonia clusters by helium atom scattering. *J. Chem. Phys.*, 106:109–115, 1997.

[83] H. Deutsch, K. Becker, and T.D. Märk. A semi-empirical method to calculate cross-sections for the electron-impact ionization of clusters. *Int. J. Mass Spectrom. Ion Processes*, 144:L9–L12, 1995.

[84] S. Schütte and U. Buck. Cluster sputtering: Complete fragmentation of large ammonia clusters by photons and electrons. *Appl. Phys.*, in press, 1999.

[85] R.E. Johnson and B.U.R. Sundqvist. Electronic sputtering - From atomic physics to continuum-mechanics. *Physics Today*, 4:28–36, 1992.

[86] B.G. DeBoer and G.D. Stein. Production and electron-diffraction studies of silver metal-clusters in the gas-phase. *Surf. Sci.*, 106:85–94, 1981.

[87] O. Abraham, S.S. Kim, and G.D. Stein. Homogenous nucleation of sulfur-hexafluoride clusters in Laval nozzle molecular-beams. *J. Chem. Phys.*, 75:402–411, 1981.

[88] J. Bauchert and O. F. Hagena. Massenbestimmung ionisierter Agglomerate in kondensierten Molekularstrahlen nach einer elektrischen Gegenfeldmethode. *Z. Naturforschg.*, 20a:1135–1142, 1965.

[89] H. Falter, O.F. Hagena, W. Henkes, and H. v. Wedel. Einfluß der Elektronenenergie auf das Massenspektrum von Clustern in kondensierten Molekularstrahlen. *Int. J. Mass Spectrom. Ion Phys.*, 4:145–163, 1970.

[90] P.U. Andersson and J.B.C. Pettersson. Ionization of water clusters by collisions with graphite surfaces. *Z. Phys. D*, 41:57–62, 1997.

[91] T. Bergmann, T.P. Martin, and H. Schaber. High-resolution time-of-flight mass spectrometers. Part III. Reflector design. *Rev. Sci. Instr.*, 61(10):2592–2600, 1990.

[92] E.W. Schlag, J. Grotemeyer, and R.D. Levine. Do large molecules ionize. *Chem. Phys. Lett.*, 190:521–527, 1992.

[93] W. Stephens. A pulsed mass spectrometer with time dispersion. *Phys. Rev.*, 69, 1946.

[94] A. Cameron and D. Eggers. An ion 'velocitron'. *Rev. Sci. Instrum.*, 19:605–606, 1948.

[95] W. Wiley and I. McLaren. Time-of-flight mass spectrometer with improved resolution. *Rev. Sci. Instrum.*, 26:1150–1157, 1955.

[96] B.A. Mamyrin, V.I. Karataev, D.V. Shmikk, and V.A. Zagulin. The mass-reflectron, a new nonmagnetic time-of-flight mass spectrometer with high resolution. *Sov. Phys.-JETP*, 37:45–48, 1973.

[97] M. Wagner and H. Schröder. A novel four grid ion reflector for saturation of laser multiphoton ionization yields in a time of flight mass spectrometer. *Int. J. Mass Spectrom. and Ion Proc.*, 128:31–45, 1993.

[98] T. Bergmann, T.P. Martin, and H. Schaber. High-resolution time-of-flight mass spectrometer. *Rev. Sci. Instrum.*, 60:792–793, 1989.

[99] I. Schechter, H. Schröder, and K. L. Kompa. A simplified method for absolute MPI cross-section measurements. Application to three-photon non-resonant ionization of Xe at 266 nm. *Chem. Phys. Lett.*, 194:128–134, 1992.

[100] P. Piseri, S. Iannotta, and P. Milani. Parametrization of a two-stage mass spectrometer performing second-order space focusing. *Int. J. Mass. Spectrom. Ion Proc.*, 153:23–28, 1996.

[101] F. Chandezon, B. Huber, and C. Ristori. A new-regime Wiley-McLaren time-of-flight mass spectrometer. *Rev. Sci. Instrum.*, 65:3344–3353, 1994.

[102] D.A. Dahl, J.E. Delmore, and A.D. Appelhans. SIMION PC/PS2 electrostatic lens design program. *Rev. Sci. Instrum.*, 61:607, 1990.

[103] J.D. Jackson. *Classical Electrodynmics.* Wiley, New York, 2 edition, 1975.

[104] K. Simonyi. *Theoretische Elektrotechnik.* VEB Deutscher Verlag der Wissenschaften, Berlin, 9 edition, 1989.

[105] W.A. de Heer and P. Milani. Large ion volume time-of-flight mass spectrometer with position- and velocity-sensitive detection capabilities for cluster beams. *Rev. Sci. Instr.*, 62:670–677, 1991.

[106] R. Meier and P. Eberhardt. Velocity and ion species dependence of the gain of microchannel plates. *Int. J. Mass Spectrom. Ion Proc*, 123:19–27, 1992.

[107] F. Thum and W.O. Hofer. No enhanced electron-emission from high-density atomic collision cascades in metals. *Surf. Sci.*, 90:331–338, 1979.

[108] R. Beuhler and L. Friedmann. Threshold studies of secondary-electron emission induced by macro-ion impact on solid-surfaces. *Nucl. Instrum. Methods*, 170:309–315, 1980.

[109] A.A. Vostrikov, D.Y. Dubov, and M.R. Predtechenskiy. Ionization of water clusters by surface collision. *Chem. Phys. Lett.*, 139:124–128, 1987.

[110] A.A Vostrikov and D.Y. Dubov. Surface induced ionization of neutral water clusters. *Z. Phys. D*, 20:61–63, 1991.

[111] A.A. Vostrikov, A.M. Zadorozhny, D.Y. Dubov, G. Witt, I.V. Kazakova, O.A. Bragin, V.G. Kazakov, V.N. Kikhtenko, and A.A. Tyutin. Ionization of water clusters by collision with surface. *Z. Phys. D*, 40:542–545, 1997.

[112] W. Christen, K.L. Kompa, H. Schröder, and H. Stülpnagel. Ionization of SO_2-clusters by scattering from surfaces. *Ber. Bunsenges. Phys. Chem*, 96:1197–1199, 1992.

[113] H.J.S. Schmidtke. Energieverteilung in molekularen Clustern nach Stößen mit Festkörperoberflächen. Diplomarbeit, Heinrich-Heine Universität Düsseldorf, 1995.

[114] B. Knight, D.M. Goodall, and R.C. Greenhow. Single-photon vibrational photochemistry. *J. Chem. Soc., Faraday Trans.*, 75:841–856, 1978.

[115] D.M. Goodall and R.C. Greenhow. Ionization of water induced by vibrational excitation using a neodymium:glass laser. *Chem. Phys. Lett.*, 9:583–586, 1971.

[116] Gmelin Handbuch. Schwefel, Erg. Bd. 3. *Springer Berlin*, 1980.

[117] G.H. Lee, S.T. Arnold, J.G. Eaton, H.W. Sarkas, K.H. Bowen, C. Ludewigt, and H. Haberland. Negative ion photoelectron spectroscopy of solvated electron cluster anions, $(H_2O)_n^-$ and $(NH_3)_n^-$. *Z. Phys. D*, 20, 1991.

[118] E.W. Rothe and S.Y. Tang. Measurement of electron affinities of O_3, SO_2, and SO_3 by collisional ionization. *J. Chem. Phys.*, 62:3829–3831, 1975.

[119] C.H. Becker and K.T. Gillen. Surface analysis of contaminated GaAs: Comparison of new laser-based techniques with SIMS. *J. Vac. Sci. Technol. A*, 3, 1985.

[120] B. Mason. *Principles of Geochemistry*. John Wiley and Sons, 1952.

[121] F.J. Pettijohn. *Sedimentary rocks*. Harper Brothers, 1948.

[122] Gmelin-Dürrer, editor. *Metallurgie des Eisens*, volume 1, chapter 425a. Verlag Chemie, 1964.

[123] G.A. Somorjai and E.L. Garfunkel. Alkali metals as structure and bonding modifiers of transition metal catalysts. In H.P. Bonzel, A.M. Bradshaw, and G. Ertl, editors, *Physics and chemistry of alkali metal adsorption*, number 57 in Material Science Monographs. Elsevier, 1989.

[124] N.N. Greenwood and A. Earnshaw. *Chemie der Elemente*. VCH, Weinheim, 1990.

[125] R.D. Diehl and R. McGrath. Structural studies of alkali metal adsorption and coadsorption on metal surfaces. *Surf. Sci. Rep.*, 23:43–171, 1996.

[126] H.P. Bonzel, A.M. Bradshaw, and G. Ertl, editors. *Physics and chemistry of alkali metal adsorption.* Number 57 in Material Science Monographs. Elsevier, 1989.

[127] I. Langmuir. Vapor pressure, evaporation, condensation and adsorption. *J. Am. Chem. Soc.*, 54:2798–2832, 1932.

[128] R.W. Gurney. Theory of electrical double layers on adsorbed films. *Phys. Rev.*, 47:479–482, 1935.

[129] J.E. Müller. Theory of the coadsorption of H_2O and CO with K on the Pt(111) surface. In H.P. Bonzel, A.M. Bradshaw, and G. Ertl, editors, *Physics and chemistry of alkali metal adsorption*, number 57 in Material Science Monographs. Elsevier, 1989.

[130] T.E. Madey and B.V. Yakshinskiy. Desorption of alkali atoms and ions from oxide surfaces: Relevance to origins of Na and K in atmoshperes of Mercury and the Moon. *J. Geophys. Res.*, 103:5873–5887, 1998.

[131] K. Wandelt. Work function changes due to alkali-metal adsorption. In H.P. Bonzel, A.M. Bradshaw, and G. Ertl, editors, *Physics and chemistry of alkali metal adsorption*, number 57 in Material Science Monographs. Elsevier, 1989.

[132] M. Kuchler and F. Rebentrost. Effect of adsorbates on second-harmonic generation at simple metal surfaces. *Phys. Rev. Lett.*, 71:2662–2665, 1993.

[133] R. Schlögl. Alkali metals in heterogeneous catalysis. In H.P. Bonzel, A.M. Bradshaw, and G. Ertl, editors, *Physics and chemistry of alkali metal adsorption*, number 57 in Material Science Monographs. Elsevier, 1989.

[134] G. Ertl, S.B. Lee, and M. Wiess. Adsorption of nitrogen on potassium promoted Fe(111) and (100) surfaces. *Surf. Sci.*, 114:527–545, 1982.

[135] F.M. Hoffmann and R.A. de Paola. Anomalous C-O bond weakening of side-on-bonded carbon monoxide on a potassium promoted Ru(001) surface. *Phys. Rev. Lett.*, 52:1697–1700, 1984.

[136] C. Benndorf and T.E. Madey. Interaction of NH_3 with adsorbed oxygen and sodium on Ru(001): Evidence for both local and long-range interactions. *Chem. Phys. Lett*, 101:59–64, 1983.

[137] M. Kiskinovainova, G. Pirug, and H.P. Bonzel. Adsorption and decomposition of H_2O on a K-covered Pt(111) surface. *Surf. Sci.*, 150:319–338, 1985.

[138] L. Surnev. Some aspects of oxygen and alkali metal coadsorption on solid surfaces. In H.P. Bonzel, A.M. Bradshaw, and G. Ertl, editors, *Physics and chemistry of alkali metal adsorption*, number 57 in Material Science Monographs. Elsevier, 1989.

[139] J. Paul, R.A. de Paola, and F.M. Hoffmann. Vibrational spectroscopy of alkal-molecule iteraction and compound formation on metal surfaces. In H.P. Bonzel, A.M. Bradshaw, and G. Ertl, editors, *Physics and chemistry of alkali metal adsorption*, number 57 in Material Science Monographs. Elsevier, 1989.

[140] R. Hemmen, M.E. Kordesch, and H. Conrad. Investigations of the coadsorption of K and CN on Pd(100) and Pd(111) with photoemission and penning spectroscopy. In H.P. Bonzel, A.M. Bradshaw, and G. Ertl, editors, *Physics and chemistry of alkali metal adsorption*, number 57 in Material Science Monographs. Elsevier, 1989.

[141] S. Kennou, S. Ladas, and C. Papageorgopoulos. The interaction of Cs and O_2 on the basal-plane of MoS_2. *Surf. Sci.*, 164:290–304, 1985.

[142] A. Caballero, J.B. Espinos, A. Fernandez, L. Soriano, and A.R. Gonzalez-Elipe. Adsorption and oxidation of K deposited on graphite. *Surf. Sci.*, 364:242–252, 1996.

[143] B. Hellsing, D.V. Chakarov, L. Österlund, V.P. Zhdanov, and B. Kasemo. Photoinduced desorption of potassium atoms from a two dimensional overlayer on graphite. *J. Chem. Phys.*, 106:982–1002, 1997.

[144] M.T. Johnson, H.I. Starnberg, and H.P. Hughes. Electronic-structure of alkali-metal overlayers on graphite. *Surf. Sci.*, 178:290–299, 1986.

[145] C.T. Campbell. Ultrathin metal films and particles on oxide surfaces: structural, electronic and chemisorptive properties. *Surf. Sci. Rep.*, 27:1–111, 1997.

[146] A.W. Grant and C.T. Campbell. Cesium adsorption on TiO_2(110). *Phys. Rev. B*, 55:1844–1851, 1997.

[147] B.E. Hayden and G.P. Nicholson. An ellipsometric study of potassium adsorption on TiO_2(110). *Surf. Sci.*, 274:277–286, 1992.

[148] C. Noguera and G. Bordier. Theoretical approach to interfacial metal-oxide bonding. *J. Phys. III*, 4:1851–1864, 1994.

[149] H. Onishi, C. Egawa, T. Aruga, and Y. Iwasawa. Adsorption of Na atoms and oxygen containing molecules on MgO(100) and (111) surfaces. *Surf. Sci.*, 191:479–491, 1987.

[150] M. Brause, D. Ochs, J. Günster, Th. Mayer, B. Braun, V. Puchin, W. Maus-Friedrichs, and V. Kempter. Cs adsorption on oxide films (Al_2O_3, MgO, SiO_2). *Surf. Sci.*, 383:216–225, 1997.

[151] B. Dillman et al. Adsorption on a polar oxide surface: O_2, C_2H_4 and Na on Cr_2O_3(0001)-Cr(110). *Faraday Discuss.*, 105:295–315, 1996.

[152] H. Öfner, R. Hofmann, J. Kraft, F.P. Netzer, J.J. Paggel, and K. Horn. Metal-overlayer-induced charge transfer effects in thin SiO_2-Si structures. *Phys. Rev. B*, 50:15120–15125, 1994.

[153] M. Szymonski, P. Poradzisz, P. Czuba, J. Kolodziej, P. Piatkowski, J. Fine, L. Tanovic, and N. Tanovic. Electron stimulated desorption of neutral species from (100) KCl surfaces. *Surf. Sci.*, 260:295–303, 1992.

[154] M. Szymonski, T. Tyliszczak, P. Aebi, and A.P. Hitchcock. Photon-stimulated desorption of Na atoms from NaCl following core-level excitations. *Surf. Sci.*, 271:287–294, 1992.

[155] T. Götz, M. Buck, C. Dressler, F. Eisert, and F. Träger. Optical second-harmonic generation by supported metal clusters: Size and shape effects. *Appl. Phys. A*, 60:607–612, 1995.

[156] T. Götz, M. Bergt, W. Hoheisel, F. Träger, and M. Stuke. Non-thermal laser-induced desorption of metal atoms with bimodal kinetic energy distribution. *Appl. Phys. A*, 63:315–320, 1996.

[157] H. Kawano, S. Kamidoi, H. Shimizu, K. Ushimaru, and H. Asada. Temperature-programmed desorption of positive ions and neutral molecules from alkali halide layers deposited on a metal surface. *Appl. Surf. Sci.*, 100/101:174–178, 1996.

[158] J. Lundin, T. Hansson, and J.B.C. Pettersson. Kinetics for potassium desoprtion from an iron oxide catalyst studied by field reversal. *Appl. Surf. Sci.*, 74:343–349, 1994.

[159] D. Liu, N. Seifert, D.J. McClure, A.V. Barnes, R.G. Albridge, N.H. Tolk, and R. Russel. Photon- and electron-stimulated desorption of excited alkali-etal atoms from alkali halide surfaces. *Phys. Rev. B*, 47:1553–1566, 1993.

[160] B.V. Yakshinskiy and T.E. Madey. Photon-stimulated desorption as a substantial source of sodium in the lunar atmosphere. *Nature*, 400:642–644, 1999.

[161] V.N. Ageev, Yu.A. Kuznetsov, and T.E. Madey. Electron-stimulated desorption of sodium atoms from an oxidized molybdenum surface. *Phys. Rev. B*, 58:2248–2252, 1998.

[162] G.M. Loubriel *et al.* Role of F-center diffusion in the electron-stimulated desorption of metal atoms from alkali halides. *Phys. Rev. Lett.*, 57:1781–1784, 1986.

[163] M. Wilde, I. Beauport, K. Al-Shamery, and H.J. Freund. Photoinduced processes on alkali covered surfaces:no desorption from $K/Cr_2O_3(0001)$. *Surf. Sci.*, 390:186–193, 1997.

[164] D. Menzel. Thirty years of mgr: How it came about and what became of it. *Nuc. Instr. and Meth. B*, 101:1–10, 1995.

[165] M. Bauer, S. Pawlik, and M. Aeschlimann. Resonance lifetime and energy of an excited Cs state on Cu(111). *Phys. Rev. B*, 55:10040–10043, 1997.

[166] S. Ogawa, H. Nagano, and H. Petek. Phase and energy relaxation in an antibonding surface state: Cs/Cu(111). *Phys. Rev. Lett.*, 82:1931–1934, 1999.

[167] V.N. Ageev, Yu.A. Kuznetsov, B.V. Yakshinskii, and T.E. Madey. Electron stimulated desorption of alkali metal ions and atoms: Local surface field relaxation. *Nucl. Instrum. Meth. B*, 101:69–72, 1995.

[168] U. Even, P.J. de Lange, H.Th. Jonkman, and J. Kommandeur. Electron emission induced by cluster bombardment of metallic surfaces. *Phys. Rev. Lett.*, 56:965–967, 1986.

[169] D. R. Lide, editor. *CRC Handbook of Chemistry and Physics.* CRC Press, 1994.

[170] N. Agmon. The Grotthuss mechanism. *Chem. Phys. Lett*, 244:456–462, 1995.

[171] D. Marx, M. E. Tuckerman, Jürg Hutter, and M. Parrinello. The nature of the hydrated excess proton in water. *Nature*, 397:601–604, 1999.

[172] J.P. Cowin, A.A. Tsekouras, M.J. Iedema, K. Wu, and G.B. Ellsion. Immobility of protons in ice from 30 to 190K. *Nature*, 398:405–407, 1999.

[173] M. Assel, R. Laenen, and A. Laubereau. Femtosecond solvation dynamics of solvated electrons in neat water. *Chem. Phys. Lett.*, 317:13–22, 2000.

[174] A.A. Mosyak, O.V. Prezhdo, and P.J. Rossky. Solvation dynamics of an excess electron in methanol and water. *J. Chem. Phys.*, 109:6390–6395, 1998.

[175] A. Baltuska, M.F. Emde, M.S. Pshenichnikov, and D.A. Wiersma. Early-time dynamics of the photoexcited hydrated electron. *J. Phys. Chem. A*, 103:10065–10082, 1999.

[176] I. Rips. Electron solvation dynamics in polar liquids. *Chem. Phys. Lett.*, 245:79–84, 1995.

[177] F.H. Long, H. Lu, and K.B. Eisenthal. Femtosecond studies of the presolvated electron: An excited state of the solvated electron. *Phys. Rev. Lett.*, 64:1469–1472, 1990.

[178] D.A. Copeland, N.R. Kestner, and J. Jortner. Excess electrons in polar solvents. *J. Chem. Phys.*, 53:1189–1216, 1970.

[179] H. Haberland, C. Ludewigt, H.-G. Schindler, and D.R. Worsnop. Field detachment of $(H_2O)_2^-$ clustered with rare gases. *Phys. Rev. A*, 36(967-970), 1987.

[180] H. Haberland, C. Ludewigt, and T. Richter. Electron attachment to clusters composed of closed shell hydrogen containing molecules. *Z. Phys. D*, 12:289–290, 1989.

[181] T. Kondow, T. Nagata, and K. Kuchitsu. A mechanism of electron attachment to small clusters. *Z. Phys. D*, 12:291–292, 1989.

[182] R.N. Barnett, U. Landman, C.L. Cleveland, N.R. Kestner, and J. Jortner. Excess electrons in ammonia clusters. *Chem. Phys. Lett.*, 148:249–252, 1988.

[183] K.A. Motakabbir, J. Schnitker, and P.J. Rossky. A comparison of classical and quantum analysis of electron localization sites in liquid water. *J. Chem. Phys.*, 97:2055–2060, 1992.

[184] B.E. Callicoatt, D.D. Mar, V.A. Apkarian, and K.C. Janda. Charge transfer within He clusters. *J. Chem. Phys.*, 05:7872–7875, 1996.

[185] U. Even, I. Schek, and J. Jortner. High-density cluster-surface collisions. *Chem. Phys. Lett.*, 202(3,4):303–307, 1993.

[186] T. Raz and R.D. Levine. On the shattering of clusters by surface impact heating. *J. Chem. Phys.*, 105:8097–8102, 1996.

[187] J.B.C. Petterson and N. Marković. Dynamics of cluster scattering from surfaces. *Chem. Phys. Lett.*, 201:421–426, 1993.

[188] R. Beuhler and L. Friedman. Large cluster ion impact phenomena. *Chem. Rev.*, 86:521–537, 1986.

[189] E. Hendell, U. Even, T. Raz, and R.D. Levine. Shattering of clusters upon surface impact: an experimental and theoretical study. *Phys. Rev. Lett.*, 75:2670–2673, 1995.

[190] H. Vach, M. Benslimane, M. Châtelet, A. De Martino, and F. Pradère. Dynamic zone structure model for the surface scattering of large van der Waals clusters at thermal kinetic energies. *J. Chem. Phys.*, 103:1972–1980, 1995.

[191] N. Marcović and J.B.C. Petterson. Evaporation model of cluster scattering from surfaces. *J. Chem. Phys.*, 100:3911–3924, 1994.

[192] W. Christen, U. Even, T. Raz, and R.D. Levine. The transition from recoil to shattering in cluster-surface impact: an experimental and computational study. *Int. J. Mass Spectrom. Ion Proc.*, 174:35–52, 1998.

[193] T. Raz, U. Even, and R.D. Levine. Fragment size distribution in cluster impact: Shattering versus evaporation by a statistical approach. *J. Chem. Phys.*, 103:5394–5409, 1995.

[194] U. Even, T. Kondow, R.D. Levine, and T. Raz. The shattering of clusters upon surface impact. submitted.

[195] P.M. St. John, R.D. Beck, and R. L. Whetten. Reactions in cluster-surface collisions. *Phys. Rev. Lett.*, 69:1467–1470, 1992.

[196] M. Svanberg and J.B.C. Pettersson. Survival of noble gas clusters scattering from hot metal surfaces. *Chem. Phys. Lett.*, 263:661–666, 1996.

[197] M. Svanberg, N. Marković, and J.B.C. Pettersson. Scattering of large argon clusters from Pt(111) surface with low collision velocities. *Chem. Phys.*, 220:137–153, 1997.

[198] P.U. Andersson, A. Tomsic, M.B. Andersson, and J.B.C. Pettersson. Emission of small fragments during water cluster collisions with a graphite surface. *Chem. Phys. Lett.*, 279:100–106, 1997.

[199] M.B. Någård and J.B.C. Pettersson. Internal excitation of ethanol molecules emitted during cluster-surface collisions. *Chem. Phys. Lett.*, 293:535–540, 1998.

[200] C. Menzel, A. Knöner, and H. Zacharias. Scattering of neutral NH_3 clusters of LiF(100): Angular distributions of nh_3 and small clusters. *Z. Phys. D*, 38:179–184, 1996.

[201] E.W. Becker, R. Klingelhöfer, and H. Mayer. . *Z. Naturforsch.*, 23a:274, 1968.

[202] J. Gspann and G. Krieg. . *J. Chem. Phys.*, 61:4037, 1974.

[203] M. Svanberg, N. Marković, and J.B.C. Pettersson. Energy transfer in water cluster scattering from solid surfaces. *Chem. Phys.*, 201:473–489, 1995.

[204] R.G. Keesee and A.W. Castleman Jr. Thermochemical data on gas-phase ion-molecule association and clustering reactions. *J. Phys. Chem. Ref. Data*, 15:1011–1071, 1986.

[205] H. Aulich, B. Baron, P. Delahay, and R. Lugo. Photoelectron emission by solvated electrons in liquid ammonia. *J. Chem. Phys.*, 58:4439–4443, 1973.

[206] U. Buck and C. Steinbach. Formation of sodium hydroxide in multiple sodium-water cluster collisions. *J. Phys. Chem. A*, 102:7333–7336, 1998.

[207] L. Bewig, U. Buck, S. Rakowsky, M. Reymann, and C. Steinbach. Reaction of sodium clusters with water clusters. *J. Phys. Chem. A*, 102:1124–1129, 1998.

[208] I.V. Hertel, C. Hüglin, C. Nitsch, and C.P. Schulz. Photoionization of $Na(NH_3)_n$ and $Na(H_2O)_n$ clusters: A step towards the liquid phase? *Phys. Rev. Lett.*, 67:1767–1770, 1991.

[209] C.P. Schulz and I.V. Hertel. Solvated atoms in polar solvents. In H. Haberland, editor, *Clusters of atoms and molecules II*, number 56 in Chemical Physics, pages 7–18. Springer, 1994.

[210] R. Takasu, F. Misaizu, K. Hashimoto, and K. Fuke. Microscopic solvation process of alkali atoms in finite clusters: Photoelectron and photoionization studies of $M(NH_3)_n$ and $M(H_2O)_n$ (M=Li, Li^-, Na^-). *J. Phys. Chem. A*, 101:3078–3087, 1997.

[211] R. Takasu, T. Taguchi, K. Hashimoto, and K. Fuke. Microscopic solvation process of single li atom in small water clusters. *Chem. Phys. Lett.*, 290:481–487, 1998.

[212] C.P. Schulz, R. Haugstätter, H.U. Tittes, and I.V. Hertel. Free sodium-water clusters. *Phys. Rev. Lett.*, 57:1703–1706, 1986.

[213] C.P. Schulz, R. Haugstätter, H.U. Tittes, and I.V. Hertel. Free sodium-water clusters: photoionisation studies in a pulsed molecular beam source. *Z. Phys. D*, 10:279–290, 1988.

[214] F. Misaizu, K. Tsukamoto, M. Sanekata, and F. Fuke. Photoionization of clusters of Cs atoms solvated with H_2O, NH_3 and CH_3CN. *Chem. Phys. Lett.*, 188:241–246, 1992.

[215] R. Takasu, K. Hashimoto, and K. Fuke. Study on microscopic solvation process of Li atom in ammonia clusters: photoionization and photoelectron spectroscopies of $M(NH_3)_n$ (M=Li, Li^-). *Chem. Phys. Lett.*, 258:94–100, 1996.

[216] C.P. Schulz, A. Gerber, C. Nitsch, and I.V. Hertel. Spectroscopy of free sodium-ammonia clusters. *Z. Phys. D*, 20:65–67, 1991.

[217] C. Nitsch, C.P. Schulz, A. Gerber, W. Zimmermann-Edling, and I.V. Hertel. Photoionization studies of free sodium ammonia clusters. *Z. Phys. D*, 22:651–658, 1992.

[218] J.V. Coe, G.H. Lee, J.G. Eaton, S.T. Arnold, H.W. Sarkas, K.H. Bowen, C. Ludewigt, H. Haberland, and D.R. Worsnop. Photoelectron spectroscopy of hydrated electron cluster anions, $(H_2O)^-_{n=2-69}$. *J. Chem. Phys.*, 92:3980–3982, 1990.

[219] R.N. Barnett and U. Landman. Hydration of sodium in water clusters. *Phys. Rev. Lett.*, 70:1775–1778, 1993.

[220] K.S. Kim, I. Park, S. Lee, K. Cho, J. Y. Lee, J. Kim, and J.D. Joannopoulos. The nature of a wet electron. *Phys. Rev. Lett.*, 76:956–959, 1996.

[221] K. Fuke, K. Hashimoto, and S. Iwata. Structures, spectroscopies and reactions of atomic ions with water clusters. In I. Priogine and S.A. Rice, editors, *Advances in Chemical Physics*, volume 110, chapter 7. J. Wiley & Sons, 1999.

[222] K. Hashimoto and T. Kamimoto. Theoretical study of microscopic solvation of Li in water clusters: Neutral and cationic $Li(H_2O)_n$ clusters (n=1-6 and 8. *J. Am. Chem. Soc.*, 120:3560–3570, 1998.

[223] F. Misaizu, K. Tsukamoto, M. Sanekata, and K. Fuke. Photoionization and photodissociation stiudies on aluminium-water clusters and their ions. *Z. Phys. D*, 26:S177–179, 1993.

[224] T. M. Di Palma, A. Latini, M. Satta, M. Varvesi, and A. Giardini. Pulsed laser reactive ablation of Al in an ammonia atmosphere: photoionization thresholds and structures of Al-NH_3 clusters. *Chem. Phys. Lett.*, 284:184–190, 1998.

[225] K. Ohshimo, H. Tsunoyama, Y. Yamakita, F. Misaizu, and K. Ohno. Photoionization and density functional study of clusters of alkali metal atoms solvated with acetonitrile molecules, $M(CH_3CN)_n$ (M=Li and Na). *Chem. Phys. Lett.*, 301:356–364, 1999.

[226] H. Abdoul-Carime and C. Desfrancois. Electrons weakly bound to molecules by dipolar, quadrupolar or polarization forces. *Eur. Phys. J. D*, 2:149–156, 1998.

[227] T. M. Di Palma, A. Latini, M. Satta, and A. Giardini-Guidoni. Photoionization thresholds and structures of third group metals clustered with ammonia. *Eur. Phys. J. D*, 4:225–229, 1998.

[228] T. M. Di Palma, A. Latini, M. Satta, and A. Giardini-Guidoni. Molecular beam studies of ammonia clustered with metals produced by pulsed laser reactive ablation. *Int. J. Mass Spec.*, 179/180:319–326, 1998.

[229] K. Hashimoto and K. Morokuma. Ab initio molecular orbital study of $Na(H_2O)_n$ (n=1-6) clusters and their ions. comparision of electronic structure of the 'surface' and 'interior' complexes. *J. Am. Chem. Soc.*, 116:11436–11443, 1994.

[230] K. Hashimoto and K. Morokuma. Ab initio MO study of $Na(NH_3)_n$ (n=1-6) clusters and their ions: A systematic comparison with hydrated Na clusters. *J. Am. Chem. Soc.*, 117:4151–4159, 1995.

[231] K. Codling, L.J. Frasinski, and P.A. Hatherly. On the field ionisation of diatomic molecules by intense laser fields. *J. Phys. B*, 22:L321–L327, 1989.

[232] S. Chelkowski and A.D. Bandrauk. Two-step Coulomb explosions of diatoms in intense laser fields. *J. Phys. B*, 28:L723–L731, 1995.

[233] T. Zuo, S. Chelkowski, and A.D. Bandrauk. Harmonic generation by the H_2^+ molecular ion in intense laser fields. *Phys. Rev. A*, 48:3837–3844, 1993.

[234] H. Schröder, C.J.G.J. Uiterwaal, and K.-L. Kompa. Analytical derivation of the critical internuclear distance for barrier suppression ionization in diatomic molecules. *in preparation*, 1999.

[235] P.L. Silvestrelli and M. Parrinello. Water molecule dipole in the gas and in the liquid phase. *Phys. Rev. Lett.*, 82:3308–3311, 1999.

[236] S.W. Rick, S.J. Stuart, and B.J. Berne. Dynamical fluctuating charge force fileds: Application to liquid water. *J. Chem. Phys.*, 101:6141–6156, 1994.

[237] E.M. Snyder, J. Purnell, S. Wei, S.A. Buzza, and A.W. Castleman Jr. Real-time dynamics of ammonia clusters excited through the $\bar{A}$ state: formation of the protonated cluster ions. *Chem. Phys.*, 207:355–366, 1996.

[238] S. Tomoda and K. Kimura. Proton-transfer potential-energy surfaces of the water dimer cation $(H_2O)_2^+$ in the 1^2A" and 1^2A' states. *Chem. Phys.*, 82:215–227, 1983.

[239] J.B. Fenn and J.B. Aderson. Background and sampling effects in free jet studies by molecular beam measurements. In H.de Leeuw, editor, *Rarefied Gas Dynamics*, volume Suppl.3 Vol.2, pages 311–330. Academic Press, .

[240] J. Vigué, P. Labastie, and F. Calvo. Evidence for $N^{1/3}$ dependence of the sticking cross-section of atoms on small and medium-sized van der Waals clusters. *Eur. Phys. J. D*, 8:265–272, 2000.

[241] O. Echt, S. Morgan, P.D. Dao, R.J. Stanley, and A.W. Castleman Jr. Multiphoton ionization of ammonia clusters with a tunable laser. *Ber. Bunsenges. Phys. Chem.*, 88:217–219, 1984.

[242] K. Stephan, J.H. Futrell, K.I. Peterson, A.W. Castleman Jr., H.E. Wagner, N. Djuric, and T.D. Märk. An electron-impact study of ammonia clusters in a supersonic molecular beam: Appearance potentials of NH_4^+, $(NH_3)_2H^+$, $(NH_3)_3^+$, $(NH_3)_3H^+$ and $(NH_2NH3)^+$. *Int. J. Mass Spectrom. Ion Phys.*, 44:167–181, 1982.

[243] Düren R., Lackschewitz U., Milošević S., and Waldapfel H.-J. Scattering on anisotropic potential energy surfaces: Na(3^2S) and Na(3^2P) with H_2O. *Chem. Phys.*, 140:199–206, 1990.

[244] Barnett R.N. and Landman U. Water adsorption and reactions on small sodium chloride clusters. *J. Phys. Chem.*, 100:13950–13958, 1996.

[245] O. Frey-Kienel. *Handbuch der Dünnschichttechnologie*. VDI-Verlag, 1987.

[246] R. Miranda. The mechanisms of the alkali-enhanced oxidation of semiconductors. In H.P. Bonzel, A.M. Bradshaw, and G. Ertl, editors, *Physics and chemistry of alkali metal adsorption*, number 57 in Material Science Monographs. Elsevier, 1989.

[247] R.G. Jahn. *Physics of electric propulsion.* McGraw-Hill, 1968.

[248] D.M. Murphy *et. al.* Influence of sea-salt on aerosol radiative properties in the Southern Ocean marine boundary layer. *Nature*, 1998.

[249] A.M. Zadorozhny, A.A. Tyutin, G. Witt, N. Wilhelm, Wälchli U., J.Y.N. Cho, and W.E. Swartz. Electric-field measurements in the vicinity of Noctilucent Clouds and PMSE. *Geophys. Res. Lett.*, 20:2299–2302, 1993.

[250] F. Balsiger, E. Kopp, M. Friedrich, K.M. Torkar, and U. Wälchli. Small-scale structure of O_2^+ and proton hydrates in a Noctilucent Cloud and Polar Mesospheric Summer Echo of August 9/10 1991 above Kiruna. *Geophys. Res. Lett.*, 20:2315–2318, 1993.

[251] R.C. Whitten and I.G. Poppoff. *Physics of the lower ionosphere*. Prentice-Hall, 1965.

[252] A.L. Sprague, R.W.H. Kozlowski, and D.M. Hunten. Caloris basin: An enhanced source for potassium in mercury's atmosphere. *Science*, 249:1140–1143, 1990.

[253] A.L. Sprague, R.W.H. Kozlowski, D.M. Hunten, W.K. Wells, and F.A. Grosse. The sodium and potassium atmosphere of the moon and its interaction with the surface. *Icarus*, 96:7–42, 1992.

[254] K.S. Noll, R.E. Johnson, M.A. McGrath, and J.J. Caldwell. Detection of SO_2 on Callsito with the Hubble Space Telescope. *Geophys. Res. Lett.*, 24:1139–1142, 1997.

[255] D. MacGorman and W.D. Rust. *The electrical nature of storms.* Oxford University Press, New York, 1998.

[256] H.R. Pruppacher and J.D. Klett. *Microphysics of Clouds and Precipitation.* Kluwer Academic Publishers, Dordrecht, 1996.

[257] A.A. Viggiano, C.A. Deakyne, F. Dale, and J.F. Paulson. Neutral reactions in the presence of alkali ions. *J. Chem. Phys.*, 87:6544–6552, 1987.

[258] Gregoire G., Mons M., Dedonder-Lardeux C., and Jouvet C. Is NaI soluble in water clusters? *Eur. Phys. J. D*, 1:5–7, 1998.

[259] R. Knochenmuss and S. Leutwyler. Proton transfer from 1-naphtol to water: Small clusters to the bulk. *J. Chem. Phys.*, 91:1268–1278, 1989.

[260] S.K. Kim, J.J. Breen, D.M. Willberg, L.W. Peng, A. Heikal, J.A. Syage, and A.H. Zewail. Solvation ultrafast dynamics of reactions. 8. Acid-base reactions in finite sized clusters of naphthole in ammonia, water and piperidine. *J. Chem. Phys.*, 99:7421–7435, 1995.

[261] T. Hornung, R. Meier, D. Zeidler, K.L. Kompa, D. Proch, and M. Motzkus. Optimal control of one- and two-photon transitions with shaped femtosecond pulses. submitted to Appl. Phys. B, 2000.

[262] A. Assion, T. Baumert, M. Bergt, T. Brixner, B. Kiefer, V. Seyfried, M. Strehle, and G. Gerber. Control of chemical reactions by feedback-optimized phase-shaped femtosecond laser pulses. *Science*, 1998.

[263] R. de Vivie-Riedle and K. Sundermann. Application of optimal control strategies for molecular reactions. Nonlinear Optics, accepted, 2000.

[264] Rabitz H., de Vivies-Riedle R., Motzkus M., and Kompa K.L. Chemistry - whither the future of controlling quantum phenomena? *Science*, 288:824–828, 2000.

Acknowlegements

Hier thront der Mann auf einem Sitze
Und ißt z. B. Hafergrütze.
Der Löffel führt sie in den Mund,
Sie rinnt und rieselt durch den Schlund.
Sie wird, indem sie weiterläuft,
Sichtbar im Bäuchlein angehäuft. –

So blickt man klar, wie selten nur,
Ins innre Walten der Natur. –

Wilhelm Busch
Maler Klecksel

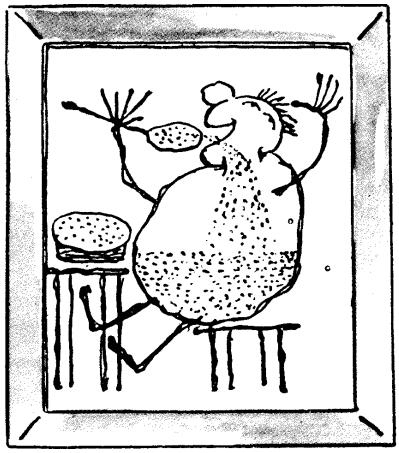

This work wouldn't have been possible without the help from others. In this context, the excellent support from the people of the Max-Planck-Institut für Quantenoptik and from the circle of my friends has to be mentioned. All of them, especially my family and Amalia, I want to thank sincerely.
In particular I thank Karl-Ludwig Kompa for his staunch, personal support throughout this venture, and for the excellent research opportunities during this time. Thanks are due to Sighart Fischer and Dietrich Menzel as my advisors from the Technische Universität München. I am especially indebted to my tutor Hartmut Schröder. We share the enthusiasm for new ideas and simple models. I greatly profited from the collaboration with this dedicated scientist. Much is owed to friends and colleagues from my group who contributed directly to the present work, namely Wolfgang Christen, Hans-Jürgen Schmidtke, Bernd Witzel, Kees Uiterwaal, Michael Dürr, Markus Raschke and Ralph Ernstorfer. Especial thank deserve Raphael D. Levine, Tamar Raz and Uzi Even for showing me the meaning of international collaboration, for stimulating discussions as well as for theoretical and experimental support.
Last but not least, I am pleased to acknowledge support from my colleagues of the Laser Chemistry Department, our technical staff and the machine shop, all of whom I could rely on at all times. Hey, I enjoyed my time with you.

Vita

Christoph Gebhardt
www.Christoph-Gebhardt.de

28.08.1969	geboren in München
1976 – 1980	Grundschule
1981 – 1989	Gymnasium Fürstenried-West, München
1989 – 1990	Gebirgsfernmeldelehrkompanie 8, Starnberg
1990 – 1996	Julius-Maximilians-Universität Würzburg, Fakultät für Physik
08/1992	Vordiplom in Physik
09/1992 – 08/1993	Julius-Maximilians-Universität Würzburg
08/1993 – 08/1994	Graduate School: State University of New York at Stony Brook, USA
05/1994	Master of Arts (SUNY at Stony Brook)
09/1994 – 04/1996	Julius-Maximilians-Universität Würzburg
04/1996	Diplom in Physik
gegenwärtig	Max-Planck-Institut für Quantenoptik, Garching bei Prof. Dr. Dr. h.c. K.L. Kompa, Abteilung Laserchemie